# Semi-submersible structural design

## Strength and fatigue assessment of a twin-pontoon semi-submersible with different bracing configurations

**Master of Science**
**Thesis**

**D.J.P. Vis**

TU Delft

Huisman

# Semi-submersible structural design

## Strength and fatigue assessment of a twin-pontoon semi-submersible with different bracing configurations

by

D.J.P. Vis

to obtain the degree of Master of Science at
the Delft University of Technology,
to be defended publicly on Thursday October 14, 2021 at 12:00 PM.

Student number: 4962273

Project duration: November 16, 2020 – October 14, 2021

Thesis committee:

| | |
|---|---|
| Ing. A. Kalloe | Huisman Equipment, supervisor |
| Ir. E. Romeijn | Huisman Equipment |
| Dr.ir. J.H. den Besten | TU Delft, supervisor |
| Ir. G. Bufalari | TU Delft |
| Prof.dr. M. Veljkovic | TU Delft |
| Dr. C.L. Walters | TU Delft |

An electronic version of this thesis is available at http://repository.tudelft.nl/.

Cover photo is the 'Shen Lan Tan Suo' semi-submersible of CMHI, from http://photo.jstv.com/a/20210121/161120899234.shtml.

TU Delft

Huisman

# Preface

The structural performance of different bracing configurations for a twin-pontoon semi-submersible is analysed in this thesis. In addition, fatigue resistance similarity is studied and a detailed fatigue assessment is performed. This thesis was executed at the Mechanical Engineering department of Huisman Equipment B.V. in Schiedam as graduation assignment for the M.Sc. study Offshore & Dredging Engineering at the Delft University of Technology.

First, I would like to thank Asif Kalloe, my daily supervisor at Huisman Equipment. The involvement and support helped me much during the assignment. Particularly, his expertise in ANSYS helped me to set-up and analyse structures in FEA. I would also like to thank Eric Romeijn at Huisman Equipment for his guidance, especially regarding the approach of the assignment. I also appreciate the support of Henk den Besten as supervisor at the Delft University of Technology.

Finally, I would like to thank family and friends for their support during the graduation period.

*D.J.P. Vis*
*Maasdijk, September 2021*

# Abstract

Semi-submersibles are common vessels in the offshore sector. These vessels usually have a bracing structure to restrain floater movement and to support the deckbox structure. The bracing configuration influences strength, fatigue and other semi-submersible parameters. The first assignment objective was to study the structural design impact on a twin-pontoon semi-submersible when applying different bracing configurations. The influence of bracings on characteristic responses, defined as loading and accelerations governing for the strength and fatigue of semi-submersibles, was studied first. Generally, an increase in bracing diameter results in an increase in characteristic response. However, bracings do not affect characteristic responses much, as differences below 11% are observed. Global strength assessments in the ultimate and accidental limit states were performed using finite element analyses (FEA) for different bracing configurations. Each bracing configuration differentiates itself being beneficial for certain load cases, or is beneficial regarding fatigue sensitive locations. The structural design of semi-submersibles with different bracing configurations were modified to have similar structural performance compared to a reference semi-submersible. The bracing configurations were evaluated based on payload, structural centre of gravity, structural redundancy and fatigue. Generally, the presence of transverse horizontal bracings affects structural performance most significantly, since a payload reduction of 22% is observed when not present due to the dominant splitting force load case and ineffective load path. Adding diagonal bracings in the horizontal or vertical plane, reduces column and deckbox loading for the longitudinal shear, torsion moment and inertia load cases, resulting in a payload increase up to 5%. Omitting braces results in the lowest amount of fatigue sensitive locations. However, since the columns and deckbox structure needs strengthening, welding volume at other fatigue sensitive locations increases, which affects fatigue negatively. The bracing configuration selection should be merely based on the semi-submersible's requirements. Therefore, the designer should first rank the requirements after which a bracing configuration can be designed.

Fatigue of semi-submersibles remains a challenge in today's practice, since service cracks are frequently found during inspections. Fatigue resistance is usually determined by S-N curves based on tested small-scale specimens (SSS). Large-scale specimen (LSS) and full-scale specimen (FSS) fatigue tests are performed less frequent. Semi-submersible tubular brace-column and brace-brace fatigue resistance is typically determined by LSS tubular joint tests. The fatigue resistance similarity between SSS planar joints and LSS tubular joints was examined by the hot spot stress and averaged effective notch stress concepts. Five different LSS tubular joint fatigue tests, derived from literature, were studied by shell FEA and volume FEA. Weld geometry in tubular joint shell FEA can affect results significantly. When not present, bending stresses are overestimated up to 208%. For most LSS tubular joints, similarity with respect to SSS planar joints is increased for the average effective notch stress concept, compared to the hot spot stress concept. Most LSS tubular joints fit inside the average effective notch stress SSS planar joint fatigue resistance data. Dissimilarity for divergent LSS tubular joints can be related to different modelling assumptions compared to actual conditions, where differences in boundary conditions and weld geometries is most likely. Fatigue resistance similarity, expressed as the strength scatter index and intercept $\log_{10}(C)$, of LSS tubular joints is increased compared to hot spot fatigue resistance. Differences in slope $m$ are similar. A SSS planar joint based design S-N curve is therefore applicable for tubular fatigue sensitive locations of semi-submersibles and other structures. Moreover, this study increases the applicability of the average effective notch stress as fatigue assessment concept. More LSS tubular joints should be studied to demonstrate similarity with higher confidence.

To accurately estimate fatigue lifetime, a detailed fatigue assessment is performed of a tubular brace-brace connection. Multi-axial loading was studied at global and local level, however at the critical saddle location, mode-I stress dominates. Therefore, multi-axial fatigue was not considered. The structural stress, $S_s$, average effective notch stress, $S_e$, and hot spot stress, $S_h$, were applied as fatigue assessment concepts. The fatigue assessment of the simple tubular joint concluded insufficient fatigue lifetime. Stress intensities at the critical saddle location were reduced by implementing internal ring-stiffeners, classifying the connection as a complex tubular joint. Stress reduction factors of 3.9 and 4.1 were achieved, resulting in fatigue damages below 1, thus acceptable. Compared to common fatigue assessment concepts, the detailed $S_s$ and $S_e$ fatigue assessments reduce the possibility of service cracks and maintenance and inspection work can be planned more precise. However, DNV-GL and IIW guidelines state a fatigue resistance slope change is present above $10^7$ cycles (N), which is not accounted for in $S_s$ and $S_e$. To study the presence of a slope change and to possibly establish a more accurate fatigue damage estimation for $S_s$ and $S_e$, a recommendation for further research is to include more fatigue tests for $N > 10^7$, from which a design S-N curve can be derived.

# Nomenclature

**Symbols**

| | |
|---|---|
| $a_{ii}$ | hydrodynamic added mass coefficient |
| $a_L$ | longitudinal deck mass acceleration |
| $a_T$ | transverse deck mass acceleration |
| $a_V$ | vertical deck mass acceleration |
| $A_{wl}$ | water plane area |
| $b_{ii}$ | hydrodynamic damping coefficient |
| $C$ | fatigue resistance intercept |
| $C_a$ | added mass coefficient |
| $C_{bw}$ | weld load carrying stress coefficient |
| $C_D$ | drag coefficient |
| $c_{ii}$ | hydrostatic stiffness coefficient |
| $C_M$ | inertia coefficient |
| $D$ | chord outer diameter |
| $d$ | brace outer diameter |
| $E$ | Young's modulus |
| $F$ | force |
| $F_{comb}$ | combined splitting and longitudinal shear force |
| $F\text{-}K$ | Froude-Krylov loading |
| $F_L$ | longitudinal shear force |
| $F_s$ | splitting force |
| $g$ | gravitational earth acceleration |
| $GM$ | metacentre height |
| $H_S$ | significant wave height |
| $h_w$ | weld height |
| $I$ | second moment of inertia |
| $KC$ | Keulegan-Carpenter number |
| $k_\zeta$ | wave number |
| $LCG$ | longitudinal centre of gravity |
| $l_e$ | extended weld length |
| $l_w$ | weld length |
| $m$ | fatigue resistance slope |
| $M$ | moment |
| $M_T$ | torsion moment |
| $n$ | normal vector |
| $N_f$ | number of cycles until failure |
| $p$ | pressure |
| $r$ | radial coordinate |
| $R_e$ | Reynolds number |
| $r_{lr}$ | loading and response ratio |
| $r_s$ | structural bending stress ratio |
| $S_e$ | average effective notch stress range |
| $S_h$ | hot spot stress range |
| $S_s$ | structural stress range |
| $S_{eff}$ | effective stress range |
| $S_\zeta$ | wave spectrum |
| $T$ | chord wall thickness |
| $t$ | brace wall thickness |
| $T_p$ | peak period |
| $T_z$, $T_0$ | zero-up crossing period |
| $T_\sigma$ | scatter index |
| $V$ | shear force |

| | |
|---|---|
| $\alpha$ | (half) notch angle |
| $\beta$ | stress angle |
| $\gamma$ | loading & response ratio coefficient |
| $\nabla$ | displaced volume |
| $\delta$ | groove angle |
| $\varepsilon$ | strain |
| $\varepsilon_{R,\zeta}$ | phase difference response w.r.t. wave |
| $\zeta_a$ | wave amplitude |
| $\eta$ | usage factor |
| $\eta_p$ | permissible usage factor |
| $\theta$ | brace in-plane angle |
| $\lambda_{a,s}$ | eigenvalue of (anti-)symmetric $\sigma_n$ part |
| $\mu$ | wave heading |
| $\mu_{a,s}$ | amplitude of (anti-)symmetric $\sigma_n$ part |
| $\nu$ | Poisson's ratio |
| $\rho$ | (real) weld notch radius |
| $\rho^*$ | material characteristic length |
| $\rho_w$ | water density |
| $\sigma_b$ | bending stress |
| $\sigma_{bw}$ | weld load carrying stress |
| $\sigma_e$ | effective notch stress |
| $\sigma_{eq}$ | equivalent (von-Mises) stress |
| $\sigma_f$ | structural field stress |
| $\sigma_h$ | hot spot stress |
| $\sigma_m$ | membrane stress |
| $\sigma_n$ | weld notch stress distribution |
| $\sigma_{nom}$ | nominal stress |
| $\sigma_s$ | structural stress |
| $\sigma_{se}$ | self-equilibrating stress |
| $\sigma_{yield}$ | yield strength |
| $\sigma_{\theta\theta}$ | structural membrane stress |
| $\phi$ | potential |
| $\chi_{s,a}$ | eigenvalue coefficient of (anti-)symmetric $\sigma_n$ part |
| $\omega_\zeta$ | wave frequency |

**Abbreviations**

| | |
|---|---|
| A.B. | above baseline |
| AF | axial forcing |
| ALS | accidental limit state |
| CHS | circular hollow section |
| CLB | confidence lower bound |
| CSYS | coordinate system |
| CUB | confidence upper bound |
| DAF | dynamic amplification factor |
| DS | double sided |
| ECA | engineering critical assessment |
| EFL | equivalent fatigue load |
| FEA | finite element analysis |
| FLS | fatigue limit state |
| FSS | full scale specimen |
| HCF | high cycle fatigue |
| IPB | in-plane bending |
| LSS | large scale specimen |
| LSW | light ship weight |
| MCF | medium cycle fatigue |
| OPB | out-of-plane bending |
| PM | Pierson-Moskowitz |
| RAO | response amplitude operator |
| SCF | stress concentration factor |
| SHS | square hollow section |
| SLS | serviceability limit state |
| SSS | small scale specimen |
| ULS | ultimate limit state |
| VCG | vertical centre of gravity |
| WSD | working stress design |

# Table of Contents

# 1 Introduction

## 1.1 Semi-submersibles

Semi-submersibles can operate in a large range of draughts and are known for their large stability capacity, favourable motions and large deck space. Therefore, these vessels are widely used in the oil and gas industry for drilling, lifting and pipeline laying operations. Nowadays, semi-submersibles are also used in the renewable energy sector, such as floating wind turbines and the Windfarm Installation Vessel, currently under development at Huisman. A semi-submersible usually has two pontoons submerged below the waterline. These pontoons provide buoyancy and are connected to a number of columns that support the deckbox, which is positioned above the waterline. Bracings are also usually present between the columns to restrain the movement of the columns and pontoons and to support the deckbox structure. Figure 1 shows semi-submersibles, where bracings are highlighted.

The semi-submersible structure is constantly loaded by static loads, such as self-weight and hydrostatic pressures. At sea, the vessel is also loaded dynamically by fluctuating wave and wind loads, as well as inertia loads due to vessel motions. During operation, operational loads occur, such as crane and deck loads. The structural performance of floating structures is generally checked for the following limit states: serviceability limit state (SLS), ultimate limit state (ULS), accidental limit state (ALS) and fatigue limit state (FLS). The SLS applies to mild sea conditions under normal use and ensures durability, such as acceptable deflections, vibrations and temperatures. The ULS is the limit state to verify the structure's ability to withstand maximum environmental loads, such as large wave and wind loads. The ALS is used to check structural integrity when accidental loads occur, such as falling objects, fire, flooding, and collisions. The FLS is usually a governing limit state with respect to structural details subjected to cyclic loading where relative large stresses occur.

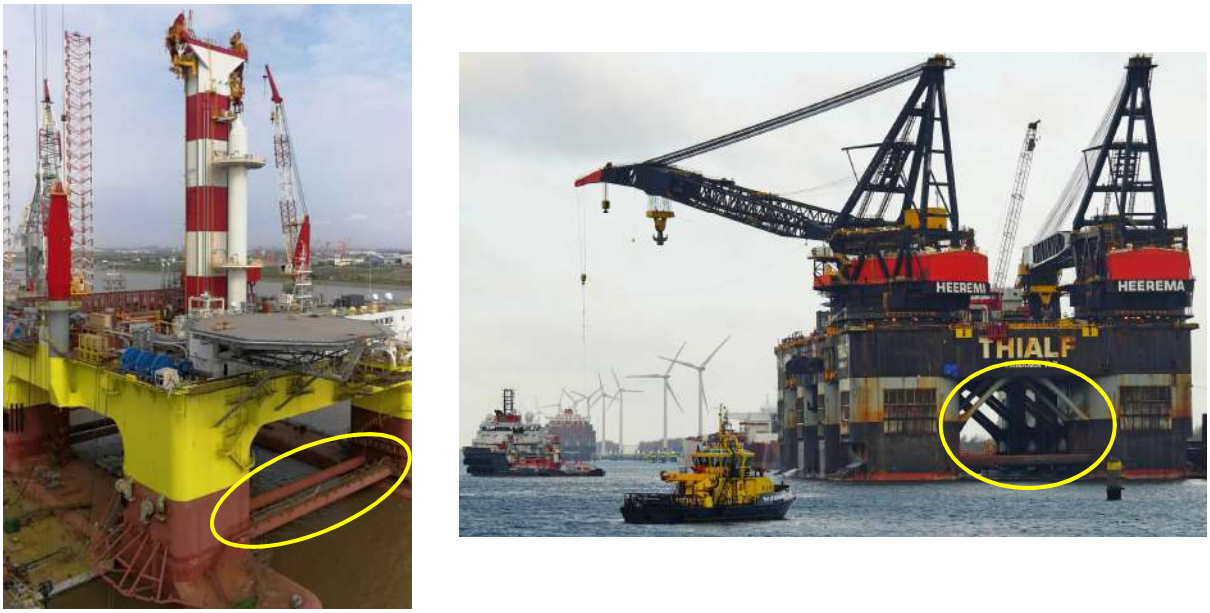


*Figure 1: Semi-submersible drilling platform (left) and semi-submersible crane vessel (right) [1], bracings highlighted in yellow*

## 1.2 Problem statement

The literature review [2] identified gaps between studied literature and assignment objectives. The gaps form the problem statement as reported below per topic.

**Bracing configurations**
The bracing configuration influences strength, fatigue and other semi-submersible parameters, such as payload, structural vertical centre of gravity (VCG) and redundancy. No references regarding semi-submersible design motivation were found during the literature review. Semi-submersible designers do not state why their design is advantageous with respect to payload, redundancy, strength or fatigue. Therefore, no referenced based conclusions can be made about the evolution of semi-submersibles and design choices, such as the bracing configuration.

**Fatigue assessment**
The FLS of semi-submersibles remains a challenge in today's practice [2]. Service cracks are frequently found in semi-submersibles during inspections, especially at the fatigue sensitive brace-column and brace-brace connections. These fatigue sensitive locations are critical with respect to the FLS due to geometric stress intensities, resulting from change in structure stiffness properties and structure discontinuity. Moreover, welded joints introduce stress intensities due to welding defects, notched geometry and stiffness changes. When a crack is found, an engineering critical assessment (ECA) must be performed to determine if the crack size is within acceptable limits. Otherwise, the crack must be repaired by grinding and re-welding.

The literature review identified fatigue sensitive locations of semi-submersibles. Some detailed structural models of brace-column, brace-brace and column-pontoon connections were found in literature. However, stress distributions are difficult to observe based on single stress contour plots. In addition, parametric hot spot SCF's at connections are not applicable due to geometric and loading differences. A detailed connection design must therefore be made and finite element analysis (FEA) is needed to obtain accurate stress results at the fatigue sensitive locations.

**Fatigue resistance similarity**
Fatigue resistance is usually determined using S-N curves for specific structural details, in which stress range is plotted against the number of cycles. These S-N curves are mostly based on fatigue tests of welded joints at small scale, also known as small-scale specimen (SSS). Because of the larger costs, less fatigue tests are done using large-scale specimen (LSS), or full-scale specimen (FSS). Also, LSS and FSS tests are performed for a specific structure, therefore cannot be applied as universal as SSS tests. Regarding semi-submersibles, if the bracings and columns are tubular members, fatigue resistance of the brace-column and brace-brace connection is typically based on LSS tubular joint fatigue tests. The literature review partly focused on fatigue resistance similarity between SSS planar joints and LSS tubular joints using the hot spot stress as fatigue assessment concept. The scatter of the fatigue resistance data, defined as the vertical offset between the 10% and 90% probability of survival, was considered large. This may be due to residual stress and local notch effects not accounted for by the hot spot stress concept, differences in load-carrying and non-load-carrying joints, thickness differences between specimens and different stress ratios. Because of the large scatter of SSS planar joints and LSS tubular joints, similarity seems lacking. Possibly, the hot spot stress used as fatigue assessment concept is one of the reasons.

## 1.3 Assignment objectives

**Bracing configurations**
Huisman Equipment aims to derive rules of thumb for the structural design of twin-pontoon semi-submersibles when applying different bracing configurations. For example, adding vertical diagonal bracings, shown on the right of Figure 1, reduces stress in columns and deckbox, therefore plating can be reduced at certain areas, but by how much?

**Fatigue assessment**
Huisman Equipment is also interested in applying detailed fatigue assessments to accurately estimate fatigue damages of fatigue sensitive locations, such as those mentioned in the problem statement.

**Fatigue resistance similarity**
Fatigue resistance similarity between SSS planar joints and LSS tubular joints is studied based on the average effective notch stress concept. Since the average effective notch stress concept includes more information regarding geometry and loading & response compared to the hot spot stress concept, it is expected that similarity between SSS planar joints and LSS tubular joints increases. If fatigue resistance similarity is proven between SSS planar joints and LSS tubular joints, a SSS planar joint based design S-N curve can be used for tubular joints as well, such as tubular brace-column connections. This S-N curve can be used for the fatigue assessment and increases the applicability of the average effective notch stress concept in fatigue design.

## 1.4 Main research question

The following main question is formulated:
*What is the impact of different bracing configurations on the structural design of a twin-pontoon semi-submersible in terms of weight, VCG, payload, structural redundancy and fatigue, and what is the fatigue lifetime of a critical connection when one bracing configuration is selected?*

## 1.5 Research plan

**Bracing configurations**
Different bracing configurations are evaluated through FEA. A twin-pontoon semi-submersible, designed by Huisman Equipment, is used as semi-submersible design and reference case. Studied during the literature review, the ULS and ALS are most appropriate for evaluating different bracing configurations. Criteria regarding yielding and buckling are applied to check stresses derived from FEA against usage factors. Stresses should be iterated to similar usage factors as the reference semi-submersible to compare semi-submersible structural designs with different bracing configurations. The locations which are checked may shift, since some bracing configurations have different load paths, resulting in different hot spot locations. Finally, the different bracing configurations are compared based on total structural weight, structural VCG, payload, structural redundancy and fatigue. Structural redundancy is related to the number of members and different load paths in the ALS. The FLS is evaluated qualitatively by the number of hot spots and the global loading a member or component must absorb. For example, if global loading for a member or component is unfavourable, i.e. highly loaded and/or in disadvantageous directions, the fatigue lifetime at detail level becomes a challenge and therefore the bracing configuration is also unfavourable regarding the FLS.

**Fatigue assessment**
Based on the comparison between different bracing configurations mentioned above, one favourable bracing configuration is selected for the fatigue assessment. Environmental loading combined with FEA result in stress ranges. The fatigue assessment concepts applied are the structural stress concept, developed by P. Dong et al. [3], and average effective notch stress concept, developed by H. den Besten [4]. Compared to common engineering fatigue assessment concepts, such as the nominal and hot spot concepts, the applied fatigue assessment concepts are more detailed regarding the loading & geometry information involved. Also, the applied fatigue assessment concepts are less sensitive to mesh specification, since nodal forces and moments from FEA are used to derive stresses analytically. Moreover, proven by fatigue resistance data plots of the structural stress concept and average effective notch stress concept, fatigue resistance scatter is lower compared to the nominal and hot spot concepts. Therefore, the applied fatigue assessment concepts should estimate fatigue damage more accurately.

Due to combined wave loading of sea and swell waves and due to structure geometry, multi-axial stresses may occur at the fatigue sensitive location. Based on the presence of a multi-axial stress state, the fatigue assessment methodology is derived.

**Fatigue resistance similarity**
LSS tubular joint fatigue tests found in literature are examined in detailed FEA to derive stress ranges. The tubular specimens are modelled based on the reported geometry and boundary conditions specified by the authors. Literature guidelines are used to set up the analyses. Hot spot SCF's are compared with the author's measured SCF's to verify the FEA. Weld toe notch stress distributions calculated by a semi-analytical formulation and volume FEA are also compared. If similarity is observed, a SSS planar joint based design S-N curve can be used for the fatigue assessment. Hot spot and average effective notch stress ranges of SSS planar joints are provided by TU Delft.

## 1.6 Thesis structure

The thesis structure is similar compared to the topics described above and is structured into 4 main chapters:

- Chapter 2: Semi-submersible loading and responses. Semi-submersible hydromechanical loading and responses are studied. This chapter forms the basis for strength and fatigue assessments.
- Chapter 3: Global strength assessment. Environmental loading in the ULS and ALS is derived. The results of the global strength assessment of the reference semi-submersible through FEA is reported first, after which the bracing configurations are analysed and evaluated.
- Chapter 4: SSS planar joint and LSS tubular joint fatigue resistance similarity. Fatigue resistance of LSS tubular joints are analysed through FEA and compared to SSS planar joints based on the hot spot stress concept and average effective notch stress concept.
- Chapter 5: Fatigue assessment. The fatigue damage of a brace-brace connection is estimated by the structural stress concept and average effective notch stress concept.

The thesis conclusion, discussion and recommendations following from the 4 main chapters are reported in Chapter 6 and 7.

# 2 Semi-submersible loading and responses

## 2.1 Hydromechanical loading

Hydromechanical loading of semi-submersibles is described in this chapter. This forms the basis for the strength and fatigue assessment performed in this study. Hydromechanical loads are the collective term of forces and moments caused by water loading. Hydromechanical loads are the superposition of the wave, $F_w$ and $M_w$, diffraction, $F_d$ and $M_d$, radiation, $F_r$ and $M_r$, and hydrostatic $F_s$ and $M_s$, loading types as shown in Eq.2-1 and Eq.2-2.

$$F = F_w + F_d + F_r + F_s \qquad \text{Eq.2-1}$$

$$M = M_w + M_d + M_r + M_s \qquad \text{Eq.2-2}$$

Hydromechanical loading is obtained by integrating the Bernoulli pressure formulation [5], Eq.2-3, over the surface area described by Eq.2-4 and Eq.2-5. In the force and moment expression, $\{n\}$ is the outward normal vector with respect to surface $dS$ and $\{r\}$ is the position vector of the surface with respect to the origin of the coordinate system. In the Bernoulli equation $\phi$ is the potential the pressure is calculated for. The different potentials used in this pressure calculation are the wave, diffraction and radiation potentials. The wave potential describes the undisturbed flow of wave particles, whereas the diffraction potential accounts for diffraction pressures when waves encounter a floating structure. The radiation potential represents the movement of water due to motions of the floating structure, resulting in pressures. More background on these types of potentials is described later in this chapter.

Hydromechanical forces are normally derived up to second order with respect to wave amplitude, i.e. $F \approx F^0 + F^1 + F^2$. The zeroth order force is the constant force the structure experiences, such as buoyancy (term (3) in the Bernoulli equation) and, if applicable, constant current forces. The first order force results from integrating the dynamic pressure (term (1) in the Bernoulli equation) up to the mean water level for the considered potentials. Lastly, second order terms result from integrating the constant hydrostatic force from mean water level up to the instantaneous surface elevation and integrating the velocity term (term (2) in the Bernoulli equation) up to the mean water level for the considered potentials.

$$p = \underbrace{-\rho_w \frac{\partial \phi}{\partial t}}_{(1)} \underbrace{-\frac{1}{2}\rho_w (\nabla\phi)^2}_{(2)} \underbrace{-\rho_w g z}_{(3)} \qquad \text{Eq.2-3}$$

$$[F] = -\iint_S (p \cdot \{n\})\, dS \qquad \text{Eq.2-4}$$

$$[M] = -\iint_S \left(p \cdot (\{r\} \times \{n\})\right) dS \qquad \text{Eq.2-5}$$

The different types of hydromechanical loading are explained in the chapters below.

### 2.1.1 Hydrostatic loading

Buoyancy loads and hydrostatic stiffness are classified as hydrostatic loads are forces and moments that do not change over time.

**Buoyancy**
Buoyancy loads on a submerged body are upward forcing, resulting from water pressure that increases linearly with water depth. The total buoyancy force is the weight of the displaced fluid as shown in Eq.2-6, with $\rho_w, g$ and $\nabla$ are the water density, gravitational acceleration and displaced volume, respectively.

When the semi-submersible mass distribution and deckload is also taken into account, the load combination, results in static moments and therefore structure deformations illustrated in Figure 2. Transverse bracings are tensile loaded due to the moment around the longitudinal axis. Mean tensile loading affects fatigue damage negatively, further discussed in Chapter 5. Depending on draught, bracing displacement and bracing structure weight, bracings are laterally loaded, resulting in global bending moments along the span.

$$F_B = \rho_w g \nabla \quad \text{Eq.2-6}$$

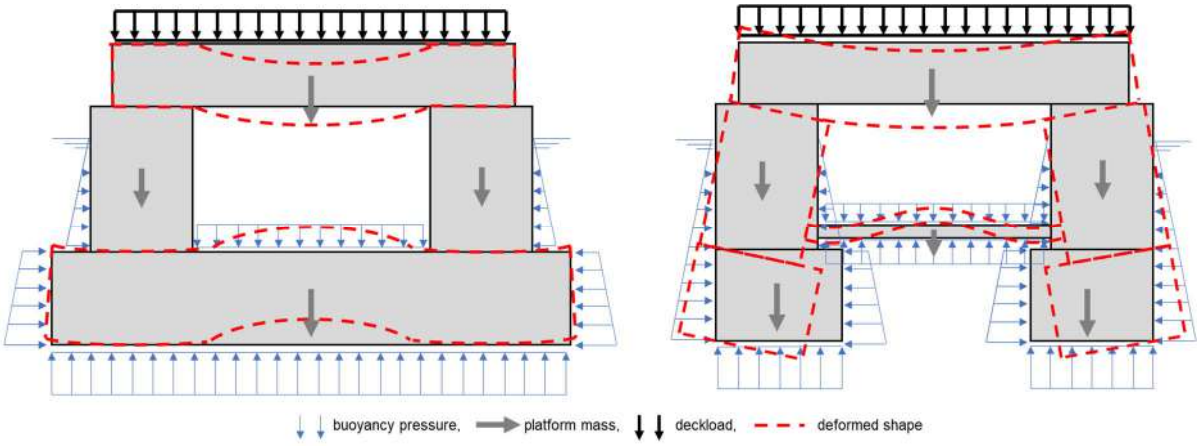


*Figure 2: Sketch of static forces and resulting deformations*

**Hydrostatic stiffness**

Hydrostatic stiffnesses describes vessel motion behaviour. For example, a large roll stiffness leads to aggressive roll accelerations, which is typical in transit condition where the transverse metacentre height is high. These stiffnesses do not change over time when the waterplane area, $A_{wl}$, displaced volume, $\nabla$, and transverse and longitudinal metacentre heights, $GM_T$ and $GM_L$, do not change as well. Relevant hydrostatic stiffnesses are heave, roll and pitch stiffnesses, $c_{33}, c_{44}$ and $c_{55}$, respectively, shown in Eq.2-7 to Eq.2-9. When multiplied with the corresponding motions, hydromechanical forces and moments are the result.

$$c_{33} = \rho_w g A_{wl} \quad \text{Eq.2-7}$$

$$c_{44} = \rho_w g \nabla G M_T \quad \text{Eq.2-8}$$

$$c_{55} = \rho_w g \nabla G M_L \quad \text{Eq.2-9}$$

## 2.1.2 Hydrodynamic/radiation loading

Hydrodynamic loads are dynamic forces and moments caused by a fluid on a moving body in still water, i.e. forces and moments due to radiated waves from the moving body. Hydrodynamic loads are also known as added mass and damping loads. The radiated flow of water can be described using the radiation potential, $\phi_r$, and is generally solved using Green's function which computes the source terms of hull pressures leading to forces and moments [6]. Green's function satisfies the Laplace equation and boundary conditions, which can be applied for 3D bodies by discretising the outer surfaces using panels, such as done by AQWA. When the radiation potential is solved, the added mass, $a_{ij}$, and damping terms, $b_{ij}$, can be calculated by Eq.2-10 and Eq.2-11 for symmetrical structures. The added mass and damping terms are then applied in the equation of motion shown in Eq.2-13 to compute the motions of the vessel.

$$a_{ij} = -\Re\left(\rho_w \iint_S \phi_{r,j} \frac{\partial \phi_{r,i}}{\partial n} dS\right) \quad \text{Eq.2-10}$$

$$b_{ij} = -\Im\left(\rho_w \omega \iint_S \phi_{r,j} \frac{\partial \phi_{r,i}}{\partial n} dS\right) \quad \text{Eq.2-11}$$

### 2.1.3 Wave and diffraction loading

Undisturbed wave and diffraction flow are described by the wave, $\phi_w$, and diffraction, $\phi_d$, potentials. The diffraction potential must fulfil the same Laplace equation and boundary conditions as the radiation potential, whereas the wave potential does not need to satisfy the kinematic boundary condition on the moving body. The wave potential can be analytically described as shown by Eq.2-12 [7]. This formula depends on wave frequency $\omega_\zeta$, wave amplitude $\zeta_a$, wave number $k_\zeta$, x- and y-location with respect to the coordinate system and wave heading $\mu$. When this wave potential is substituted in the dynamic pressure part (term (1) in the Bernoulli equation) and integrated up to mean water level over the surface, the so-called Froude-Krylov (F-K) force is derived. This physical meaning of this linear term is the force excited by waves, assuming the fluid is not affected by the presence of the vessel, i.e. when visualizing, the waves move 'through' the vessel's hull.

$$\phi_w = \frac{\omega_\zeta \zeta_a}{k_\zeta} \cdot \frac{\cosh\left(k_\zeta(d + z)\right)}{\sinh\left(k_\zeta d\right)} \cos\left(\omega_\zeta t - k_\zeta x \cdot cos(\mu) - k_\zeta y \cdot sin(\mu)\right) \quad \text{Eq.2-12}$$

The diffraction potential accounts for this unrealistic matter where the kinematic boundary condition on the moving body ensures a watertight hull. Diffraction forces are important for large structures when compared to the wave length. For slender structures, for example bracings, diffraction forces are usually ignored. The importance of diffraction forces for bracings is reported in Chapter 2.4.

## 2.2 Semi-submersible responses

### 2.2.1 Motion RAO's

With hydromechanical loading known, the response of the semi-submersible can be computed. Responses can both imply motions and loading. The most well-known response is the linear motion RAO, $RAO_\eta$, which is obtained as shown by Eq.2-13 and Eq.2-14, assuming the response frequency is equivalent to the wave frequency. In these equations $[M]$ and $[A]$ are the structural and added mass matrices, $[B]$ the damping matrix, $[C]$ the stiffness matrix, $\{\eta\}$ the motion vector and $\{F_w\}$ and $\{F_d\}$ are the wave and diffraction force and moment vectors. For a linear motion RAO, the forces are linearised with respect to wave amplitude, as shown by Eq.2-14.

$$([M] + [A])\{\ddot{\eta}\} + [B]\{\dot{\eta}\} + [C]\{\eta\} = \{F\} = \{F_w\} + \{F_d\} \quad \text{Eq.2-13}$$

$$\{RAO_\eta\} = \left\{\left|\frac{\eta}{\zeta_a}\right|\right\} = \left|\left(\omega_\zeta^2([M] + [A]) + i\omega_\zeta[B] + [C]\right)^{-1} \cdot \frac{\{F\}}{\zeta_a}\right| \quad \text{Eq.2-14}$$

Velocities and accelerations can be easily obtained by multiplying the linearised RAO's with the wave frequencies, see Eq.2-15 and Eq.2-16. Motion RAO's are normally computed at the centre of gravity location, however can be calculated at any specified location P($x_P$, $y_P$, $z_P$) shown by Eq.2-17 to Eq.2-19. The indices 1 to 6 represent the 6DOF motions of the vessel, namely the surge, sway, heave, roll, pitch and yaw motions, respectively.

$$\left\{\left|\frac{\dot{\eta}}{\zeta_a}\right|\right\} = \omega_\zeta \left\{\left|\frac{\eta}{\zeta_a}\right|\right\} \quad \text{Eq.2-15}$$

$$\left\{\left|\frac{\ddot{\eta}}{\zeta_a}\right|\right\} = \omega_\zeta^2 \left\{\left|\frac{\eta}{\zeta_a}\right|\right\} \quad \text{Eq.2-16}$$

$$\eta_{1,P} = \eta_1 - y_P\eta_6 + z_P\eta_5 \quad \text{Eq.2-17}$$

$$\eta_{2,P} = \eta_2 + x_P\eta_6 - z_P\eta_4 \quad \text{Eq.2-18}$$

$$\eta_{3,P} = \eta_3 - x_P\eta_5 + y_P\eta_4 \quad \text{Eq.2-19}$$

### 2.2.2 Characteristic responses

Characteristic responses are governing for the ultimate and fatigue strength and therefore structural design of semi-submersibles. Specifically, observed by global strength assessments of different bracing configurations, see Chapter 3, bracing global dimensions are governed by the characteristic loading, while the column-deckbox connection and deckbox structure global dimensions are governed by both characteristic loading and accelerations. Characteristic responses are illustrated in Figure 3 and are elaborated in this chapter.

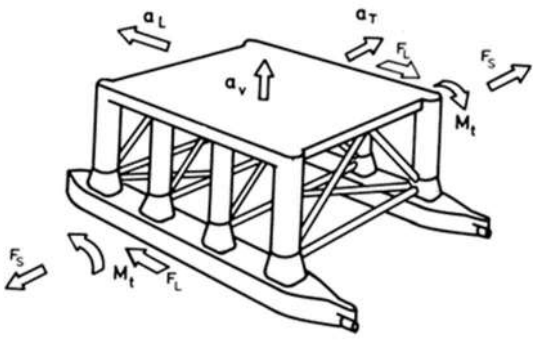


*Figure 3: Characteristic responses semi-submersible [8]*

**Splitting force between pontoons, $F_S$**

The splitting force is a horizontal transverse force, resulting in sway motions of floaters in opposite directions, see Figure 4. Splitting forces are generally the largest when the semi-submersible is loaded by beam waves and the wave length is about twice the overall breadth. This response is governing for the tensile and buckling strength of horizontal transverse bracings, if present.

**Longitudinal shear force between pontoons, $F_L$**
Longitudinal shear forces are typically the largest in headings between 45 and 60 degrees, as these waves cause opposite surge motions of the pontoons, see Figure 4. The wavelength corresponding to maximum longitudinal shear forces is about 1.5 times the diagonal length between pontoon ends. The opposite pontoon surge motions cause torsional moments in the deckbox and bending forces in transverse horizontal bracings.

**Torsion moment, $M_T$**
Similar to the longitudinal shear force, the torsion moment is critical for headings between 45 and 60 degrees, however is maximum when the wave length is about the diagonal length between pontoon ends. The torsion moment, which is around the transverse axis, is caused by opposite vertical pressure difference as shown in Figure 4. The torsion moment is governing for axial forces in the horizontal diagonal and vertical diagonal braces. When these bracings are absent in the design, the torsion moment will be absorbed by the deckbox structure.

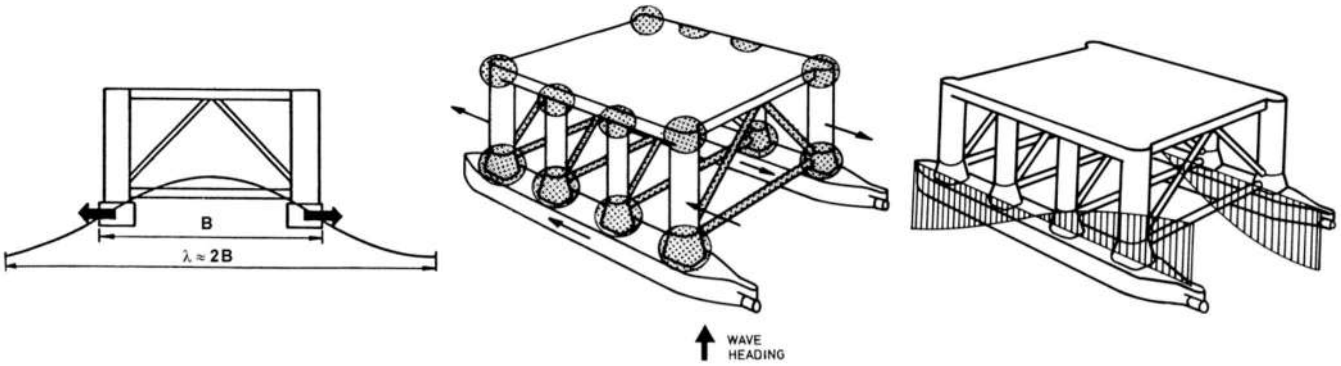


*Figure 4: Sketches of characteristic loading: splitting force (left), longitudinal shear force (mid) and torsion moment (right) [8]*

**Longitudinal acceleration of deck mass, $a_L$**
For wave headings where the surge and pitch motions dominate, therefore head or following waves, the longitudinal deck mass acceleration will also be maximum. This response will lead to shear and bending moments in the columns if no longitudinal diagonal bracings are present.

**Transverse acceleration of deck mass, $a_T$**
Transverse accelerations are critical for beam seas and small draught. In transit condition, only the floaters of semi-submersibles are partly submersed, which cause large waterplane inertia, leading to large metacentre heights and therefore aggressive transverse motions. For semi-submersibles with vertical diagonal bracings, the racking loads will be transferred through these members to the pontoon. Without vertical diagonal bracings, the transverse acceleration must pass through the columns, introducing shear and bending moments.

**Vertical acceleration of deck mass, $a_V$**
According to DNV-GL [8], this response is typically not governing for any member in submerged condition. The vertical acceleration will mostly cause solely axial loading in the columns.

## 2.3 Bracing influence on global loading and responses

To study the bracing influence on global loading and responses, motion RAO's and wave and diffraction loading RAO's are analysed through motion analysis software ANSYS AQWA. This program is able to account for diffraction and radiation forces using a panel method to solve for the diffraction and radiation potentials. The input for this analysis is reported in APPENDIX A.

Two models were created as illustrated in Figure 5. The pontoons and columns of the simple geometry have the same geometric properties as the reference semi-submersible. The four modelled transverse bracing diameters are equivalent to the reference semi-submersible bracing diameter, namely 1.8 meters. The operational basic condition is used as input for the draft and mass properties of the semi-submersible. This condition is considered appropriate to perform this comparison study, since displacement and stability particulars are comparable to the survival condition, see Table 7. Therefore, no large differences in conclusions are expected. The transit condition is not relevant, since bracings are not submerged in this condition. Therefore, have no influence on the global loading and motions of the semi-submersible. In addition, concluded during the seakeeping and resistance model tests of the reference semi-submersible [9], no slamming was noticed during all tests. This however is only valid for the position of the bracings shown in Figure 5. For other locations this conclusion has to be re-evaluated.

The computed motion, force and characteristic response RAO's using the simple geometry are not used as input for further calculations. The analyses are only made to study the influence of the bracings on motions and occurring forces. The performed hydrodynamic analyses for the reference semi-submersible involved an exact outer geometry, more accurate mass distribution and additional damping coefficients based on model tests. For some cases, the amplitude and peak periods of the motion and force RAO's are about 30% off compared to the results of the reference semi-submersible. This is considered acceptable, since the goal is to study differences, not to achieve similarity.

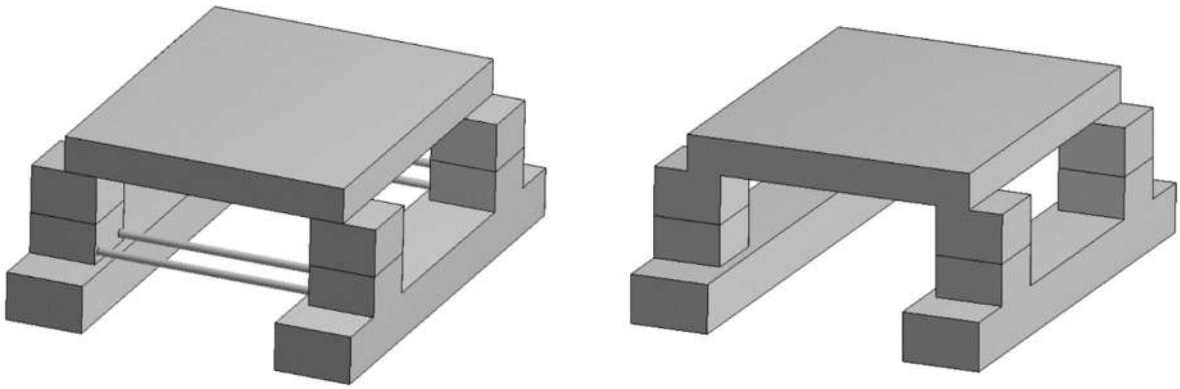

*Figure 5: AQWA simple geometries with bracings (left) and without bracings (right)*

### 2.3.1 Global loading and motions

Bracing influence is studied by motion RAO's and Froude-Krylov (F-K) and diffraction loading RAO's, see Figure 6. All RAO's are calculated at the centre of gravity of the semi-submersible, located at [x=39.6m, y=0m, z=26.2m] with respect to the global coordinate system shown in Figure 14. The relevant wave periods to compare results are between 6 and 15 seconds, since large wave energy is present for these wave periods [7]. Outside of this wave range, wave energy is lower, thus will not result in significant hydrodynamic loading and therefore motions. Figure 6 concludes bracings have little influence on global loading and motion RAO's for the relevant wave periods. When bracings are added, both motions and loading increase. Intuitively, as shown in the plots, the pitch motion and moment is affected the most by the absence of the bracings. Since the bracing location in x-direction, with respect to the centre of gravity, leads to relative large differences in pitch loading. The relative differences at the peak periods, $T_p$, are summarised in Table 1, concluding the largest difference occurs for the pitch moment.

Motions are less affect by the presence of bracings, while the loading is more effected. When for instance bracings are added, total loading will increase, since a larger area is subjected to wave loading. This is the right side (forcing) of Eq.2-13. The addition of bracings will also increase the added mass to be displaced when motions occur, which adds up to the left side of Eq.2-13. Resulting in less affected motions when bracings are added. Based on the relative differences, motions are about 50% less affected compared to loading.

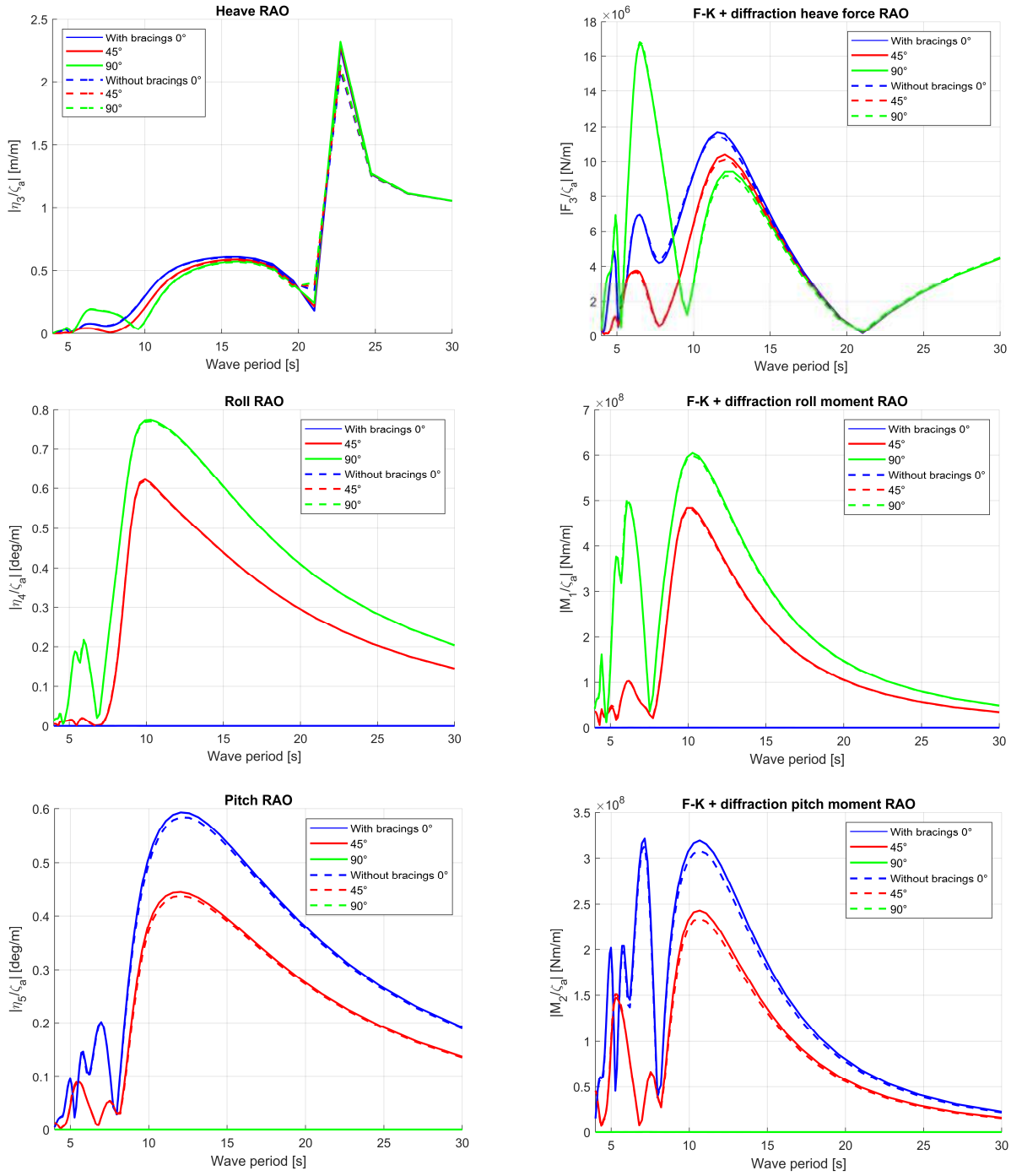


*Figure 6: Loading and motion RAO's, with and without bracings*

*Table 1: Relative differences motion and loading RAO's with and without bracings*

| RAO | Peak period, $T_p$ [s] | Relative difference [%] | | |
|---|---|---|---|---|
| | | 0° | 45° | 90° |
| Heave, $\lvert\eta_3/\zeta_a\rvert$ | 15 | -0.9 | -1.0 | -1.0 |
| Roll, $\lvert\eta_4/\zeta_a\rvert$ | 10 | 0 | -0.6 | -0.5 |
| Pitch, $\lvert\eta_5/\zeta_a\rvert$ | 12 | -1.5 | -1.7 | 0 |
| Heave force, $\lvert F_3/\zeta_a\rvert$ | 7-12 | -1.7 | -2.9 | 0.6 |
| Roll moment, $\lvert M_1/\zeta_a\rvert$ | 10 | 0 | -0.8 | -1 |
| Pitch moment, $\lvert M_2/\zeta_a\rvert$ | 11 | -3.4 | -3.7 | 0 |

### 2.3.2 Characteristic responses

To study the influence of bracings further, characteristic response RAO's are derived for various bracing diameters, see Figure 7 as example. Again, the operational condition is used as input. The heading to study the characteristic responses is selected as the critical headings reported in Chapter 2.2.2. All characteristic response RAO's were calculated at the centre of the deckbox, located at [x=39.6m, y=0m, z=36.9m], with respect to the global coordinate system shown in Figure 14.

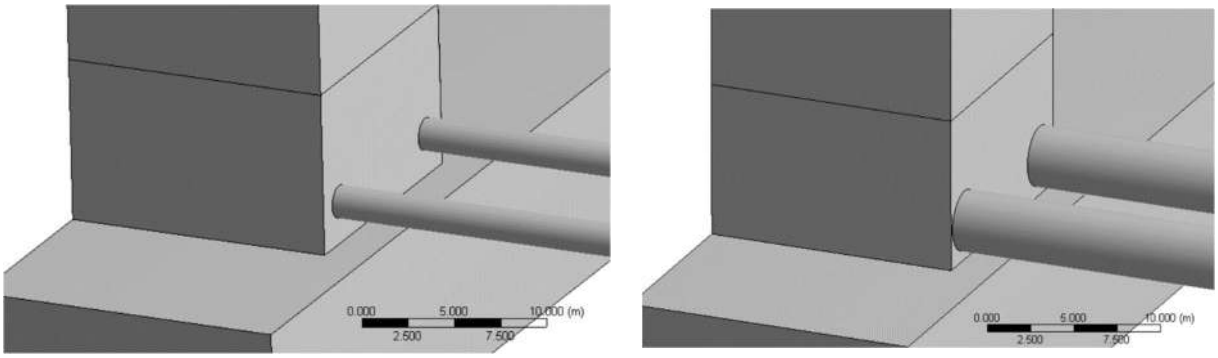


*Figure 7: AQWA simple geometries with bracing diameter D = 1.8 m (left) and D = 3.6 m (right)*

Characteristic response RAO's are plotted in Figure 8. The RAO plots illustrate differences are most significant for responses where the critical heading corresponds to the largest change in frontal area. Namely, splitting force and transverse acceleration RAO's for the critical heading of 90 degrees do not alter much, since the horizontal transverse bracings are parallel to the water flow.

Similar to the force and motion RAO's, characteristic responses are governing for wave periods between 6 and 15 seconds. The relative large differences of the vertical acceleration of the deck mass for wave periods from 20 to 25 seconds are therefore not important.

Figure 8 shows an increasing bracing diameter will increase the characteristic response RAO's at the peak periods. The relative differences of the RAO's at the peak period is reported in Table 2. This relative difference is calculated with respect to the response RAO without bracings, i.e. D = 0 m. For the peak periods, the relative differences are considered low, as relative differences are below 11%. However, for some wave periods, where the RAO is relatively low, such as the longitudinal shear force at 7.5 seconds and the longitudinal acceleration at 8.5 seconds, the relative differences are amplified (> 50%). Nonetheless, these large differences are neglectable as the RAO is low and is therefore not governing for the strength of the semi-submersible.

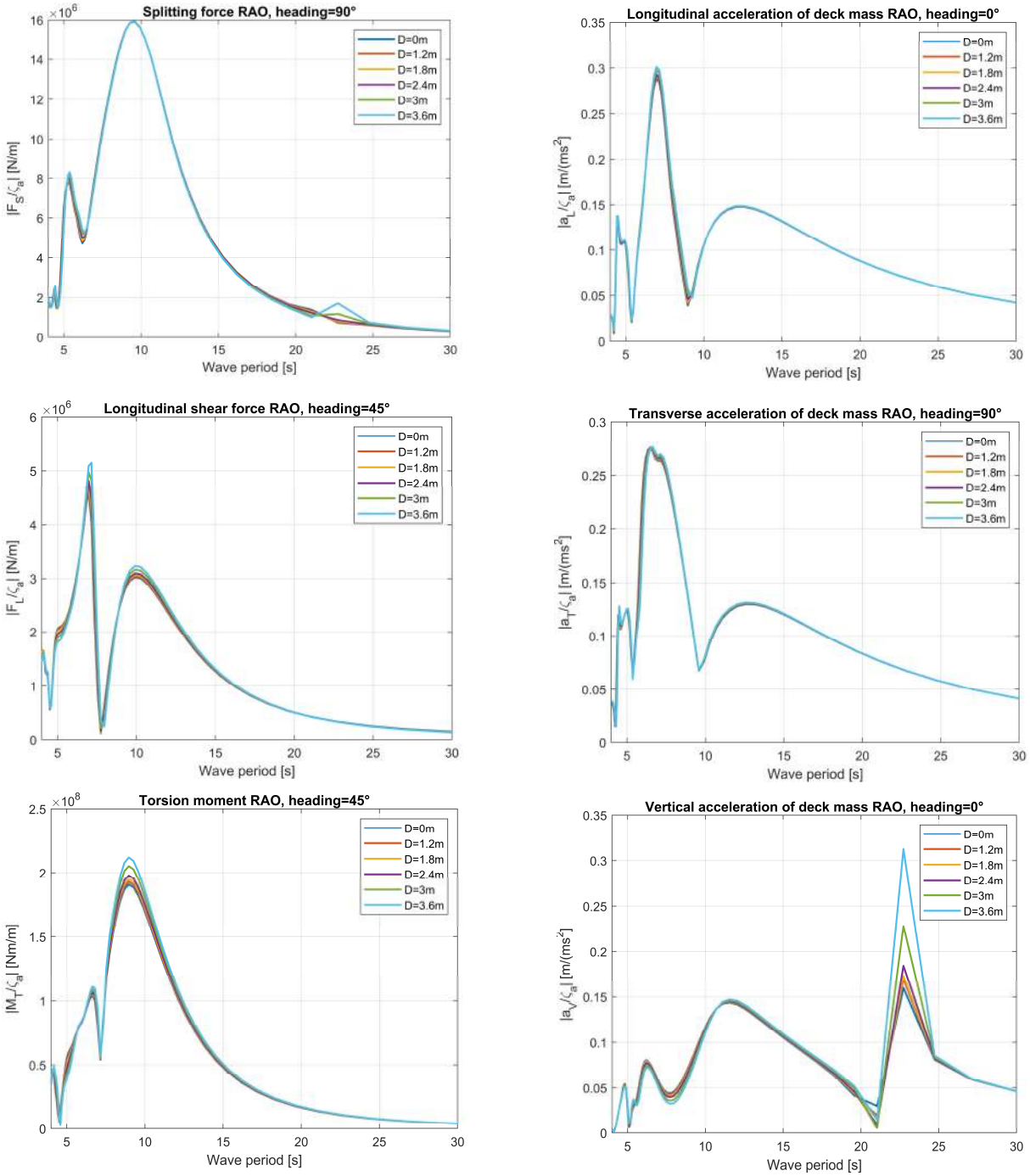


*Figure 8: Characteristic response RAO's, varying bracing diameter*

*Table 2: Relative differences characteristic response RAO's w.r.t. 0 m bracing diameter at peak period*

| Characteristic response RAO | Peak period, $T_p$ [s] | Relative difference [%] | | | | |
|---|---|---|---|---|---|---|
| | | D = 1.2 m | D = 1.8 m | D = 2.4 m | D = 3.0 m | D = 3.6 m |
| $F_S$ | 9.6 | 0.0 | 0.0 | 0.1 | 0.1 | 0.1 |
| $F_L$ | 7.0 | 0.6 | 1.3 | 2.0 | 3.6 | 5.7 |
| $M_T$ | 9.0 | 1.1 | 2.2 | 3.8 | 7.6 | 11.1 |
| $a_L$ | 7.0 | 0.5 | 1.0 | 1.5 | 3.0 | 4.2 |
| $a_T$ | 6.5 | 0.2 | 0.2 | 0.5 | 0.5 | 0.6 |
| $a_V$ | 11 | 0.2 | 0.4 | 0.6 | 1.0 | 1.4 |

For wave periods between 6 and 15 seconds, characteristic responses are non-linear proportional to displacement or frontal area. The changes of displacement and frontal area are summarised in Table 3. Displacement is quadratically proportional to bracing diameter, while frontal area is linearly proportional to bracing diameter. If the change in characteristic response would be coupled to displacement or frontal area, a fitting curve accompanying those parameters could be made. However, this would only be applicable to horizontal transverse bracings. Hydrodynamic diffraction analyses for other bracing combinations would have to be made to correctly approximate the characteristic responses. Therefore, it is checked if the Morison equation can account for different bracing diameters reported below.

*Table 3: Relative differences displacement and frontal area w.r.t. 0 m bracing diameter*

| Parameter | Heading [deg] | Relative difference [%] | | | | |
|---|---|---|---|---|---|---|
| | | D = 1.2 m | D = 1.8 m | D = 2.4 m | D = 3.0 m | D = 3.6 m |
| Displacement | N/A | 0.5 | 1.1 | 1.9 | 3.0 | 4.3 |
| Frontal area | 0 | 13 | 19 | 25 | 32 | 38 |
| | 45 | 3.2 | 4.8 | 6.4 | 8.0 | 10 |
| | 90 | 0.0 | 0.0 | 0.0 | 0.0 | 0.0 |

For the global strength assessment of different bracing configurations, global loading is kept constant. To account for different loading bracing configurations may have, local bracing loading is derived by the Morison equation, described in Chapter 2.4. To check if the Morison equation can account for the difference in characteristic force responses for different bracing diameters, hydrodynamic forces on the bracings were calculated for the same range of bracing diameters using the Morison equation. Then, the splitting force, longitudinal shear force and torsion moment RAO's were calculated for the same location and added to the RAO's of the semi-submersible without bracings. For simplicity, the accelerations of the deck mass were not recalculated, since no large change was observed in motions reported in Chapter 2.3.1.

The results are shown in Figure 9. Compared to the RAO's shown in Figure 8, solely computed by AQWA, it concludes the Morison equation can account for the difference in characteristic responses for different bracing diameters. It should be noted for some wave periods the amplitude does not match the amplitude solely computed by AQWA, such as the torsion moment RAO at around 6.5 seconds. Therefore, this approach does not approximate the characteristic responses as accurate when computed solely by AQWA. The splitting force RAO does not change for different bracing diameters, because the bracing load calculation using the Morison equation does not lead to changes in frontal area. This can also be observed in the splitting force RAO in Figure 8, solely computed by AQWA. The longitudinal shear force peak is slightly lower, whereas the torsion moment peak is comparable. The relative difference of the AQWA+Morison calculation with respect to the AQWA calculation is calculated for the peak periods, see Table 4. Overall, the relative difference is considered acceptable as this approach simplifies the evaluation of bracing concepts. The difference is the largest for the longitudinal shear force with 6.4%. However, the trend of increased loading for increased bracing diameter is present.

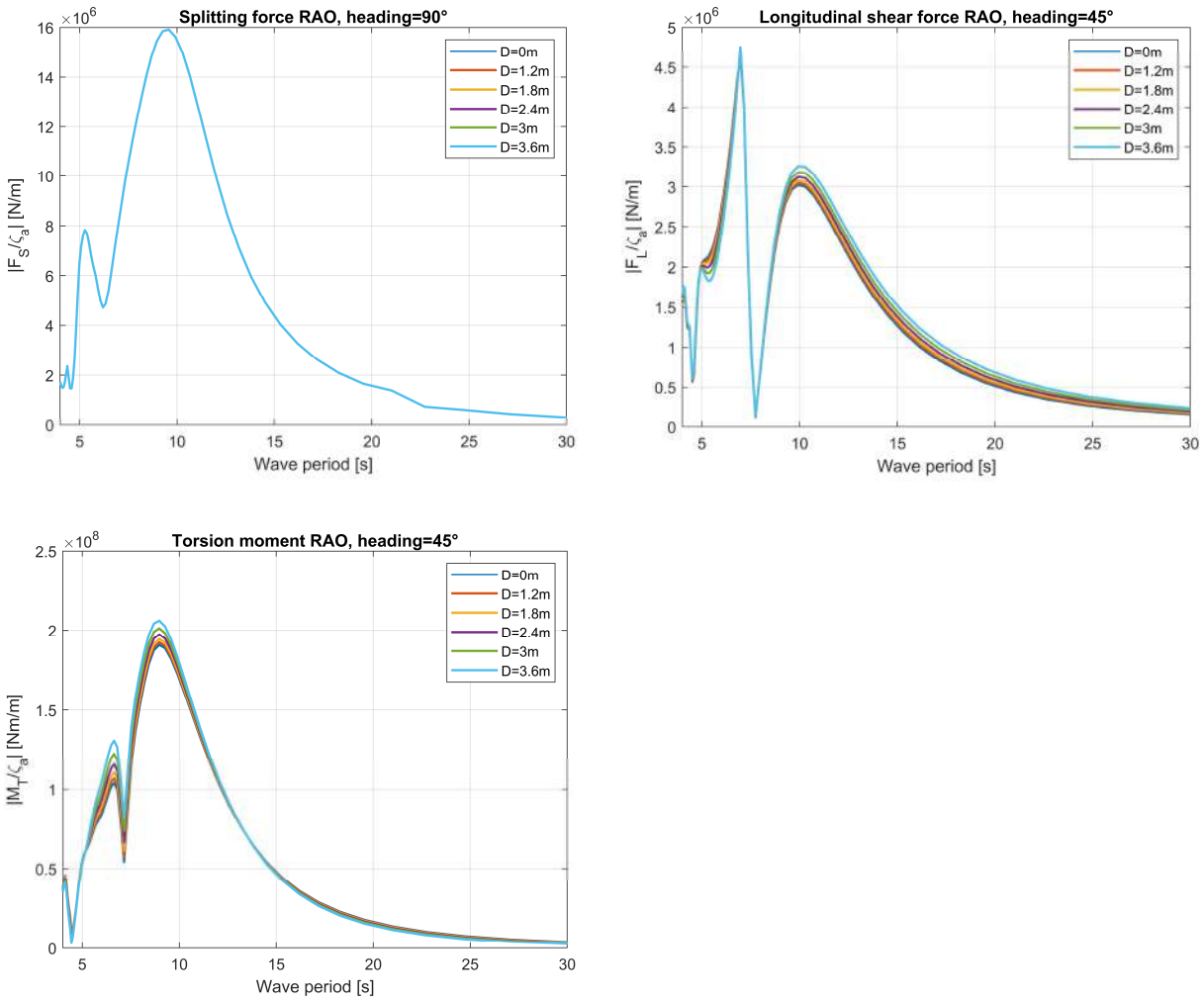


*Figure 9: Characteristic response force and moment RAO's, bracing loading calculated by Morison*

*Table 4: Relative differences characteristic force response AQWA+Morison RAO's w.r.t. solely AQWA calculation at peak period*

| Characteristic response RAO | Peak period, $T_p$ [s] | Relative difference [%] | | | | |
|---|---|---|---|---|---|---|
| | | D = 1.2 m | D = 1.8 m | D = 2.4 m | D = 3.0 m | D = 3.6 m |
| $F_S$ | 9.6 | 0.0 | 0.0 | 0.1 | 0.1 | 0.1 |
| $F_L$ | 7.0 | 1.2 | 2.3 | 3.2 | 5.1 | 6.4 |
| $M_T$ | 9.0 | 0.3 | 0.3 | 0.2 | 1.9 | 2.8 |

### 2.3.3 Conclusion

Bracings have little influence on the motions and global loading of the semi-submersible. The maximum difference is observed in the pitch moment, where the difference is 3.7% at the peak period. Motions are even less affected by the presence or absence of bracings, since both loading and added mass increases, resulting in a lower increase in motion amplitude compared to loading.

The influence of bracings is further studied for characteristic responses that are governing for the strength and fatigue of the semi-submersible. Generally, an increase in bracing diameter results in an increase in characteristic response. However, bracings do not affect characteristic responses much, as differences below 11% are observed. Compared to characteristic loading, characteristic deck mass accelerations are less affected when bracing diameter is varied. The RAO plots illustrate differences are the highest for responses where the critical heading corresponds to a change in frontal area.

When the Morison equation is used to approximate the change in characteristic loading for varying bracing diameters, similar results are obtained compared to the characteristic loading solely computed by AQWA. It should be noted that for some wave periods the amplitude does not match the amplitude solely computed by AQWA, however the relative difference is considered acceptable as this approach simplifies the evaluation of bracing concepts. This justifies the use of constant global wave loading for evaluating bracing configurations in the global strength assessment. To account for different local loading the bracing configurations may have, the Morison equation as explained in Chapter 2.4 will be used.

## 2.4 Bracing local loading

The force per unit length, resulting from the local water pressure on bracings is calculated by the Morison equation shown by Eq. 2-20 [10]. In this equation $\dot{u}$ and $u$ are the wave particle acceleration and velocity. $\ddot{\eta}_b$ and $\dot{\eta}_b$ are the velocity and acceleration of the moving bracing, respectively. Furthermore, $\rho_w$ is the water density and $D$ is the bracing diameter.

$$f = \rho_w \frac{\pi D^2}{4}\dot{u} + \rho_w C_a \frac{\pi D^2}{4}(\dot{u} - \ddot{\eta}_b) + \frac{1}{2}\rho_w C_D D|u - \dot{\eta}_b|(u - \dot{\eta}_b) \qquad \text{Eq. 2-20}$$

The first term in the Morison equation is known as the Froude-Krylov component, relating the change in wave particle acceleration due to the impermeable cylinder to inertia forces. The second term is the added mass component due to the distortion of flow by the moving bracing. These two terms form the resultant inertia force. The last term is the drag force, consisting of form drag and viscous skin friction drag.

The added mass coefficient, $C_a$, accounts for real flow phenomena such as vortices in the wake of the cylinder and is computed by the inertia coefficient, $C_M$, shown in Eq.2-21. The drag coefficient, $C_D$, accounts for drag effects caused by the geometrical shape of the bracing. Both the coefficients are based on literature findings shown in Table 5 and are dependent on the Keulegan-Carpenter number (KC) and Reynolds number (Re).

$$C_a = C_M - 1 \qquad \text{Eq.2-21}$$

*Table 5: Inertia and drag coefficients Morison equation [11]*

| | $Re = \frac{uD}{\nu}$ | | | |
|---|---|---|---|---|
| | $< 10^5$ | | $\geq 10^5$ | |
| $KC = \frac{uT_\zeta}{D}$ | $C_M$ | $C_D$ | $C_M$ | $C_D$ |
| < 10 | 2.0 | 1.2 | 2.0 | 0.6 |
| ≥ 10 | 1.5 | 1.2 | 1.5 | 0.6 |

The Morison equation neglects diffraction forces. This assumption generally applies when a slender structure is analysed [6], such as bracings in this study. One can also justify this modelling choice by the diffraction parameter shown by Eq.2-22 [12], [13]. If the diffraction parameter is larger than 0.2, wave flow scatters from the surface of the structure and different inertia forces will be present. If the diffraction parameter is smaller than 0.2, estimating the inertia forces by Froude-Krylov is sufficient and errors of smaller than 4% are expected. When the diffraction parameter is smaller than 0.02, no diffraction forces will be present. Relevant for this assignment, if the current bracing diameter of the reference semi-submersible is used (1.8 meters), the wave length must be larger than 9 meters to be below the theoretical relative error of 4%. In deep water this corresponds to a wave period larger than 2.4 seconds. Since wave periods larger than 4 seconds are used in this study, diffraction may be neglected in the local water pressure calculation when the bracing diameter is smaller than 4 meters.

The importance of drag forces on a slender structure may be analysed by Eq.2-23 [12], which should be smaller than two for neglectable drag. The factor of wave height versus cylinder diameter is proportional to the Keulegan-Carpenter number in deep water conditions, namely for large wave heights the water particle velocity increases, which is proportional quadratically to the drag the structure experiences. The bracing concepts will be evaluated using the design wave analysis to simulate extreme wave conditions in the ULS and ALS, i.e. large wave heights, drag is therefore included in the local water pressure calculation.

$$\frac{D}{\lambda} \leq \begin{cases} 0.02 \rightarrow neglectable\ diffraction \\ 0.2 \rightarrow \epsilon_{rel} \leq 4\% \end{cases} \qquad \text{Eq.2-22}$$

$$\frac{H}{D} \leq 2 \rightarrow negletable\ drag \qquad \text{Eq.2-23}$$

Wave particle kinematics is calculated by equations Eq.2-24 and Eq.2-25, assuming linear harmonic waves in deep water [7]. Below formulas depend on the wave frequency, $\omega_\zeta$, wave amplitude, $\zeta_a$, wave number, $k_\zeta$, x- and y-location with respect to the reference system and wave heading, $\mu$. The bracing velocities and accelerations are computed by known linear RAO's of the reference semi-submersible as shown in Eq.2-15 to Eq.2-19. The motion analysis [14] was performed using the AQWA-LINE diffraction program in the frequency domain. In above computations, phase differences are accounted for with respect to the location of the bracings.

$$u_x = \omega\zeta_a e^{kz} \sin(\omega t - kx\,cos(\mu) - ky\,sin(\mu)) \qquad \textit{Eq.2-24}$$

$$u_z = \omega\zeta_a e^{kz} \cos(\omega t - kx\,cos(\mu) - ky\,sin(\mu)) \qquad \textit{Eq.2-25}$$

Morison loading is validated through AQWA hydrodynamic response analyses using the simple geometry shown in Figure 5. Reference is made to APPENDIX B, where the input of the response analysis is specified. Figure 10 to Figure 12 conclude the amplitudes and phases of all force types are similar, therefore validating the Morison load calculation. Increasing AQWA force amplitudes for $t > 0\ s$ are due to the specified wave ramp up period to reduce transient motions at the beginning of the analysis.

For quartering and beam waves, differences between forces are the largest. This is due to the low frequency response of the semi-submersible, not accounted for by the Morison equation since linear RAO's are used. As an example, the heave motion of the semi-submersible is shown in Figure 13 where the low frequency response can be observed. The period of the low frequency response is close to the heave natural frequency of the semi-submersible.

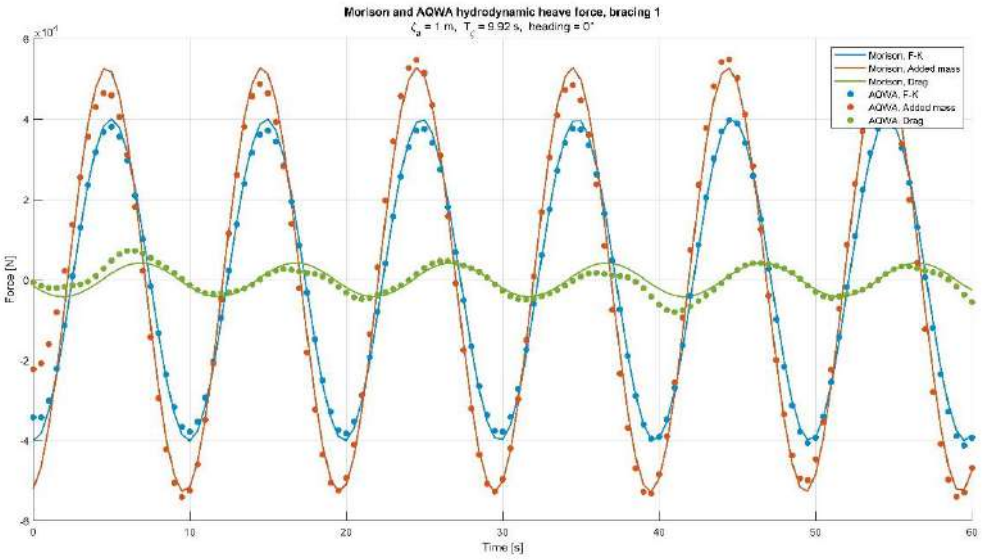


*Figure 10: Morison and AQWA hydrodynamic heave force comparison, head waves*

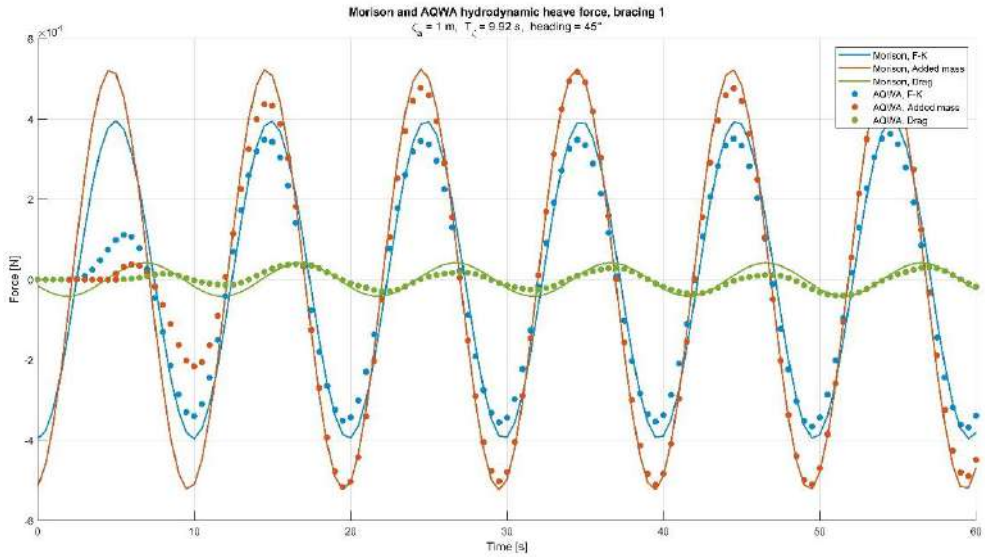


*Figure 11: Morison and AQWA hydrodynamic heave force comparison, quartering waves*

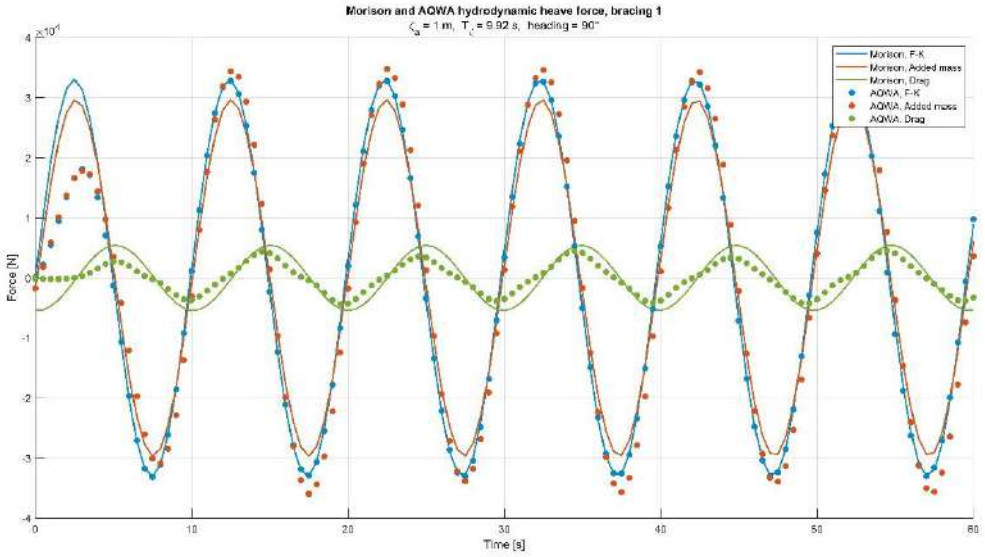


*Figure 12: Morison and AQWA hydrodynamic heave force comparison, beam waves*

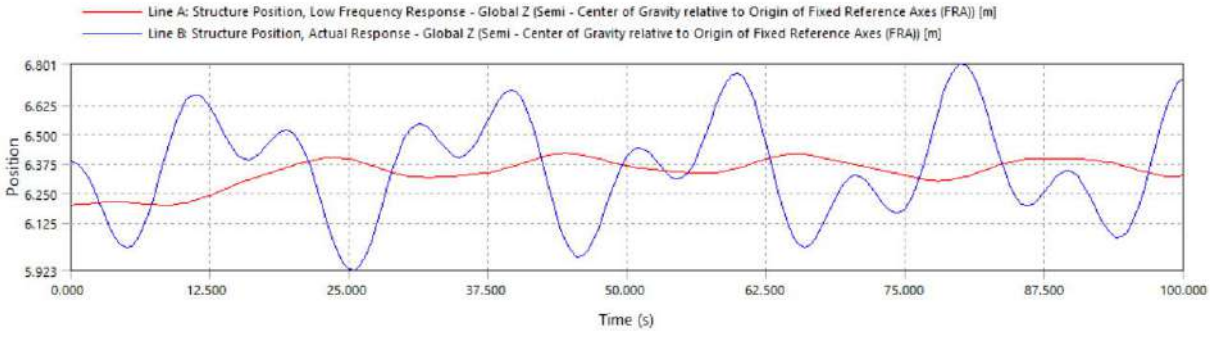


*Figure 13: AQWA heave response semi-submersible 1,$\zeta_a$=1m, $T_\zeta$=9.92s, heading=45°*

It should be noted that the force amplitude and phase similarity is most accurate for small wave amplitudes. For extreme environmental conditions, therefore large wave heights, nonlinear terms have increased influence on total forcing, as they scale with $\zeta_a^2$ as further explained below.

The Bernoulli pressure formulation, also explained in Chapter 2.1 summarises the pressure calculation AQWA performs, resulting in forces and moments when integrated over surfaces. In this equation, $\phi$ is the potential the pressure is calculated for. The different potentials used in this pressure calculation are the wave, diffraction and radiation potentials. The wave potential describes the undisturbed flow of wave particles, whereas the diffraction potential accounts for diffraction pressures when waves encounter a floating structure. The radiation potential accounts for the movement of water due to the motions of the floating structure, resulting in pressures. See Chapter 2.1 for more information about these loading types.

AQWA computes hydromechanical loading up to second order with respect to wave amplitude [15], i.e. $F_{tot} \approx F^0 + F^1 + F^2$. The zeroth order force is the constant force the structure experiences, such as the hydrostatic pressure (term (3) in the Bernoulli equation) and, if applicable, constant current forces. The first order force results from integrating the dynamic pressure (term (1) in the Bernoulli equation) from the draught of the vessel up to the mean water level for the considered potentials. Lastly, the second order terms result from integrating the constant hydrostatic force from mean water level up to the instantaneous surface elevation and integrating the velocity term (term (2) in the Bernoulli equation) from the draught of the vessel up to the mean water level for the considered potentials.

Accounting for second order terms do not only result in additional forces proportional to the wave amplitude squared, but also lead to low and high force frequencies forces and therefore responses other than the wave frequency. These high and low frequencies are clearly visible in the heave motion of the semi-submersible shown in Figure 13.

For extreme environmental conditions, similar to ULS and ALS load cases in the global strength assessment, total surge and heave force amplitudes of Morison loading and the AQWA response analysis are compared in Table 6. The mean force amplitude is taken for AQWA due to the high and low frequency forces as explained above. Table 6 concludes differences between force amplitudes are larger for high wave amplitudes than previously illustrated in Figure 10 to Figure 12. The relative differences show differences up to 20% are possible. This difference is considered acceptable, since the approach of using known constant global loading and local bracing loading through the Morison equation, simplifies the evaluation of different bracing configurations. Otherwise, hydrodynamic diffraction analyses should be performed for each different bracing configuration.

*Table 6: Force amplitudes Morison and AQWA calculation, bracing 1*

| Heading | Wave conditions | Surge force amplitude [kN] | | | Heave force amplitude [kN] | | |
|---|---|---|---|---|---|---|---|
| | | Morison | AQWA (mean) | $\Delta_{rel}$ [%] | Morison | AQWA (mean) | $\Delta_{rel}$ [%] |
| 0° | $\zeta_a$ = 5 m<br>$T_\zeta$ = 7 s | 794 | 787 | 1 | 583 | 506 | 15 |
| | $\zeta_a$ = 7 m<br>$T_\zeta$ = 8 s | 935 | 786 | 19 | 706 | 746 | -5 |
| | $\zeta_a$ = 8 m<br>$T_\zeta$ = 10 s | 481 | 519 | -7 | 970 | 1135 | -15 |
| 45° | $\zeta_a$ = 5 m<br>$T_\zeta$ = 7 s | 249 | 274 | -9 | 343 | 376 | -9 |
| | $\zeta_a$ = 7 m<br>$T_\zeta$ = 8 s | 333 | 357 | -7 | 526 | 515 | 2 |
| | $\zeta_a$ = 8 m<br>$T_\zeta$ = 10 s | 351 | 314 | 12 | 850 | 717 | 19 |
| 90° | $\zeta_a$ = 5 m<br>$T_\zeta$ = 7 s | 0 | ≈ 0 | N/A | 316 | 328 | -4 |
| | $\zeta_a$ = 7 m<br>$T_\zeta$ = 8 s | 0 | ≈ 0 | | 599 | 528 | 13 |
| | $\zeta_a$ = 8 m<br>$T_\zeta$ = 10 s | 0 | ≈ 0 | | 469 | 469 | 0 |

# 3 Global strength assessment

## 3.1 Introduction

Global strength assessments are performed for the reference semi-submersible and semi-submersibles with different bracing configurations. The reference semi-submersible is discussed first in Chapter 3.2. The structural performance of semi-submersibles with different bracing configurations is evaluated in the same manner as the reference case and are discussed in Chapter 3.3.

## 3.2 Reference case

The reference semi-submersible design is used to study different bracing configurations. A reference case is performed first, which is presented in this chapter. In the subchapters below, the load cases and the FEA results of the global strength assessment are reported. In APPENDIX C, input for the FEA is summarised. This appendix touches on the geometry, mesh specification and load application.

Important for the global strength assessment is the basic condition, since this determines the draught and therefore the water and inertia loading. The basic conditions of the reference semi-submersible are reported in Table 7, where the longitudinal centre of gravity (LCG) and VCG are calculated with respect to the main coordinate system (CSYS) shown in Figure 14.

*Table 7: Basic conditions reference semi-submersible*

| Basic condition | Draught [m] | Displacement [t] | LCG [m] | VCG [m] | Ixx [tm$^2$] | Iyy [tm$^2$] | Izz [tm$^2$] |
|---|---|---|---|---|---|---|---|
| Transit | 10.5 | 32109 | 39.6 | 29.1 | 2.62E+07 | 3.22E+07 | 3.43E+07 |
| Operational | 20.0 | 42045 | 39.6 | 26.2 | 3.77E+07 | 4.19E+07 | 4.65E+07 |
| Survival (transit) | 17.4 | 39692 | 39.6 | 26.8 | 3.79E+07 | 3.73E+07 | 4.37E+07 |
| Survival (operational) | 17.4 | 39681 | 39.6 | 24.7 | 3.42E+07 | 3.90E+07 | 4.22E+07 |

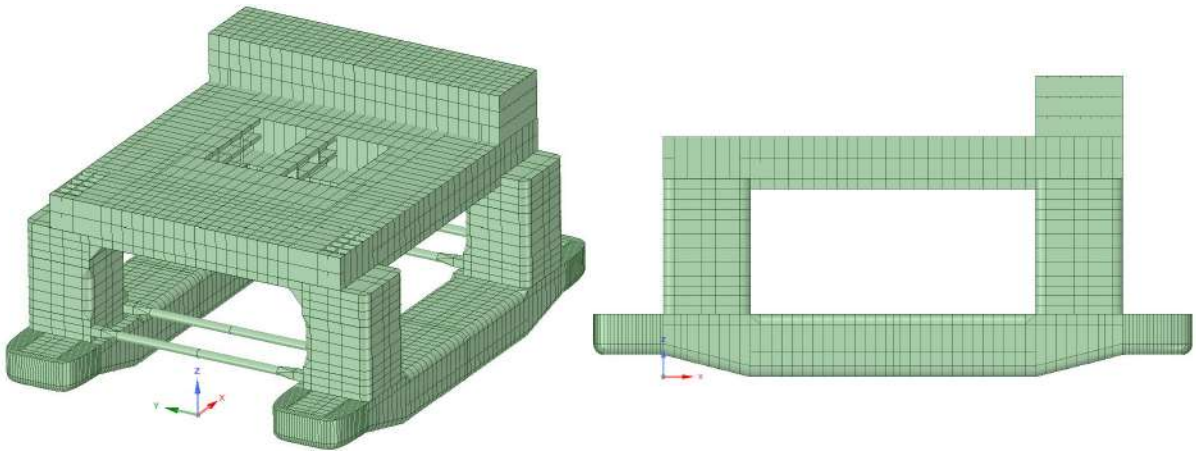

*Figure 14: Main CSYS semi-submersible*

The operational basic condition is chosen for the global strength assessment. This basic condition is considered most appropriate because of the following reasons. First, the semi-submersible operates most of its design life in operational condition [16], [17], [18], [19], therefore is most representable for fatigue. Also, the operation basic condition has the highest deckbox mass compared to the other basic conditions, relevant for static and inertia column and deckbox stresses. Since the draught of the operational and survival basic conditions are similar, the magnitude of the characteristic responses are also similar [20]. However, the transit condition differs from the operation condition. Namely, the magnitude of characteristic loading are 1.5 to 2.5 times smaller in transit, while deckbox accelerations are 1.3 to 1.8 times higher. Results in Chapter 3.2.3 show higher deckbox accelerations particularly results in higher column-deckbox connection stresses. Only considering the operational basic condition

does therefore not cover the complete global strength assessment of the semi-submersible. However, this study aims to compare different bracing configurations and not aims for a certified structural design. By only considering the operational basic condition, the different bracing configurations can be compared efficiently.

### 3.2.1 Load cases

The structural integrity of offshore and marine structures is typically checked according to 4 limit states. The 4 limit states are the SLS, ULS, ALS and FLS. The ULS and ALS in damaged condition are most appropriate limit states to evaluate different bracing configurations, since these limit states determine the global structural dimensions of the semi-submersible. The FLS is evaluated qualitatively. In the paragraphs below, the choice for limit states is elaborated. Further, this chapter presents the static loading and dynamic loading in the ULS and ALS. As reported in Chapter 2, global loading is kept constant for all bracing configurations, while bracing loading is manually calculated by the Morison equation to account for different loading bracing configurations may have.

The SLS is applicable during normal use and ensures durability, such as acceptable deflections, vibrations and temperatures. Compared to the ULS and ALS, this limit state does not govern the global structural design as much to compare different bracing configurations.

The FLS is usually a governing limit state regarding structural details, therefore mainly defines the local structural design. No fatigue assessment is performed for all bracing configurations, since this requires detailed local strength models and extensive calculations to accurately estimate the fatigue damage at fatigue sensitive locations. However, qualitatively the FLS can be evaluated by the fatigue sensitive locations and the global loading a member or component has to absorb. For example, a certain bracing configuration is unfavourable if a large number of fatigue sensitive locations are present. In this case, the possible number of cracks increases and because these connections should be checked and maintained, larger inspection and maintenance costs are the result as well. Moreover, if the global loading for a member or component is unfavourable, i.e. highly loaded and/or in disadvantageous directions, the fatigue lifetime at detail level becomes a challenge and therefore the bracing configuration is also unfavourable regarding the FLS.

The ULS is the limit state to check the structures ability to withstand maximum loads. This limit state is used to establish the dimensions of global structural members and is therefore applicable to study the impact of certain bracing configurations on the structural design.

The ALS considers load cases that usually occur every 10.000 years. Similar to the ULS, this limit state also defines the dimensions of global structural members, therefore should also be considered when bracing configurations are evaluated. With the ALS the integrity is checked when accidental loads occur, such as dropped objects, fire, flooding and collisions. An important load case for bracings in the ALS is the damaged condition. With the damaged condition, the redundancy of the semi-submersible can be evaluated when one bracing or brace-joint fails, therefore has impact on the overall structural design of the semi-submersible. For instance, the column-deckbox connection and deckbox structural capacity is larger for a semi-submersible with one bracing fore and aft than for a semi-submersible with 2 bracings fore and aft. Therefore, this limit state should also be considered when bracing designs are evaluated. Local yielding and buckling is acceptable if it can be demonstrated that the excessive forces can be redistributed to other members. The importance of structural redundancy was shown by the Alexander L. Kielland incident.

#### *3.2.1.1 Static loading*

The static loading consists of hydrostatic pressure and mass distributions. Based on the operational condition, point masses were applied to the pontoon and deckbox geometry. The combination of hydrostatic pressures and masses will result in static forces and moments and therefore structure deformations as sketched in Figure 2. In Figure 15 the FEA static loading is illustrated, showing the hydrostatic pressure applied to the outer surfaces below the waterline and the point masses based on the operational basic condition. The point masses are the total part's masses minus the structural masses. Please be referred to APPENDIX C where the input of the FEA is reported in more detail.

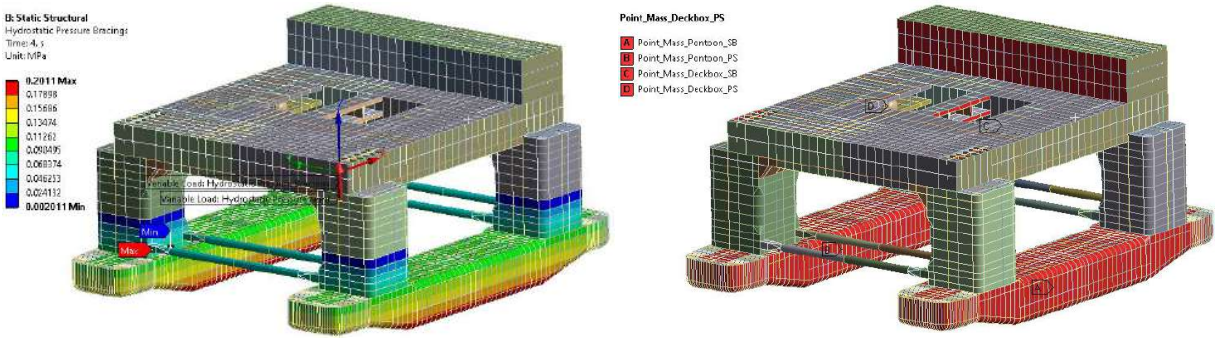


*Figure 15: Static loading semi-submersible, hydrostatic pressure (left) and applied point masses (right)*

### *3.2.1.2 Dynamic loading*

Known splitting forces of the reference semi-submersible are used as input for the dynamic loading. The load case selection is explained first, after which the splitting forces are discussed.

**Load case selection**

Characteristic responses govern the structural design of a semi-submersible, see Chapter 2.2.2. Load cases are therefore defined based on maximum characteristic responses. The characteristic response RAO's at the peak periods, $T_p$, and corresponding phases, $\varepsilon_{R,\zeta}$, are summarised for the reference semi-submersible in operation condition in Table 8. Here, the force, moment and acceleration RAO's units are kN/m, kNm/m and m/(ms$^2$), respectively, and are all calculated for the point [x=39.6m, y=0m, z=36.9m] with respect to the main CSYS as defined in Figure 14, which is the centre of the deckbox. In Table 8 the maximum characteristic response RAO's are highlighted in red, showing the critical headings.

*Table 8: Characteristic response RAO's reference semi-submersible*

| Heading [°] | Characteristic response RAO | $F_S$ | $F_L$ | $M_T$ | $a_L$ | $a_T$ | $a_V$ |
|---|---|---|---|---|---|---|---|
| 0 | \|RAO\| | 1,720 | 178 | 2,800 | 0.25 | 0 | 0.19 |
| | $T_p$ [s] | 7.72 | 7.21 | 9.77 | 6.98 | 0 | 11.28 |
| | $\varepsilon_{R,\zeta}$ [°] | -87 | 118 | 73 | -57 | 0 | 86 |
| 15 | \|RAO\| | 1,473 | 4,567 | 112,620 | 0.17 | 0.09 | 0.16 |
| | $T_p$ [s] | 7.72 | 6.76 | 6.98 | 7.21 | 8.62 | 11.28 |
| | $\varepsilon_{R,\zeta}$ [°] | -87 | 78 | 125 | -62 | -131 | 86 |
| 30 | \|RAO\| | 3,500 | 5,532 | 117,644 | 0.10 | 0.14 | 0.15 |
| | $T_p$ [s] | 6.02 | 6.98 | 6.57 | 4.35 | 8.98 | 11.28 |
| | $\varepsilon_{R,\zeta}$ [°] | 31 | 125 | 83 | 162 | -151 | 86 |
| 45 | \|RAO\| | 4,790 | 3,730 | 136,000 | 0.1 | 0.12 | 0.13 |
| | $T_p$ [s] | 10.23 | 6.98 | 8.62 | 5.57 | 8.62 | 11.88 |
| | $\varepsilon_{R,\zeta}$ [°] | 135 | 125 | 85 | -26 | -151 | -102 |
| 60 | \|RAO\| | 8,060 | 2,360 | 150,216 | 0.07 | 0.14 | 0.12 |
| | $T_p$ [s] | 9.77 | 9.77 | 7.72 | 4.44 | 8.62 | 11.88 |
| | $\varepsilon_{R,\zeta}$ [°] | 162 | 86 | 84 | -26 | -151 | -102 |
| 75 | \|RAO\| | 10,888 | 1,589 | 124,721 | 0.07 | 0.24 | 0.15 |
| | $T_p$ [s] | 9.77 | 6.98 | 5.43 | 4.44 | 7.99 | 20.94 |
| | $\varepsilon_{R,\zeta}$ [°] | 162 | 125 | -60 | 123 | -100 | -102 |
| 90 | \|RAO\| | 11,977 | 2 | 2,420 | 0 | 0.28 | 0.19 |
| | $T_p$ [s] | 9.77 | 4.73 | 6.2 | 0 | 6.98 | 6.2 |
| | $\varepsilon_{R,\zeta}$ [°] | 162 | -83 | 102 | 0 | -75 | 8 |

With the critical headings and the peak periods known, load cases can be defined using the design wave analysis. More information about the design wave analysis can be found in DNVGL-RP-C103 [8]. The design wave analysis is a method of calculating a design wave amplitude, $\zeta_{ad}$, that results in a maximum response in irregular waves. The method is explained by Eq.5-10 to Eq.3-3. First, the irregular response is obtained by multiplying the squared characteristic response RAO, $RAO_{CR}$, with the wave spectrum, $S_\zeta$, shown by Eq.5-10. Maximum wave steepness, therefore ratio of wave height and period, is accounted for using a ULS 100 year return period. Then, the maximum response is obtained assuming Rayleigh distribution using Eq.3-2. In this equation a 90% percentile, $p$, is used to account for the probability of different wave headings in a short term response where a 3 hour sea state is assumed for

the number of waves, $N$. $\sigma_s$ is the significant response of $S_{CR}$. By dividing the maximum response by the RAO of the characteristic response at the critical wave period in Eq.3-3, the design wave amplitude is calculated.

$$S_{CR} = RAO_{CR}^2 \cdot S_\zeta \qquad \text{Eq.3-1}$$

$$Resp(max) = \sigma_s \sqrt{-0.5 \ln(1 - p^{\frac{1}{N}})} \qquad \text{Eq.3-2}$$

$$\zeta_{ad} = \frac{Resp(max)}{RAO_{CR}(T_C)} \qquad \text{Eq.3-3}$$

The calculated design wave amplitude, critical heading and peak period should result in an environmental condition where a maximum characteristic response occurs. Hence, the ULS of a semi-submersible can be evaluated. The ULS environmental conditions for maximum characteristic responses are reported in in Table 9. Important to note is that a response $F_{comb}$ is added as load case. $F_{comb}$ is a load case where the combination of the splitting and longitudinal shear force is the largest.

*Table 9: ULS Environmental conditions for maximum characteristic response*

| Characteristic response | $F_S$ | $F_L$ | $F_{comb}$ | $M_T$ | $a_L$ | $a_T$ | $a_V$ |
|---|---|---|---|---|---|---|---|
| Heading [°] | 90 | 30 | 60 | 60 | 0 | 90 | 0 |
| $\zeta_{ad}$ | 7.6 | 5.64 | 7.94 | 6.63 | 3.88 | 6.60 | 6.84 |
| $T_C$ [s] | 9.77 | 6.98 | 9.77 | 7.72 | 6.98 | 6.98 | 11.28 |
| $\varepsilon_{R,\zeta}$ [°] | 162 | 125 | 86 | 84 | -57 | -75 | 86 |
| Response amplitude | 91000 kN | 31000 kN | 82000 kN | 996000 kNm | 0.97 m/s$^2$ | 1.85 m/s$^2$ | 1.30 m/s$^2$ |

Abovementioned ULS environmental conditions correspond to a 100 year return period. For the damaged condition in the ALS, a 1 year return period may be used. According to DNV-GL [8], if a 100 year return period is used for the analysis, the 1 year stress response may be taken as calculated by Eq.3-5. $\sigma_1$ and $\sigma_{100}$ are the 1 and 100 year stress response respectively and $h$ is the Weibull shape parameter, where a value of 1.1 may be taken for twin pontoon units.

$$\sigma_1 = 0.77^{1/h}\sigma_{100} \approx 0.79\sigma_{100} \qquad \text{Eq.3-4}$$

However, care should be taken when using Eq.3-4, because stresses due to static loading are also scaled. Therefore, stress resulting from dynamic loading should be identified first, after which the dynamic stresses can be scaled. Because linear elastic structural steel is used for the FEA, another approach is to scale the applied dynamic loading with Eq.3-4. This approach is less cumbersome than scaling the dynamic stresses afterwards, therefore is applied to define the dynamic loading for the ALS when the semi-submersible is damaged.

**Splitting forces**

Splitting forces, not to be confused by the splitting force reported in Chapter 2.3.2, can be summarised as reaction forces and moments at the centre of the deckbox. These loads can be obtained by a diffraction and radiation analysis, such as in AQWA. In AQWA, a bounding box must be specified for the included geometry and the coordinates of the point for which the splitting forces are calculated. As example, Figure 16 illustrates the bounding box and the point of a semi-submersible for which the splitting forces are calculated.

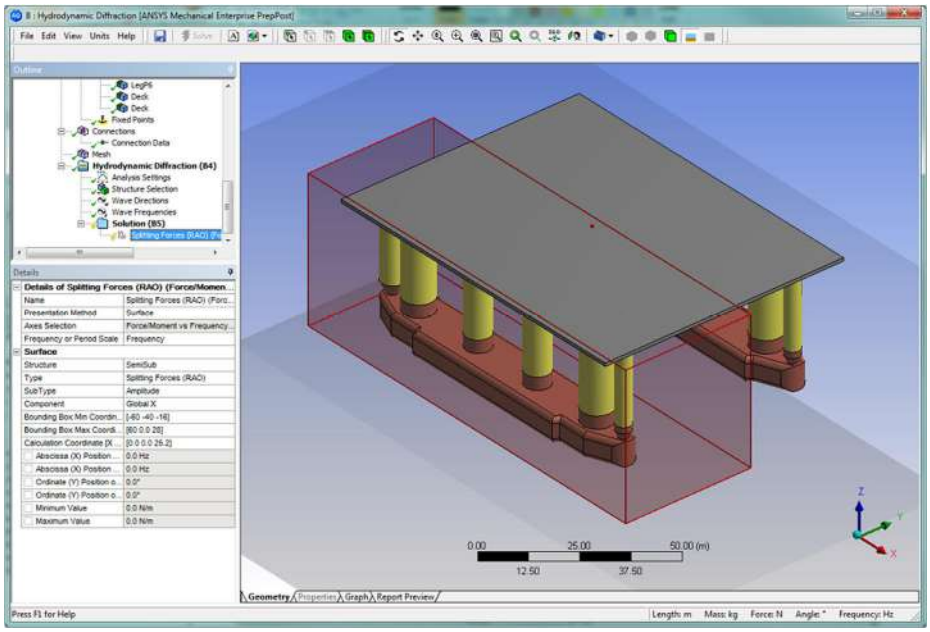

*Figure 16: Splitting force calculation in AQWA [15]*

The splitting forces, $\{F_{split}\}$, are the sum of the gravitational (1), hydrostatic + hydrodynamic (2) and inertia loads (3), as shown by Eq.3-5. The gravitational and hydrostatic loads should cancel each other out when hull shape, draught and masses are correctly defined, resulting in equilibrium. The dynamic and inertia loads therefore remain.

$$\{F_{split}\} = \underset{(1)}{\{F_g\}} + \underset{(2)}{\{F_f\}} + \underset{(3)}{\{F_m\}} \qquad \text{Eq.3-5}$$

The known splitting forces of the reference semi-submersible are calculated linearly with respect to wave amplitude in the frequency domain. This makes it advantageous to quickly calculate the characteristic forces and moments, such as the splitting force, longitudinal shear force and torsion moment important for the global strength of the semi-submersible.

**Water loading**

For load application in ANSYS, the splitting forces are first converted to water loads, $\{F_w\}$, using force and moment equilibrium, as illustrated by Figure 17. The centre of the water loading $(x_w, y_w, z_w)$ is assumed to be the centre of the wetted surfaces. Because splitting forces are simply reaction forces at the centre of the semi-submersible, water loading for the hull on the other side is its negative, i.e. $\{F_{w,SB}\} = -\{F_{w,PS}\}$. Then, inertia loads are subtracted from the water loads. The inertia loads are the result of the known masses and mass moments of inertia in operational condition multiplied by the known accelerations from the motion RAO's, i.e. Newton's second law. The phase difference between the water loading and inertia loads is accounted for in this calculation.

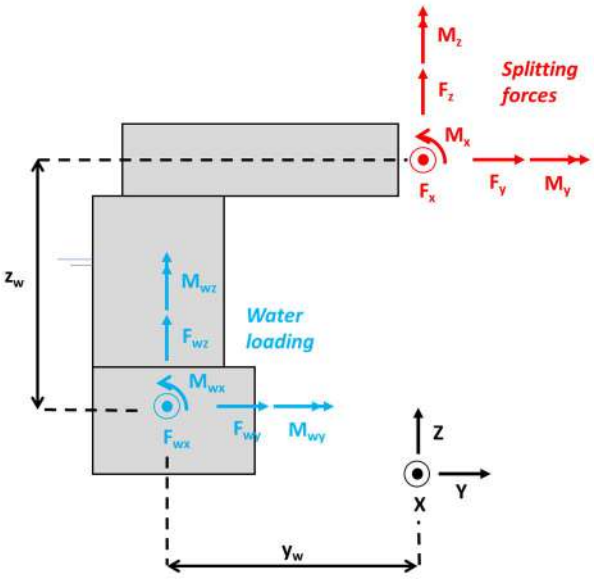


*Figure 17: Sketch of splitting forces and water loading*

By subtracting the inertia loads from the water loading an imbalance in loading occurs, which ANSYS has to counteract by applying global translational and rotational accelerations by the inertia relief boundary condition. This results in stresses important for load cases where the characteristic responses $a_L, a_T$ and $a_V$ are maximum. The resulting loading is applied uniformly over the wetted surfaces of the model. Reference is made to APPENDIX C where the input of the FEA is covered. As reported in Chapter 2.4, the bracing forces and moments based on the wave amplitude, period and phase difference are calculated per load case by the Morison equation. Bracing loading is also applied uniformly over the outer surfaces of the bracings.

### 3.2.2 Criteria

This chapter reports criteria to evaluate results of the global strength assessment. The aim is to apply simple checks to quickly evaluate the reference semi-submersible and the semi-submersibles with different bracing configurations.

For the ultimate strength of ships, not only the yield strength should be taken as criterion but also the buckling strength [21]. Buckling is generally important for structures that are slender. Important parameters for the slenderness of a structure are the span and the structures moment and compression resistance. Due to the large bracing span and the relative low moment and compression resistance of plated sections, the buckling strength is governing for some locations.

The equivalent stress, that contains multi-axial stress states, is retrieved from the analyses to check if yielding may occur. By obtaining normal and shear stresses, buckling of bracings and plated sections are checked. The buckling strength of plating between stiffeners can be derived using simple Euler plate buckling formulas [21], [22]. Mode I-VI buckling for stiffened panels covered in Hughes and Paik [21] were considered, however for a simple buckling check, the resulting procedure would be too comprehensive. In Eq.3-6 to Eq.3-8, elastic plate buckling formulas are shown, used to calculate the unidirectional buckling strength. The coefficients $C_{p,i}$ are added to account for lateral pressure, if present. To account for yielding, the Johnson-Ostenfield formula is applied as shown by Eq.3-9 and Eq.3-10. For the axial buckling strength of bracings, the Perry-Robertson formula is used briefly shown by Eq.3-11 [21]. This formula accounts for initial deflections, lateral pressure and yielding. For the lateral pressure, the bracing submerged weight is used.

$$\sigma_{Ex} = C_{px} k_x \frac{\pi^2 D}{b^2 t} \qquad \text{Eq.3-6}$$

$$\sigma_{Ey} = C_{py} k_y \frac{\pi^2 D}{b^2 t} \qquad \text{Eq.3-7}$$

$$\tau_E = k_\tau \frac{\pi^2 D}{b^2 t} \qquad \text{Eq.3-8}$$

$$\sigma_{ci} = \begin{cases} \sigma_{Ei}, & \sigma_{Ei} \leq 0.5\sigma_y \\ \sigma_y \left(1 - \dfrac{\sigma_y}{4\sigma_{Ei}}\right), & \sigma_{Ei} > 0.5\sigma_y \end{cases} \qquad \text{Eq.3-9}$$

$$\tau_c = \begin{cases} \tau_E, & \tau_E \leq 0.5\tau_y \\ \tau_y \left(1 - \dfrac{\tau_y}{4\tau_E}\right), & \tau_E > 0.5\tau_y \end{cases} \qquad \text{Eq.3-10}$$

$$\sigma_{cr} = \sigma_y \left( \frac{1}{2}\left(1 - \mu + \frac{1+\eta}{\lambda^2}\right) - \left( \frac{1}{4}\left(1 - \mu + \frac{1+\eta}{\lambda^2}\right)^2 - \frac{1-\mu}{\lambda^2} \right)^{0.5} \right) \qquad \text{Eq.3-11}$$

The Working Stress Design (WSD) method [22], [23] is frequently applied in engineering practice. Shown by Eq.3-12 to Eq.3-16, the equivalent stress, $\sigma_{eq}$, normal stresses, $\sigma_x$ and $\sigma_y$, and shear stress, $\tau_{xy}$, resulting in usage factors, $\eta$, is checked against the permissible usage factor $\eta_p$. The permissible usage factor is dependent on limit state; $\eta_0$ = 0.8 for the ULS and $\eta_0$ = 1 for the ALS; and is dependent on the type of check; $\beta$ = 1 for the yield check and $0.8 \leq \beta \leq 1$ for the buckling check. In this manner, a relatively simple evaluation of results can be performed, resulting in a structural design with acceptable stresses.

$$\eta = \frac{\sigma_{eq}}{\sigma_{yield}} \qquad \text{Eq.3-12}$$

$$\eta = \sqrt{\left(\frac{\sigma_x}{\sigma_{cx}}\right)^2 - \left(\frac{\sigma_x}{\sigma_{cx}}\right)\left(\frac{\sigma_y}{\sigma_{cy}}\right) + \left(\frac{\sigma_y}{\sigma_{cy}}\right)^2 + \left(\frac{|\tau_{xy}|}{\tau_c}\right)^2} \qquad \text{Eq.3-13}$$

$$\eta = \frac{\sigma_x}{\sigma_{cr}} \qquad \text{Eq.3-14}$$

$$\eta_p = \beta\eta_0 \qquad \text{Eq.3-15}$$

$$\eta \leq \eta_p \qquad \text{Eq.3-16}$$

### 3.2.3 Results

This chapter summarises the results of the reference global strength assessment. Critical areas, corresponding to critical load cases, are identified, after which yield and buckling checks are performed at selected locations.

Please note the following for the results covered in this and upcoming chapters. First, in some deformation and stress plots, deformations are scaled to clearly illustrate the different load cases and occurring deformations. Therefore, some plots may seem unrealistic. Second, the middle position is taken to derive the stresses from the analyses, i.e. stresses at neutral axis of the plating. Because of the absence of small stiffeners in the structural model, the stress would be unrealistically high when outer fibre stresses are used. However, for the wetted areas and main deck, adopting the middle stress will result in a underestimation of stresses, since hydrostatic and dynamic loading at the wetted areas and deck loading result in bending stress at the outer fibres. Additional outer fibre stresses, reported in Chapter 3.2.3.2, are accounted for by manually calculating bending stresses. Finally, peak stresses above yielding strength shown in some stress plots only occur in concentrated areas due to mesh concentration and/or the absence of the small stiffeners. These areas were ignored when evaluating results.

#### *3.2.3.1 Static loading*

As explained in Chapter 3.2.1.1, static loading, consisting of mass and hydrostatic pressure, should result in equilibrium. Small differences in resulting forces and moments are counteracted by the inertia relief setting that applies global translational and rotational accelerations. These accelerations should be small when only static loading is considered. The inertia relief accelerations are reported in Table 10 when only static loading is considered, showing a balanced model.

*Table 10: Inertia relief summary, static loading*

| Accelerations | x-axis | y-axis | z-axis |
|---|---|---|---|
| Translational [m/s$^2$] | 6.2E-15 | -3.0E-15 | -1.6E-3 |
| Rotational [rad/s$^2$] | 1.4E-2 | -2.3E-2 | 2.0E-4 |

Static loading results in deformations shown by Figure 18, similar to the deformations sketched in Figure 2. It is observed that the pontoons are buoyant leading to bending moments and therefore stresses at the pontoon-column connection. Also, the column-deckbox connection is a hot spot due to the overhanging deckbox. Since the bracings are buoyant and due to the outward deflection of the floaters, bending and axial tensile stresses are present. The outward floater deflections dominate mean tensile stress. The total bracing mean tensile stress magnitude is approximately 50 MPa, which affects fatigue lifetime negatively. In Figure 19, the stresses due to static loading can be observed, showing the hot spots. The stress at the pontoon-column and column-deckbox connections are approximately 60 MPa and 180 MPa, respectively.

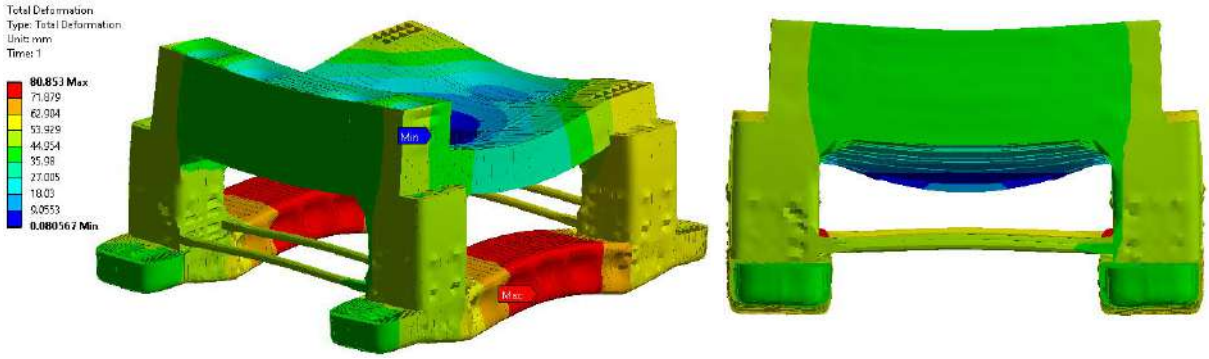


*Figure 18: Deformation due to static loading*

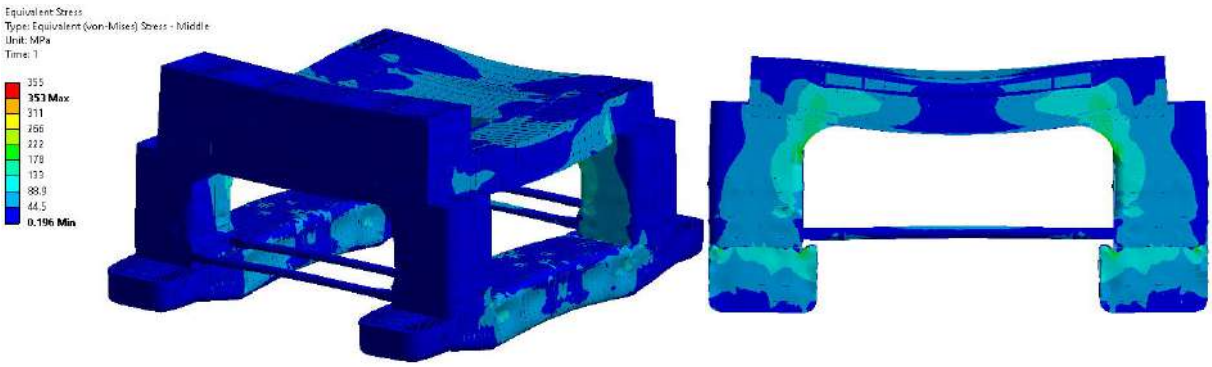


*Figure 19: Equivalent stresses due to static loading*

### *3.2.3.2 Total loading*

With total loading, static and dynamic loading are both considered. As explained in Chapter 3.2.1, load cases are defined that each result in a maximum characteristic response in the ULS. In Figure 21 to Figure 26 the equivalent stresses are presented for the ULS and ALS, showing the clear deformations and hot spots resulting from each load case. The in-phase load cases correspond with the phase angles reported in Table 9, whereas the out-of-phase load cases are equivalent to the in-phase angles plus 180 degrees, i.e. $\varepsilon_{F,\zeta}$ + 180°.

Another result from the strength assessment are the inertia relief accelerations ANSYS solves for. The global accelerations as a result of imbalanced loading are shown in Figure 28 per load case. Figure 28 shows an increase in applied accelerations for load cases where the accelerations should be the highest. When the accelerations of the $a_L, a_T$ and $a_V$ ULS load cases are compared with the ULS accelerations in Table 9, the accelerations from inertia relief are similar, therefore confirming the load calculation method described in 3.2.1.

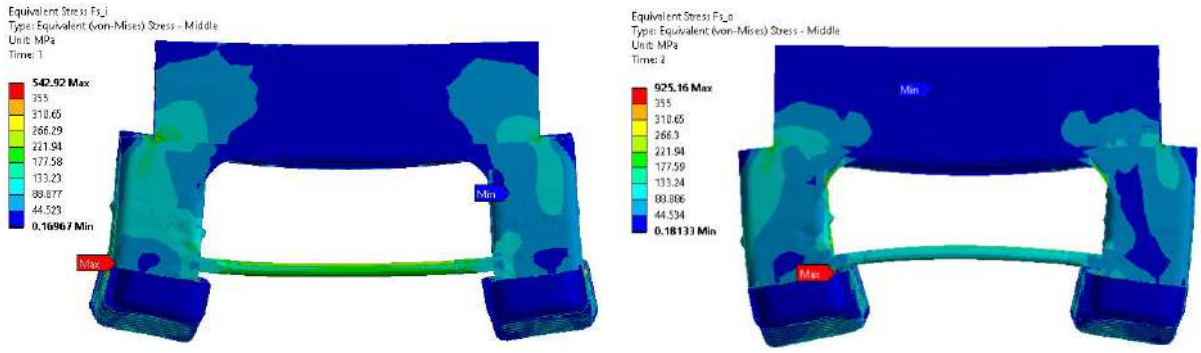


*Figure 20: Equivalent stress plot, ULS $F_S$ load case: in-phase (left) and out-of-phase (right)*

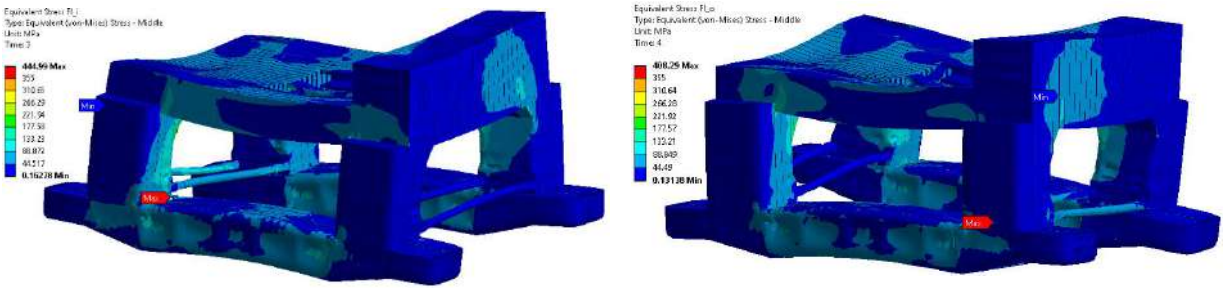

*Figure 21: Equivalent stress plot, ULS $F_L$ load case: in-phase (left) and out-of-phase (right)*

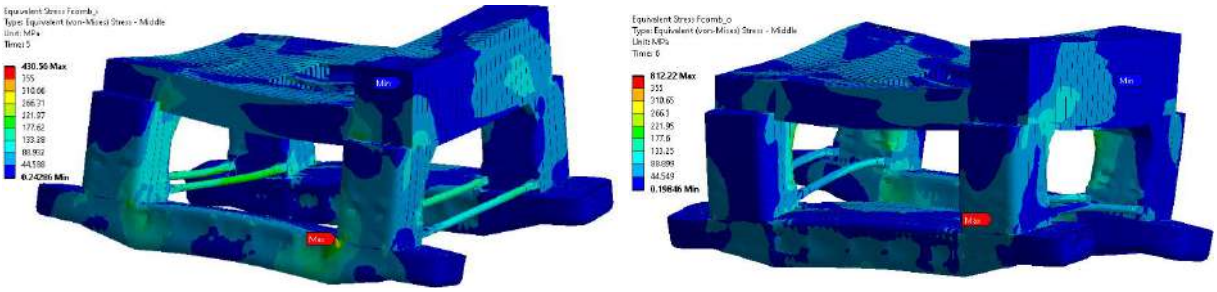

*Figure 22: Equivalent stress plot, ULS $F_{comb}$ load case: in-phase (left) and out-of-phase (right)*

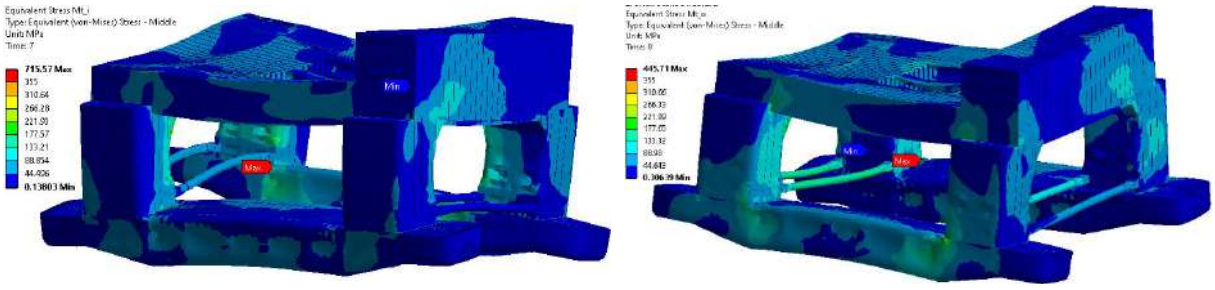

*Figure 23: Equivalent stress plot, ULS $M_T$ load case: in-phase (left) and out-of-phase (right)*

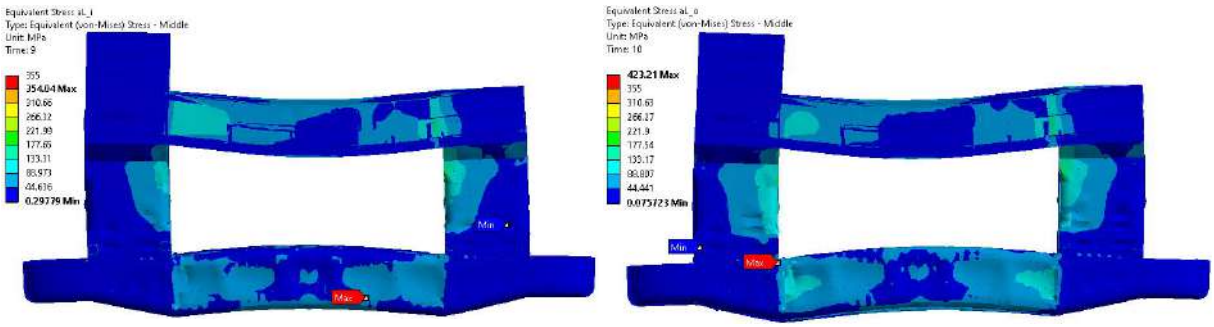


*Figure 26: Equivalent stress plot, ULS $a_L$ load case: in-phase (left) and out-of-phase (right)*

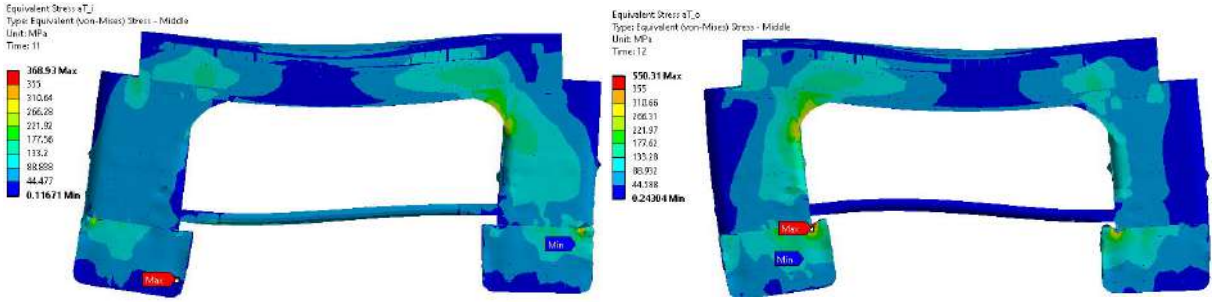


*Figure 25: Equivalent stress plot, ULS $a_T$ load case: in-phase (left) and out-of-phase (right)*

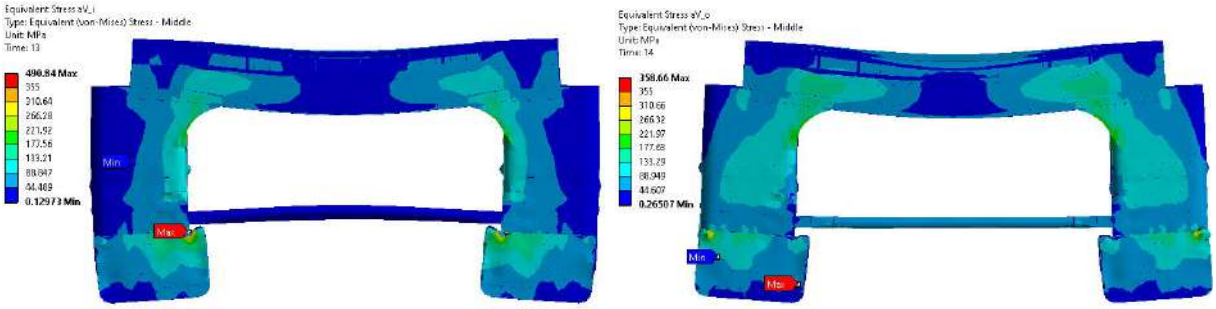


*Figure 24: Equivalent stress plot, ULS $a_V$ load case: in-phase (left) and out-of-phase (right)*

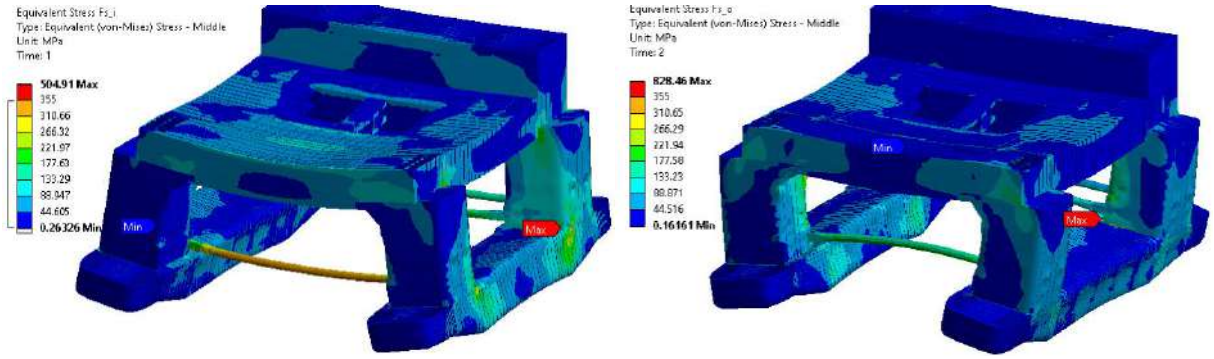


*Figure 27: Equivalent stress plot, ALS $F_S$ load case (aft bracing suppressed): in-phase (left) and out-of-phase (right)*

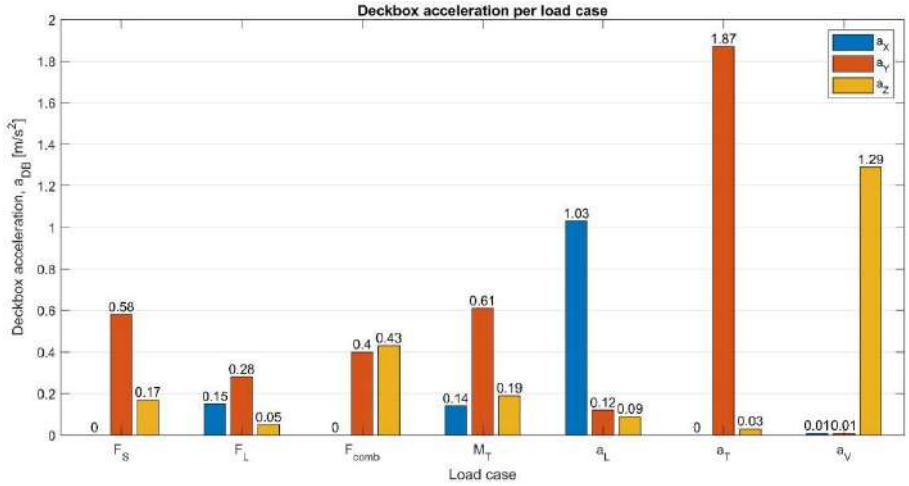


*Figure 28: Deckbox accelerations of ULS per load case*

To summarise the results in more detail, locations and areas are selected at which stresses are evaluated. In Figure 29, the selected areas and locations are highlighted in blue. For the strength assessment of other bracing configurations, selected areas and locations remain constant. However, for some bracing configurations, locations may shift due to added or removed bracing members. Because of the large main deck area, two transverse and longitudinal paths were defined in ANSYS to extract the normal and shear stresses quickly and precisely for the buckling check. Locations, such as the brace-column connection, were not chosen due to the absence of structural details and the sharp edge resulting in stress singularities. Therefore, stresses are difficult to compare between different bracing configurations.

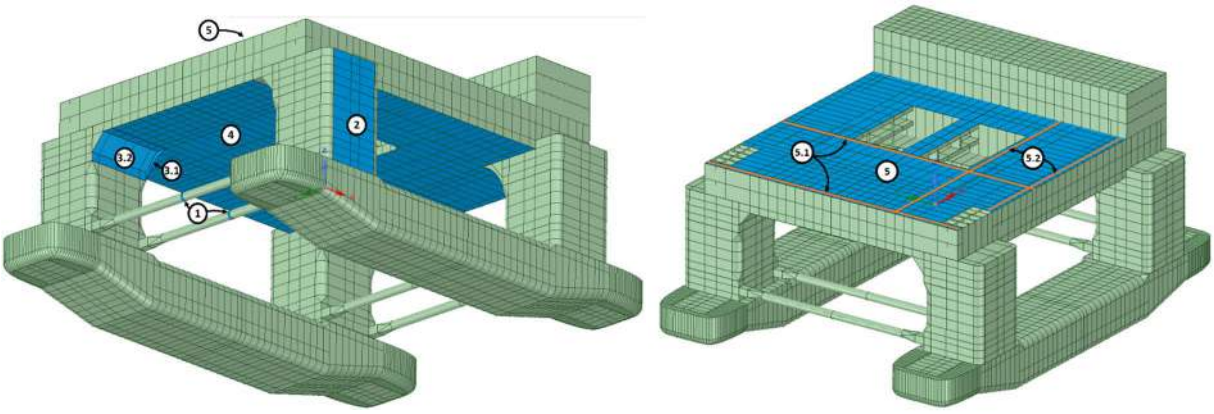


*Figure 29: Locations stress check*

The maximum equivalent, normal and shear stresses per location or area is summarised in Table 11. Briefly discussed in the beginning of Chapter 3.2.2, the middle stress is taken from the FEA, which is the stress at the neutral axis of the plate. Compared to the outer fibre stress, the middle stress is a more realistic presentation of the actual stresses, since the small stiffeners are absent in the structural model. However, for plating subjected to lateral pressures, such as the pontoon hull, column outer plating and main deck, the extracted FEA stresses are not correct. Additional stresses, reported in Table 12, are therefore manually calculated for the column outer plating (2) and main deck (5) areas. The additional plate stresses reported in the bottom row of Table 12 are added to the column outer plating and main deck stresses reported in Table 11.

*Table 11: Maximum equivalent, normal and shear stress at selected locations, reference case*

| Limit state | Area / location | | Yield check | | | Buckling check | | | | |
|---|---|---|---|---|---|---|---|---|---|---|
| | | | FEA $\sigma_{eq}$ | Gov. load case | $\frac{\eta}{\eta_p}$ | FEA | | | Gov. load case | $\frac{\eta}{\eta_p}$ |
| | | | | | | $\sigma_x$ | $\sigma_y$ | $\tau_{xy}$ | | |
| ULS | 1 | Mid-bracing | 245 | $F_S$ | 0.86 | 169 | 0 | 0 | $F_S$ | 0.85 |
| | 2 | Column outer plating | 260 | $F_S$ | 0.92 | 215 | 51 | 3 | $F_S$ | 0.85 |
| | 3.1 | Column-deckbox connection, bracket | 283 | $a_T$ | 1.00 | 232 | 0 | 89 | $a_T$ | 1.00 |
| | 3.2 | Column-deckbox connection, outer plating | 253 | $a_T$ | 0.89 | 245 | 25 | 30 | $a_T$ | 0.96 |
| | 4 | Bottom deck | 200 | $F_{comb}$ | 0.70 | -* | | | | |
| | 5.1 | Main deck, transverse | 188 | $M_T$ | 0.66 | 115 | 99 | 59 | $M_T$ | 0.64 |
| | 5.2 | Main deck, longitudinal | | | | 93 | 8 | 20 | $F_{comb}$ | 0.39 |
| ALS** | 1 | Mid-bracing | 347 | $F_S$ | 0.98 | 199 | 0 | 0 | $F_S$ | 0.80 |
| | 2 | Column outer plating | 243 | $F_S$ | 0.68 | 199 | 48 | 1 | $F_S$ | 0.63 |
| | 3.1 | Column-deckbox connection, bracket | 280 | $a_T$ | 0.79 | 225 | 0 | 114 | $a_T$ | 0.86 |
| | 3.2 | Column-deckbox connection, outer plating | 270 | $a_T$ | 0.76 | 250 | 20 | 50 | $a_T$ | 0.82 |
| | 4 | Bottom deck | 180 | $F_{comb}$ | 0.51 | -* | | | | |
| | 5.1 | Main deck, transverse | 181 | $M_T$ | 0.51 | 103 | 85 | 53 | $M_T$ | 0.45 |
| | 5.2 | Main deck, longitudinal | | | | 78 | 8 | 20 | $a_V$ | 0.27 |

** tensile stress only*
*** ALS, most aft horizontal transverse bracing suppressed*

*Table 12: Additional stresses column outer and main deck plating*

| | | Column outer plating | Main deck plating | Ref. |
|---|---|---|---|---|
| Stiffened panel parameters | Frame spacing<br>Stiffener spacing<br>Stiffener type<br>Lateral pressure | 2400 mm<br>600 mm<br>HP300x10<br>0.09 MPa | 2400 mm<br>600 mm<br>HP160x8<br>0.05 MPa | [24], [25] |
| Bending stress outer fibre stiffened panel | | 54 MPa * | 217 MPa * | |
| Bending stress at longitudinal mid-length plate | | 50 MPa ** | 23 MPa ** | [26] |

** Free longitudinal edges and clamped transverse edges assumed*
*** Clamped edges assumed for all edges*

Figure 27 and Table 11 present stresses in the ALS where the most aft bracing is suppressed. This damaged condition is governing for maximum bracing stresses, due to the less stiff aft deckbox structure and because the remaining aft bracing is the closest to the centre of the wetted surfaces, therefore absorbs more water loading. This damaged condition defines global bracing dimensions, such as diameter and wall thickness. Intuitively, the splitting force load case results in the highest stress in the bracings.

The ULS defines the dimensions of the other areas reported in Table 11. Also reported in Chapter 2.2.2, the $a_T$ load case results in high stresses at the column-deckbox connection due to the large transverse inertia loads of the deckbox. The large stresses at this connection can also be clearly observed in Figure 25. Deckbox stresses are the largest for load cases where torsion and/or bending occurs in the deckbox, such as the $F_L$, $F_{comb}$ and $M_T$ load cases. The maximum equivalent stresses for both the bottom and main deck occurs at the moonpool, where stress concentrates at the corners shown in Figure 30. Due to these stress concentrations, the defined transverse and longitudinal paths near the moonpool illustrated in Figure 29 are governing for the buckling check of the main deck. No compressive stresses are present in the bottom deck due to the deckbox mass of 25582 tonnes.

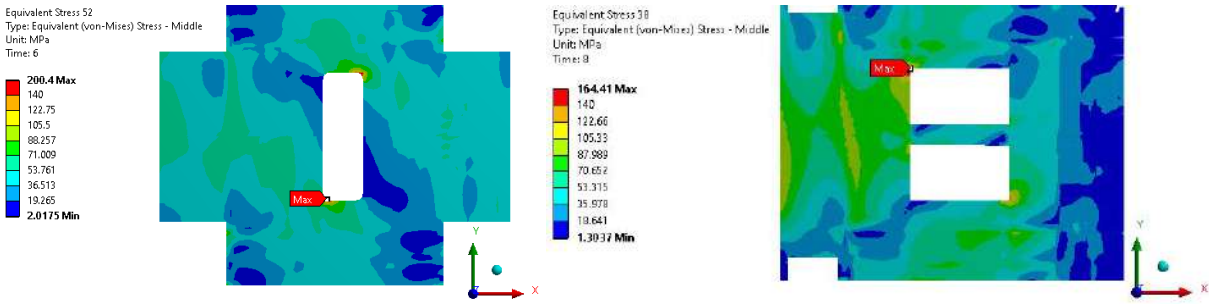


*Figure 30: Equivalent stress plot of bottom deck $F_{comb}$ ULS load case (left) and main deck $M_T$ ULS load case (right)*

The usage and permissible usage factor ratio, $\eta/\eta_p$, for the yielding and buckling check is relatively low for the bottom and main deck, see Table 11. Outside the moonpool area, stresses are even lower. One could say that the deckbox height could be designed smaller and/or plate thicknesses can be reduced of the bottom and main deck. However, because the reference semi-submersible is designed to be a drilling vessel, storage and equipment space is needed for its functionalities when operating [27]. Compared to pipelaying or crane semi-submersibles, drilling vessels require additional space for example mud tanks, mud treatment facilities and blowout prevention (BOP) equipment. A smaller deckbox size is therefore not possible. A larger deckbox size results in a structure with larger bending and torsion sectional properties and therefore lower stresses. Regarding plate thicknesses, not only the ULS and ALS are of importance for the structural design, but also the SLS. The SLS is applicable during normal use of the semi-submersible under moderate environmental conditions and ensures durability of the structure, such as acceptable deflections. The main deck of the reference semi-submersible is designed for a deck load of 0.05 MPa, see Table 12. When assuming free longitudinal edges and simply supported transverse edges, since deck loading may not be applied everywhere on deck, the resulting deformation at mid length is 4 mm. When compared to the guidelines of DNV [28], where the allowable deflection is $w_{all} = \frac{L}{350} = 7\,mm$, demonstrates the SLS is also a governing limit state for the structural design of the main deck. Also, the bending stress of 217 MPa at the outer fibre of the stiffened panel reported in Table 12, concludes the SLS is a governing limit state. Finally, the main deck should be able to absorb point loads when operating. When a point load of $P = 1.5q = 75\,kN$ is assumed, bending stresses of around 230 MPa occur when Roark's formulas are applied [26].

## 3.3 Bracing configurations

This chapter presents the different bracing configurations analysed using the same procedure as the reference case as discussed in Chapter 3.2. The paragraphs below summarise the results of the different configurations briefly. Chapters 3.3.1 to 3.3.5 reports the results and findings of different configurations in more detail.

For the comparison of the different bracing configurations, the following notes are of importance. First, the aim of the strength assessment is to iterate to similar usage factors of the reference semi-submersible for the selected areas and locations discussed in Chapter 3.2.3. In this manner, the structural performance of a semi-submersible with a different bracing configuration is similar to the reference case and therefore the impact on mass properties can be studied. For added structural members, i.e. members not present in the reference semi-submersible, usage factors for the ULS and ALS are iterated to magnitudes of $0.7 \leq \eta/\eta_p \leq 1$. Finally, global water loading of the reference semi-submersible, derived from the splitting forces reported in Chapter 3.2.1, is kept constant. Per bracing configuration, local water loading is calculated to account for different bracing loading using the Morison equation reported in Chapter 2.4. The outer geometry of the pontoons and columns below the waterline are not modified. The motivation of this approach is discussed in Chapter 2.3.

Figure 31 illustrates the different bracing designs studied, where each bracing configuration differentiates itself being beneficial for certain load cases, or is beneficial regarding fatigue sensitive locations.

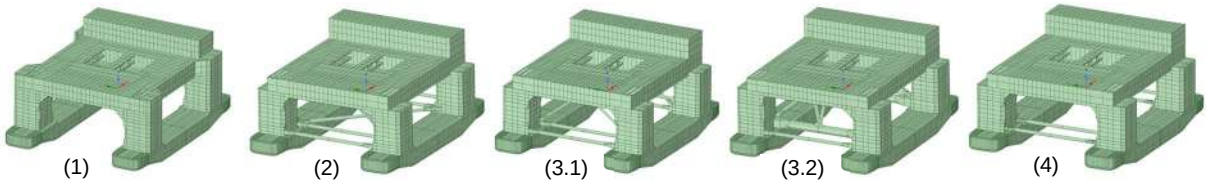


*Figure 31: Bracing configurations*

Configuration 1, shown on the left of Figure 31, has no bracings, therefore omits fatigue sensitive locations such as the brace-column connection. Due to the absence of transverse bracings, larger shear and bending moments occur at the column-deckbox connection and in the deckbox structure. Structural dimensions of these parts are increased, which results in an increase of total structural mass of 13% and VCG of 7%. The payload of configuration 1 is reduced by 22%. The amount of fatigue sensitive locations is reduced, however global loading is more unfavourable since static loading and especially beam wave loading results in large shear and bending moments at the column-deckbox connection and in the deckbox structure.

Configuration 2 has added diagonal bracings in the horizontal plane to restrain floater motions in surge and sway direction, resulting in lower bending and torsion stress in the deckbox structure. Deckbox plate thicknesses, especially of the bottom deck, are therefore reduced, resulting in a payload increase of 4%. Compared to configurations 3.1 and 3.2, configuration 2 is more effective to increase payload and structural redundancy.

Configuration 3 includes added vertical diagonal bracings that support the deckbox plus has a more effective load path for transverse inertia loads. For configuration 3, two different designs are analysed; configuration 3.1 and 3.2. Bracing configuration 3.1 consists of 4 horizontal transverse and 4 vertical diagonal bracings. For load cases where the floaters deform outward, the diagonal braces of configuration 3.1 show insufficient support of deckbox mass as the diagonal braces also move outward. Consequently, the impact on deckbox stresses is marginal. Therefore, an extra version named configuration 3.2 is analysed, which has 4 additional vertical diagonal bracings supported by large horizontal transverse bracings, resulting in a more rigid structure with increased deckbox support compared to configuration 3.1. A reduction in deckbox mass of 6% and deckbox VCG meters is therefore achieved. However, bracing mass increases considerably by 323%. For the total VCG of the semi-submersible, a reduction of 4% is achieved. The increase in payload of 5% is similar compared to configuration 2. The added diagonal bracings of configuration 3.2 increases structural redundancy, however stresses increase significantly when the larger horizontal bracing is damaged, therefore ineffectively increase structural redundancy. Regarding fatigue, configuration 3.2 is unfavourable

compared to other configurations, since the large horizontal transverse bracings result in a significant larger welding volume at fatigue sensitive locations.

Configuration 4 consists of 4 hinged horizontal transverse bracings, which can rotate freely around the z-axis at the brace-column connection. When opposite surge motion and rotation of the columns occur, moments at the brace-column connection are omitted. In addition, moments around the z-axis are not present due to local water loading at the bracing. This can be advantageous to reduce ULS stresses and fatigue damage at the fatigue sensitive brace-column connection. However, because motion differences between the PS and SB floaters are small, the impact of hinged bracings on brace-column stresses is therefore limited. Since the hinged bracings do not affect floater motions significantly, the structural design of the semi-submersible is not modified, therefore mass properties are equivalent to the reference semi-submersible. Also, due to similar load paths and welding volume at fatigue sensitive locations, structural redundancy and fatigue is expected to be similar.

### 3.3.1 Configuration 1: No bracings

The first semi-submersible design studied has no bracings, therefore the floaters are less restrained for opposite surge, sway and heave motions. Compared to the reference semi-submersible with transverse bracings, load paths change when bracings are omitted, especially for the splitting force load case, $F_S$. Without bracings, larger shear and bending moments occur at the column-deckbox connection and in the deckbox structure. For these parts, structural dimensions are to be increased, which results in larger column and deckbox mass and an increase in VCG.

This chapter reports the structural design changes of configuration 1. First, the strength assessment is reported of the reference semi-submersible without bracings. Then, the final structural design of the modified semi-submersible without bracings is presented. Finally, the effect of transverse bracings on the floater sway vibrations are studied. The impact on mass properties, floater motions, structural redundancy and fatigue for all studied bracing configurations are discussed in Chapter 3.3.5.

#### *3.3.1.1 V0 (reference semi-submersible without bracings)*

To analyse what structural design changes are needed, the reference semi-submersible design without bracings is studied first for the ULS only. Due to the absence of bracings, no ALS strength assessment is performed for configuration 1. The result of the strength assessment can be summarised by Figure 32, showing large stresses in the column-deckbox connection, where $\sigma_{eq} \approx 600$ MPa, and main deck plating, where $\sigma_{eq} \approx 450$ MPa for the splitting force load case. Also, transverse bulkheads are subjected to a significant increase in bending and shear stresses. For all locations and areas where stresses are checked using the WSD method, the splitting force load case is the governing load case, resulting in usage factors 1.3 to 2.5 times higher compared to the reference case. Other load cases did not result in higher stresses at any area or location.

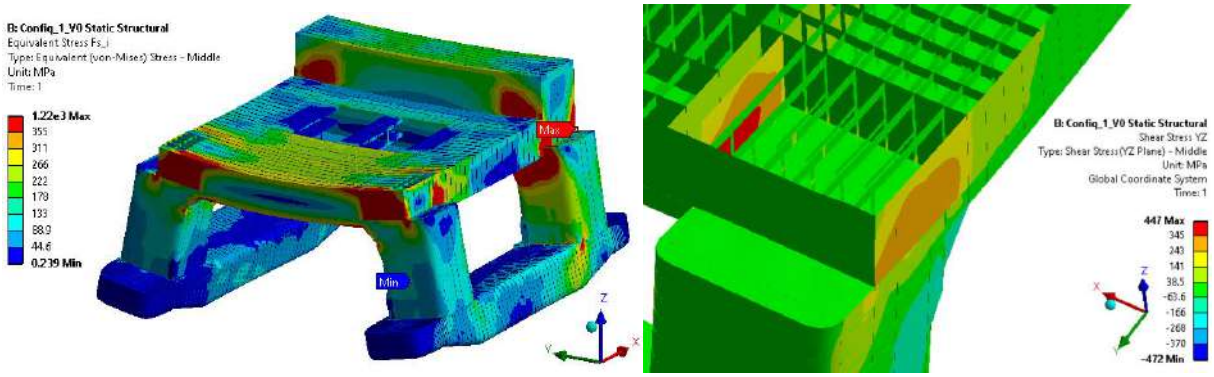


*Figure 32: Configuration 1 V0, ULS $F_S$ load case, equivalent stress plot total semi-submersible (left) and shear stress plot PS aft column-deckbox connection (right), where lower, tween and main deck are hidden*

Similar to the column-deckbox connection is the knee joint sketched in Figure 34. Here, the tensile or compressive forces in the beam flange will transfer through the web connection as shear into the supporting column. The shear plot of Figure 32 shows similar results, therefore explains the increase of shear stress in the deckbox transverse side plating and bulkhead. The column-deckbox connection also has an increase in normal stress at the outer plating and brackets on the inner faces of the columns shown in Figure 33. This stress concentration is due to the radius of curvature at the column-deckbox connection where the neutral axis will shift toward the inner face, also illustrated by Figure 34. Above phenomena are also present in the strength assessment of the reference semi-submersible with transverse bracings, however not as dominant due to the transverse bracings.

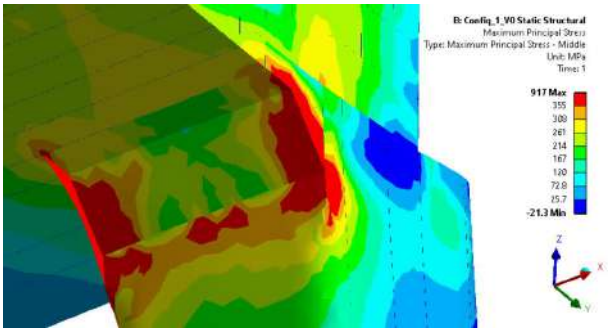


*Figure 33: Maximum principle stress plot of inner face PS forward column-deckbox connection, ULS $F_S$ load case*

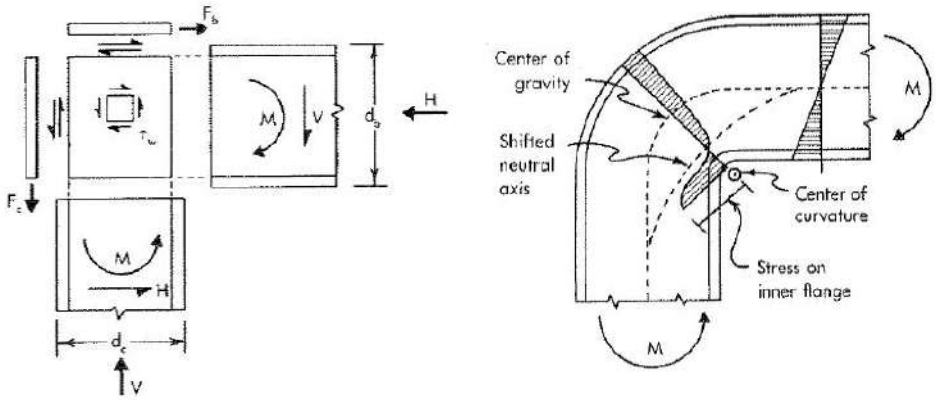


*Figure 34: Knee joints illustrating shear in web (left) and shift in neutral axis (right) [29]*

### *3.3.1.2 Final design*

Based on the strength assessment of the reference semi-submersible without bracings, the structural design is modified. The main objective is to transfer shear forces and bending moments from the column structure into the deckbox structure for the splitting force load case. In Table 13, the modifications are summed for the final design of configuration 1. In the paragraphs below, the modifications are elaborated.

The bending capacity of the column-deckbox connection is increased by raising the columns from lower deck, 34200 above baseline (A.B.) to main deck, 41400 A.B.. Therefore, column height is increased by 7.2 meters. In addition, the radius of curvature is increased by increasing the size and plate thicknesses of the chamfer at the inner face of the column-deckbox connection. By adding a side chamfer between the column and deckbox, shown by modification 7 in Figure 35, the transverse and longitudinal bending capacity increases as well. The shear capacity is increased by adding transverse bulkheads at the column-deckbox connection. By extending these bulkheads into the deckbox structure, stress continuity improves and increases the bending capacity of the deckbox. Further, the deckbox bottom, main aft deck and transverse forward and aft side plating thickness is increased.

By above modifications, no increase in deckbox height is needed to enhance bending capacity. Namely, the increased inner face chamfer size results in lower deckbox bending moments. Further, the added transverse bulkheads and increasing the aft bottom and main deck thicknesses, increases bending capacity. If the deckbox height would be increased, the entire deck height has to raised, which is less efficient, since only the deckbox section from aft to midship lacked bending capacity, also illustrated by Figure 32.

*Table 13: Structural design modifications semi-submersible Configuration 1, see Figure 35*

| Part | Structural design modification | | Design | |
|---|---|---|---|---|
| | | | V0 | Final |
| Column | 1 | Outer plating thickness | 18 mm | 20, 30 mm |
| Column-deckbox connection | 2 | Column height | 34200 A.B. (lower deck) | 41400 A.B. (main deck) |
| | 3 | Transverse bulkheads added (per column-deckbox connection) | 2(fwd.), 1(aft) | 5(fwd.), 4(aft) |
| | 4 | Inner face chamfer size | 2300 mm | 3800 mm |
| | 5 | Inner face chamfer outer plating thickness | 25 mm | 50 mm |
| | 6 | Inner face chamfer, bracket thickness | 15 mm | 50 mm |
| | 7 | Side chamfer added | - | 3000 mm |
| Deckbox | 8 | Transverse bulkheads added (total deckbox) | 7 | 11 |
| | 9 | Bottom and main aft deck thickness | 20 mm | 30 mm |
| | 10 | Forward and aft transverse side plating thickness | 20 | 30 mm |

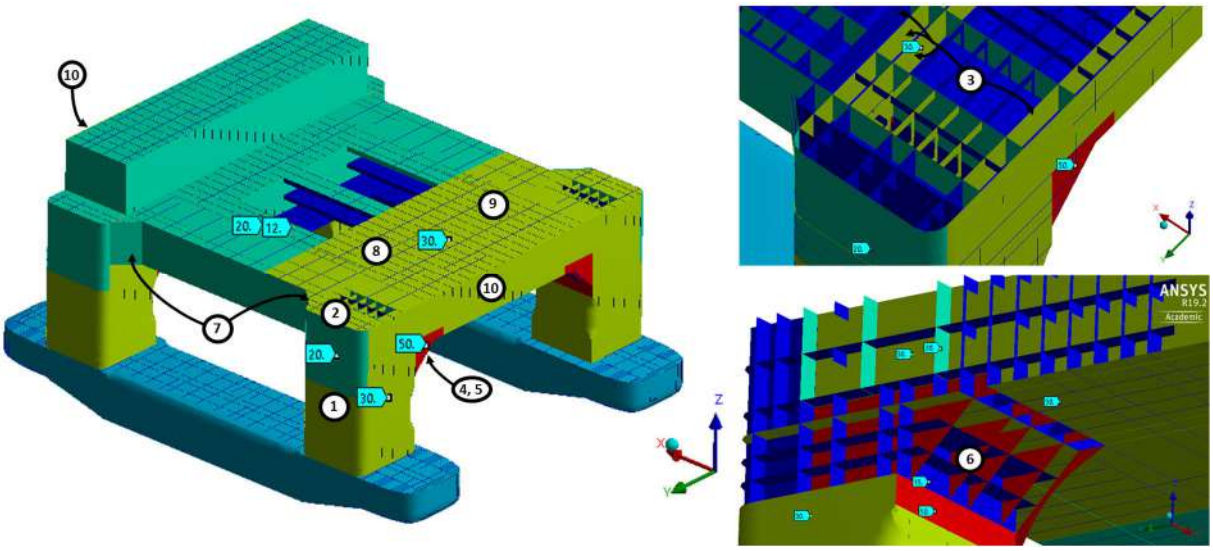


*Figure 35: Plate thickness plot configuration 1, final design*

The structural design modifications result in a strength assessment with similar usage factors like the reference case. Figure 36 clearly illustrates the increase in bending and shear capacity of the column-deckbox connection and deckbox structure. In APPENDIX D an overview of stresses and WSD-check of the selected areas and locations is presented.

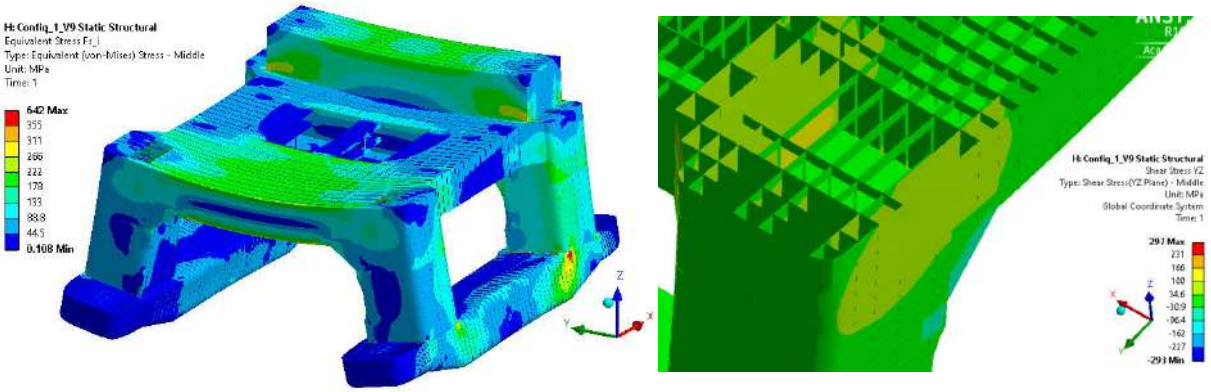


*Figure 36: Configuration 1 final design, ULS $F_S$ load case, equivalent stress plot of total semi-submersible (left) and shear stress plot of PS aft column-deckbox connection (right), where main deck is hidden*

### 3.3.1.3 *Vibration assessment*

Due to the absence of transverse bracings, sway deformations of the floaters are significantly larger compared to the reference semi-submersible, see Table 30 in Chapter 3.3.5. The smaller stiffness in sway direction result in a smaller natural frequency near occurring wave frequencies. It is therefore studied if the difference in semi-submersible sway stiffness affects the dynamic sway motion of the floaters. No vibration assessment is performed for the other bracing configurations discussed in the chapters below, since these configurations have similar or higher directional stiffnesses. Therefore, similar or higher natural frequencies are expected remote from occurring wave frequencies.

The semi-submersible is modelled as a simple single degree of freedom system (SDOF) with viscous damping; the 1-mass-spring-dashpot system sketched in Figure 37. The system properties used are summarised in Table 14. The structural stiffness in sway direction, $k_{22}$, is estimated by the deformation of the floater for the splitting force load case in the ULS. Wave loading is assumed to be harmonic and the added mass and damping values in sway direction, which depend on wave frequency, are extracted from the radiation and diffraction analysis reported in APPENDIX A.

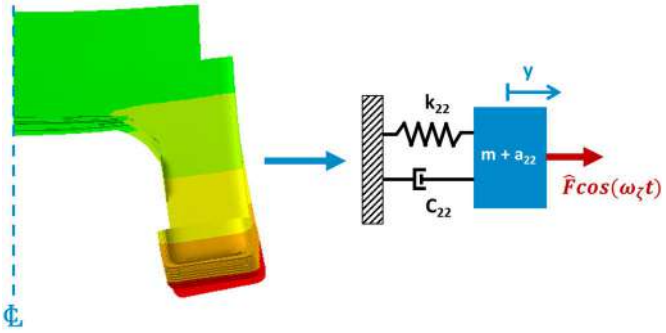


*Figure 37: Mass-spring-dashpot system semi-submersible loaded by beam waves*

The equation of motion of the mass-spring-dashpot system is shown by Eq.3-17. Due to the small magnitude of damping, the normalised damping coefficient, $\xi$, which is the ratio between the damping and critical damping, is considerable smaller than 1. Therefore, the damped natural frequency, $\omega_d$, is similar to the natural frequency of an undamped system, $\omega_n$, shown by Eq.3-18. The dynamic amplification factor (DAF) of the mass-spring-dashpot system is presented by Eq.3-19 [30], which is the ratio between the dynamic motion amplitude and static deformation. When plotted for a range of wave frequencies, see Figure 38, it demonstrates that each floater has one natural frequency, namely 4.9 rad/s and 12.3 rad/s for Configuration 1 and the reference semi-submersible, respectively. The smaller natural frequency of Configuration 1 results from the smaller sway stiffness and increased mass of the floater. Waves with notable energy usually have frequencies below 1.6 rad/s [7], equivalent to a wave period of 4 seconds. At this wave frequency the DAF of the floater of Configuration 1 is 1.13, whereas the DAF of the reference semi-submersible is 1.02. Therefore, some dynamic amplification of the floaters may occur for Configuration 1 for beam waves with large frequencies. If a fatigue assessment is performed for this configuration, the natural frequencies and the dynamic amplification should be studied more thoroughly as the amplification of the motions has negative impact on fatigue damage of hot spots, such as the column-deckbox connection.

*Table 14: System properties for floater dynamics in sway direction*

| System property | | Value | Reference |
|---|---|---|---|
| Force amplitude | $\hat{F}$ | 91000 kN ($F_S$ in ULS) | Table 9 |
| Static floater deformation | $y_{static}$ | 25 mm (Ref. case),<br>150 mm (Config. 1, final) | Table 30 |
| Structural sway stiffness | $k_{22} = \frac{\hat{F}}{y_{static}}$ | 3640 MN/m<br>607 MN/m | |
| Mass floater | $m = m_{s,pontoon} + m_{p,pontoon} + 2m_{s,column}$ | 5637 t (Ref. case)<br>6492 t (Config. 1, final) | Table 29,<br>APPENDIX C |
| Added sway mass floater | $a_{22}$ | ≈ 27000 t - 18000 t | APPENDIX A |
| Sway damping floater | $c_{22}$ | ≈ 6400 t/s | |

$$(m + a_{22})\ddot{y} + c_{22}\dot{y} + k_{22}y = \hat{F}\cos(\omega_\zeta t) \qquad \text{Eq.3-17}$$

$$\omega_{d,\xi \ll 1} = \omega_n\sqrt{1-\xi^2} \approx \omega_n = \sqrt{\frac{k_{22}}{m + a_{22}}} \qquad \text{Eq.3-18}$$

$$DAF = \frac{\hat{y}}{y_{static}} = \frac{k_{22}}{\sqrt{\left(k_{22} - (m + a_{22})\omega_\zeta^2\right)^2 + \left(c_{22}\omega_\zeta\right)^2}} \qquad \text{Eq.3-19}$$

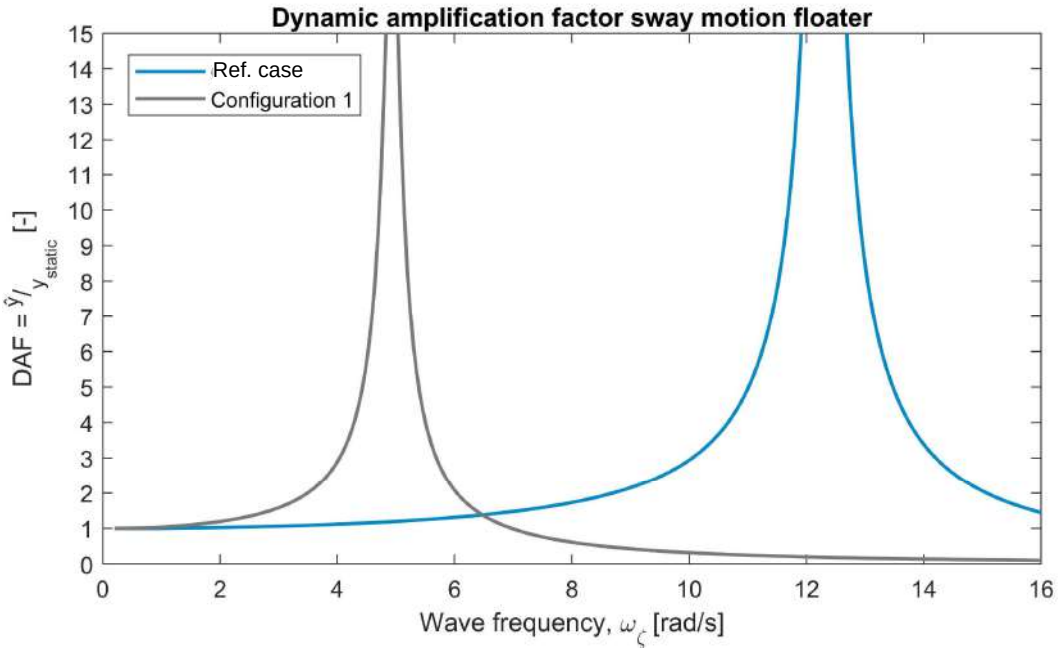


*Figure 38: Dynamic amplification factor sway motion of floaters reference case and Configuration 1*

### 3.3.2 Configuration 2: Horizontal transverse and horizontal diagonal bracings

The second bracing configuration studied, shown in Figure 39, consists of 4 horizontal transverse bracings and 2 horizontal diagonal bracings. The added diagonal bracings restrain floater motions in surge and sway direction, however the sway motion is restrained less effective compared to the transverse bracings. This bracing configuration results in lower bending and torsion stress in the deckbox structure, therefore structural dimensions can be reduced at these areas.

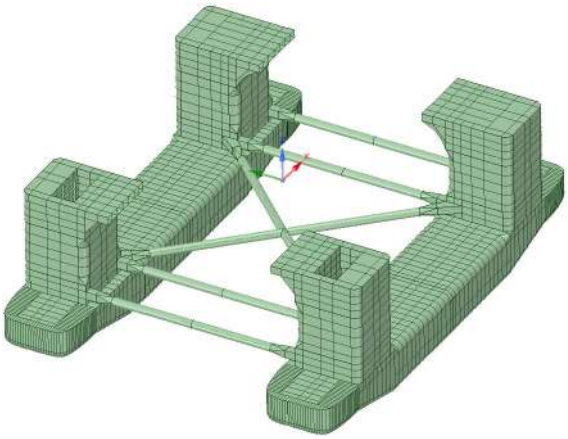

The global strength assessment performed for configuration 2 is reported in this chapter. First, the strength assessment is reported of the reference semi-submersible with configuration 2. Then, the final structural design of the modified semi-submersible is presented. The impact on mass properties, floater motions, structural redundancy and fatigue for all studied bracing configurations are discussed in Chapter 3.3.5.

*Figure 39: Structural model of configuration 2 (deckbox hidden)*

#### *3.3.2.1 V0 (reference semi-submersible with horizontal transverse and horizontal diagonal bracings)*

The impact on surge deformations when adding diagonal bracings is demonstrated by Figure 40, where a reduction of 30% in surge deformation is achieved. Other deformation differences between the PS and SB brace-column connection are reported by Table 15 for each load case in the ULS. Floater deformations in sway direction are reduced as well, since the horizontal transverse bracing dimensions are not modified, therefore sway stiffness increases. The difference in heave deformation reduces as well, however is linked to the reduction in surge and sway deformations.

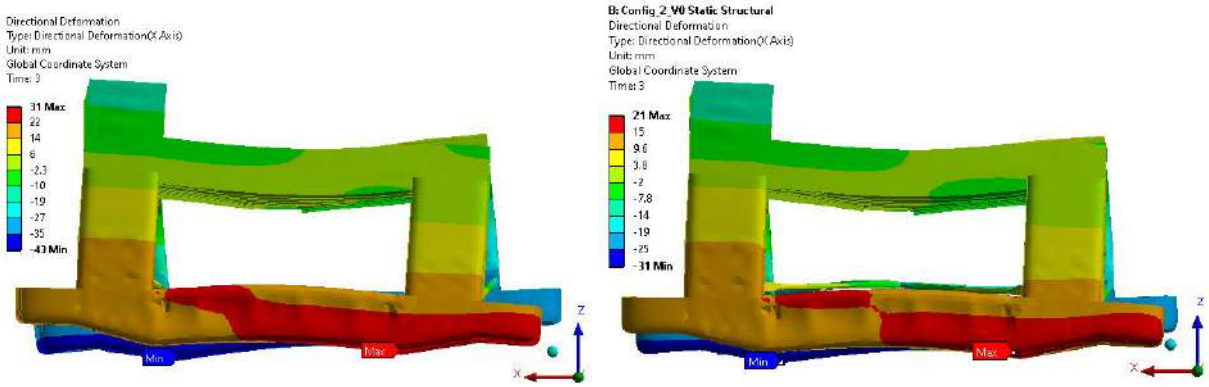


*Figure 40: Surge deformation reference semi-submersible (left) and Configuration 2 V0 semi-submersible (right), ULS $F_L$ load case*

*Table 15: Absolute translational differences between PS and SB brace-column connections [mm], reference semi-submersible and Configuration 2 V0 in ULS*

| Load case | Reference case | | | Configuration 2, V0 | | |
|---|---|---|---|---|---|---|
| | \|Δx\| | \|Δy\| | \|Δz\| | \|Δx\| | \|Δy\| | \|Δz\| |
| $F_S$ | 3 | 53 | 1 | 2 | 46 | 0 |
| $F_L$ | 40 | 17 | 12 | 23 | 15 | 8 |
| $F_{comb}$ | 45 | 40 | 22 | 18 | 35 | 16 |
| $M_T$ | 30 | 35 | 20 | 13 | 31 | 16 |
| $a_L$ | 1 | 11 | 0 | 0 | 9 | 0 |
| $a_T$ | 4 | 17 | 10 | 1 | 14 | 10 |
| $a_V$ | 1 | 18 | 0 | 1 | 15 | 0 |

Since floater deformations for the $F_L$, $F_{comb}$ and $M_T$ load cases are smaller, bending and torsion moments are lower in the deckbox structure. Presented by Table 11, these ULS load cases are governing for deckbox structure of the reference semi-submersible. As example, Figure 41 shows the shear stress of the bottom deck plating, where the positive shear stress is lower for Configuration 2. In general for the $F_L$, $F_{comb}$ and $M_T$ load cases, equivalent stresses at the moonpool area are about 20% and 5% lower for the bottom deck and main deck, respectively. The stress difference for the bottom deck is higher due to the load path of the torsional load generated by the $F_L$, $F_{comb}$ and $M_T$ load cases. Namely, because the columns do not extend fully to the upper deck, shear forces and moments are not equally distributed between bottom and main deck first, whereafter it is distributed to higher deck levels through shear.

Stress differences of around -15% are also observed in the deckbox transverse outer side plating for the $F_L$, $F_{comb}$ and $M_T$ load cases. This difference is related to the lower torsion moment $M_z$ in the deckbox structure, which is now partly absorbed by the diagonal bracings by forming a rigid structure between pontoons. For the deckbox transverse bulkheads, similar stress magnitudes are observed.

Regarding the column-deckbox connection, some stress reduction (<-5%) is observed for the $F_L$, $F_{comb}$ and $M_T$ load cases. However, the splitting force and transverse acceleration load cases, $F_S$ and $a_T$ respectively, remain the governing load cases for the column-deckbox connection. Therefore, structural dimensions cannot be reduced at these areas.

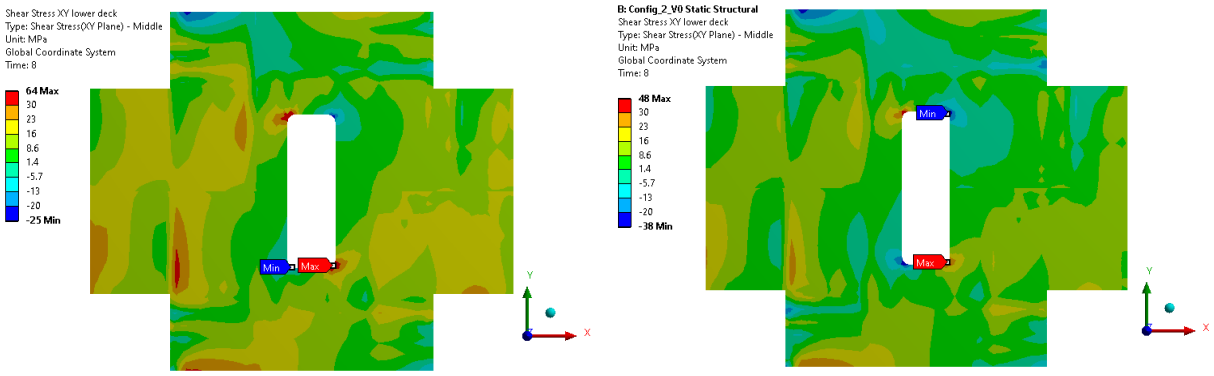


*Figure 41: Shear stress XY-plane plot of bottom deck reference case (left) and Configuration 2 V0 (right) semi-submersibles, ULS $M_T$ load case*

### *3.3.2.2 Final design*

The structural design of the reference semi-submersible is modified based on the results of Configuration 2 V0. First, for the final bracing design, bracing dimensions of both the transverse and diagonal bracings are modified, see Table 16 Because the diagonal bracings absorb some loading in the splitting force load case, the wall thickness of the transverse bracing is reduced to 32 mm. The diameter of the diagonal bracings is increased to 1800 mm, because it lacked buckling strength in the $F_{comb}$ load case. The second reason for increasing the diagonal bracing diameter was to analyse if its effectiveness increases to reduce deckbox stresses further. Similar to the strength assessment of the reference case, the splitting force load case in the ALS, where the most aft bracing is suppressed, remains the governing load case for the yielding check of the transverse bracing stress. Regarding compressive loading, the ULS is governing. Finally, the geometric stress concentration present at the X-joint of the diagonal bracings shown in Figure 42 is relatively high (factor of 4). The coarse mesh used in the strength assessment, resulting in uneven surfaces at the connection is possibly one of the reasons. If this hot spot is to be analysed in a fatigue assessment, a refined mesh is needed to accurately determine the SCF.

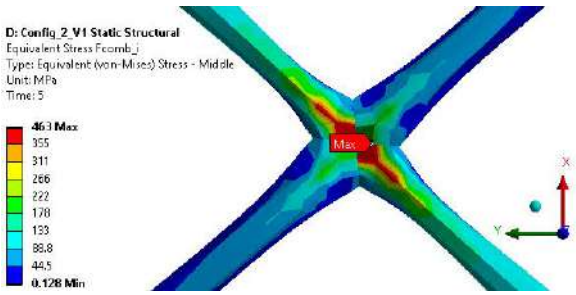


*Figure 42: Stress concentration at the X-joint of diagonal bracings configuration 2 final design, ULS, $F_{comb}$ load case*

*Table 16: Bracing dimensions of Configuration 2, V0 and final design*

| Bracing | Dimension [mm] | V0 | Final |
|---|---|---|---|
| Horizontal transverse | Diameter<br>Wall thickness | 1800<br>40 | 1800<br>32 |
| Horizontal diagonal | Diameter<br>Wall thickness | 1250<br>40 | 1800<br>40 |

The modifications made to the structural design of the semi-submersible are reported in Table 17. As reported for Configuration 2 V0, due to the added diagonal bracings, bending and torsion moments are lower in the deckbox structure for the $F_L$, $F_{comb}$ and $M_T$ load cases, which are governing for the deckbox stresses. Bottom and main deck thicknesses are therefore reduced from 20 mm to 14 mm and 19 mm, respectively. Further, transverse outer side plate thicknesses are lowered from 20 mm to 18 mm. For the diagonal brace-column connection, a longitudinal girder is added in each column shown in Figure 43. The structural design modifications result in a strength assessment with similar usage factors like the reference semi-submersible. In APPENDIX D an overview of stresses and WSD-check of the selected areas and locations is presented.

*Table 17: Structural design modifications semi-submersible Configuration 2, see Figure 43*

| Part | Structural design modifications | | Design | |
|---|---|---|---|---|
| | | | V0 | Final |
| Column | 1 | Longitudinal girder added for diagonal brace-column connection | - | Thickness at brace-column connection: 40 mm, above: 15 mm |
| Deckbox | 2 | Bottom deck thickness | 20 mm | 14 mm |
| | 3 | Main deck thickness | 20 mm | 19 mm |
| | 4 | Transverse outer side plating thickness | 20 mm | 18 mm |

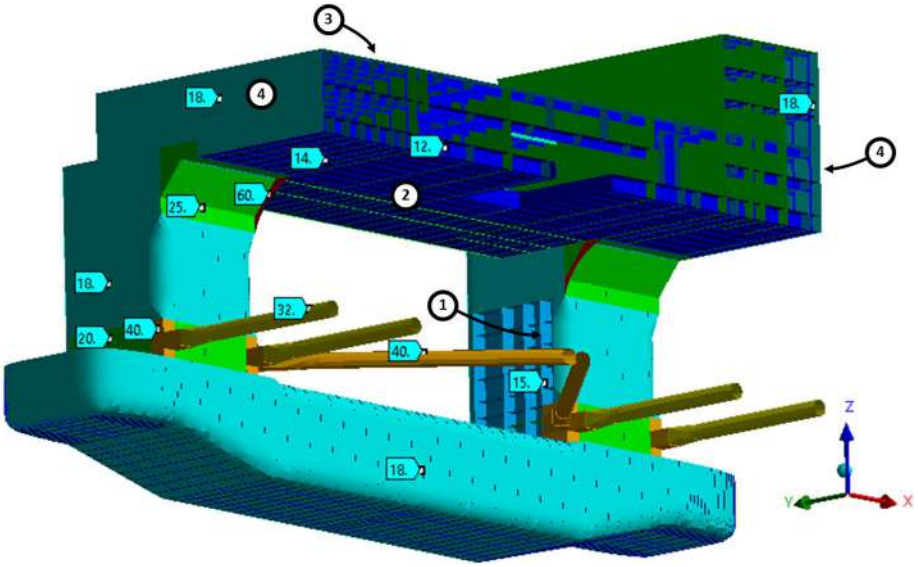


*Figure 43: Plate thickness plot configuration 2, final design*

### 3.3.2.3 *Alternative configuration*

Since the diagonal bracings has considerable sway stiffness, axial transverse bracing stresses are reduced by about 20% in V0. To reduce fatigue sensitive locations, two transverse bracings can therefore be omitted in the alternative bracing configuration as illustrated in Figure 44. By reducing the amount of fatigue sensitive locations, inspection and maintenance costs reduces accordingly. This alternative configuration is analysed in FEA for the ULS and ALS load cases to estimate the impact on the structural design, however is not included in the evaluation between different bracing configurations in Chapter 3.3.5. The final design of configuration 2 is used to study the differences in stresses and therefore structural design and mass properties.

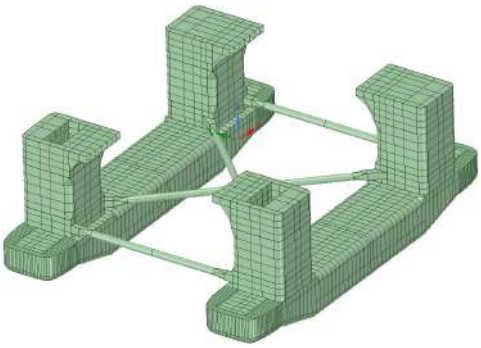

*Figure 44: Structural model of alternative configuration 2 (deckbox hidden)*

When omitting two transverse bracings, axial loading increases by 43% for the remaining transverse bracings for the ULS splitting force load case as shown in Figure 45. The reduction in sway stiffness increases axial and bending stresses in the diagonal bracings. However, the diagonal bracings are subjected to a larger increase in stress for the ALS shown in Figure 45, where the most aft transverse bracing is damaged. For this limit state, axial and bending stresses increase by a factor of 2.4. For the out-of-phase splitting force load case, the diagonal bracings lacks buckling strength as well. Bracing dimensions of alternative configuration 2 should therefore be increased as shown in Table 18.

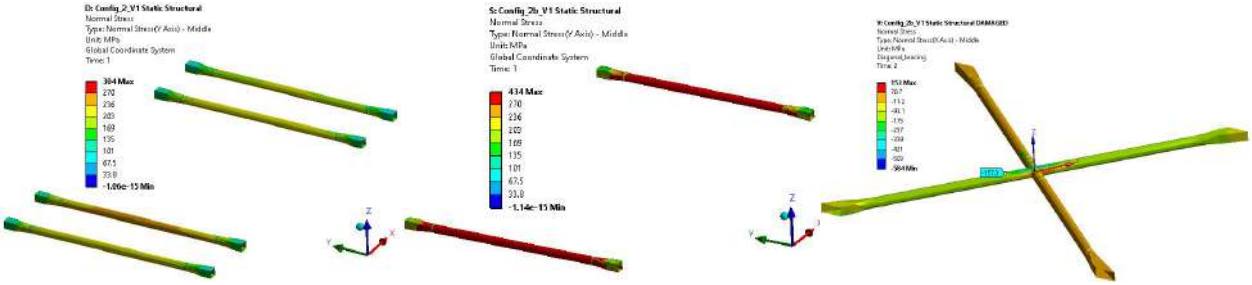

(a) (b) (c)

*Figure 45: Normal stress plot in y-direction of transverse bracings in ULS $F_S$ load case, final design (a), alternative design (b) and normal stress plot in x-direction diagonal bracings in ALS $F_S$ load case (c)*

*Table 18: Bracing dimensions of Configuration 2, final and alternative design*

| Bracing | Dimension [mm] | Final | Alternative |
|---|---|---|---|
| Horizontal transverse | Diameter<br>Wall thickness | 1800<br>32 | 2200<br>40 |
| Horizontal diagonal | Diameter<br>Wall thickness | 1800<br>40 | 2400<br>40 |

Due to the smaller stiffness in sway direction, column-deckbox connection and deckbox normal and shear stresses increase by factors of 1.1 to 1.4, depending on location and load case. However, if bracing dimensions are increased, floater deformation differences between the final and alternative design are expected to be limited, therefore the required structural design modifications are minor as well. No study is performed to iterate to similar stress levels similar to the reference semi-submersible, however the impact on structural mass compared to the final design of configuration 2 is estimated as shown in Table 19. If bracing buoyancy is neglected, the payload is estimated to be 237 tonnes lower compared to the final design of configuration 2.

*Table 19: Structural mass change alternative configuration 2, compared to final design configuration 2*

| Part | Structural mass change | |
|---|---|---|
| | Absolute [tonnes] | Relative |
| Deckbox | 150 | 3% |
| Columns (4x) | 100 | 5% |
| Pontoons (2x) | 0 | 0% |
| Bracings | -13 | -2% |
| Other | 0 | 0% |
| | | |
| Total | 237 | 2% |

### 3.3.3 Configuration 3: Horizontal transverse and vertical diagonal bracings

The third bracing configuration includes added vertical diagonal bracings for deckbox support, plus adds a more effective load path for transverse inertia loads. Since the total deckbox mass, including structural mass, equipment and payload, equals half the total semi-submersible mass, partly supporting the deckbox structure could reduce deckbox stresses significantly. For configuration 3, two different designs are analysed; configuration 3.1 and 3.2. Bracing configuration 3.1 consists of 4 horizontal transverse and 4 vertical diagonal bracings shown on the left of Figure 46. For load cases where the floaters deform outward, the diagonal braces of configuration 3.1 show insufficient support of the deckbox mass as the diagonal braces also move outward. Consequently, the impact on deckbox stresses is marginal. Therefore, an extra version named configuration 3.2 is analysed shown on the right of Figure 46. This design has 4 additional vertical diagonal bracings which are supported by large horizontal transverse bracings, resulting in a more rigid structure with increased deckbox support. A reduction in deckbox dimensions is therefore achieved.

This chapter reports the structural design changes of configuration 3. First, the strength assessment is reported of the reference semi-submersible with configuration 3.1. Then, the final structural design of the modified semi-submersible with configuration 3.1 and 3.2 are presented. The impact on mass properties, floater motions, structural redundancy and fatigue for all studied bracing configurations are discussed in Chapter 3.3.5.

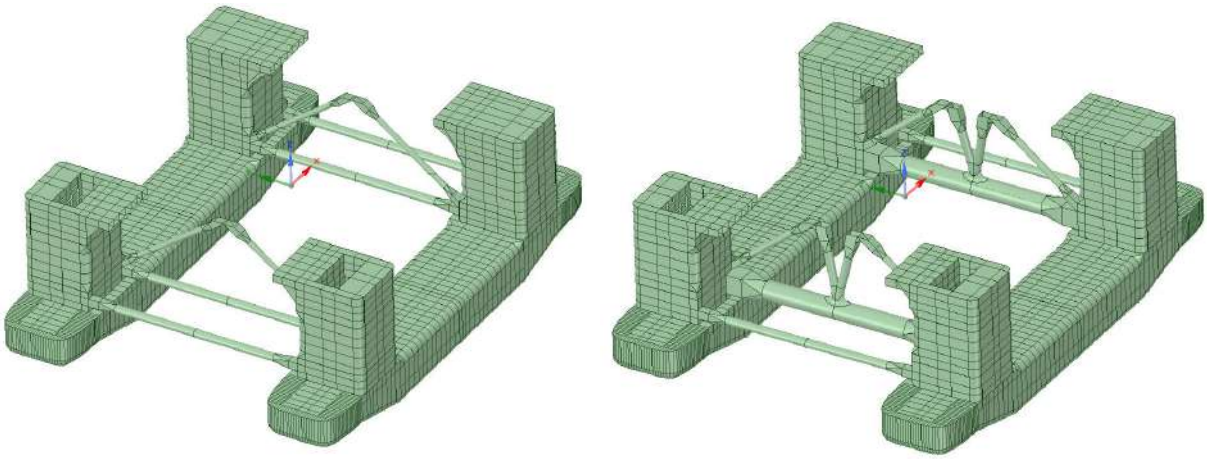

*Figure 46: Structural model of configuration 3.1 (left) and 3.2 (right) (deckbox hidden)*

#### *3.3.3.1 Configuration 3.1, V0 (reference semi-submersible with horizontal transverse and vertical diagonal bracings)*

The aim of adding vertical diagonal bracings is to support the deckbox's structural mass, equipment mass and operational mass, therefore deckbox bending stresses are reduced. When only static loading is considered, the diagonal bracings each support the deckbox mass vertically by 702 tonnes, which accumulates to a total support of 2807 tonnes, equivalent to 10% of the total deckbox mass. A reduction of about 10% in deckbox normal stress is observed. However, this effect is limited as the diagonal bracings lacks support in the ULS $F_{comb}$ and $M_T$ load cases, where the floaters deform outward shown in Figure 47. In Figure 47 the relative low stress in the diagonal bracings and the deformed shape show the ineffectiveness of the diagonal bracings.

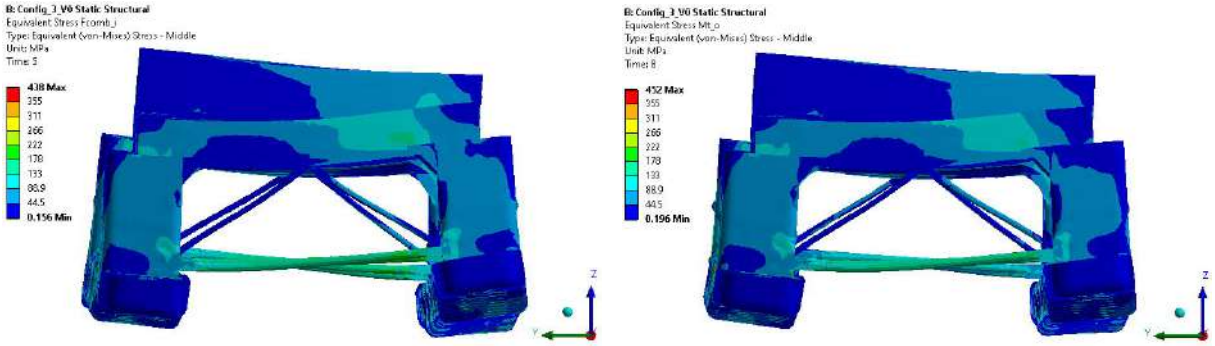


*Figure 47: Equivalent stress plot of configuration 3.1 V0 ULS $F_{comb}$ (left) and $M_T$ (right) load cases*

The second aim of adding vertical diagonal bracings, is the more effective load path for the transverse inertia loads, therefore reducing column-deckbox stresses shown by the stress plot of the reference semi-submersible in Figure 25. The stress plot on the left of Figure 48 clearly shows the compressive loading of the SB diagonal bracings due to the transverse deckbox inertia load. For the $a_T$ load case, normal stresses in the column deckbox connection are 35% lower. Normal stresses are also reduced by 20% at the inner faces of the outer column plating, especially for the $F_S$ load case shown on the right of Figure 48. Here, all diagonal bracings are loaded by compressive forces, which direct loading into the deckbox structure.

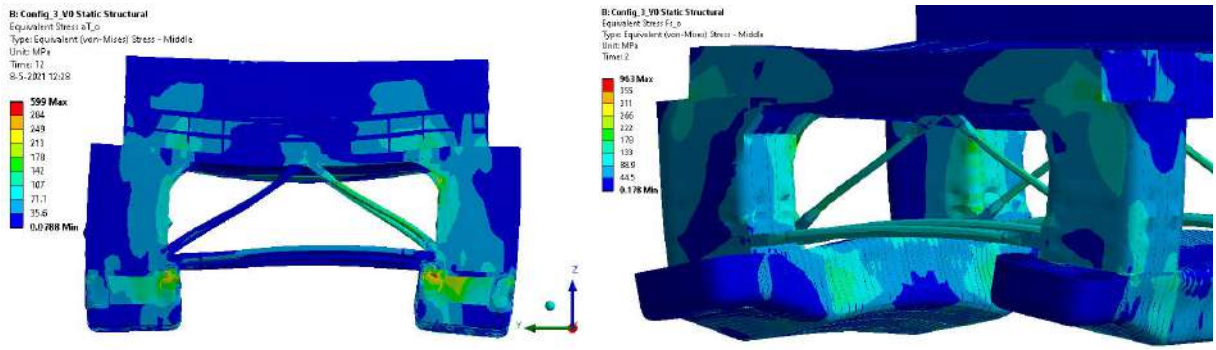


*Figure 48: Equivalent stress plot configuration 3.1 V0 ULS $a_T$ (left) and $F_S$ (right) load cases*

The diagonal bracings result in a 40% increase of tensile stress in the transverse bracings when only static loading is present, since the diagonal bracings push the floaters outward due to the deckbox mass. For the ULS splitting force load case, transverse bracing tensile stresses are similar compared to the reference semi-submersible, while compressive stresses are 25% lower. The latter is explained by the paragraph above and Figure 48.

For the damaged condition in the ALS, two different scenarios are studied, see Figure 49. The first scenario is where the most aft bracing is damaged, which is the same scenario as the reference semi-submersible ALS, and results in the highest possible tensile stresses in the remaining aft transverse bracing for the $F_S$ load case (340 MPa). The second scenario is where the second from aft transverse bracing is damaged, resulting in relatively large compressive loading of the diagonal bracings for the $F_S$ load case (160 MPa). However, when comparing usage factor ratios ($\eta/\eta_p$), the ULS for the diagonal bracings remains governing. The first damaged scenario is therefore governing for maximum bracing stress. Other scenarios, such as suppressing a diagonal bracing, were studied, however do not result in a larger increase in usage factor ratios of the column-deckbox connection compared to the ULS.

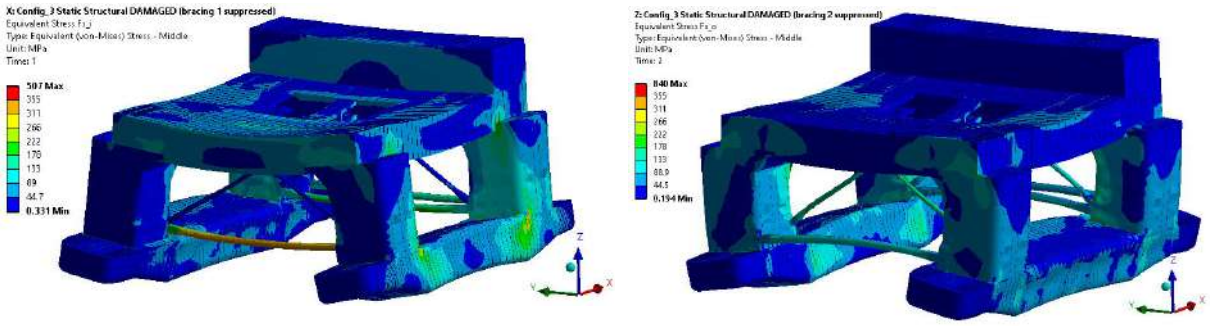

*Figure 49: Equivalent stress plot configuration 3.1 V0 the damaged ALS scenario 1 (left) and scenario 2 (right)*

### *3.3.3.2 Configuration 3.1, final design*

As reported above, the added diagonal bracings result in minor normal stress differences in the deckbox structure. Only the bottom deck thickness was reduced from 20 mm to 18 mm to obtain similar stress levels compared to the reference semi-submersible. Regarding the column-deckbox connection, the $a_T$ load case shows a reduction in normal stress, therefore the inner face chamfer outer plating and bracket thicknesses are lowered from 25 mm and 60 mm to 15 mm and 40 mm, respectively. Further, normal stresses are lower at the inner faces of the outer column plating, allowing to reduce outer plating to 15 mm. The semi-submersible modifications are summarised in Table 20 and illustrated by Figure 50.

Based on the yielding and buckling check of the diagonal bracings in both the ULS and ALS, the wall thickness of the diagonal bracings are reduced from 40 mm to 20 mm. The damaged ALS analysed for the final design of configuration 3.1 is the 1st scenario as reported above. See Table 21 for an overview of bracing dimensions of configuration 3. In APPENDIX D, the stress results and WSD check of the final design is reported.

*Table 20: Structural design modifications semi-submersible Configuration 3.1, see Figure 50*

| Part | Structural design modifications | | Design | |
|---|---|---|---|---|
| | | | V0 | Final |
| Column | 1 | Inner face, outer column plating thickness | 18 mm | 15 mm |
| Column-deckbox connection | 2 | Inner face chamfer, outer plating thickness | 25 mm | 15 mm |
| | 3 | Inner face chamfer, bracket thickness | 60 mm | 40 mm |
| Deckbox | 4 | Bottom deck thickness | 20 mm | 18 mm |

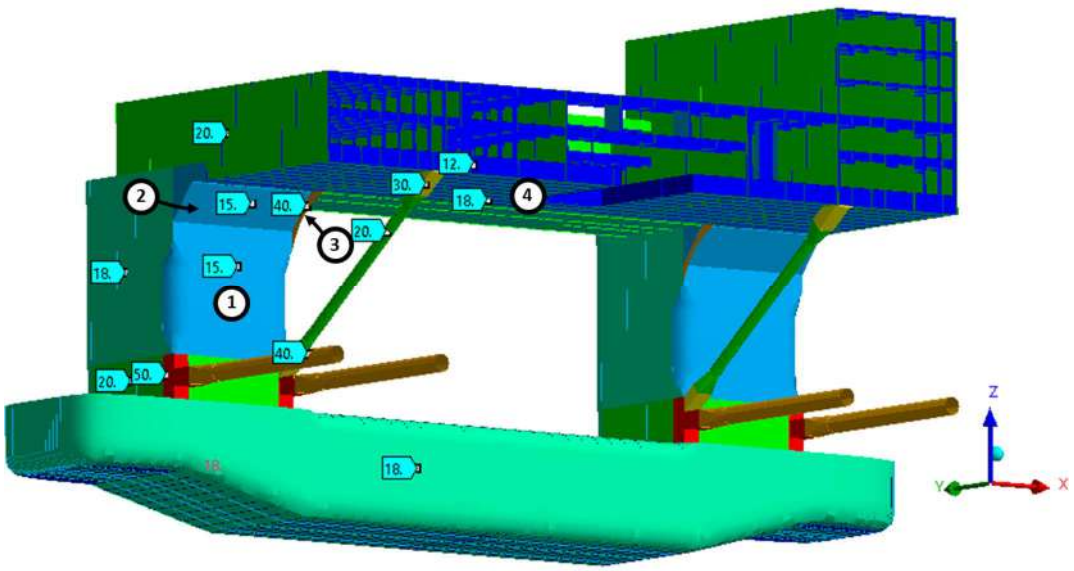


*Figure 50: Plate thickness plot configuration 3.1, final design*

### *3.3.3.3 Configuration 3.2, final design*

Because configuration 3.1 shows insufficient support of the deckbox mass, an additional version named configuration 3.2 is analysed. This design is based on the Moss CS50 semi-submersible design and consists of 4 horizontal transverse bracings and 8 vertical diagonal bracings, see Figure 46. Different from the Moss CS50 design are the lower angles the outer diagonal bracings are orientated, since this results in a more effective load path for the racking loads present in the $a_T$ load case. The disadvantage of this bracing orientation is the lower accessibility of the brace-brace K-joint at the crown toes. Also, the edge blend modelled at the brace-brace joint may not be feasible regarding manufacturing.

The middle diagonal bracings are supported by large transverse bracings with a diameter of 4.2 meters and wall thicknesses of 100 mm. These dimensions are not based on occurring stresses, but to obtain a large bending stiffness for an effective support of the middle diagonal bracings. The axial stiffness is also larger compared to the smaller transverse bracings. Therefore, the floaters sway deformations are lower, resulting in increased deckbox support from the outer diagonal braces as well. Based on a static analysis of configuration 3.2, the outer and middle diagonal bracings each support the deckbox mass vertically by 712 and 545 tonnes, respectively, which accumulates to a total support of 5027 tonnes, equivalent to 20% of the total deckbox mass. A reduction of approximately 20% in normal deckbox stress is achieved.

Due to the large axial stiffness of the 4.2 meter transverse bracings, the 1.8 meter transverse bracings have relatively low stresses in the ULS. The 1.8 meter transverse bracings could therefore be omitted in the bracing configuration. However, if one of the 4.2 meter transverse bracings is suppressed in the damaged ALS, load paths change, resulting in increased stresses in the columns and deckbox structure, which is not the aim of this bracing configuration. The aim of this bracing configuration is to decrease column and deckbox dimensions, by increasing bracing capacity. Therefore, the small transverse bracings with reduced wall thicknesses remain in configuration 3.2. See Table 21 for the bracing dimensions of the final design of configuration 3.2.

*Table 21: Bracing dimensions of Configuration 3, V0 and final designs 3.1 and 3.2*

| Bracing | Dimension [mm] | V0 | 3.1, final | 3.2, final |
|---|---|---|---|---|
| Horizontal transverse | Diameter<br>Wall thickness | 1800<br>40 | 1800<br>40 | 1800/4200<br>35/100 |
| Vertical diagonal | Diameter<br>Wall thickness | 1200<br>40 | 1200<br>20 | 1400/1800<br>20/20 |

Configuration 3.2 was analysed using the final semi-submersible design of configuration 3.1. The FEA concludes a more rigid structure with increased deckbox support. For example, the deckbox deflection is plotted in Figure 51 for the $M_T$ load case, which illustrates the lower deflections. The left plot of Figure 51 also shows configuration 3.2 is more rigid compared to 3.1, since deflections at the PS and SB diagonal bracings are similar for configuration 3.2, while the diagonal bracings of 3.1 show asymmetric deflections. For all load cases, mid-deckbox deflections and main deck normal stresses are reduced by about 15%.

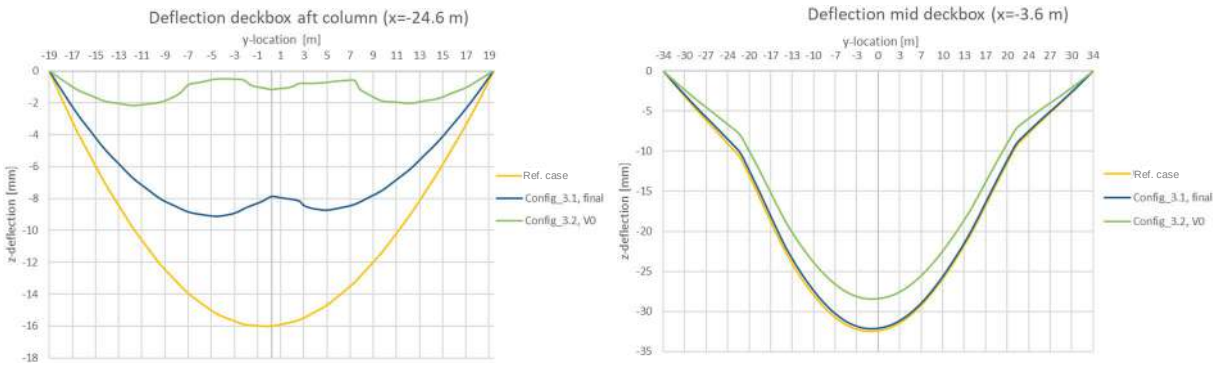


*Figure 51: Deckbox deflection ULS $M_T$ load case ref. case, 3.1 (final design) and 3.2 (3.1 semi-submersible)*

Solely reducing plate thicknesses of the deckbox, resulting in similar deflections and stresses compared to the reference semi-submersible, would result in unacceptable outer fibre stresses when additional deck loading of 50 kN/m$^2$ is also considered, see Table 12. Therefore, the reduction of deckbox bending stiffness was achieved by lowering the deckbox height by 1 meter. This height reduction was estimated by hand calculations of the deckbox deflection, resulting in the required deckbox area moment of inertia. Similar deckbox deflections and stresses are then achieved by adjusting bottom and main deck plating in FEA shown in Table 22.

The aim of this study is analyse what structural design changes are possible or needed when applying different bracing configurations, inherent to the general arrangement of the semi-submersible. However, worthwhile to note is that reducing the deckbox height may not be feasible regarding the general arrangement of the reference drilling semi-submersible, also discussed in Chapter 3.2.3.2. Namely, some equipment, such as mud treatment or BOP equipment, requires storage below the main deck. Therefore, reducing the deckbox height may not be feasible, or some equipment is to be relocated in non-structural compartments above deck. Also noteworthy, when bracings are submerged, the increased frontal area of the bracing configuration requires an increase in propulsive power.

The rigid diagonal bracing structure of configuration 3.2 is advantageous regarding outer column plating and column-deckbox connection stresses, which are governed by the $F_S$ and $a_T$ load cases, see Figure 48. Namely, at the inner face column outer plating and column-deckbox connection a reduction of 15% and 40% was observed, respectively. The chamfer size of the column-deckbox connection and plating at both areas are therefore reduced, see Table 22. Further, because of the relative low axial stiffness of the 1.8 meter transverse bracings, the outer column plating stress, located at x = ± 79.2 meter, reduces as well. Consequently, outer column plating stresses increase at x = ± 24.6 meter.

For the damaged condition in the ALS, two different scenarios are studied, see Figure 52. In the first scenario, the aft 4.2 meter transverse bracing is omitted, resulting in relatively large tensile loading for the remaining aft 1.8 meter transverse bracing (324 MPa) when loaded by the in-phase $F_S$ load case. When loaded by the out-of phase $F_S$ load case, large compressive loading in the outer diagonal bracings occurs (263 MPa). This damaged condition results in the highest $\eta/\eta_p$ ratio of the small transverse bracings, therefore defines the global dimensions. For the outer diagonal bracings, the ULS results in a slightly higher $\eta/\eta_p$ ratio, see APPENDIX D. In the second damaged scenario, the aft middle diagonal bracings are suppressed in the analysis, where $a_T$ is the governing load case, shown in Figure 52(c). However, compared to the ULS and the first damaged scenario, this analysis did not result in governing $\eta/\eta_p$ ratios for all selected areas and locations.

In APPENDIX D, the stress results and WSD check of the final design is reported.

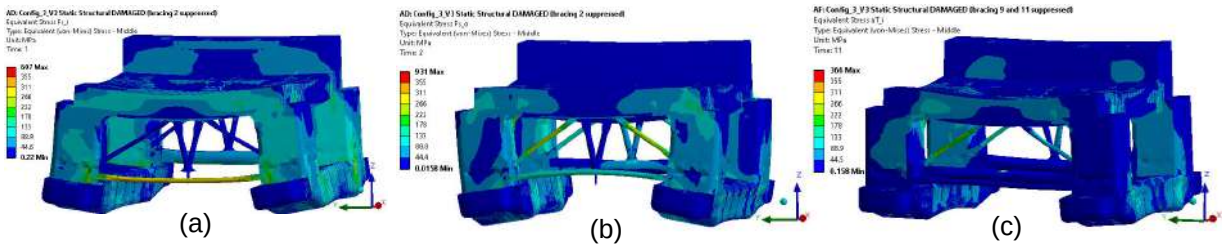


*Figure 52: Equivalent stress plot of the damaged ALS scenario 1 $F_S$ in-phase (a) and $F_S$ out-of-phase (b) load cases and scenario 2 $a_T$ in-phase load case (c)*

*Table 22: Structural design modifications semi-submersible Configuration 3.2, see Figure 53*

| Part | Structural design modifications | | Design | |
|---|---|---|---|---|
| | | | 3.1, final | 3.2, final |
| Column | 1 | Outer column plating thickness, x = ± 24.6 m | 18 mm | 25 mm |
| | 2 | Outer column plating thickness, x = ± 79.2 m | 18 mm | 13 mm |
| | 3 | Inner face, outer column plating thickness | 15 mm | 13 mm |
| Column-deckbox connection | 4 | Inner face, chamfer size | 2300 mm | 1150 mm |
| | 5 | Inner face, outer plating thickness | 15 mm | 13 mm |
| Deckbox | 6 | Height | 9000 mm | 8000 mm |
| | 7 | Main aft deck thickness | 20 mm | 18 mm |
| | 8 | Aft side plating thickness | 20 mm | 18 mm |
| | 9 | Accommodation forward and aft plating thickness | 25 mm | 23 mm |

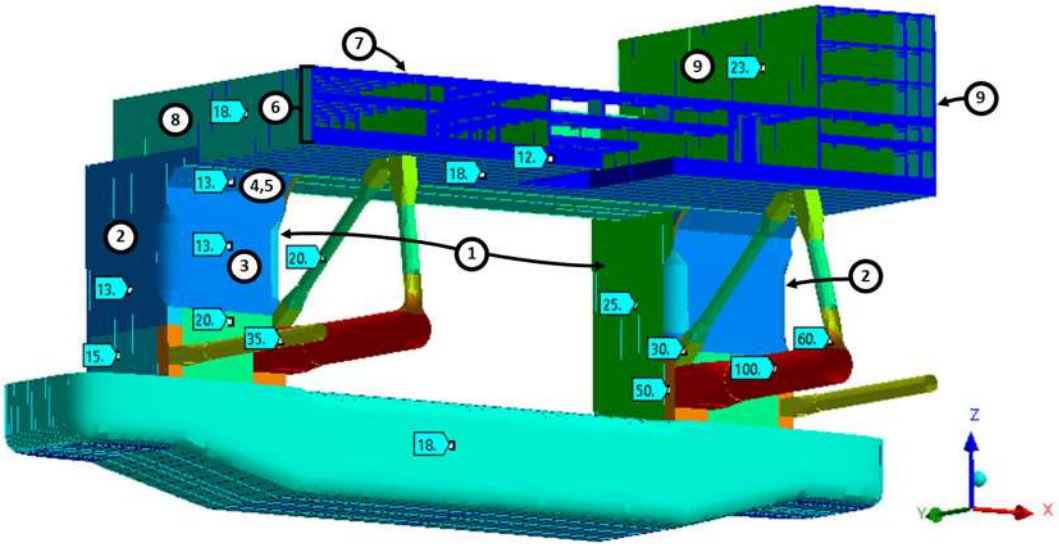


*Figure 53: Plate thickness plot configuration 3.2, final design*

### 3.3.4 Configuration 4: Hinged horizontal transverse bracings

The fourth, and last bracing configuration studied, are hinged horizontal transverse bracings, which can rotate freely around the z-axis at the brace-column connection. When opposite surge motion and rotation of the columns occurs, moments at the brace-column connection are omitted. Also, moments around the z-axis are not present due to local water loading at the bracing. Hinged bracings can therefore be advantageous regarding ULS stresses and fatigue damage of the critical brace-column connection.

Since clamped or hinged horizontal transverse bracings do not affect floater motions significantly, similar stresses in the column and deckbox structure are observed. Therefore, apart from the brace-column connection, hinged transverse bracings have no impact on the structural design of the semi-submersible. Because motion differences between the PS and SB floaters are small, the impact of hinged bracings is therefore limited. When local water loading is also considered, the total bending stress for a clamped bracing in the ULS are around 35 MPa, which relatively small compared to other loading in the ULS.

The strength assessment of the reference semi-submersible with hinged bracings is reported first. Then, the final structural design is presented. Finally, the effect of hinged bracings on brace-column stresses is discussed. The impact on mass properties, floater motions, structural redundancy and fatigue for all studied bracing configurations are discussed in Chapter 3.3.5.

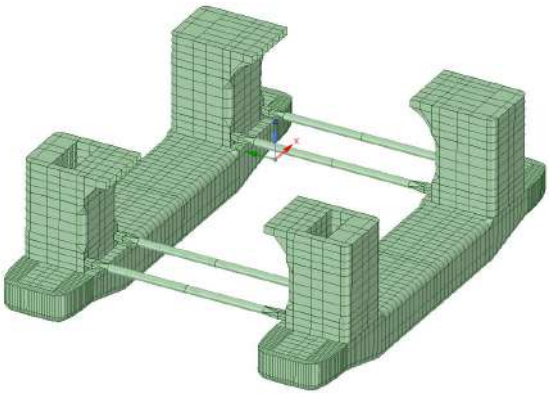

*Figure 54: Structural model of configuration 4 (deckbox hidden)*

#### *3.3.4.1 V0 (reference semi-submersible with hinged horizontal transverse bracings)*

The hinged bracing design of V0 is shown in Figure 55(a). For V0, the structural dimensions of the tubular and brace-column connection are identical to the reference semi-submersible bracings, see Table 25, stresses and floater deformations can therefore be compared. Because of assembly reasons, the hinge, which can rotate freely around the z-axis, is located outside the columns. This connection is disadvantageous regarding stress distributions, since normal stresses are mainly located in the top and bottom flange of the brace-column connection and cannot distribute adequately from the pin hole to column structure, see Figure 55(c). Compared to the reference semi-submersible brace-column connection, normal stresses are approximately 50% higher for the $F_S$ load case. Further, one flange is attached to the tubular bracings, which affects bracing stresses adversely. Shown by the deformed shape of Figure 55(b) and (c), due to the single flange, the tubular ends have little to none moment resistance around the x-axis. Therefore, the bracings are similar to a simply supported beam where larger bending moments occur at mid-length compared to the clamped bracings. Consequently, mid-bracing normal stresses are about 20% higher for the $F_S$ load case in both the ULS and ALS. The same damaged ALS scenario was studied as the reference semi-submersible, since this results in the highest possible bracing stresses that defines bracing dimensions.

In Table 23 and Table 24, the absolute translational differences and rotations of the PS and SB columns at the brace-column connections in the ULS is reported for the reference semi-submersible and the reference semi-submersible with hinged bracings (Configuration 4, V0). Opposite surge motion of the floaters are the largest for the $F_L$, $F_{comb}$ and $M_T$ load cases. The translational and rotational differences between the bracing configurations show that bracings have neglectable effect on the motions of the floaters. Hence, similar stresses in the column and deckbox structure in the FEA of configuration 4 V0 are observed.

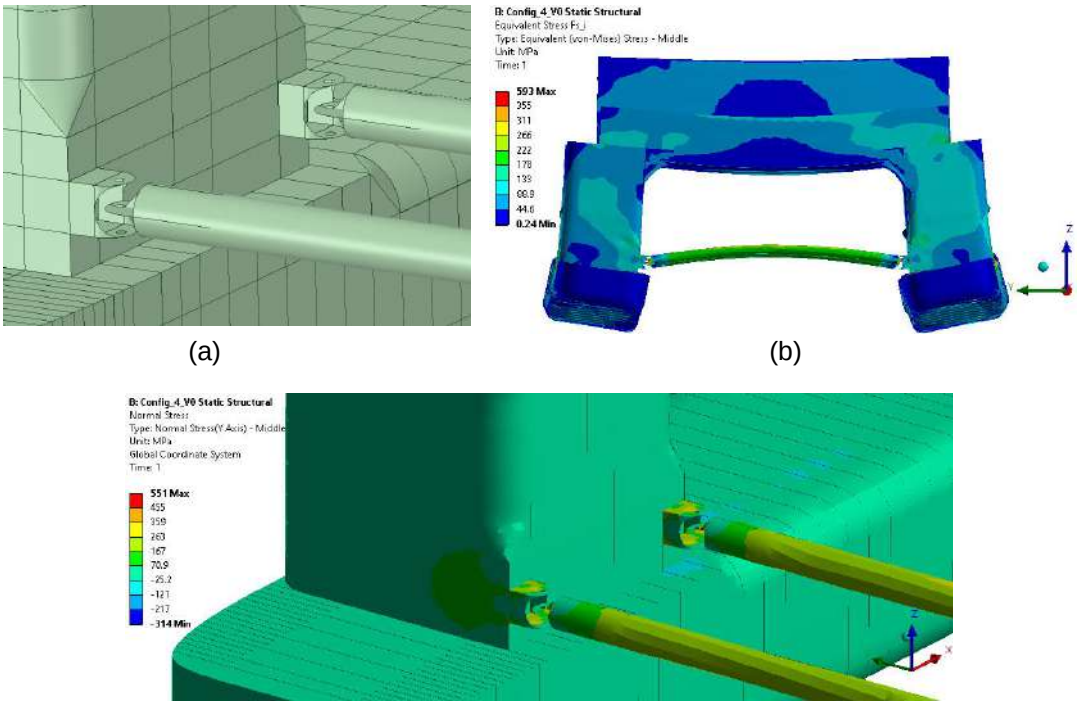


*Figure 55: Hinged brace-column connection design V0 (a), equivalent stress plot ULS $F_S$ load case total semi-submersible (b) and maximum principal stress plot brace-column connection (c)*

*Table 23: Absolute translational differences between PS and SB brace-column connections [mm], Reference case and Configuration 4 V0 in ULS*

| Load case | Reference case | | | Configuration 4, V0 | | |
|---|---|---|---|---|---|---|
| | \|Δx\| | \|Δy\| | \|Δz\| | \|Δx\| | \|Δy\| | \|Δz\| |
| $F_S$ | 3 | 53 | 1 | 4 | 55 | 0 |
| $F_L$ | 40 | 17 | 12 | 42 | 18 | 13 |
| $F_{comb}$ | 45 | 40 | 22 | 47 | 41 | 22 |
| $M_T$ | 30 | 35 | 20 | 30 | 36 | 20 |
| $a_L$ | 1 | 11 | 0 | 1 | 11 | 0 |
| $a_T$ | 4 | 17 | 10 | 5 | 17 | 11 |
| $a_V$ | 1 | 18 | 0 | 1 | 19 | 0 |

*Table 24: Rotations of PS and SB brace-column connections [deg], Reference case and Configuration 4 V0 in ULS*

| Load case | Reference case | | | | | | Configuration 4, V0 | | | | | |
|---|---|---|---|---|---|---|---|---|---|---|---|---|
| | PS | | | SB | | | PS | | | SB | | |
| | $\theta_x$ | $\theta_y$ | $\theta_z$ | $\theta_x$ | $\theta_y$ | $\theta_z$ | $\theta_x$ | $\theta_y$ | $\theta_z$ | $\theta_x$ | $\theta_y$ | $\theta_z$ |
| $F_S$ | -0.11 | -0.02 | -0.05 | 0.14 | -0.03 | 0.04 | -0.11 | -0.02 | -0.07 | 0.14 | -0.01 | 0.04 |
| $F_L$ | -0.04 | 0.04 | -0.02 | 0.00 | -0.07 | 0.01 | -0.05 | -0.06 | -0.01 | -0.01 | 0.05 | 0.02 |
| $F_{comb}$ | -0.08 | 0.05 | -0.05 | 0.09 | -0.09 | 0.01 | -0.09 | -0.07 | -0.07 | 0.08 | 0.07 | 0.00 |
| $M_T$ | -0.10 | 0.03 | -0.03 | 0.06 | -0.07 | 0.01 | -0.11 | -0.05 | -0.05 | 0.06 | 0.06 | 0.00 |
| $a_L$ | -0.01 | 0.00 | -0.01 | 0.01 | 0.00 | 0.01 | -0.02 | -0.02 | -0.01 | 0.01 | -0.02 | 0.02 |
| $a_T$ | 0.03 | 0.00 | -0.01 | 0.11 | -0.01 | 0.02 | 0.03 | -0.01 | -0.02 | 0.12 | 0.00 | 0.02 |
| $a_V$ | -0.03 | -0.02 | -0.01 | 0.03 | -0.02 | 0.01 | -0.04 | -0.01 | -0.02 | 0.04 | 0.00 | 0.01 |

### 3.3.4.2 Final design

To reduce mid-bracing bending stresses when laterally loaded, the number of brace-end flanges are increased to 2. The additional reason for increasing the brace-end flanges is to reduce bending moments at the hinged connection, since the brace end moments are now converted to torque at the hinged connection. For the final design of configuration 4, the hinged connection is moved inside the column, see Figure 56. Discussed in previous chapter, stresses at the brace-column connection were mainly located in the flanges, which could not distribute adequately from pin hole to column structure. Increasing the length of the brace-column connection would not be beneficial as higher bending moments would occur when not loaded axially. The main advantage locating the hinged connection inside the column is bracing stresses are directly distributed into the column structure, therefore no geometric stress intensities are present and the number of fatigue sensitive locations are reduced. The disadvantages of moving the hinge inside the column are the increased risk of crevice corrosion and challenges during assembly. A possible solution is to preassemble the hinged connection before attaching it to the column structure. In addition, maintenance of the hinged connection is a challenge during its lifetime.

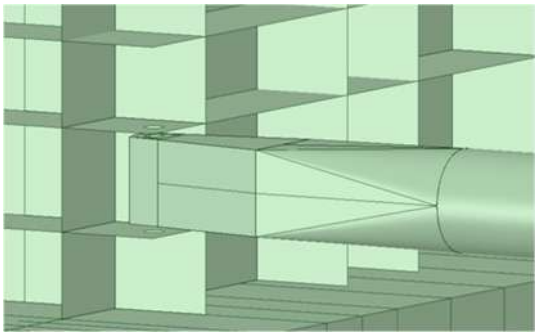

*Figure 56: Brace-column connection final design configuration 4*

The flange thicknesses at the bracing ends, reported in Table 25, are defined using Roark's bearing contact stress formulation of a cylinder in a cylindrical socket [26], see Eq.3-20 and Eq.3-21. The bearing clearance is assumed to be 1 mm, therefore $D_1$ and $D_2$ are 351 mm and 350 mm respectively, and the $F_S$ load case is used to define the distributed flange loading $p$. The resulting contact stress, $\sigma_c$, is then estimated at 295 MPa.

$$K_D = \frac{D_1 D_2}{D_1 - D_2} \qquad \text{Eq.3-20}$$

$$\sigma_c = 0.591 \sqrt{\frac{pE}{K_D}} \qquad \text{Eq.3-21}$$

Because bending stiffness of the hinged bracing ends is smaller compared to the reference semi-submersible bracing ends, mid-length bending stresses due to lateral loading are higher for configuration 4, also discussed in Chapter 3.3.4.1. Therefore, the wall thickness of the tubular bracing section is increased by 5 mm to obtain similar mid-length stresses, see Table 25.

*Table 25: Bracing dimensions of Configuration 4, V0 and final design*

| Part | Dimension [mm] | V0 | Final |
|---|---|---|---|
| Tubular | Diameter | 1800 | 1800 |
| | Wall thickness | 40 | 45 |
| Bracing ends | Flange thickness | 50 | 75 |
| | Web thickness | - | 75 |
| | Pin diameter | 350 | 350 |

As reported in previous chapter, configuration 4 results in similar stress magnitudes compared to the reference semi-submersible. Other than the brace-column connection, no structural design changes are therefore made. At the brace-column connection, horizontal column plate thicknesses are increased to obtain similar stress levels. In Table 26 the modifications are reported. In APPENDIX D, the stress results and WSD check of the final design is reported.

*Table 26: Structural design modifications semi-submersible Configuration 3.2, see Figure 57*

| Part | Structural design modifications | | Design | |
|---|---|---|---|---|
| | | | V0 | Final |
| Column | 1 | Outer column plating thickness | 50 mm | 25 mm |
| | 2 | Horizontal plate thickness at brace-column connection | 40 mm / 15 mm | 75 mm / 40 mm |

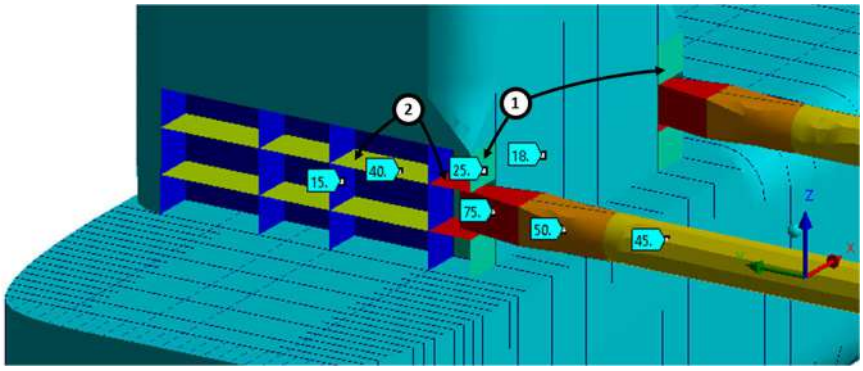


*Figure 57: Plate thickness plot brace-column connection configuration 4, final design*

### *3.3.4.3 Effect of hinged bracings on brace-column stresses*

To study how floater motions affect the brace-column stresses exclusively, the shear and moment distribution along the length of the reference case bracing design is calculated analytically using the double integration method for beams. In Figure 58(a) the deformed shape of the bracing is sketched when opposite surge motion of the floaters occurs, plus rotation of the columns around the z-axis. This beam is statically indeterminate due to the clamped edges, deformation in x-direction and rotations around the z-axis, resulting in unknown reaction forces, $F_{x,A}$ and $F_{x,B}$, and reaction moments, $M_{z,A}$ and $M_{z,B}$, sketched in the free body diagram of Figure 58(b). Based on the segment's internal shear forces and moments, shown by Figure 58(c), the moment function, given by Eq.3-22, can be derived. By integrating the moment function twice, the bracing deformation in x-direction is formulated by Eq.3-23. The constants, $C_1$ and $C_2$, and the unknown shear force $V'$ and moment $M'$ can be derived by solving the deformations and slopes using the boundary conditions reported in Table 27. This results in reaction forces and moments given by Eq.3-24 and Eq.3-25, and the normalised deformation, shear and moment diagram shown in Figure 59, where $x_d$, $\theta_1$ and $\theta_2$ are negative.

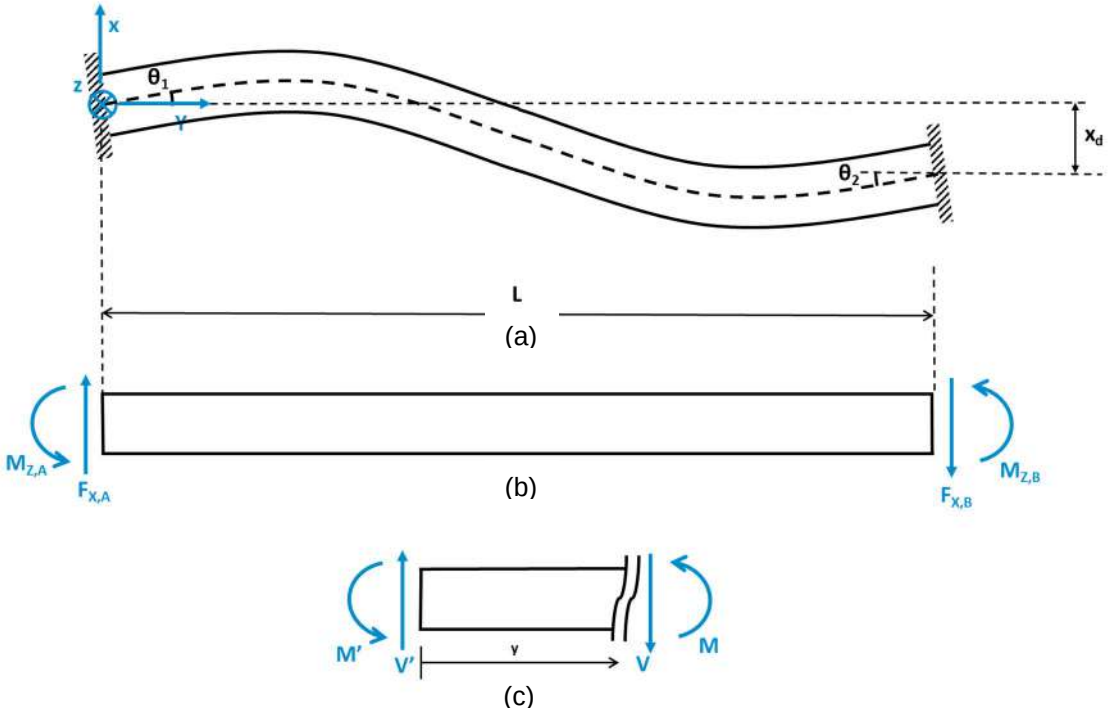


*Figure 58: Deformation (a), free body diagram (b), and segment internal shear forces and moments (c) of a clamped transverse bracing, loaded by surge motion of the floaters and column rotation around the z-axis*

$$EI\frac{d^2x}{dy^2} = -V'y + M' \qquad \text{Eq.3-22}$$

$$x = \frac{1}{EI}\left(-\frac{1}{6}V'y^3 + \frac{1}{2}M'y^2 + C_1y + C_2\right) \qquad \text{Eq.3-23}$$

$$F_{x,A} = -F_{x,B} = 12\frac{x_dEI}{L^3} + 6\frac{EI}{L^2}(\theta_1 + \theta_2) \qquad \text{Eq.3-24}$$

$$M_{z,A} = M_{z,B} = 6\frac{x_dEI}{L^2} + 2\frac{EI}{L}(2\theta_1 + \theta_2) \qquad \text{Eq.3-25}$$

*Table 27: Boundary conditions clamped transverse bracings*

| Location | $y = 0$ | $y = L$ |
|---|---|---|
| **Boundary conditions** | $x = 0$<br>$\frac{dx}{dy} = \theta_1$ | $x = x_d$<br>$\frac{dx}{dy} = \theta_2$ |

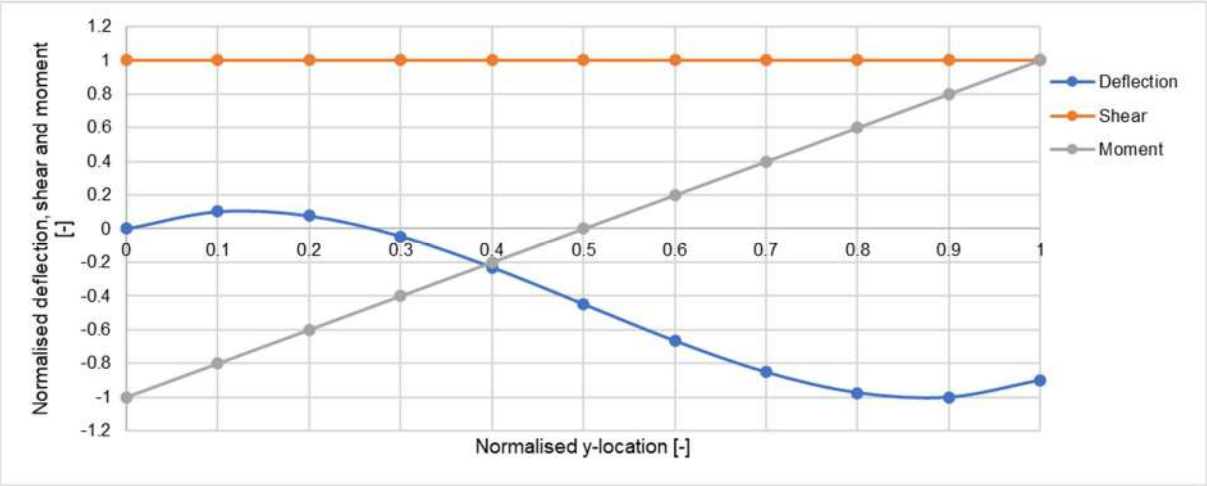


*Figure 59: Normalised deflection, shear and moment diagram clamped transverse bracings*

The maximum difference in surge motion in the ULS of the reference semi-submersible, shown in Table 23, occurs for the $F_{comb}$ load case ($|\Delta x| = 45\ mm$), where the corresponding column rotations around the z-axis are -0.05 and 0.01 degrees. When this maximum surge difference is used as $x_d$, with the corresponding z-rotations for $\theta_1$ and $\theta_2$, the magnitude of the reaction force and moment at the clamped edges are 117 kN and 6758 kNm. For the bending stiffness property of the beam, $EI$, the square bracing end cross section is used. Therefore, it is assumed this cross section is present along the entire length of the beam, which overestimates the reaction force and moment at the clamped edges. However, demonstrates an upper bound of the expected moments omitted when hinged bracing are applied.

Above reaction force and moment are equivalent to a maximum shear stress of 1 MPa and a maximum bending stress of 31 MPa. Considering that these stresses occur in the ULS and an upper bound of bending stiffness is used, the advantage of hinged bracings, which can rotate freely around the z-axis, is limited for the stress at the brace-column connection. When other bracing loading is also considered for the $F_{comb}$ load case reported in Table 28, such as reaction moments due to bracing water loading, $F_x$ and $M_z$, the resulting bending stresses are still minor. Even when absolute values are summed, therefore moment direction is not accounted for. The same holds for reaction moments around the x-axis, also shown in Table 28. Here, the total bending stress is smaller due to smaller heave motion differences reported in Table 23.

*Table 28: Reaction moments at transverse horizontal bracing reference semi-submersible, ULS $F_{comb}$ load case*

| \|Reaction moment\| [kNm] | | | | \|Bending stress\| [MPa] | | | Loading |
|---|---|---|---|---|---|---|---|
| $M_x$ | $M_{x,1}$ | 712 | | $\sigma_{y,1}$ | 3 | | $F_z$ bracing |
| | $M_{x,2}$ | 592 | | $\sigma_{y,2}$ | 3 | | $M_x$ bracing |
| | $M_{x,3}$ | 1515 | | $\sigma_{y,3}$ | 7 | | Buoyancy bracing |
| | $M_{x,4}$ | 2089 | | $\sigma_{y,4}$ | 10 | | Heave motion columns |
| | $M_{x,5}$ | 2037 | + | $\sigma_{y,5}$ | 9 | + | Rotation columns around x-axis |
| | $M_{x,total}$ | 6945 | | $\sigma_{y,total}$ | 32 | | - |
| $M_z$ | $M_{z,1}$ | 838 | | $\sigma_{y,1}$ | 4 | | $F_x$ bracing |
| | $M_{z,2}$ | 116 | | $\sigma_{y,2}$ | 1 | | $M_z$ bracing |
| | $M_{z,3}$ | 4376 | | $\sigma_{y,3}$ | 20 | | Surge motion columns |
| | $M_{z,4}$ | 2382 | + | $\sigma_{y,4}$ | 11 | + | Rotation columns around z-axis |
| | $M_{z,total}$ | 7712 | | $\sigma_{y,total}$ | 36 | | - |

When direction is accounted for, the resulting bending stress magnitudes are small compared to the axial stress, see Figure 60. Here, the axial stress resulting from the sway deformation is calculated as $\sigma_y = \frac{\Delta y}{l_0} E$. For mild sea conditions, the same proportionality between axial and bending stresses are expected, since wave loading is predominantly linear with respect to wave amplitude [7]. Also, related to the FLS, Fei et al. [31] concluded that the splitting force is the most dominant loading type for horizontal transverse bracings during its service life, therefore the impact on fatigue damage is expected to be limited as well.

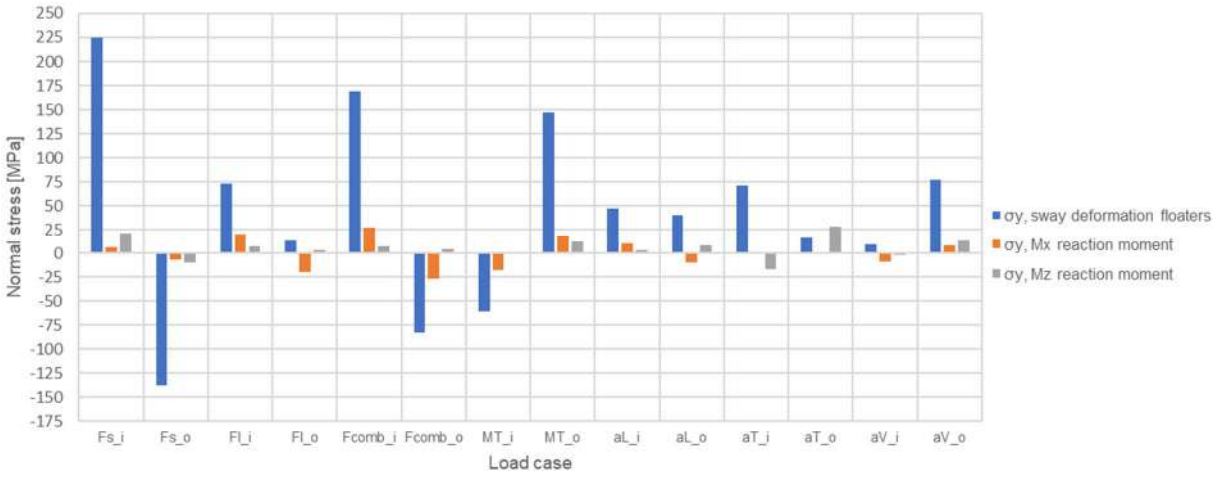


*Figure 60: Normal bracing stress ULS per load case*

In conclusion, the effect of hinged bracings is limited for stresses at the brace-column connection due to the small bending stresses present resulting from floater deformations. The dominant loading type is axial loading to restrain floater deformations in sway direction. For a semi-submersible with a less stiff column-deckbox and deckbox structure in surge or heave direction, the magnitude of the bending stresses resulting from floater deformations may increase, therefore the benefit of hinged bracings increases as well. The hinge design is challenging due to the high loading capacity that is required, which is around 5000 tonnes for the $F_S$ load case, and the cyclic loading.

### 3.3.5 Bracing configuration evaluation

#### *3.3.5.1 Mass properties*

The mass properties of the final semi-submersible designs with different bracing configuration are summarised in Table 29. In the paragraphs below, the impact on mass properties are elaborated. The following notes are of importance regarding the mass properties. First, the draught of the semi-submersibles is kept constant at the operational draught of 20 meters. This is equivalent to a constant wetted area of the semi-submersible hull, therefore constant global water loading may be used. Second, constant weight and VCG is assumed for the LSW equipment, ballast and other structural mass. The mass properties of these items are derived from the weight estimation of the reference semi-submersible. Other structural mass involves compartments, small stiffeners and structural details not included in the global strength model. Finally, the payload VCG is assumed constant.

Due to the increase in bending and shear capacity needed in the column-deckbox connection and deckbox structure, configuration 1 has the largest increase in structural weight and VCG compared to other configurations. Specifically, total structural mass and VCG increased by 13% and 7%. Also, due to the absence in bracings, which provide buoyancy above a ratio of $D/t_{wall} \geq 29.6$, configuration 1 displaces less water than the reference semi-submersible. Above mentioned differences result in a reduction of 22% in payload compared to the reference semi-submersible.

For configuration 2, the added diagonal bracings decrease floater deformations in both sway and surge directions, therefore reduces deckbox stresses reported in Chapter 3.3.2. In the final design, deckbox plate thicknesses are reduced, resulting in a deckbox mass reduction of 5%. Combined with the increase in buoyancy, payload increases by 4%. Compared to bracing configuration 3.2, which has a similar payload increase, configuration 2 more effectively reduces structural mass when considering the bracing modifications.

Due to the ineffective deckbox support of configuration 3.1, no significant increase in payload is achieved. For configuration 3.2, deckbox size and plate thicknesses are reduced as a result of increased axial and bending stiffness of the horizontal transverse bracings and therefore a larger deckbox support by the diagonal bracings. Followed from the modifications, the deckbox mass not only reduces by 6%, but also the VCG is located lower compared to the reference semi-submersible. Bracing mass increased considerably by 323%. Both mass property changes result in a total structural VCG reduction of 4%. For the total VCG of the semi-submersible, a reduction of 2% is achieved. Because of the large increase in bracing mass, the increase in payload of 5% is similar compared to configuration 2.

Since hinged horizontal transverse bracings do not affect floater motions significantly, the structural design of the semi-submersible is not modified for configuration 4. As reported in Chapter 3.3.4, tubular bracing wall thickness and brace end plating is increased, therefore resulting in a slightly lower payload compared to the reference semi-submersible.

*Table 29: Mass properties semi-submersibles with different bracing configurations*

| Configuration | | Config. 1 | | Config. 2 | | Config. 3.1 | | Config. 3.2 | | Config. 4 | |
|---|---|---|---|---|---|---|---|---|---|---|---|
| Weight properties | | $\Delta_{mass}$ | $\Delta_{VCG}$ | $\Delta_{mass}$ | $\Delta_{VCG}$ | $\Delta_{mass}$ | $\Delta_{VCG}$ | $\Delta_{mass}$ | $\Delta_{VCG}$ | $\Delta_{mass}$ | $\Delta_{VCG}$ |
| Structural mass | Deckbox | 11% | 0% | -5% | 1% | -1% | 0% | -6% | -1% | 0% | 0% |
| | Columns (4x) | 64% | 11% | 1% | 0% | -3% | 0% | 0% | -2% | 2% | -1% |
| | Pontoons (2x) | 0% | 0% | 0% | 1% | 0% | 0% | 0% | 1% | 0% | 1% |
| | Bracings | - | 0% | 60% | 0% | 30% | 16% | 323% | 19% | 32% | 0% |
| | Other | 0% | 0% | 0% | 0% | 0% | 0% | 0% | 0% | 0% | 0% |
| | Total | 13% | 7% | 0% | -2% | 0% | 0% | 6% | -4% | 1% | 0% |
| Light Ship Weight, LSW | | 8% | 1% | 0% | -1% | 0% | 0% | 3% | -3% | 1% | 0% |
| Displacement, Δ | | -1% | 2% | 1% | 0% | 0% | 0% | 3% | -2% | 0% | 0% |
| Δ - LSW | | -15% | -7% | 3% | 1% | 1% | 0% | 3% | 1% | -1% | 0% |
| Ballast | | 0% | 0% | 0% | 0% | 0% | 0% | 0% | 0% | 0% | 0% |
| Payload | | -22% | 0% | 4% | 0% | 1% | 0% | 5% | 0% | -2% | 0% |

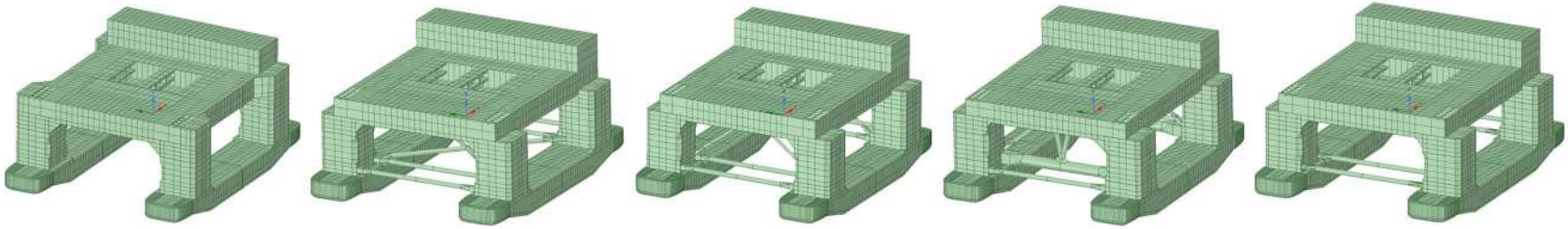

### 3.3.5.2 Floater deformations

Floater deformations are presented for configuration 2 and 4 in Chapter 3.3.2 and 3.3.4, respectively. In Table 30, an overview is provided of the absolute floater deformations per load case of all final configuration designs in the ULS. All PS and SB floater deformation differences are calculated for the same location at the brace-column connection shown in Figure 61.

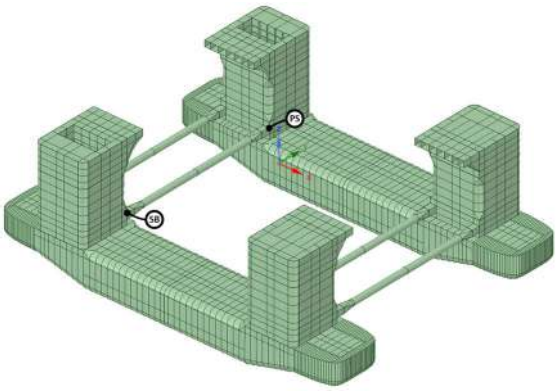


*Figure 61: Locations PS and SB brace-column connection*

The sway deformations of configuration 1 are significantly larger compared to the reference semi-submersible since transverse bracings are absent. Because transverse bracings do not affect floater surge and heave deformations significantly and due to the reinforced column-deckbox and deckbox structure, floater surge and heave deformations are lower for configuration 1. The added diagonal bracings in horizontal plane for configuration 2 decrease floater deformations in surge direction. Configuration 3.1 shows similar floater deformation, whereas configuration 3.2 has smaller sway deformations due to the increase of axial stiffness of the transverse bracings. Because the tubular wall and brace end plate thicknesses are increased of the hinged bracings, a small reduction in sway deformations for configuration 4 is the result.

*Table 30: Absolute ULS deformation differences final configurations between PS and SB brace-column connection [mm]*

| LC | Ref. case | | | Configuration 1 | | | Configuration 2 | | | Configuration 3.1 | | | Configuration 3.2 | | | Configuration 4 | | |
|---|---|---|---|---|---|---|---|---|---|---|---|---|---|---|---|---|---|---|
| | \|Δx\| | \|Δy\| | \|Δz\| | \|Δx\| | \|Δy\| | \|Δz\| | \|Δx\| | \|Δy\| | \|Δz\| | \|Δx\| | \|Δy\| | \|Δz\| | \|Δx\| | \|Δy\| | \|Δz\| | \|Δx\| | \|Δy\| | \|Δz\| |
| $F_S$ | 3 | 53 | 1 | 7 | 318 | 0 | 4 | 54 | 1 | 4 | 52 | 1 | 5 | 19 | 2 | 4 | 45 | 0 |
| $F_L$ | 40 | 17 | 12 | 30 | 107 | 6 | 23 | 19 | 9 | 42 | 20 | 10 | 37 | 6 | 10 | 42 | 15 | 12 |
| $F_{comb}$ | 45 | 40 | 22 | 27 | 240 | 12 | 16 | 41 | 16 | 47 | 40 | 20 | 41 | 15 | 23 | 47 | 36 | 22 |
| $M_T$ | 30 | 35 | 20 | 13 | 208 | 11 | 10 | 37 | 17 | 29 | 36 | 18 | 26 | 13 | 19 | 29 | 31 | 20 |
| $a_L$ | 1 | 11 | 0 | 2 | 71 | 0 | 1 | 11 | 0 | 1 | 14 | 0 | 1 | 4 | 0 | 1 | 10 | 0 |
| $a_T$ | 4 | 17 | 10 | 6 | 102 | 5 | 4 | 17 | 10 | 4 | 19 | 6 | 3 | 7 | 4 | 5 | 15 | 10 |
| $a_V$ | 1 | 18 | 0 | 3 | 112 | 0 | 1 | 18 | 1 | 1 | 21 | 0 | 1 | 7 | 0 | 1 | 16 | 0 |

### 3.3.5.3 Structural redundancy

The FE-analyses in the ALS damaged condition evaluates the structural redundancy of the semi-submersibles with different bracing configurations, see Chapters 3.3.1 to 3.3.4. The WSD check resulted in acceptable yielding and buckling stresses, which is summarised in APPENDIX D. The usage factor ratios ($\eta/\eta_p$) for horizontal transverse bracings are the highest in the ALS damaged condition where one other horizontal transverse bracing is suppressed in the analysis, see Table 31. Therefore, the ALS damaged condition generally defines the global structural dimensions of the horizontal transverse bracings. For the horizontal or vertical diagonal bracings, load cases in the ULS results in slightly higher usage factor ratios. The FE-analyses demonstrate the bracing configurations have sufficient redundancy when classification society guidelines are followed. To conclude which bracing configuration excels in structural redundancy, the parameters discussed below are analysed.

First, the number of bracings can be related to structural redundancy. For example, a larger number of bracings increases structural redundancy, since a larger number of load paths are present when one bracing or joint is damaged. When only considering the number of bracings, configuration 3.2 has the highest structural redundancy, whereas configuration 1 has the lowest structural redundancy. However, when also the increase in bracing usage factor ratio between the ALS and ULS is considered, configuration 3.2 shows an ineffective increase in structural redundancy. Since the horizontal transverse bracing usage factor ratio increases by 2 when the large 4.2 meter diameter transverse bracing is damaged. Configuration 4 has a similar bracing usage factor ratio compared to the reference semi-submersible due to the equal load paths when one bracing is damaged. The same holds for

configuration 3.1, since the added diagonal braces do not absorb much loading, also discussed in Chapter 3.3.3.1. The usage factor ratios of configuration 2 conclude a more effective structural redundancy due to the added horizontal diagonal bracings, which increases load capacity in sway direction.

*Table 31: Structural redundancy parameters final bracing configurations*

| Bracing configuration | Number of bracings | Bracing usage factor ratio $\left(\frac{\eta_{ALS}}{\eta_{p,ALS}}/\frac{\eta_{ULS}}{\eta_{p,ULS}}\right)$ | | |
|---|---|---|---|---|
| | | Horizontal transverse | Horizontal diagonal | Vertical diagonal |
| Ref. case | 4 | 1.13 | - | - |
| 1 | 0 | - | - | - |
| 2 | 6 | 1.08 | 0.85 | - |
| 3.1 | 8 | 1.13 | 0.76 | - |
| 3.2 | 12 | 2.06 | - | 0.99 |
| 4 | 4 | 1.14 | - | - |

### *3.3.5.4 Fatigue*

The FLS is usually a governing limit state regarding structural details, therefore mainly defines the local structural design. No fatigue assessment is performed for all bracing configurations, since this requires detailed local strength models and extensive calculations to accurately estimate the fatigue damage at fatigue sensitive locations. However, qualitatively the FLS is evaluated by the fatigue sensitive locations and the global loading a member or component has to absorb. For example, a certain bracing configuration is unfavourable if a large number of fatigue sensitive locations are present. In this case, the possible number of cracks increases and because these connections should be checked and maintained, larger inspection and maintenance costs are the result as well. Moreover, if the global loading for a member or component is unfavourable, i.e. highly loaded and/or in disadvantageous directions, the fatigue lifetime at detail level becomes a challenge and therefore the bracing configuration is also unfavourable regarding the FLS.

Fatigue sensitive locations are based on the literature review [2], summarising detected fatigue cracks on semi-submersibles. At the horizontal transverse brace-column connection most fatigue cracks were detected, therefore can be identified as the most fatigue sensitive location on a semi-submersible. Worthwhile to note is the report of DNV, reporting fatigue cracks in the Aker H-3 semi-submersible design, concluding the horizontal diagonal brace-column, vertical diagonal brace-deck and chord-brace connections are also fatigue sensitive locations. The literature review also summarised fatigue assessments of semi-submersible designs, where also the horizontal brace-column connection was identified as most fatigue sensitive. Other locations analysed for fatigue assessments were the column-deckbox connection, moonpool area and pontoon-column connection.

The fatigue sensitive locations are localised more precisely based on hot spots from FEA, i.e. locations with high stress concentrations. Due to the coarsely meshed model, stress concentrations magnitudes cannot be determined accurately. However, identifies fatigue sensitive locations shown in Figure 62 and further discussed below.

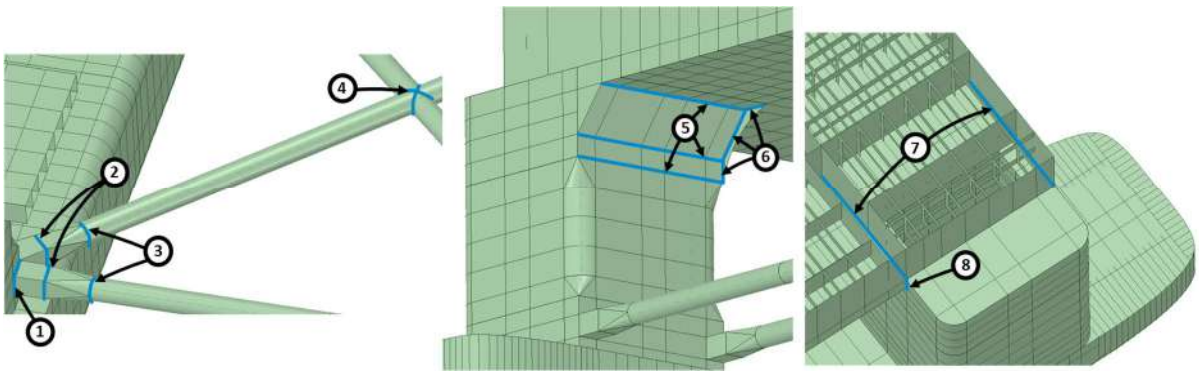


*Figure 62: Fatigue sensitive locations semi-submersible*

For the bracing members, several fatigue sensitive locations are identified. The first location, (1) in Figure 62, is the brace-column connection, which is most frequently mentioned in reports regarding detected cracks and fatigue assessments. If floater deformations and bracing bending stiffness is substantial, a brace-column connection is not only axially loaded but also bending moments occur at the bracing ends. Larger stresses are therefore present at the brace-column connection. In adition, stress intensities occur due to the change in stiffness properties and structure discontinuity between brace and column structure. Because of the orthotropic orientation of the column structure, the plated brace-column connection is also orthotopically orientated, also referred to as planar joint. The connection at small scale can be identified as a double sided (DS) cruciform joint. To increase fatigue resistance, the heavily loaded brace plating must be continuous into the column structure, where the outer column plating is welded trough a groove weld at the top and bottom brace plating. Above also applies to the fatigue sensitive brace-deckbox connection. The second and third location, (2) and (3) in Figure 62, are the bracing square-tubular transition pieces. Due to the geometry transition, stress intensities occur. To increase fatigue resistance, a butt joint with a groove weld is most appropriate to reduce stress intensities. The fourth location, (4) in Figure 62, is the brace-brace connection. The non-uniform stiffness distribution around the circumference of a tubular joint results in non-uniform stress distributions and therefore stress concentrations. Depending on brace orientation, the chord-brace connection can be classified as a tubular circular hollow section (CHS) T-, K, KK-, or X-joint. The brace orientation may limit welding accessibility, therefore a groove weld may not be applicable along the entire circumference of the joint. Based on the ULS FEA of the different bracing configurations, mode-I loading is governing for bracing members, i.e. normal stresses are relatively large compared to shear stresses. Some shear stress is present at the corners of the brace-column connection.

For the column-deckbox area, the following fatigue sensitive locations are identified. The first locations, (5) and (6) in Figure 62, are the inner face outer plating and bracket at the knee joint. Also discussed in Chapter 3.3.1.1, due to the shift in neutral axis, stress intensifies towards the inner faces of the column-deckbox connection. Outer plating of offshore and marine structures are typically connected through a butt joint [32]. The bracket should be connected by a butt joint with a groove weld as well to increase fatigue resistance. Based on the FE-analyses, mode-I loading is mainly present in the outer plating. In-plane shear stress magnitudes are greater for the bracket, therefore mode-I and mode-III loading should be taken into account. The third location, (7) in Figure 62, is the deckbox transverse side plating and bulkheads. Discussed in Chapter 3.3.1.1, relative large normal and shear stresses are observed in the ULS and ALS for the $F_S$ and $F_{comb}$ load cases. Therefore, mode-I and mode-III should be considered. Similar to the bracket connection, a butt joint with a groove weld is most appropriate to increase fatigue resistance. The final location is the deckbox longitudinal side plating, (8) in Figure 62, where stress intensities are observed at the connection between the deckbox longitudinal side and column outer plating, resulting from stiffness changes and structural discontinuities. Due to the deckbox mass and bending and torsion loading present in the $F_L$, $F_{comb}$ and $M_T$ load cases, both normal and shear stresses are present. Mode-I and mode-III loading should therefore be taken into account.

The FLS becomes more unfavourable and inspection and maintenance costs increase when the number of fatigue sensitive locations, weld length and volume increases as well. The weld length, $L_{weld}$, and weld volume, $V_{weld}$, of the fatigue sensitive bracing and column-deckbox locations are shown in Table 32. The last 3 columns of Table 32 present the total number of fatigue sensitive locations and total weld length and volume. A groove weld where plating is bevelled at an angle of 45 degrees is assumed for the weld volume calculation. Since total weld volume includes the number of hotspots, weld length and plate thickness, this parameter describes the possibility of cracks more completely. For example, a structure with a larger welding volume has a larger quantity of weld defects, therefore the possibility of a severe defect increases as well. When ranking the bracing configurations based on weld volume, configuration 3.1 is most favourable. Although configuration 1 has no bracings, the column-deckbox connection has a relative large welding volume due to the increased plate thicknesses at the inner face outer plating and bracket at the knee joint, locations (5) and (6) in Figure 62, and the added transverse bulkheads, location (7) in Figure 62. Configuration 4 consists of a slightly higher welding volume compared to the reference semi-submersible as a result of the larger wall thickness of tubular members and thicker bracing end plating. Because of the large transverse bracings present in configuration 3.2, welding volume increases significantly with a factor of 3.7, therefore this design is most unfavourable with respect to the FLS and has the largest inspection and maintenance costs.

*Table 32: Final bracing configurations weld length and volume*

| Bracing configuration | Bracings | | Column-deckbox | | Total | | |
|---|---|---|---|---|---|---|---|
| | $L_{weld}$ [m] | $V_{weld}$ [$dm^3$] | $L_{weld}$ [m] | $V_{weld}$ [$dm^3$] | Number of locations | $L_{weld}$ [m] | $V_{weld}$ [$dm^3$] |
| Ref. case | 160 | 180 | 338 | 145 | 52 | 498 | 325 |
| 1 | 0 | 0 | 496 | 398 | 40 | 496 | 398 |
| 2 | 268 | 215 | 338 | 145 | 65 | 606 | 360 |
| 3.1 | 228 | 207 | 338 | 73 | 64 | 566 | 280 |
| 3.2 | 588 | 1134 | 325 | 58 | 98 | 912 | 1192 |
| 4 | 103 | 208 | 338 | 145 | 44 | 441 | 353 |

Regarding global loading, for almost all different bracing configurations, axial loading is balanced between similar bracing types. Such as horizontal transverse, horizontal diagonal and vertical diagonal bracings. This is due to symmetry of the wetted area and bracing structure, which is favourable with respect to the global loading of the bracings. Because the horizontal transverse bracings of configuration 3.2 differ in global dimensions, above is not applicable to configuration 3.2. Namely, the 4.2 meter diameter horizontal transverse bracings absorb larger axial loading compared to the smaller 1.8 meter diameter horizontal transverse bracings. Also, the large diameter horizontal transverse bracings are loaded laterally by the middle diagonal bracings. When comparing different bracing types, the horizontal transverse bracings are loaded most unfavourable regarding fatigue, since static loading results in outward floater deformations and therefore a mean tensile stress is present. In addition, shown by Table 30, the sway deformations of the floaters are larger compared to other directions, since sway stiffness of the floaters is lower, therefore the horizontal transverse bracings are most highly loaded. Configuration 1 is considered most unfavourable regarding global loading, due to the relative small sway stiffness and the absence of bracings, resulting in large shear and bending moments at the column-deckbox connection for both the static and dynamic load cases. Moreover, larger dynamic motions in sway direction are expected for configuration 1 when beam waves are present, which affects fatigue damage adversely at fatigue sensitive locations of the column-deckbox connection.

### *3.3.5.5 Configuration selection*

The ranking of bracing configurations regarding payload, structural VCG, structural redundancy and fatigue is provided in Table 33. Configurations are ranked based on relative differenced with respect to the reference semi-submersible. Elaborated in above chapters, structural redundancy is favourable when a higher number of bracings are present. Regarding fatigue, a bracing configurations ranks higher if the weld volume at fatigue sensitive locations is lower.

*Table 33: Ranking bracing configurations*

| Ranking | Payload | | Structural VCG | | Structural redundancy | | Fatigue | |
|---|---|---|---|---|---|---|---|---|
| | Config. | $\Delta_{payload}$ | Config. | $\Delta_{VCG}$ | Config. | $\Delta_{\#bracings}$ [-] | Config. | $\Delta_{Vweld}$ [$dm^3$] |
| 1 | 3.2 | +5% | 3.2 | -4% | 3.2 | 8 | 3.1 | -45 |
| 2 | 2 | +4% | 2 | -2% | 3.1 | 4 | Ref. case | 0 |
| 3 | 3.1 | +1% | 4 | 0% | 2 | 2 | 4 | +28 |
| 4 | Ref. case | 0% | 3.1 | 0% | 4 | 0 | 2 | +35 |
| 5 | 4 | -2% | Ref. case | 0% | Ref. case | 0 | 1 | +73 |
| 6 | 1 | -22% | 1 | +7% | 1 | -4 | 3.2 | +867 |

Table 33 concludes configuration 3.2 ranks most favourable with respect to payload, structural VCG and structural redundancy. However, configuration 3.2 ranks lowest for fatigue, since welding volume increases with 867 $dm^3$ at the fatigue sensitive locations. Contrary, configuration 1 ranks the most unfavourable with respect to payload, structural VCG and structural redundancy. Although the number of fatigue sensitive locations is lower for configuration 1, the reinforced column-deckbox connection increases welding volume considerably, therefore ranks second to last with respect to fatigue.

The bracing configuration selection is merely based on the semi-submersible's requirements. Therefore, the designer should first rank the requirements. If for instance payload and VCG are most important, configuration 3.2 would be the preferred choice. Configuration 3.1 is most favourite if the aim is to reduce the possibility of fatigue failure and to reduce maintenance and inspection costs. Other requirements not considered, are for instance construction costs and the required propulsion power. Steel and labour costs are approximately 20 to 25 percent of the total semi-submersible construction costs [33]. Reported in Table 29, the semi-submersible structural weight of configurations 2, 3.1, 3.2 and 4 differ respectively 0%, 0%, 6% and 1% compared to the reference semi-submersible. Therefore, impact on total construction costs are limited. The structural weight of configuration 1 increased by 13%, therefore the total construction costs may increase by 3%. Regarding the propulsion power, when the reference semi-submersible is in operational condition or in survival transit condition, the bracing structure is submersed. Based on the differences in frontal surge area, it is estimated that configuration 1 reduces the required power by 22%, while configuration 2, 3.1 and 3.2 increase the required power by 10%, 1% and 16%, respectively. The frontal surge area of configuration 4 is equivalent to the reference semi-submersible, therefore no difference in propulsion power is expected.

When the differences in Table 33 are normalised and summed, therefore payload, structural VCG, structural redundancy and fatigue are all of equal importance, configuration 2 would be preferred. Also, when the amount of bracing modifications are considered, configuration 2 increases payload more effectively compared to configuration 3.2. The same holds for structural redundancy, where configuration 2 has a more effective increase compared to other configurations.

# 4 SSS planar joint and LSS tubular joint fatigue resistance similarity

## 4.1 Introduction

Fatigue resistance is usually determined by S-N curves for specific structural details, in which stress range is plotted against the number of cycles. S-N curves are mostly based on fatigue tests of welded joints at small scale, also known as small scale specimen (SSS). Because of the larger costs, less fatigue tests are done using large-scale specimen (LSS) or full-scale specimen (FSS). Also, LSS and FSS tests are made for a specific structure, and therefore cannot be applied as universal as SSS tests. Regarding semi-submersibles, if the bracings and columns are tubular members, fatigue resistance of the brace-column and brace-brace connections are typically based on LSS tubular joint fatigue tests. Another objective of this assignment is to study whether similarity can be established between SSS planar joints and LSS CHS tubular joints. If similarity is proven, a SSS planar joint based design S-N curve can be used for tubular joints as well. This chapter summarises the study on similarity between SSS planar joints and LSS tubular joints, applying the hot spot stress concept and average effective notch stress concept to assess fatigue. Hot spot and average effective notch stress ranges of SSS planar joints are provided by TU Delft. LSS tubular joint fatigue tests, derived from literature, are analysed in FEA by shell and volume models.

Fatigue resistance is defined by four dimensions [34]. Material and geometry are the first two dimensions and define the fatigue resistance of a structural detail. The material dimension is related to micro stress concentrations, which occur due to grain boundaries, material defects and the manufacturing process. An important material parameter related to crack growth is the Young's modulus. The geometry dimension is related to macro stress concentrations that occur at notch geometries, such as the weld toe, weld root and structure discontinuities, but also arise by non-uniform stiffness distributions. Loading & response and the environment are the third and fourth dimensions, which define the fatigue damage process of a structural detail. The loading & response of marine and offshore structures is typically cyclic and stochastic, i.e. a random process over time. Generally, structural members in marine and offshore structures are mainly loaded by mode-I loading, therefore membrane and bending stresses are the dominant stress type. Due to structure geometry and/or a combination of sea and swell waves, multi-axial loading may occur [35]. Multi-axiality in marine and offshore structures is mainly a combination of mode-I and mode-III, therefore considering both normal and in-plane shear stresses. For example, bulkheads located at the column-deckbox connection both absorb mode-I and mode-III loading, as discussed in Chapter 3.3.5.4. Finally, the environment dimension accelerates the fatigue damage process if the structure is present in a more corrosive environment. Corrosion pits appear at the surface, increasing micro stress concentrations, and over time also result in macro stress concentrations.

A larger fatigue resistance accuracy is achieved when the four dimensions are included in more detail in the fatigue assessment concept. Over the years, fatigue assessment concepts have become increasingly detailed regarding the geometry and loading & response information involved [34]. Since marine and offshore structures, such as semi-submersibles [2], increasingly operate in remote areas, the demand to accurately estimate the fatigue damage increases as well. In addition, the computational power has increased, which enables to implement detailed fatigue assessment concepts.

The two most common engineering fatigue methods are the nominal stress concept and hot spot stress concept. The effective notch stress concept is also a well-known concept, however is less applied because of the relatively large effort needed to retrieve stress ranges. The above mentioned concepts are assuming intact geometry, therefore no stress intensities are considered due to internal or external weld defects. Weld defects are included in the S-N curves based on fatigue tests. Another approach is to assume a cracked geometry, where stress intensities at the cracked notch are calculated. By using $da/dN$ curves, the crack growth and therefore fatigue damage can be calculated over time. Cracked

geometry assessment concepts, such as the crack tip stress intensity concept and total stress concept, are less applied in engineering practise.

The literature review partly focused on fatigue resistance similarity between SSS planar joints and LSS tubular joints using the hot spot stress as fatigue assessment concept. The scatter of the fatigue resistance data, defined as the vertical offset between the 10% and 90% probability of survival, was considered large. This may be due to residual stress and local notch effects not accounted for by the hot spot stress concept, differences in LC and NLC joints, thickness differences between specimens and different stress ratios. Since the effective notch stress concept includes more information regarding geometry and loading & response compared to the hot spot stress concept, it is expected that similarity between SSS planar joints and LSS tubular joints increases.

## 4.2 LSS tubular joints

The selected LSS CHS and SHS tubular joints are illustrated in Figure 63. In Table 34 the geometric and loading properties are summarised. Tubular dimensions and critical locations, such as the crown toe, saddle and crown heel are shown in Figure 64. Specifically, the selected LSS tubular specimens can be classified as simple tubular joints. Simple tubular joints consists of two or more tubular members only, not stiffened by ring stiffeners. The specimens were loaded by various load types, such as axial forcing (AF), in-plane bending (IPB) and out-of-plane bending (OPB). Fatigue tests are selected based on the available information reported by the authors regarding specimen dimensions, weld geometry, boundary conditions, failure locations, stress distributions and hot spot SCF's. Also, only as-welded joints tested in air with weld toe failures are studied. As welded joints imply joints not treated thermally or mechanically after welding. Post-weld treatments are for example peening to add a mean compressive stress and post weld heat treatment to reduce residual stresses. Reported welds with excessive or insufficient weld reinforcement are also excluded.

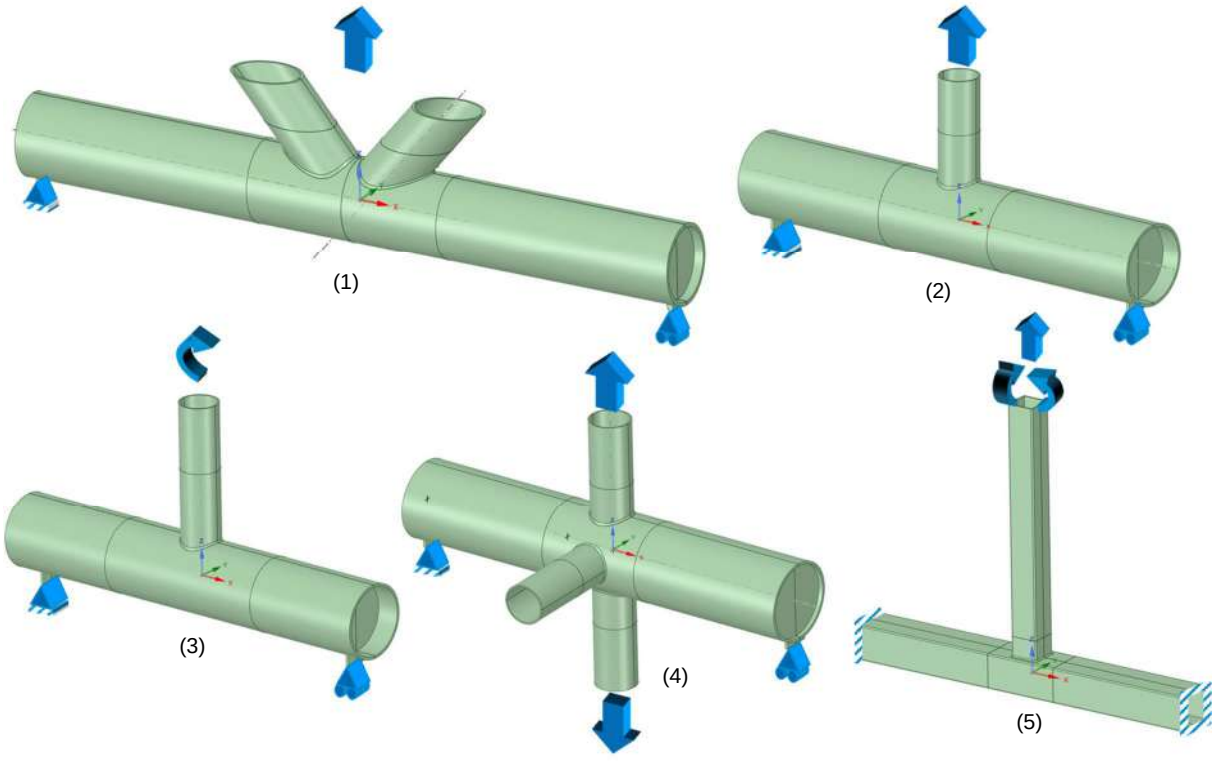


*Figure 63: LSS tubular joints*

*Table 34: LSS tubular joints*

| # | Authors | Year | Weld type | Joint type | Loading type | D or B, T [mm] | α = L/D = L/B | β = d/D = b/B | γ = D/2T = B/2T | τ = t/T | Stress ratio, $r_{lr}$ | Ref |
|---|---|---|---|---|---|---|---|---|---|---|---|---|
| 1 | C.H. Jo et al. | 2011 | Groove | CHS K-joint | IPB | 610, 27 | 9.8 | 0.75 | 11 | 0.71 | 0.1 | [36] |
| 2-4 | O.D. Dijkstra et al. | 1980 | Groove | CHS T-joint | AF | 457, 16 | 5 | 0.5 | 14 | 0.5 | 0 | [37] |
| | | | | CHS T-joint | IPB | 168, 6 | 5 | 0.5 | 13 | 0.5 | 0 | |
| | | | | CHS X-joint | AF | 914, 32 | 5 | 0.5 | 14 | 0.5 | 0 | |
| 5 | M.S. Zhao et al. | 2013 | Groove | SHS T-joint | AF, IPB, OPB | 300, 12 | 10 | 0.67 | 13 | 1.0 | 0 | [38] |

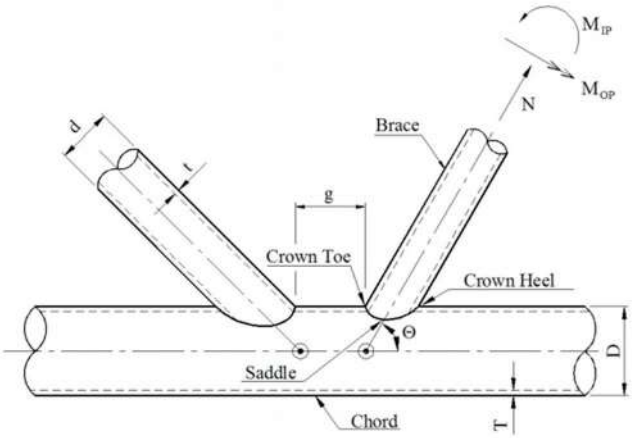


*Figure 64: Tubular joint dimensions and critical locations [39]*

An example of a tubular joint fatigue test is shown on the left of Figure 65, which is the K-joint specimen tested by Jo et al.. This specimen was simply supported at the chord ends and loaded by vertical forcing, resulting in a dominant IPB at the tubular joint. The specimen failed at the crown heel chord weld toe, illustrated by the through thickness crack in the chord shown on the right of Figure 65.

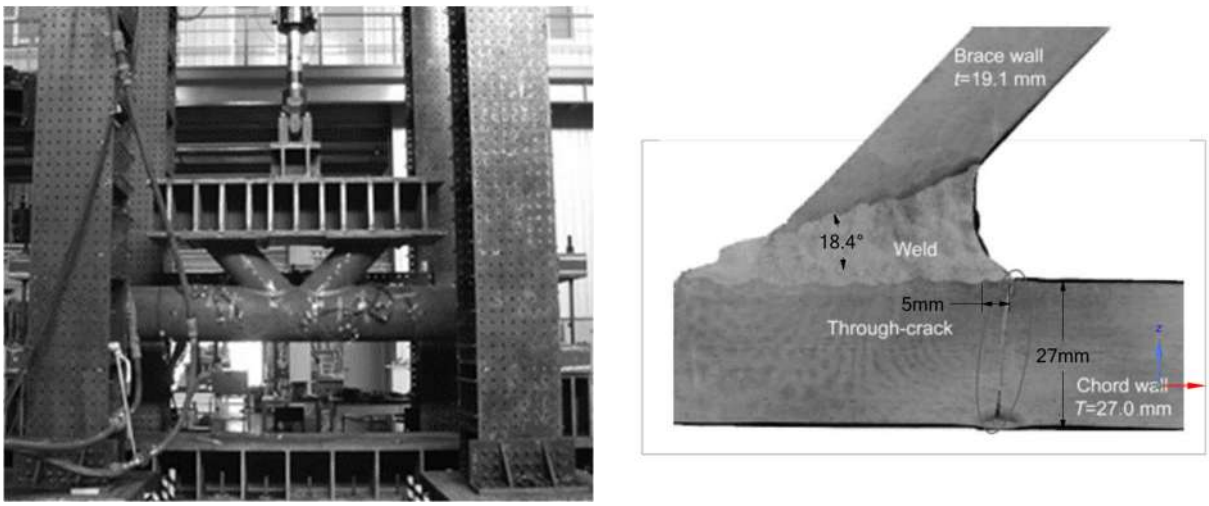


*Figure 65: Fatigue test K-joint Jo et al. (left) and failed crown heel (right)*

## 4.3 Hot spot stress fatigue resistance

The hot spot stress concept was originally developed within the offshore industry for tubular joints [40]. This fatigue assessment concept accounts for stress concentrations due to local structure geometry, therefore captures the structural field stress, $\sigma_f$, information, see Figure 66. The weld induced nonlinear stress distribution is not accounted for. This nonlinear stress distribution is also referred to as the self-equilibrating stress, $\sigma_{se}$. The self-equilibrating stress is influenced by weld geometry, which is described by weld notch angle, $2\alpha$, weld leg length, $l_w$, weld height, $h_w$ and notch radius, $\rho$. To define weld geometry of tubular joints in particular, the length of the extended weld section, $l_e$, and groove angle, $\delta$, are often specified by authors of fatigue tests and are also incorporated by standards, such as AWS [41]. $r$ is the location measured from weld toe in chord thickness direction. The self-equilibrating stress consists of the V-shaped notch stress, $\sigma_{\theta\theta}$, and the weld load carrying stress, $\sigma_{bw}$, further discussed in Chapter 4.5.2. The hot spot stress concept is limited to only assess weld toe failures, where stresses perpendicular to the weld toe are dominant. The hot spot stress is usually evaluated by three different methods [42]. The first method is by through-thickness stress linearisation in FEA to obtain the linear membrane, $\sigma_m$, and bending stress, $\sigma_b$, components. Both stress components form the structural field stress distribution when summed. The second method is to determine hot spot stress by linear or nonlinear surface extrapolation at two or more reference points at certain distances from the weld toe. This method is used in fatigue tests using strain gauges, but is also applicable in FEA. The final method is to derive a stress at a single point outside the influence area of the nonlinear self-equilibrating stress. An example of the latter method is to derive the stress 1 mm below the weld toe developed by Xiao and Yamada [43] for planar joints, which is proven to be less sensitive to element size and element type.

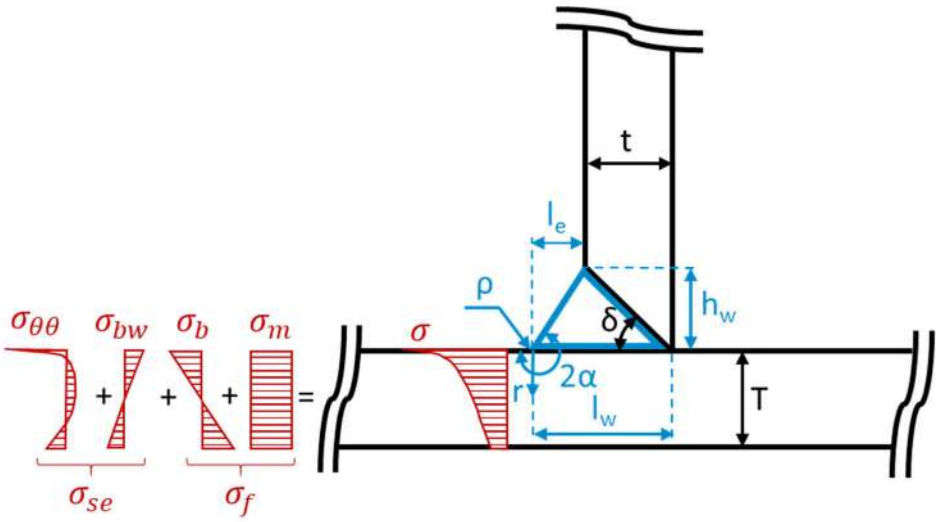


*Figure 66: Tubular joint dimension and stress definitions*

Due to the non-uniform stiffness distribution of tubular joints, non-uniform stress distributions and therefore stress concentrations occur. Depending on geometric and loading properties, SCF's can vary significantly, such as hot spot SCF's varying from 1.1 to 11.2 as measured by Dijkstra using linear surface extrapolation. Parametric formulas can also provide hot spot SCF's of tubular joints, such as those from DNV-GL [39], M. Efthymiou [44] and P. Smedley et al. [45]. Stress concentrations of tubular CHS joints depend on the ovalisation of the chord body [46]. For example, the multiplanar X-joint of Dijkstra, where both braces in vertical direction are axially loaded, result in a larger ovalisation and therefore larger SCF compared to the single side loaded specimens, such as T- and K-joints.

All specimens for which fatigue failure was reported showed similar crack initiation and growth. The crack initiated at the weld toe at the chord, then crack length increased along part of the circumference. Finally, the crack advances in the thickness direction of the chord until a through thickness crack is present. The reported hot spot fatigue resistance data is summarised in Table 35. Since specimen and/or failure locations undergo different stress ratios, $r_{rl}$, the measured hot spot stress ranges are corrected by Walker's mean stress model formulated as Eq.5-10. A value $\gamma = 0.92$ is adopted based on most likely estimates calculated by Y. Qin et al. [47] for SSS planar joints.

$$S_{h,eff} = \frac{S_h}{(1 - r_{rl})^{1-\gamma}} \qquad \text{Eq.4-1}$$

Jo defined the nominal stress as the measured chord stress away from the joint, while Dijkstra measured the nominal strain in the brace. Zhao did not specify nominal stresses and SCF's, therefore are manually calculated based on the measured hot spot stress range. Dijkstra reported the fatigue data as nominal and hot spot strain measured perpendicular to the weld toe, $\varepsilon_\perp$. Strain measurements parallel to the weld toe, $\varepsilon_\parallel$, are not specified to convert strain to stress as $\sigma_\perp = \frac{E}{1-\nu^2}(\varepsilon_\perp + \nu\varepsilon_\parallel)$, therefore the following stress-strain relation is applied: $\sigma_\perp = \frac{E}{1-\nu^2}\varepsilon_\perp$. The number of cycles to failure, $N_f$, is defined as the number of cycles until a through thickness crack in the chord was observed.

*Table 35: Hot spot fatigue resistance data*

| # | Joint type | Measured nominal stress $\sigma_{nom}$ [MPa] | Load range $\Delta_{load}$ | Failure location | Measured hot spot SCF | Measured hot spot stress range $S_{h,eff}$ [MPa] | Number of cycles to failure $N_f$ [-] |
|---|---|---|---|---|---|---|---|
| 1 | CHS K-joint | 44<br>38<br>32 | $\Delta_F$ = 397 kN<br>$\Delta_F$ = 353 kN<br>$\Delta_F$ = 309 kN | Chord weld toe, crown heel | 2.74 - 2.96 | 129<br>110<br>98 | 9.7E+5<br>1.3E+6<br>2.6E+6 |
| 2 | CHS T-joint | 33[(a)]<br>29[(a)]<br>29[(a)]<br>17[(a)]<br>33[(a)] | $\Delta_{AF}$ = 160 kN<br>$\Delta_{AF}$ = 144 kN<br>$\Delta_{AF}$ = 144 kN<br>$\Delta_{AF}$ = 85 kN<br>$\Delta_{AF}$ = 160 kN | Chord weld toe, saddle | 6.70 | 189[(b)]<br>170[(b)]<br>170[(b)]<br>100[(b)]<br>189[(b)] | 6.8E+5<br>1.1E+6<br>8.4E+5<br>7.5E+6<br>7.6E+5 |
| 3 | CHS T-joint | 247[(a)]<br>278[(a)]<br>194[(a)] | $\Delta_{IPB}$ = 4000 Nm<br>$\Delta_{IPB}$ = 4500 Nm<br>$\Delta_{IPB}$ = 3150 Nm | Chord weld toe, crown heel | 1.10 | 297[(b)]<br>333[(b)]<br>233[(b)] | 3.3E+5<br>4.7E+5<br>1.5E+6 |
| 4 | CHS X-joint | 7[(a)]<br>19[(a)] | $\Delta_{AF}$ = 150 kN<br>$\Delta_{AF}$ = 390 kN | Chord weld toe, saddle | 9.80 | 72[(b)]<br>190[(b)] | 2.0E+7<br>5.0E+5 |
| 5 | SHS T-joint | 49[(c)]<br><br><br>28[(c)] | $\Delta_{AF}$ = 120 kN<br>$\Delta_{IPB}$ = 4kN<br>$\Delta_{OPB}$ = 4kN<br>$\Delta_{AF}$ = 70 kN<br>$\Delta_{IPB}$ = 1kN<br>$\Delta_{OPB}$ = 3.6kN | Weld toe | 11.0[(c)]<br><br><br>11.6[(c)] | 535<br><br><br>325 | 4.2E+4<br><br><br>9.0E+4 |

[(a)] *Calculated as* $\sigma_{nom} = \frac{E}{1-\nu^2} \cdot \varepsilon_{nom,\perp}$

[(b)] *Calculated as* $S_h = \frac{E}{1-\nu^2} \cdot S\varepsilon_{h,\perp}$

[(c)] *Not reported by authors, manually calculated*

The hot spot stress fatigue resistance of SSS planar joints and LSS tubular joints is plotted in Figure 67. The run-outs, which are specimens where no through thickness crack was observed, are grey marked with an arrow. Figure 67 shows all LSS tubular joints fits the SSS planar joint fatigue data. The two-sided 10% and 90% probability of survival for the LSS tubular joints is plotted as dashed lines shown in Figure 67. The probability of survival is determined by mean fitting the LSS tubular joint fatigue resistance data by the "polyfit" function in MATLAB using a least-squares approach. The probability of survival is determined as $R = \mu \pm 1.645\sigma$, where $\mu$ represents the fitted mean and $\sigma$ is the standard deviation, therefore a Gaussian distribution is assumed. To define the scatter of fatigue resistance, the strength scatter index, $T_{\sigma S}$, is implemented. The strength scatter index, as formulated in Eq.4-2, is the ratio of vertical offset between the 10% and 90% probability of survival. For SSS planar joints, excluding run-outs, $T_{\sigma S_h} = 1{:}\,2.18$ and $T_{\sigma S_h} = 1{:}\,2.15$ for LSS tubular joints.

$$T_{\sigma S} = 1{:}\left(\frac{S_{R10}}{S_{R90}}\right) \qquad \text{Eq.4-2}$$

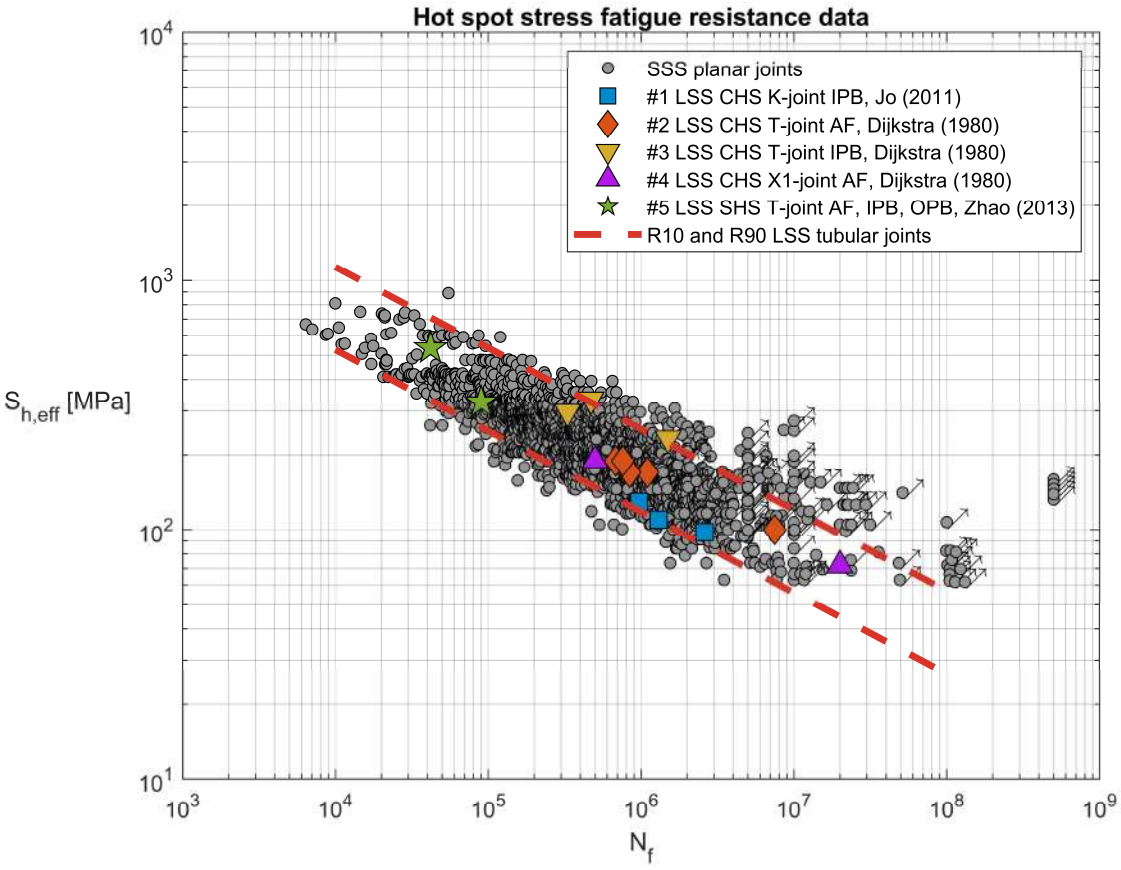


*Figure 67: Hot spot stress fatigue resistance*

## 4.4 Tubular joint response

This chapter presents stress distributions along the circumference, i.e. weld seam, and discusses the finite element modelling of the LSS tubular joints.

### 4.4.1 Stress distributions

The circumferential stress distribution of the LSS tubular joints is derived by shell FEA. In APPENDIX E, the specimen's boundary conditions, geometry details and FEA modelling interpretations are reported.

The surface models are modelled with identical global dimensions as specified in the fatigue reports. All authors reported weld dimensions or provided pictures of joints, from which weld geometry is determined, see APPENDIX E. A. Romeijn [48] concluded that modelling the weld improves the SCF's accuracy. Finite element stress differences with and without weld geometry is reported in Chapter 4.4.2, also concluding the significant impact of including weld geometry in shell FEA. Including weld geometry results in better agreement of the structural stress compared to volume FEA, since local bending moments are more accurate. The weld geometry is taken into account by modelling a mid-surface of the extended groove weld section as sketched in Figure 68. The offset type of the surfaces is set to middle. The modelling principle of the weld is similar as advised by E. Niemi [42]. The modelled weld surface extends to the weld toes of the groove weld, where extended weld throat thickness, $t_w$, is taken as thickness of the modelled weld surface for crown T-joints, saddle T-joints and K-joints and crown toe K-joints, see Figure 68. The thickness for the crown heel K-joint is taken as shown on the right of Figure 68. The modelled thickness overestimates the cross-sectional area, therefore stiffness, at the brace weld toe, however has representative stiffness at the chord weld toe, which is the failure location of all specimens. Examples of surface models are shown in Figure 69, where the weld surface is coloured in red. Emphasises is put on modelling the weld geometry accurately at the location of failure. Weld height is kept constant along the circumference of the joint, since this results in geometry less likely to be problematic for meshing in ANSYS.

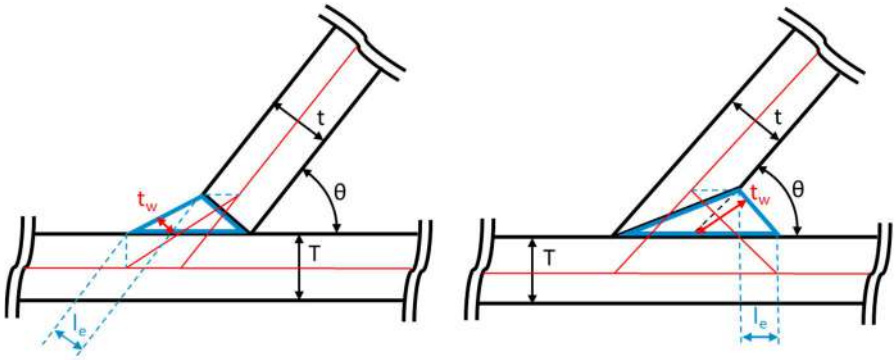


*Figure 68: Volume and surface model crown toe K-joint, crown T-joint ($\theta = 90°$), saddle T-joint and K-joint (left) and crown heel K-joint (right)*

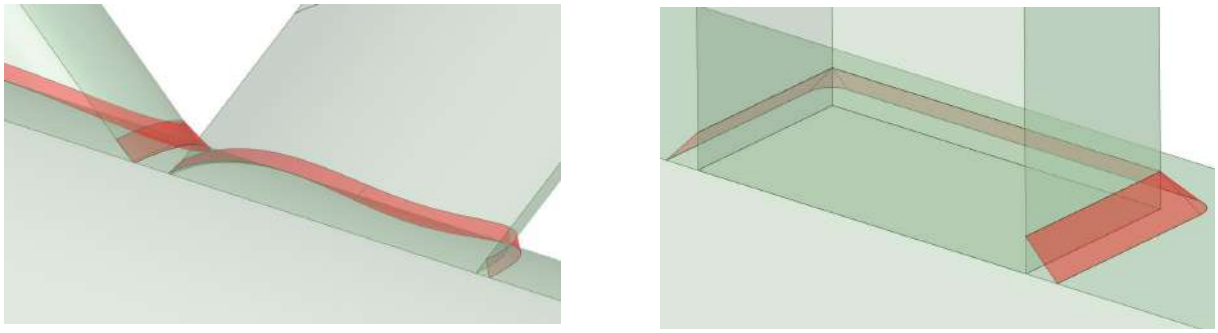

*Figure 69: Tubular joint geometry of surface models CHS K-joint (left) and SHS T-joint (right)*

All specimens failed at the chord weld toe. The nodal forces, nodal moments and element Euler angles are therefore derived at the intersection between chord and weld surface, see Figure 70 as example. The chord body outside the weld surface is selected to request nodal forces and moments associated with the chord. Otherwise, the sum of nodal forces and moments of the surrounding bodies is taken, which is incorrect.

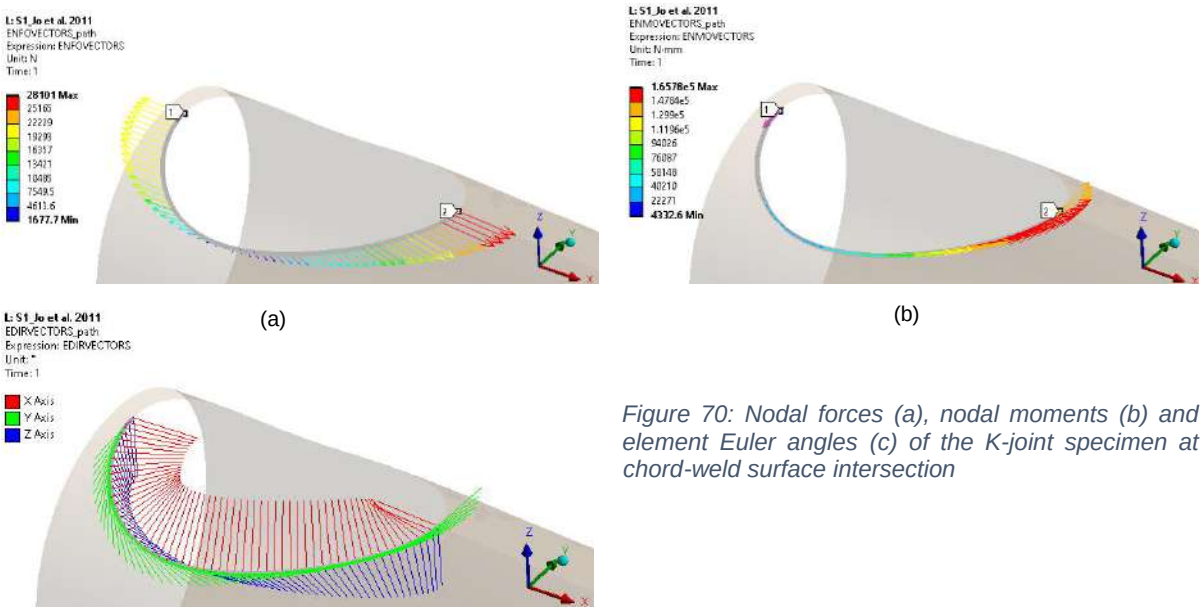


*Figure 70: Nodal forces (a), nodal moments (b) and element Euler angles (c) of the K-joint specimen at chord-weld surface intersection*

Nodal forces and moments are derived from ANSYS with respect to the global CSYS. The element Euler angles are extracted to convert the nodal force and moment orientation to the local weld CSYS, x', y' and z' as sketched in Figure 71. Nodal force and moment orientation to local weld CSYS is performed by rotation matrices, see Eq.4-3 taking nodal forces as example. Since all fatigue tests specified the hot spot stress as perpendicular to the weld seam, i.e. mode-I, membrane and bending stresses along the x'-direction are of importance. The method developed by Dong [49] for linear elements is applied to convert nodal forces and moments to line forces, $f_1, f_2, \dots, f_n$ and moments, $m_1, m_2, \dots, m_n$, see Eq.4-4. Linear SHELL181 elements are used in shell FEA. The membrane, bending and structural stress along the x'-direction are calculated as shown by Eq.4-5.

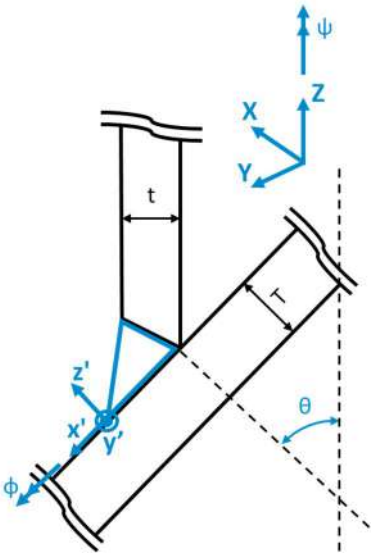


*Figure 71: Local weld CSYS tubular joint*

$$\{F_{x'y'z'}\} = \begin{bmatrix} 1 & 0 & 0 \\ 0 & \cos(\phi) & \sin(\phi) \\ 0 & -\sin(\phi) & \cos(\phi) \end{bmatrix} \begin{bmatrix} \cos(\theta) & 0 & -\sin(\theta) \\ 0 & 1 & 0 \\ \sin(\theta) & 0 & \cos(\theta) \end{bmatrix} \begin{bmatrix} \cos(\psi) & sin(\psi) & 0 \\ -\sin(\psi) & \cos(\psi) & 0 \\ 0 & 0 & 1 \end{bmatrix} \{F_{XYZ}\} \qquad \text{Eq.4-3}$$

$$\begin{Bmatrix} F_1 \\ F_2 \\ F_3 \\ \vdots \\ F_n \end{Bmatrix} = \begin{bmatrix} \frac{l_1}{3} & \frac{l_1}{6} & 0 & 0 & 0 & \cdots & 0 \\ \frac{l_1}{6} & \frac{l_1 + l_2}{3} & \frac{l_2}{6} & 0 & 0 & \cdots & 0 \\ 0 & \frac{l_2}{6} & \frac{l_2 + l_3}{3} & \frac{l_3}{6} & 0 & \cdots & 0 \\ 0 & 0 & \ddots & \ddots & \ddots & \ddots & 0 \\ \vdots & \ddots & \ddots & \ddots & \frac{l_{n-2}}{6} & \frac{l_{n-2} + l_{n-1}}{3} & \frac{l_{n-1}}{6} \\ 0 & \cdots & \cdots & \cdots & 0 & \frac{l_{n-1}}{6} & \frac{l_{n-1}}{3} \end{bmatrix} \begin{Bmatrix} f_1 \\ f_2 \\ f_3 \\ \vdots \\ f_n \end{Bmatrix} \quad \text{Eq.4-4}$$

$$\sigma_s = \sigma_m + \sigma_b = \frac{f_{x'}}{T} + \frac{6m_{y'}}{T^2} \quad \text{Eq.4-5}$$

The specimen mode-I stress distributions along the circumference are shown in Figure 73. The stress distribution is plotted as a SCF, therefore ratio between stress and nominal stress, i.e. $\frac{\sigma}{\sigma_{nom}}$. The structural hot spot SCF's, defined as $\frac{\sigma_s}{\sigma_{nom}}$, are comparable to the measured hot spot SCF's reported in Table 35, although the shell FEA is an approximation of the fatigue test and both SCF's are obtained by different methods. Figure 73 shows some bumpy stress distributions along the circumference due to uneven shaped mesh (quad to triangle-shaped), resulting in bumpy nodal forces and moments and element angles.

Specimens 1 to 3 have symmetric geometry and boundary conditions with respect to the xz-plane, therefore only the stress distribution around half the circumference is plotted. Specimen 4, which is the multiplanar X-joint shown in Figure 63, is nonsymmetric in geometry, therefore the stress distribution of the full circumference is reported. Figure 72 presents the maximum principal stress of the axial loaded CHS X-joint with scaled deformation. Due to the horizontal brace located on one side of the chord, the stiffness on that side is larger, therefore ovality is smaller, resulting in smaller local bending moments and therefore SCF compared to the other side. The SHS T-joint is loaded by two different non-proportional in-phase AF, IPB and OPB during the fatigue test, therefore two different stress distributions are present. Maximum SCF's occur at the corners of the SHS T-joint for both load cases.

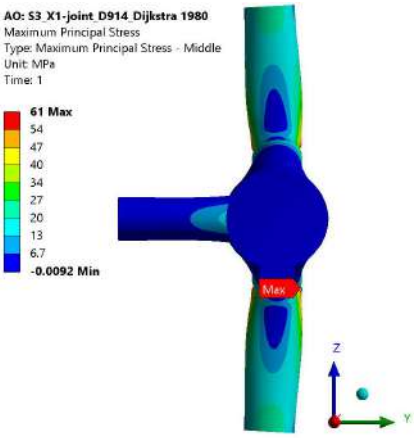


*Figure 72: Maximum principal stress plot tubular CHS X-joint*

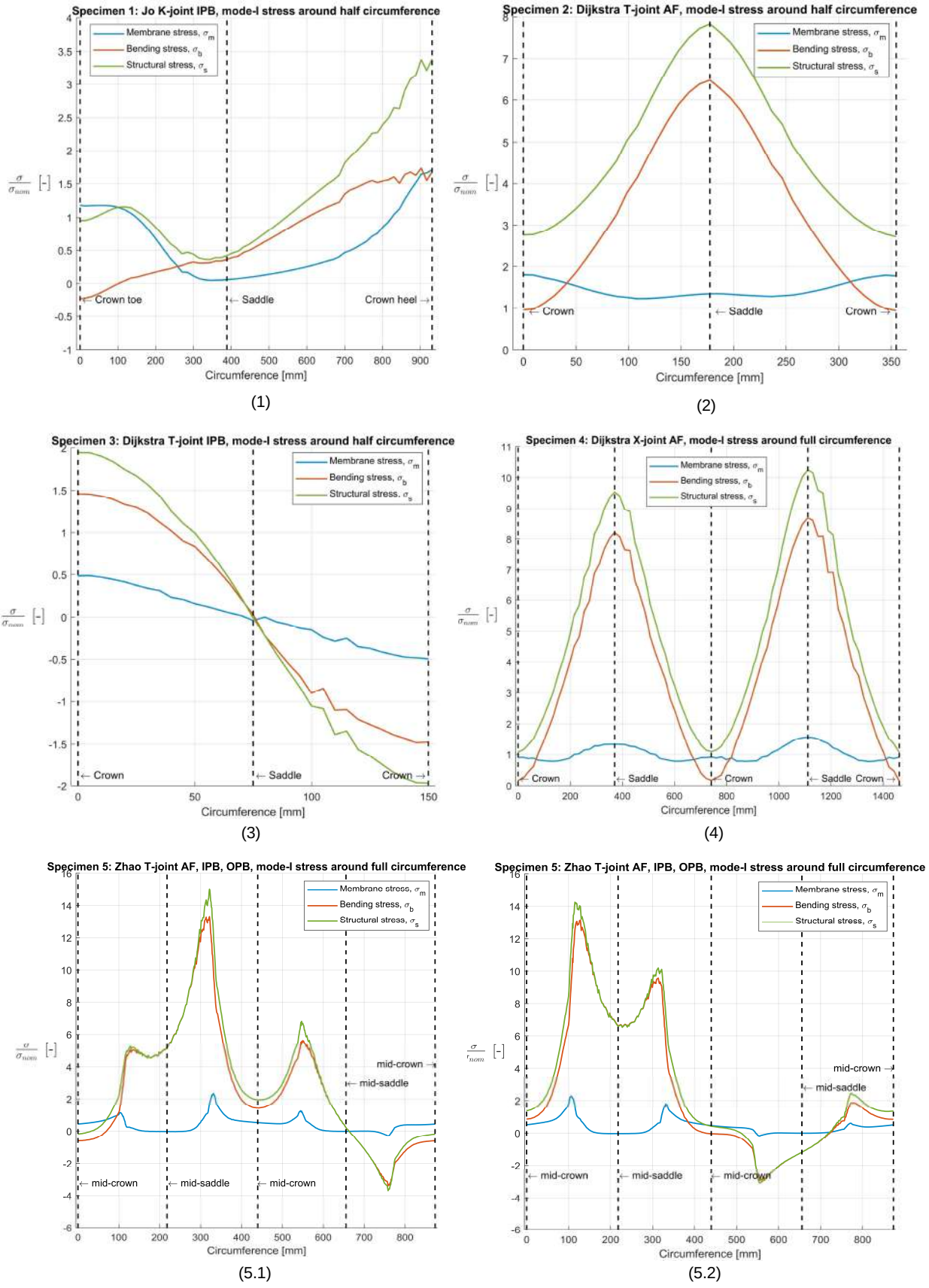


*Figure 73: Mode-I stress distributions specimen 1, 2, 3, 4, 5.1 (load case 1) and 5.2 (load case 2)*

Since nodal forces and moments are used to determine the structural stress distribution, results are more invariant to mesh specifications compared to stresses directly derived from FEA, also demonstrated by P. Dong [49]. For example, the structural stress at the saddle for an axial loaded T-joint varied 53.7 MPa to 53.6 MPa for 25 mm and 10 mm element sizes, respectively. The shell FEA of tubular CHS were therefore meshed coarse with element sizes of around T/1.6, see Figure 74. However, this not applies to the tubular SHS specimen of Zhao due to the small corner radius shown in Figure 74, where element size is T/15. Coarser meshed models of the tubular SHS specimen result in similar structural stress magnitudes compared to the fine mesh, however show unsmooth stress distributions around the circumference.

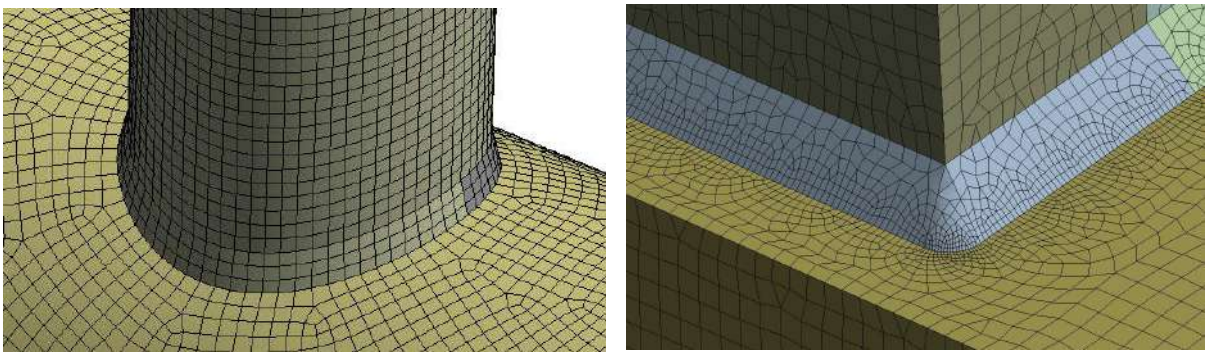

*Figure 74: Mesh shell FEA Dijkstra CHS T-joint (left) and Zhao SHS T-joint (right)*

### 4.4.2 Finite element stress differences with and without weld modelling

Differences are observed in membrane and bending stress between shell FEA with and without weld geometry. Specifically, shell FEA without weld overestimates bending stresses compared to results of volume FEA which includes the weld geometry. Chord nodal forces and moments of the shell FEA without weld are obtained at the intersection between brace and chord surface. The volume FEA are discussed in 4.5.1, where membrane and bending stress are obtained by stress linearisation in the thickness direction of the chord. The membrane and bending stress of the volume and shell FEA is reported in Table 36. The relative difference reported in Table 36 is calculated as follows: $\Delta_{rel} = \frac{\sigma_{shell} - \sigma_{volume}}{\sigma_{volume}}$. The load cases and length of the extended weld section with respect to brace wall thickness is also reported. The relative differences conclude that relative large weld dimensions affects local bending moments at the weld toe significantly. Loading type does not seem to affect results much. Moreover, including weld geometry in the shell FEA results in more accurate membrane and bending stresses and therefore better fit of the structural field stress distribution. The influence of weld geometry is similar for coarser meshed tubular joints, since mesh insensitive nodal forces and moments are used.

*Table 36: Membrane and bending stress differences tubular joint FEA with and without weld*

| # | $l_e$ | Load case | Location | Volume FEA | | Shell FEA | | | | | | | |
|---|---|---|---|---|---|---|---|---|---|---|---|---|---|
| | | | | With weld | | Without weld | | | | With weld | | | |
| | | | | $\sigma_m$ | $\sigma_b$ | $\sigma_m$ | | $\sigma_b$ | | $\sigma_m$ | | $\sigma_b$ | |
| | | | | [MPa] | [MPa] | [MPa] | $\Delta_{rel}$ | [MPa] | $\Delta_{rel}$ | [MPa] | $\Delta_{rel}$ | [MPa] | $\Delta_{rel}$ |
| 1 | $t/4$ | AF = 392 kN | Crown heel | 71 | 72 | 69 | -3% | 71 | -1% | 72 | 0% | 70 | -2% |
| 2 | $t/1.5$ | AF = 160 kN | Saddle | 36 | 201 | 41 | 12% | 223 | 11% | 40 | 10% | 190 | -5% |
| 3 | | IPB = 4.5 kNm | Crown | 119 | 413 | 125 | 5% | 502 | 22% | 123 | 3% | 368 | -11% |
| 4 | | AF = 390 kN | Saddle | 26 | 165 | 28 | 9% | 179 | 8% | 28 | 7% | 154 | -7% |
| 5 | $t$ | FA: 120 kN<br>IPB: 4 kN<br>OPB: 4 kN | Corner | 17 | 536 | 16 | -6% | 863 | 61% | 20 | 18% | 561 | 5% |
| | | FA: 70 kN<br>IPB: 1 kN<br>OPB: 3.6 kN | Corner | 57 | 302 | 22 | -61% | 929 | 208% | 48 | -16% | 351 | 16% |

To illustrate the effect of including weld geometry, an clockwise IPB loaded T-joint is sketched in Figure 75. The arrows in blue represent nodal forces, $F$, and nodal moments, $M$. The left brace surface is in tensile, while the right brace surface is in compression. Reported in Table 36, including the weld geometry results in lower membrane and bending stress and therefore lower nodal forces and moments.

For the shell model with weld geometry included, forces are divided among the brace surface and weld surface, which explains the lower membrane and bending stress at the chord weld toe. For increasing weld geometry relative to brace wall thickness, weld surface thickness and therefore stiffness increases as well. Resulting in larger chord nodal forces and moments at the weld and chord interface. However, since $l_e$ increases, weld notch angle, $2\alpha$, decreases, which lowers the chord nodal moments since the weld nodal force direction is more aligned with the chord surface.

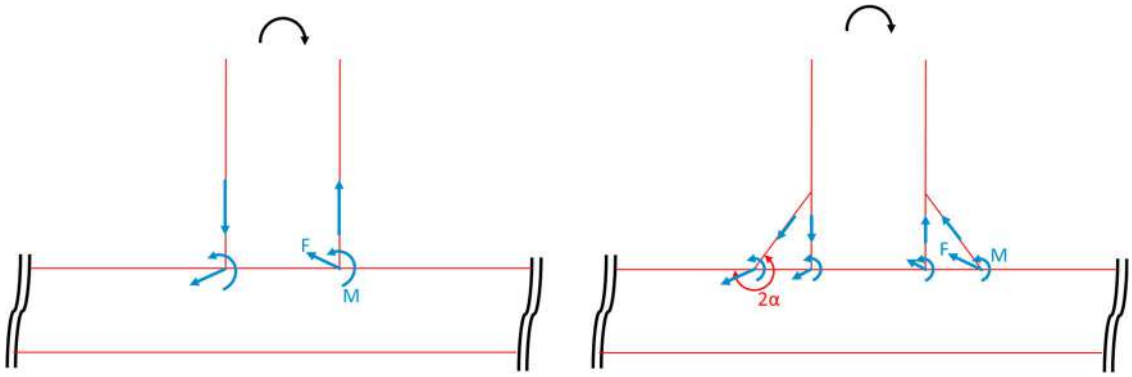


*Figure 75: Nodal force and moment differences shell FEA without (left) and with weld (right)*

Shown by Table 36, relative differences of the tubular SHS T-joint are most significant. This is partly related to the relative large weld size, but also due to the brace that is close to the chord web shown by Figure 76. Figure 76 illustrates including weld geometry results in a closer location of the hot spot to the chord web, therefore a more continuous global stress flow is present. Thus, lower local bending moments occur at the chord weld toe and explains bending stress differences are more significant for the tubular SHS T-joint.

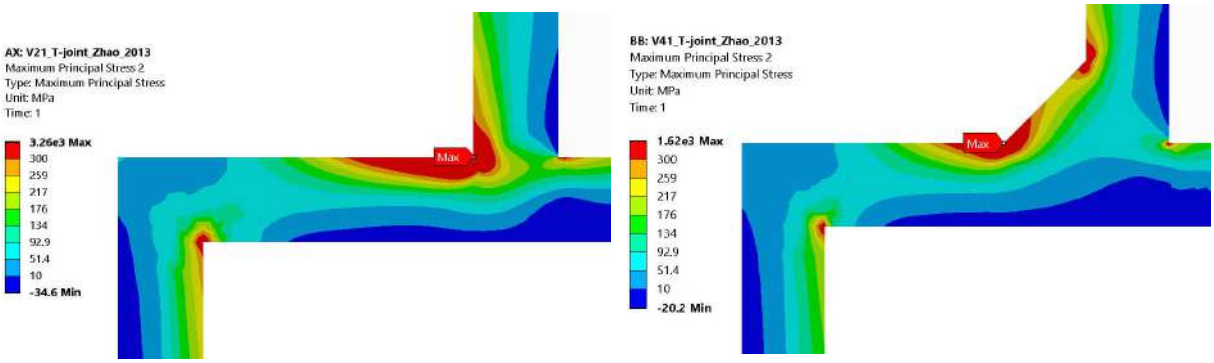


*Figure 76: Maximum principal stress plot volume FEA tubular SHS T-joint without (left) and with weld geometry (right)*

The effect of including weld geometry for tubular joints may be higher compared to planar joints due to geometric and loading differences. For example, a planar double sided (DS) T-joint and cruciform joint are normally loaded at the horizontal base plate by mode-I loading, perpendicular to the attached plating. Mode-I loading at the horizontal base plate can be solely AF or OPB, shown in Figure 77, or a combination of both. Since the attached plate stiffness in loading direction is low, the base plate stress distribution is not affected much. Hence, the minor influence of weld geometry in FEA.

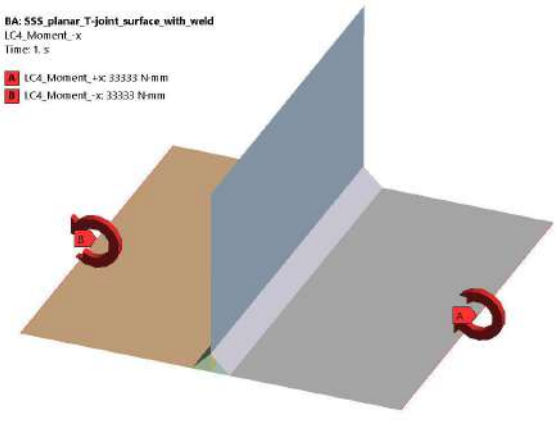


*Figure 77: Shell FEA planar DS T-joint, base plate loaded by OPB*

To demonstrate the differences, a planar DS T-joint is studied in FEA by a volume model including weld geometry and a surface model with and without weld geometry. Plate thicknesses of the base and attached plate are both 20 mm and weld height and length are both 15 mm. Weld geometry for the surface model is modelled as shown in Figure 68 [42]. In Table 37 the membrane and bending stress of the different FEA is reported, where $\Delta_{rel} = \frac{\sigma_{shell} - \sigma_{volume}}{\sigma_{volume}}$. When the attachment is loaded by AF or OPB, neglecting weld geometry in shell FEA results in the largest relative differences compared to volume FEA. Including weld geometry results in more accurate stresses, similar as for tubular joints. No significant differences are observed when the base plate is loaded, thus demonstrates weld geometry is neglectable for common load cases of planar joints.

*Table 37: Membrane and bending stress differences planar DS T-joint FEA with and without weld*

| Load case | Volume FEA | | Shell FEA | | | | | | | |
|---|---|---|---|---|---|---|---|---|---|---|
| | With weld | | Without weld | | | | With weld | | | |
| | $\sigma_m$ | $\sigma_b$ | $\sigma_m$ | | $\sigma_b$ | | $\sigma_m$ | | $\sigma_b$ | |
| | [MPa] | [MPa] | [MPa] | $\Delta_{rel}$ | [MPa] | $\Delta_{rel}$ | [MPa] | $\Delta_{rel}$ | [MPa] | $\Delta_{rel}$ |
| AF, attachment | ≈0 | 34.7 | ≈0 | 0% | 39 | 11% | ≈0 | 0% | 34.5 | -0.3% |
| OPB, attachment | ≈0 | -0.47 | ≈0 | 0% | -0.52 | 11% | ≈0 | 0% | -0.46 | -0.3% |
| AF, base plate | 1.04 | ≈0 | 1.03 | -0.5% | ≈0 | 0% | 1.03 | -0.5% | ≈0 | 0% |
| OPB, base plate | ≈0 | 1.04 | ≈0 | 0% | 1.04 | 0.6% | ≈0 | 0% | 1.03 | -0.3% |

Moreover, load paths of planar joints in offshore and marine structures can be more continuous compared to tubular joints. For example, a DS cruciform joint connecting longitudinal stiffeners to a web frame has a more continuous load path. Since loading of one longitudinal stiffener is directly transferred to the other. Loading of a tubular brace is directed into the chord, resulting in large local bending moments, which are more dependent on weld geometry.

## 4.5 Weld toe notch stress distribution

Weld geometries introduce notches at the weld toes, also illustrated by the sketched self-equilibrating stress in Figure 66. The mode-I weld toe notch stress distributions of the LSS tubular joints are presented in this chapter by volume FEA and a semi-analytical formulation based on the shell FEA structural stress.

### 4.5.1 Volume FEA

Solid models of the specimens with identical global dimensions as specified in the fatigue reports are modelled as shown in Figure 63. The weld geometry is included in all models as illustrated in Figure 78, taking the Jo K-joint and Dijkstra T-joint as example. Similar to the surface models, emphasises is put on modelling the weld geometry accurately at the location of failure and weld height is kept constant. Since this results in geometry less likely to be problematic for meshing in ANSYS. In APPENDIX E, the specimen's boundary conditions, geometry details and FEA modelling interpretations are reported.

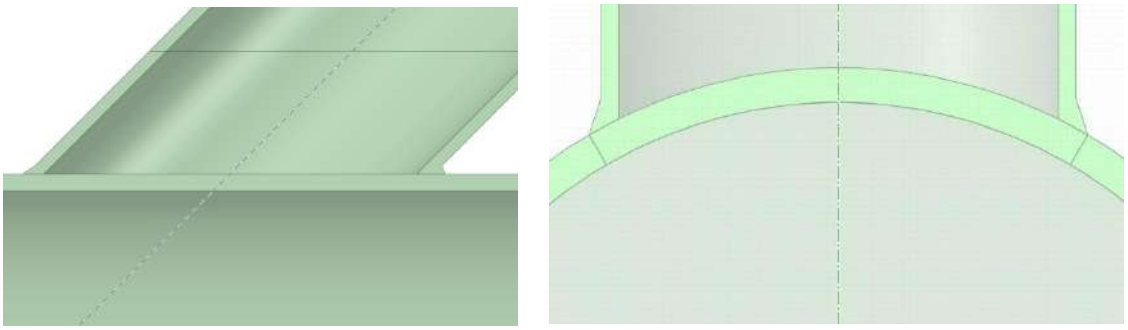

*Figure 78: Solid model tubular K-joint at centreline, specimen 1 (left), and T-joint at saddle location, specimen 2 (right)*

Other than the purple bodies shown in Figure 79(a), the solid models are meshed relatively coarse, also displayed in Figure 79(a) and Figure 79(b). For all specimens, the minimum mesh size of the purple bodies is equal to around $T/2$. To accurately derive the weld toe notch stress distribution and to keep computational costs to a minimum, sphere of influences are applied at the crown toe, saddle and crown heel locations shown in red in Figure 79(a). A sphere of influence enables bodies to be meshed according to a specified element size within a specified sphere radius. Therefore, mesh can be refined at locations of interest to capture the notch stress. Element size at the weld toe are refined smaller than $e = T/30$ for all volume FEA. Figure 81 demonstrates most stress results are converged for multiple element sizes, $e$. This is with exception of the saddle of specimen 1 and specimen 3, however these locations are not critical with respect to the failure location. Another method to determine the convergence of results is to plot the unaveraged stress between elements as shown in Figure 80. The contour lines show smooth transitions of stress magnitudes, therefore concludes mesh refinement is sufficient. If meshed too coarse, the unaveraged stress between elements would result in a uneven and discontinuous stress plot.

Shown by the coloured lines and legends in Figure 81, different weld geometries are analysed. The orange lines represent the stress distributions related to the weld geometry as specified by the authors, see APPENDIX E. Groove angle, $\delta$, therefore weld height, $h_w$, does not seem to affect the stress distribution as much compared to the length of the extended weld section, $l_e$, therefore weld leg length, $l_w$. This was also observed by Y. Qin [50] when comparing different weld geometries. The location 1 mm below the weld toe is plotted as a dashed line, demonstrating the stress 1 mm below the weld toe of most tubular joints is located in the nonlinear notch effected region. The single point criterion to derive the hot spot stress 1 mm below the weld toe developed by Xiao and Yamada [43] for planar joints is therefore not applicable. Moreover, varying weld geometry, shown in Figure 81(1) and (4), affects stress magnitudes 1 mm below the weld toe, whereas the affecting range of weld geometries of planar joints is localised above the 1 mm, concluded by Xiao and Yamada. A single point criterion $0.1T$ below the weld toe is more appropriate, since the stress distribution linearises below this point for most tubular joints.

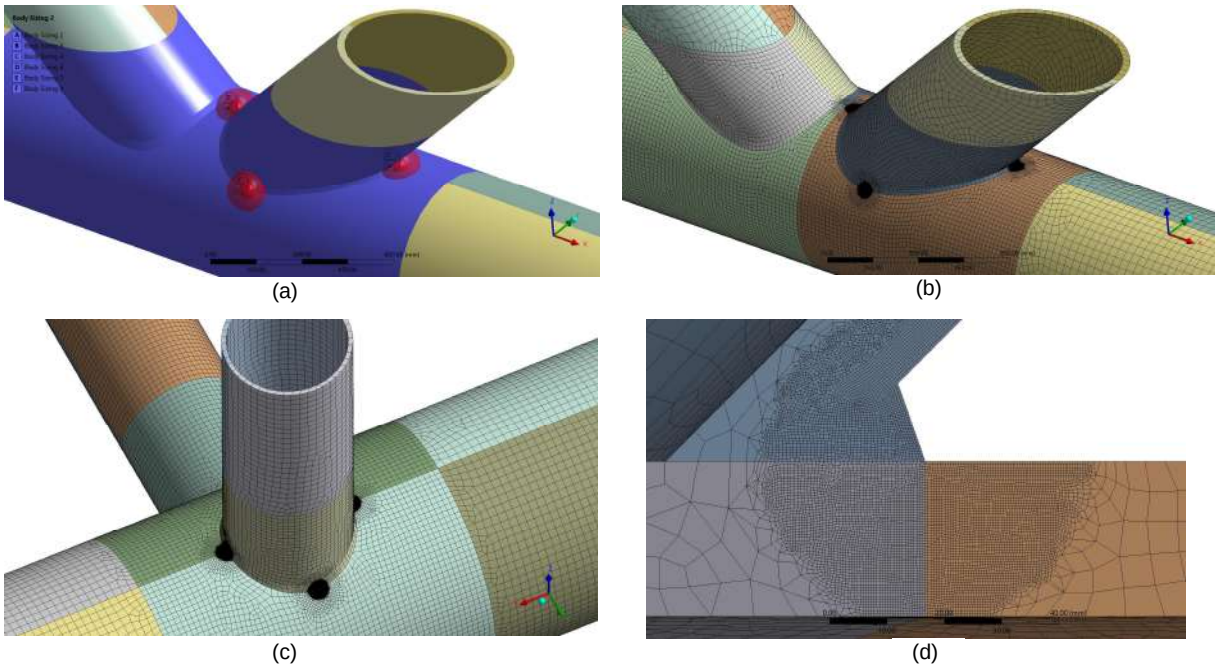


*Figure 79: Sphere of influences in K-joint (a), overall mesh display of K-joint (b) and X-joint (c), mesh display at crown heel K-joint (d)*

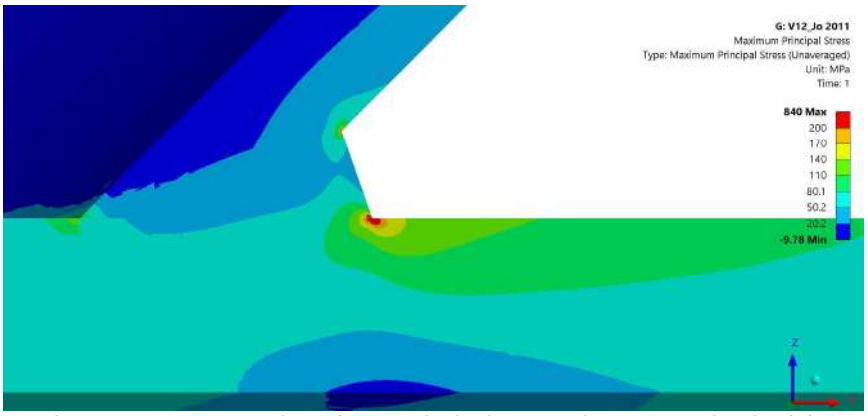


*Figure 80: Unaveraged maximum principal stress plot at crown heel K-joint*

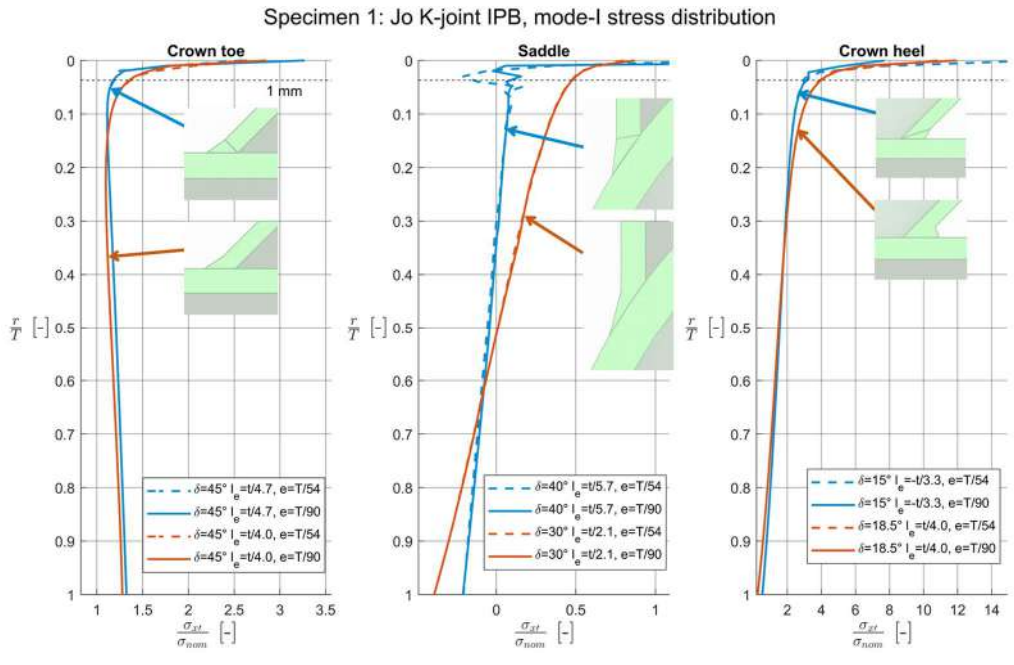


(1)

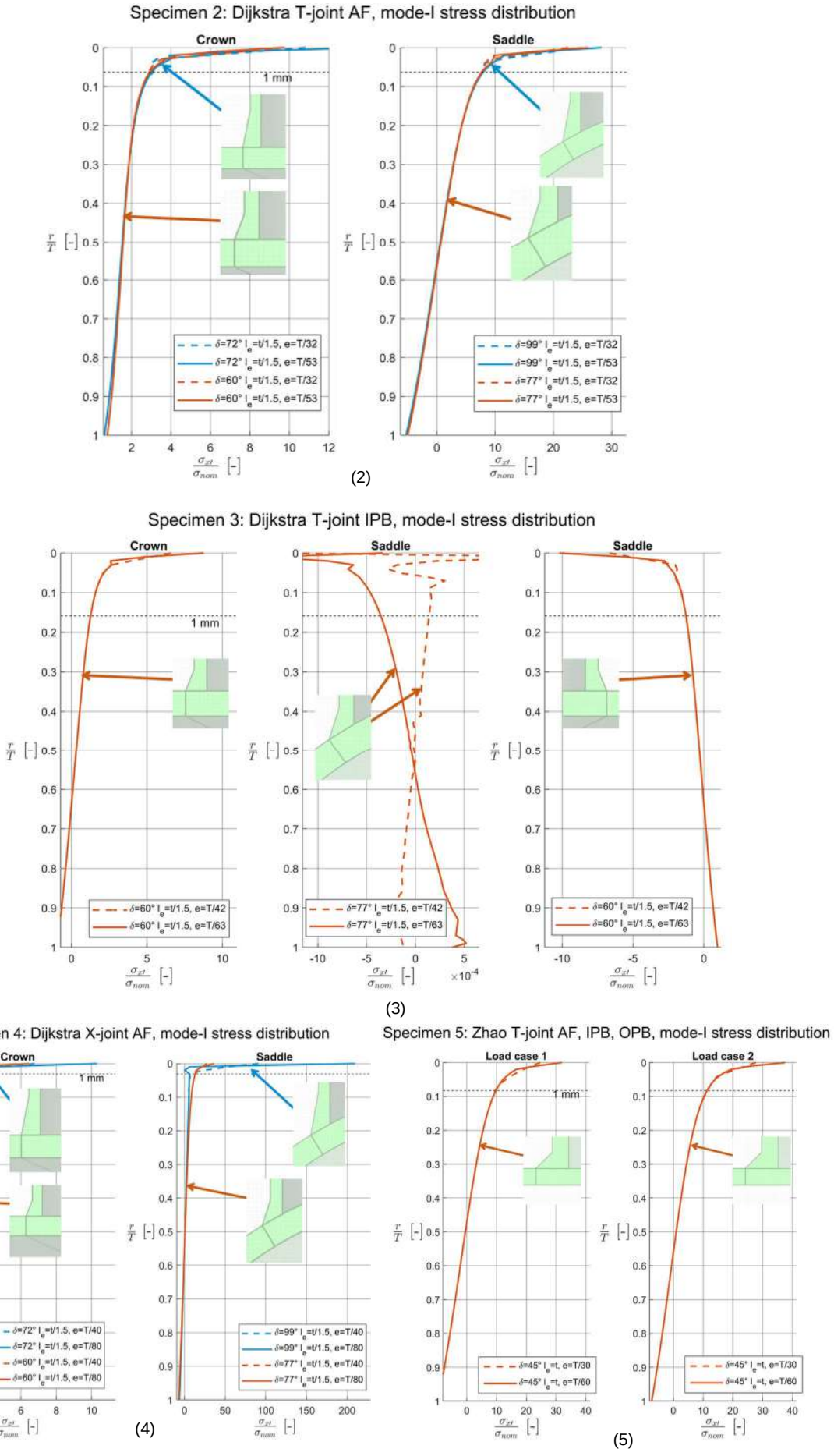


*Figure 81: Mode-I weld toe notch stress distributions specimen (1), (2), (3), (4) and (5)*

SCF's calculated by volume FEA through the hot spot methods mentioned in Chapter 4.3 are reported in Table 38. Most authors calculated SCF's by FEA or parametric formulas as well, which are also summarised in Table 38. Compared to the measured hot spot SCF's reported by the authors, surface extrapolation SCF's show good correspondence, as relative differences are within 11%. Extracting structural stresses through stress linearisation result in relative high SCF's. Concluded in previous paragraph, adopting the 1 mm stress below the weld toe as single point criterion, results in an overestimation of most SCF's, since stress 1 mm below the weld toe of most tubular joints is located in the nonlinear notch effected region. The suggested $0.1T$ point below the weld toe results in similar SCF's compared to the measured SCF's.

*Table 38: Hot spot SCF's*

| # | Location | Measured by authors | Calculated by authors | Volume FEA | | | |
|---|---|---|---|---|---|---|---|
| | | | | Stress linearisation | Surface extrapolation | Single point criterion | |
| | | | | | | 1 mm | 0.1T |
| 1 | Crown heel | 2.74 - 2.96[a] | 2.68 | 3.41 | 3.27[a] | 3.96 | 2.87 |
| 2 | Saddle | 6.70[b] | 6.25-6.66 | 8.05 | 7.41[b] | 7.68 | 6.35 |
| 3 | Crown | 1.10[c] | 1.60-2.09 | 2.07 | 1.77[c] | 1.26 | 1.59 |
| 4 | Saddle | 11.2[b] | 9.59 | 10.8 | 9.96[b] | 13.4 | 8.46 |
| 5 | Corner, load case 1<br>Corner, load case 2 | 11.0[d]<br>11.6[d] | - | 11.4<br>12.8 | 11.3[d]<br>11.6[d] | 12.2<br>11.3 | 11.1<br>10.3 |

[a] *Linear surface extrapolation at 0.37T and 1.30T*
[b] *Linear surface extrapolation at* $0.2\sqrt{rt}$ *and* $0.2\sqrt{rt}$ + 5°
[c] *Linear surface extrapolation at* 4 $mm$ *and* $0.5\sqrt{RT}$
[d] *Nonlinear surface extrapolation at 0.4T, 0.9T and 1.4T, measured SCF's not reported by authors, therefore manually calculated*

Above findings regarding hot spot SCF's do not apply to specimen 3, where the author measured a SCF of 1.10 at the crown. Calculated volume FEA SCF's by stress linearisation and surface extrapolation are calculated as 2.07 and 1.77, respectively. SCF's calculated by the authors, ranged from 1.60 to 2.09, are similar to the volume FEA SCF's. Since these specimens are loaded by relatively high IPB magnitudes, resulting in relatively high nominal stresses, FEA is performed with bilinear material properties. Geometric nonlinearity is accounted for in this analysis, i.e. stiffness is affected by deformations. Through this analysis, strain and stress results are analysed to check if yielding occurs at the extrapolation points. The material specification for specimen 3 is reported as BS4350 Grade 50C, which should have a yield strength of 355 MPa. The tangent modulus for the analysis is calculated as $E_t = \frac{\sigma_{UTS}-\sigma_{yield}}{\varepsilon_{UTS}-\varepsilon_{yield}}$, using mechanical properties as specified in [51]. Figure 82 demonstrates no yielding occurs at the extrapolation points, therefore measured SCF's are not affected by yielding of the material. Shown on the right of Figure 82, yielding occurs 2 mm before the weld toe. Calculating the SCF by $\sigma_{x'}$ and $\sigma_{hs} = \frac{E}{1-\nu^2}(\varepsilon_{x'} + \nu\varepsilon_{y'})$, as specified by the authors, results in SCF's of 1.71 and 1.79, respectively. The strain concentration factor (SNCF), reported by the authors as 1.2, has better correspondence for both volume analysis with linear, SNCF=1.30, and bilinear, SNCF=1.31, material properties. Discarding geometric nonlinearly does not affect results. The FEA with bilinear materials does not clarify the differences in SCF's. Since the SCF's calculated by the authors are similar to the volume FEA SCF's, a measurement fault is possible. Moreover, the first extrapolation point is only 4 mm away from the weld toe. This extrapolation point, located at a relative small distance from the weld toe, is difficult to install precisely, therefore is prone to measurement errors. However, above possibilities are difficult to verify.

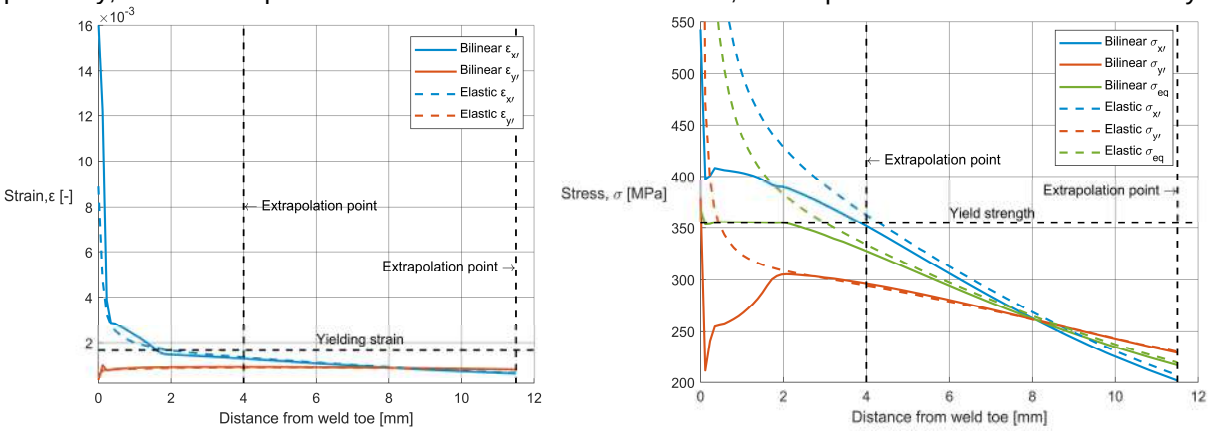


*Figure 82: Surface strain (left) and surface stress (right) perpendicular to crown weld toe bilinear volume FEA*

### 4.5.2 Semi-analytical weld toe notch stress distribution

The semi-analytical weld toe notch stress formulation, derived by H. den Besten [4], is shown in Eq.4-6 for a nonsymmetric joint with respect to $T/2$. This equation describes the mode-I stress as a superposition of the self-equilibrating stress and structural field stress using $\sigma_s$ from the shell FEA with weld. See Figure 66 for stress definitions. The self-equilibrating stress consists of the V-shaped notch stress, $\sigma_{\theta\theta}$, and the weld load carrying stress, $\sigma_{bw}$. The V-shaped notch stress is singular for $r = 0$, since it is derived for $\rho = 0$, and is dependent on $\alpha$ as weld geometry parameter. $\lambda_s$ and $\lambda_a$ are eigenvalues solved for boundary conditions the notch stress must adhere. $\chi_s$ and $\chi_a$ are the eigenvalue coefficients related to the eigenvalues. The stress angle, $\beta$, is defined as $\beta = \alpha - \frac{\pi}{2}$. The presence of the weld results in a shift of the neutral axis that introduces bending stress at the weld toe, which $\sigma_{bw}$ simulates. A larger weld carrying level of the joint, results in a larger bending stress as sketched in Figure 66. The weld load carrying coefficient, $C_{bw}$, can be derived by beam FEA and is dependent on weld geometry and loading conditions. In this study, $C_{bw}$ is determined by parametric equations derived by Y. Qin et al. [50], based on curve fitted beam FEA results of double sided planar T-joints. The last part of the weld toe notch stress formulation describes the structural field stress distribution, also shown in Eq.4-8. $r_s$ is defined as the ratio between bending and structural stress, i.e. $r_s = \frac{\sigma_b}{\sigma_s}$.

$$\sigma_n\left(\frac{r}{T}\right) = \sigma_s\Bigg[\underbrace{\left(\frac{r}{T}\right)^{\lambda_s-1}\mu_s\lambda_s(\lambda_s+1)[\cos\{(\lambda_s+1)\beta\}-\chi_s\cos\{(\lambda_s-1)\beta\}] + \left(\frac{r}{T}\right)^{\lambda_a-1}\mu_a\lambda_a(\lambda_a+1)[\sin\{(\lambda_a+1)\beta\}-\chi_a\sin\{(\lambda_a-1)\beta\}]}_{\sigma_{\theta\theta}} + \underbrace{C_{bw}\left\{2\left(\frac{r}{T}\right)-1\right\}}_{\sigma_{bw}} - \underbrace{2r_s\left(\frac{r}{T}\right)}_{\sigma_f}\Bigg] \quad \text{Eq.4-6}$$

$$\sigma_{se}\left(\frac{r}{T}\right) = \sigma_n\left(\frac{r}{T}\right) - \sigma_f\left(\frac{r}{T}\right) \quad \text{Eq.4-7}$$

$$\sigma_f\left(\frac{r}{T}\right) = \sigma_s\left[1 - 2r_s\left(\frac{r}{T}\right)\right] \quad \text{Eq.4-8}$$

The mode-I weld toe notch stress distributions derived by the semi-analytical formulation and volume FEA are shown in Figure 83. The maximum $\sigma_s$ is taken for specimen 1 to 4 and specimen 5 loaded by load case 2. $\sigma_s$ of specimen 5 loaded by load case 1 is taken at the initiation point specified by the authors, see APPENDIX E. This initiation point is located 20 mm from the corner where maximum stress occurs. The stress distributions are presented as dimensionless stress, taking the structural stress of the shell FEA to divide the stress components. The self-equilibrating and structural field stress are extracted from volume FEA by stress linearisation in the chord thickness direction. The stress distributions obtained by the two different methods show good agreement, therefore confirms the weld toe notch stress distribution calculation as explained above. However, the saddle stress distributions of specimen 3 demonstrates dissimilar results, as the shell FEA calculates membrane and bending stress of about 10 MPa at this location, while the volume FEA structural field stress is almost zero. Since the saddle stress for IPB loading is small, demonstrated by Figure 73, this location is not of importance.

Figure 83(1) illustrates the K-joint stress distributions are dominated by the structural field stress for the crown toe, saddle and crown heel locations, since the self-equilibrating stress is virtually zero below $r/T = 0.1$. For the Dijkstra and Zhao specimens, where weld geometry is larger with respect to brace wall thickness, $l_e = t/1.5$ and $l_e = t$ respectively, the notch affected region increases to $r/T = 0.2$. Below $r/T = 0.2$, the stress distribution is mainly linear and therefore mostly defined by the structural field stress.

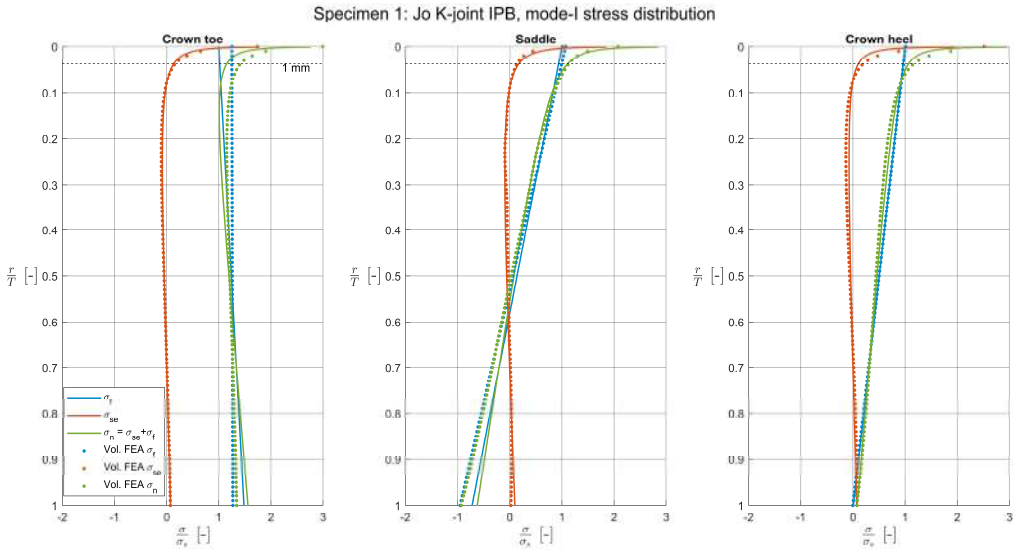
Specimen 1: Jo K-joint IPB, mode-I stress distribution
Crown toe
Saddle
Crown heel
1 mm
Vol. FEA σf
Vol. FEA σsb
Vol. FEA σn

(1)

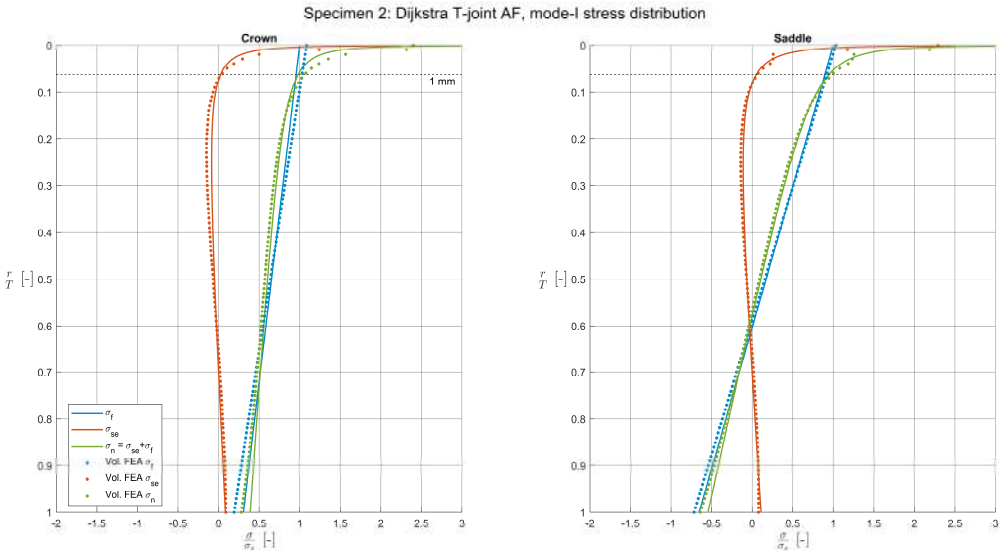
Specimen 2: Dijkstra T-joint AF, mode-I stress distribution
Crown
Saddle
1 mm
Vol. FEA σf
Vol. FEA σse
Vol. FEA σn

(2)

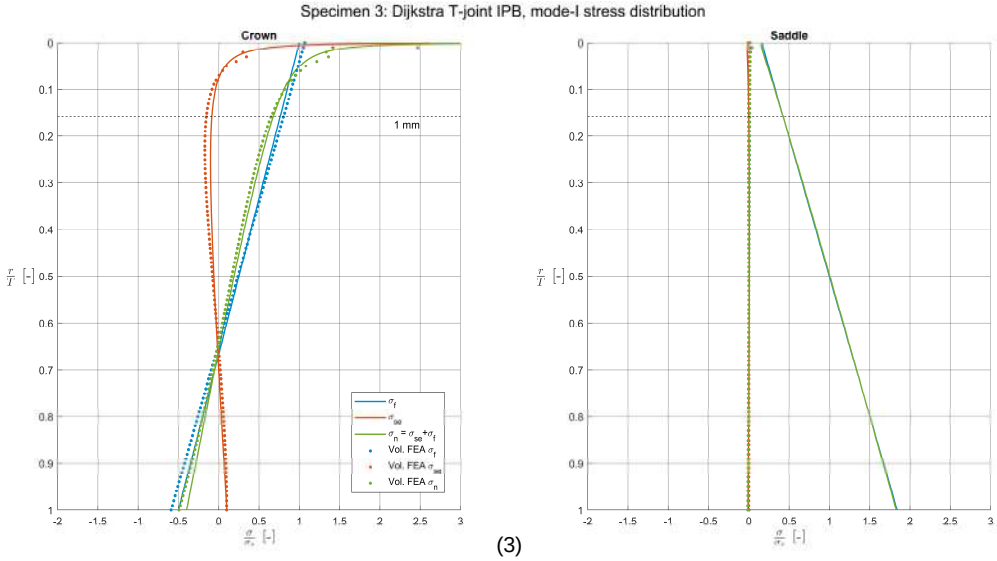


(3)

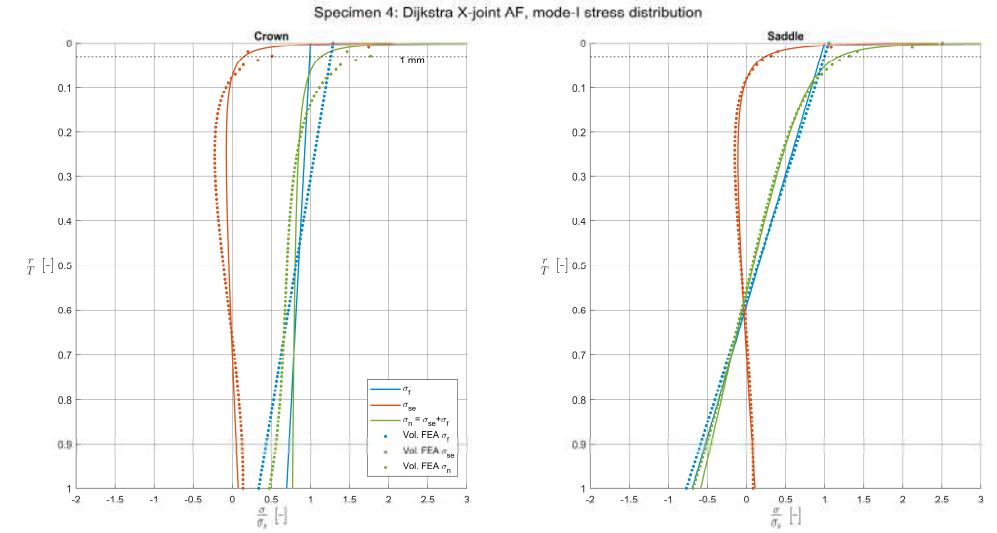


(4)

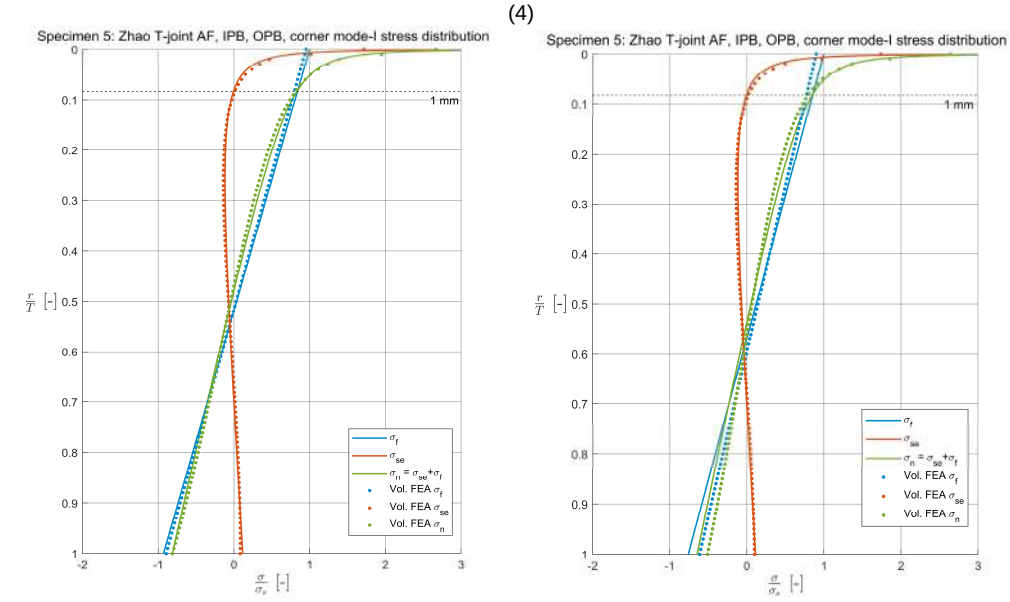


(5.1) (5.2)

*Figure 83: Mode-I weld toe notch stress distributions of specimen 1, 2, 3, 4, 5.1 (load case 1) and 5.2 (load case 2)*

## 4.6 Effective notch stress fatigue resistance

The effective notch stress is normally obtained by modelling an effective notch radius at the location of interest for FEA. The weld notch stress is therefore a fictitious stress, assuming linear elastic material behaviour. Based on similarity between FEA and fatigue resistance data, an effective notch radius of 1.0 mm leads to consistent results, as concluded by IWW [52] and DNV-GL [39]. K. Rother et al. [53] propose smaller radii, such as 0.05 mm and 0.3 mm for plate thicknesses smaller than 5 mm. Since the geometry and loading & response is more accurately described with respect to the actual structural detail compared to the hot spot stress concept, the number of S-N curves is reduced to one; the FAT225 suggested by IWW and DNV-GL for structural steels.

Another approach is to implement the weld toe notch stress distribution formulation as formulated by Eq.4-6. By integrating the stress distribution from weld toe to the material characteristic length, $\rho^*$, and by dividing it by $\rho^*$, an averaged effective notch stress from $r = 0$ to $r = \rho^*$ is obtained as derived by Y. Qin et al. [50], see Eq.4-9. Values of $\rho^* = 1.14$ and $\gamma = 0.92$ are adopted based on most likely estimates calculated by Y. Qin et al. for SSS planar joints. It is therefore assumed that these values apply to LSS tubular joints as well to result in minimal variance of fatigue resistance data. The average effective notch stress is converted to stress ranges as formulated by Eq.4-10, where $\Delta_{load}$ and $F_{FEA}$ are the fatigue test load range and reference loading applied in FEA, respectively. Similar to the hot spot stress fatigue resistance, Walker's mean stress correction is applied to account for the mean stress effect.

$$\sigma_e = \frac{1}{\rho^*}\int_0^{\rho^*} \sigma_n(r)dr$$

$$= \sigma_s\left(\frac{T}{\rho^*}\right)\cdot\left\{\left(\frac{\rho^*}{T}\right)^{\lambda_s}\mu_s(\lambda_s+1)[\cos\{(\lambda_s+1)\beta\}-\chi_s\cos\{(\lambda_s-1)\beta\}]\right.$$
$$+\left(\frac{\rho^*}{T}\right)^{\lambda_a}\mu_a(\lambda_a+1)[\sin\{(\lambda_a+1)\beta\}-\chi_a\sin\{(\lambda_a-1)\beta\}]$$
$$\left.+\ C_{bw}\left\{\left(\frac{\rho^*}{T}\right)^2-\left(\frac{\rho^*}{T}\right)\right\}-r_s\left(\frac{\rho^*}{T}\right)^2\right\} \qquad \text{Eq.4-9}$$

$$S_{e,eff} = \frac{\Delta_{load}}{F_{FEA}}\cdot\frac{\sigma_e}{(1-r_{lr})^{1-\gamma}} \qquad \text{Eq.4-10}$$

The fatigue resistance defined as hot spot and average effective notch stress ranges are summarised in Table 39. In Figure 84 the average effective notch stress fatigue resistance of SSS planar joints and LSS tubular joints are plotted, demonstrating similarity between SSS planar joints and most LSS tubular joints. Average effective notch stress fatigue resistance data of SSS planar joints of Y. Qin et al. [47] were provided. The scatter of LSS tubular joint fatigue resistance is reduced compared to the hot spot fatigue resistance, since $T_{\sigma S_h} = 1{:}\,2.15$ and $T_{\sigma S_e} = 1{:}\,1.91$, see Table 40. Moreover, intercept $\log_{10}(C)$ differences are smaller, see Table 40 and Figure 85. In Figure 85 the probability density distributions are plotted for $\log_{10}(C)$, assuming a Gaussian distribution. Figure 85 demonstrates the average effective notch stress $\log_{10}(C)$ distributions are more narrow banded and $\log_{10}(C)$ offset is reduced. Demonstrating an increase in similarity for LSS tubular joints. Differences in slope $m$ are similar, therefore similarity between SSS planar joints and LSS tubular joints is comparable to that respect. C95LB and C95UB in Table 40 represent the upper and lower bounds of the 95% confidence intervals, respectively. More LSS tubular joints should be studied to demonstrate similarity with higher confidence. It is expected by including more LSS tubular joints, average effective notch stress similarity indicators, $T_{\sigma S}$, $\log_{10}(C)$ and $m$, converge to magnitudes similar to SSS planar joint fatigue resistance data.

*Table 39: Hot spot and average effective notch stress fatigue resistance*

| # | Joint type | Failure location | Measured hot spot stress range $S_{h,eff}$ [MPa] | Average effective notch stress range $S_{e,eff}$ [MPa] | Number of cycles to failure $N_f$ [-] |
|---|---|---|---|---|---|
| 1 | CHS K-joint | Chord weld toe, crown heel | 129<br>110<br>98 | 203<br>181<br>158 | 9.7E+5<br>1.3E+6<br>2.6E+6 |
| 2 | CHS T-joint | Chord weld toe, saddle | 189[(a)]<br>170[(a)]<br>170[(a)]<br>100[(a)]<br>189[(a)] | 306<br>276<br>276<br>163<br>306 | 6.8E+5<br>1.1E+6<br>8.4E+5<br>7.5E+6<br>7.6E+5 |
| 3 | CHS T-joint | Chord weld toe, crown heel | 297[(a)]<br>333[(a)]<br>233[(a)] | 425<br>478<br>335 | 3.3E+5<br>4.7E+5<br>1.5E+6 |
| 4 | CHS X-joint | Chord weld toe, saddle | 72[(a)]<br>190[(a)] | 115<br>298 | 2.0E+7<br>5.0E+5 |
| 5 | SHS T-joint | Chord weld toe | 535<br>325 | 708<br>487 | 4.2E+4<br>9.0E+4 |

[(a)] *Calculated as* $S_h = \frac{E}{1-\nu^2} \cdot S\varepsilon_{h,\perp}$

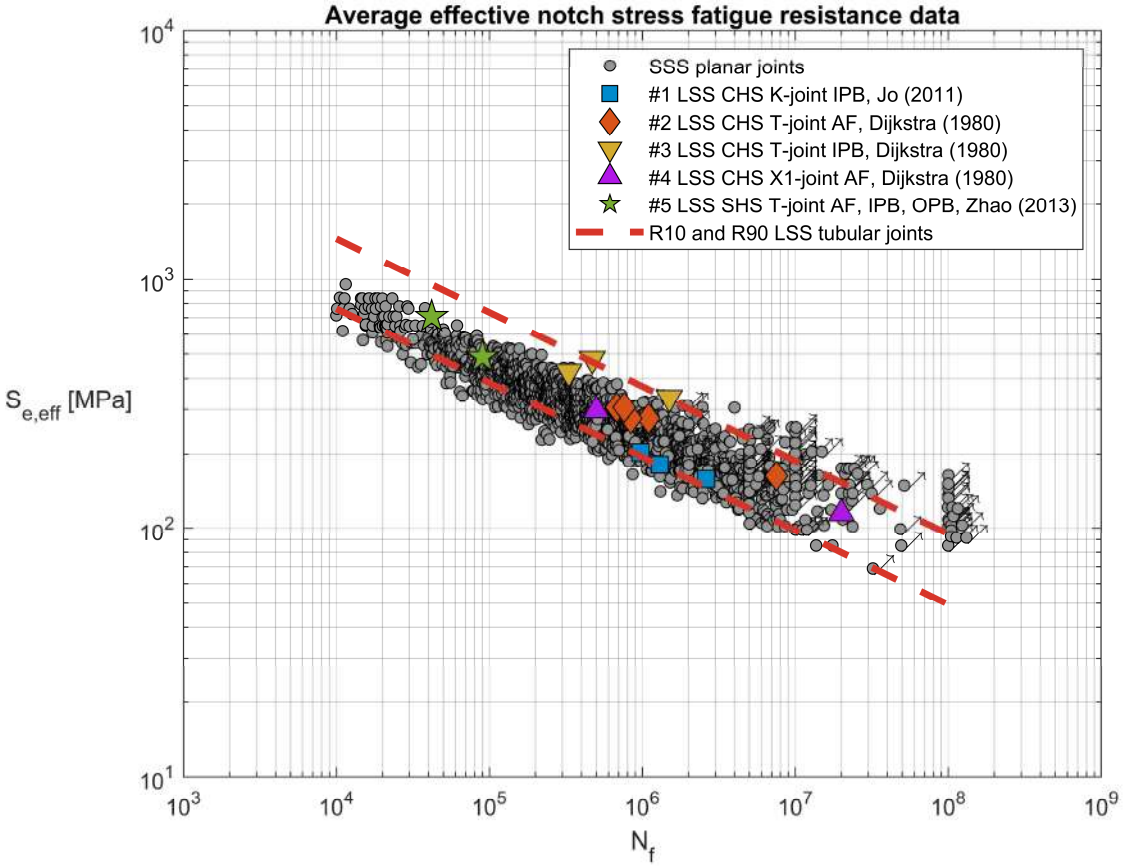


*Figure 84: Average effective notch stress fatigue resistance*

*Table 40: Fatigue resistance similarity comparison*

| Similarity indicator | Specimen | Hot spot stress concept | | | Average effective notch stress concept | | |
|---|---|---|---|---|---|---|---|
| | | C95LB | $\mu$ | C95UB | C95LB | $\mu$ | C95UB |
| $T_{\sigma s}$ | SSS planar joints<br>LSS tubular joints | - | 1 : 2.18<br>1 : 2.15 | - | - | 1 : 1.64<br>1 : 1.91 | - |
| $\log_{10}(C)$ | SSS planar joints<br>LSS tubular joints | 13.13<br>12.27 | 13.86<br>12.89 | 14.58<br>13.52 | 14.44<br>13.61 | 14.94<br>14.19 | 15.43<br>14.76 |
| $m$ | SSS planar joints<br>LSS tubular joints | 3.21<br>2.81 | 3.51<br>3.08 | 3.83<br>3.36 | 3.57<br>3.13 | 3.76<br>3.37 | 3.98<br>3.61 |

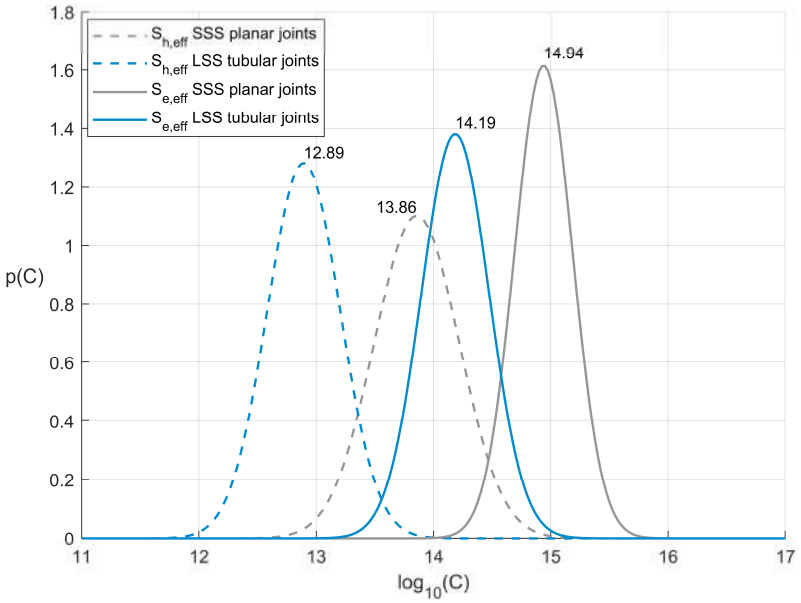


*Figure 85: $log_{10}(C)$ Gaussian probability density distributions*

The Dijkstra T-joint loaded by IPB have relatively high fatigue resistance and are located outside the SSS planar joint fatigue resistance data. Dissimilarity for these specimens can be related to divergent modelling assumptions compared to actual conditions. First, residual welding stresses are not accounted for in FEA. However, for a pulsating tensile stress, i.e. $0 < r_{lr} < 0.9$ similar to the tested LSS tubular joints, residual welding stresses should have a neglectable effect on fatigue lifetime, since residual welding stresses redistribute over time [54]. Moreover, according to C.H. Jo et al. [36], after 20 cycles no residual stress is present in a LSS tubular joint. Differences are therefore most likely linked to diverged actual and interpreted specimen boundary conditions and weld geometries. For example, a lower weld notch angle, $\alpha$, reduces the weld notch stress concentration. The weld geometry of Dijkstra specimens are based on a joint where $d$ = 457.2 $mm$, see APPENDIX E, whereas $d$ = 88.9 $mm$ for the T-joint loaded by IPB. Increasing $l_e$ unintentionally by the welder by an extra welding pass around the tubular joint takes less effort for a smaller tubular joint, resulting in a lower weld notch stress concentration. The SCF's of the T-joint loaded by IPB calculated by Dijkstra are similar to the SCF's derived in this study, however differ significantly from the measured SCF's. Volume FEA with bilinear material properties and nonlinear stiffness result in similar SCF's compared to FEA with elastic material properties and linear stiffness, therefore not clarifies the relative high fatigue resistance. Since the SCF's calculated by the authors are similar to the volume FEA SCF's through various methods, a measurement fault is possible. Moreover, the first extrapolation point is only 4 mm away from the weld toe. This extrapolation point, located at a relative small distance from the weld toe, is difficult to install precisely, therefore is prone to measurement errors. Further, it is probable that Dijkstra's specimens are not simply supported purely, but some moment resistance is present at the chord ends. A. Romeijn [48] concluded clamped chord ends result in smaller hot spot SCF's compared to simply supported chord ends for an axial loaded KK-joint. By volume FEA of the T-joint loaded by IPB a difference of 12% in hot spot SCF's was observed when clamped instead of simply supported boundary conditions are applied, therefore still results in significant differences compared to the measured hot spot SCF by Dijkstra. Above three possibilities regarding weld geometry, measurement errors and boundary conditions are difficult to verify.

M.S. Zhao et al. reported the crack initiation point, see APPENDIX E, however did not specify the failure location. The crack of Zhao's specimen loaded by load case 1 did not initiate at the corner as expected from the shell and volume FEA, but around 20 mm away from the corner. This could indicate a high quality corner weld with relative low amount of weld defects and/or low quality weld at the straight section where the crack initiated. Since no further information is provided, the initiation point is taken to define $\sigma_s$ for the specimen loaded with load case 1. The crack initiation point of the specimen loaded with load case 2 is located at the corner, which is the maximum stress location and used to derive the structural stress for the average effective notch stress.

The K-joint specimens tested by Jo et al. have relative low fatigue resistance compared to the specimens studied by Dijkstra et al. and Zhao et al.. This is possibly related to the small groove opening of 18.5 degrees at the crown heel shown in Figure 65. According to AWS specifications [41] for tubular joints, the crown heel groove opening should be no less than 30 degrees for sufficient accessibility. Poor weld accessibility may result in lack of fusion and/or larger welding defects, therefore lower fatigue resistance.

# 5 Fatigue assessment

## 5.1 Introduction

Offshore and marine structures are exposed to cyclic loading during their lifetime. Wind and wave loading are most frequently identified as loading types for semi-submersibles [2]. Due to vessel motions, fluctuating inertia loads are also present. The cyclic loading results in progressive local structural damage, ultimately resulting in fracture [34]. Since welded joints introduce stress intensities due to welding defects, notched geometry and stiffness changes, the FLS is usually a governing limit state regarding welded structural details, therefore mainly defines the local structural design.

This chapter summarises the fatigue assessment performed for a tubular CHS X-joint of the semi-submersible with bracing configuration 2. The tubular CHS X-joint geometry is presented first, after which the fatigue assessment methodology is reported. The fatigue assessment of the simple tubular CHS X-joint in Chapter 5.4.1 concludes insufficient fatigue longevity. Therefore, a complex tubular CHS X-joint, including ring-stiffeners, is analysed in Chapter 5.4.2, resulting an acceptable fatigue lifetime.

## 5.2 Tubular CHS X-joint

The bracing configurations are evaluated in Chapter 3.3.5. Bracing configuration 2 is preferred when payload, structural VCG, structural redundancy and fatigue are all of equal importance. In addition, when the amount of bracing modifications are considered, configuration 2 increases payload more effectively compared to configuration 3.2. The same holds for structural redundancy, where configuration 2 has a more effective increase compared to other configurations. The semi-submersible design with bracing configuration 2 is therefore selected for the fatigue assessment.

Semi-submersible fatigue sensitive locations are identified in Chapter 3.3.5.4. Based on the literature review and global strength assessment, the following connections for the total structural design are identified as fatigue sensitive locations: brace-column, brace transition pieces, brace-brace, column-deckbox knee joint, deckbox transverse and longitudinal side and bulkheads, see Figure 62. Discussed in Chapter 3.3.2 and illustrated in Figure 42, large geometric stress concentrations occur at the brace-brace connection of configuration 2. Tubular joint stress concentrations are related to non-uniform stiffness distributions. Moreover, measured by O.D. Dijkstra et al. [37] and calculated by FEA, tubular CHS X-joints have relative large SCF's compared to other tubular joint types due to larger chord ovalisation, see Chapter 4.4.1. The welded brace-brace connection, also referable as tubular CHS X-joint, is therefore selected as structural detail studied in the fatigue assessment. It should be noted that fatigue assessments of all identified fatigue sensitive locations should be performed to ensure structural longevity of the entire semi-submersible.

Figure 86 shows the global structural surface model analysed in the fatigue assessment, highlighting the tubular CHS X-joint. Tubular joint geometry parameters are summarised in Table 41, also reporting the weld geometry. See Figure 64 and Figure 66 for the definition of geometric parameters. The tubular CHS X-joint weld type is classified as a groove weld around the full circumference, where weld geometry is based on AWS specifications of tubular joints [41] and is comparable to the studied LSS tubular joints in Chapter 4. Since including weld geometry in shell FEA can affect results significantly, see Chapter 4.4.2, weld geometry is accounted for by modelling a mid-surface of the extended groove weld section similar as sketched in Figure 68.

Both diagonal bracings of configuration 2 have equal diameters, i.e. $\beta = \frac{d}{D} = 1$. Observed by O.D. Dijkstra et al. [37] where $\beta = 1$, two possible crack initiation points exists: the weld toe or weld root. A weld root as fatigue sensitive location is not preferred, since this increases the complexity of inspections and has limited or no accessibility. An $\beta \leq 0.9$ is advised by DNV-GL [39] to avoid weld root failure for tubular joints. Therefore, one bracing diameter is increased locally, further referred to as chord, resulting in $\beta = 0.75$, see Figure 86 and Table 41. It is expected that the local increase in diameter does not affect the structural performance of configuration 2, therefore the mass properties and structural redundancy

remain similar. The disadvantage of increasing the bracing diameter locally are stress intensities at the transitions from bracing diameters, which increases the number of fatigue sensitive locations. However, as discussed in Chapter 5.4.1.1, SCF's at the transitions are lower compared to the tubular CHS X-joint.

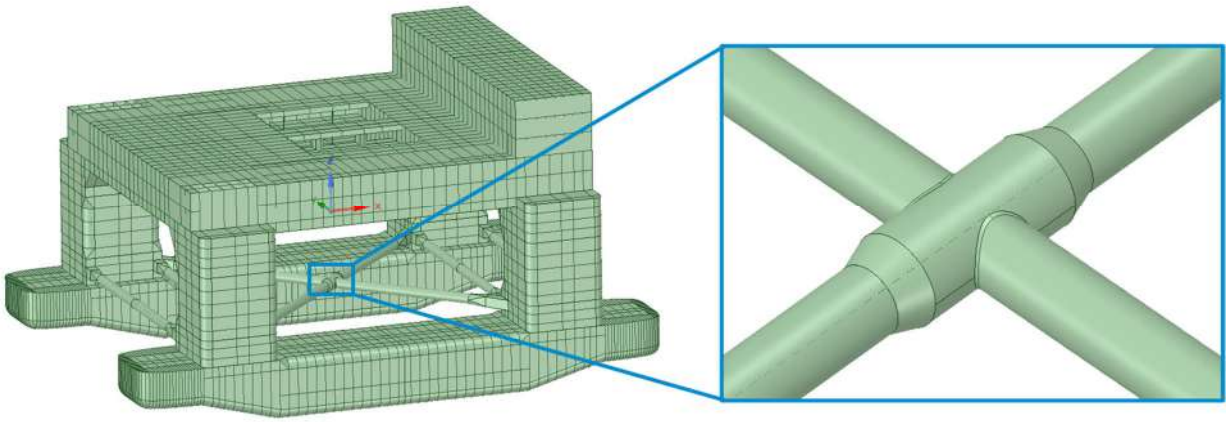

*Figure 86: Global structural surface model fatigue assessment, highlighting the tubular CHS X-joint*

*Table 41: Tubular CHS X-joint geometry*

| | | |
|---|---|---|
| **Tubular geometry** | D, T [mm] | 2460, 60 |
| | β = d/D | 0.75 |
| | γ = D/2T | 20.5 |
| | τ = t/T | 0.67 |
| | Θ [deg] | 88.5 |
| **Weld geometry** | δ [deg] | Crown toe 47<br>Saddle 53<br>Crown heel 43 |
| | $l_e$ | t/2 |

## 5.3 Methodology

The fatigue assessment methodology is reported in this chapter, covering the operational profile, load spectrum, stress RAO's, fatigue assessment concepts and fatigue damage accumulation approach.

### 5.3.1 Operational profile

The semi-submersible operational profile normally depends on expected order book, operational area, maintenance periods and owners requirements. Therefore, the fatigue assessment is usually based on owner's input. Since owner specifications are not available, assumptions regarding the operational profile are made and discussed below. See Table 42 for the operational profile summary used for the fatigue assessment.

*Table 42: Operational profile fatigue assessment*

| Operational profile parameters | | Lifetime distribution |
|---|---|---|
| Basic conditions | Operational<br>Harbour/idle | 85%<br>15% |
| Wave headings | 0°<br>22.5°<br>45°<br>67.5°<br>90°<br>112.5°<br>135°<br>157.5°<br>180° | 6.25%<br>12.5%<br>12.5%<br>12.5%<br>12.5%<br>12.5%<br>12.5%<br>12.5%<br>6.25% |
| Operational area | Worldwide | Table 43 |

The literature review partly focused on fatigue assessments performed for semi-submersibles [2]. Most authors assumed the semi-submersible is operational for the complete lifetime, or specified a percentage of time where the semi-submersible lays idle in the harbour, therefore no fatigue damage is accumulated. An accurate fatigue assessment should consider the operational basic condition, transit basic condition and harbour condition, all properly distributed over the estimated lifetime. The increased accuracy comes however with added effort as additional load spectrums and FEA should be performed. The survival basic conditions are normally ignored as they do not occur as frequent compared to the other basic conditions. Moreover, the reference semi-submersible survival basic conditions have similar characteristic responses compared to the operational basic condition [20], since draught is similar. Therefore, accounting for survival basic conditions has insignificant effect on fatigue damage. The transit basic condition is ignored in this fatigue assessment, resulting in conservative fatigue damage as motivated below. First, based on the global strength assessments in Chapter 3, the bracing global dimensions are governed by the characteristic loading, while column-deckbox connection and deckbox structure global dimensions are governed by both characteristic loading and accelerations. The characteristic forces and moments are 1.5 to 2.5 times smaller in transit compared to the operational basic condition [20]. Also, the dominant wave heading in transit condition is 0 degrees, for which structural stress RAO's are the lowest, see Figure 98. Therefore, not accounting for the transit basic condition results in a conservative fatigue damage for the bracing structure. Since a semi-submersible is approximately 15% of its lifetime in transit, the conservative operational profile results in an expected 2 times higher fatigue damage. Based on the literature review, a harbour time of 15% of its lifetime is taken.

The semi-submersible is symmetric in wetted area and structural response, with respect to the centreline. Therefore, only wave headings from 0 to 180 degrees are considered, see Table 42. When operating, the semi-submersible is positioned by anchors or dynamic positioning. Hence, an equal distribution of wave headings is applied.

A scatter diagram defines the probability of occurrence of certain sea states. A sea state is described by the significant wave height, $H_s$, defining the mean of the highest one-third waves, and mean zero-up crossing period, $T_z$, which defines the mean wave period of all waves. The operational area of the semi-submersible is unknown, therefore a worldwide scatter diagram prescribed by DNV-GL [55] is used, see Table 43.

*Table 43: Scatter diagram worldwide operation [55]*

| Tz [s] | 3.5 | 4.5 | 5.5 | 6.5 | 7.5 | 8.5 | 9.5 | 10.5 | 11.5 | 12.5 | 13.5 | 14.5 | 15.5 | 16.5 | 17.5 | Sum |
|---|---|---|---|---|---|---|---|---|---|---|---|---|---|---|---|---|
| Hs [m] | | | | | | | | | | | | | | | | |
| 1 | 311 | 2734 | 6402 | 7132 | 5071 | 2711 | 1202 | 470 | 169 | 57 | 19 | 6 | 2 | 1 | 0 | 26287 |
| 2 | 20 | 764 | 4453 | 8841 | 9045 | 6020 | 3000 | 1225 | 435 | 140 | 42 | 12 | 3 | 1 | 0 | 34001 |
| 3 | 0 | 57 | 902 | 3474 | 5549 | 4973 | 3004 | 1377 | 518 | 169 | 50 | 14 | 4 | 1 | 0 | 20092 |
| 4 | 0 | 4 | 150 | 1007 | 2401 | 2881 | 2156 | 1154 | 485 | 171 | 53 | 15 | 4 | 1 | 0 | 10482 |
| 5 | 0 | 0 | 25 | 258 | 859 | 1338 | 1230 | 776 | 372 | 146 | 49 | 15 | 4 | 1 | 0 | 5073 |
| 6 | 0 | 0 | 4 | 63 | 277 | 540 | 597 | 440 | 240 | 105 | 39 | 13 | 4 | 1 | 0 | 2323 |
| 7 | 0 | 0 | 1 | 15 | 84 | 198 | 258 | 219 | 136 | 66 | 27 | 10 | 3 | 1 | 0 | 1018 |
| 8 | 0 | 0 | 0 | 4 | 25 | 69 | 103 | 99 | 69 | 37 | 17 | 6 | 2 | 1 | 0 | 432 |
| 9 | 0 | 0 | 0 | 1 | 7 | 23 | 39 | 42 | 32 | 19 | 9 | 4 | 1 | 1 | 0 | 178 |
| 10 | 0 | 0 | 0 | 0 | 2 | 7 | 14 | 16 | 14 | 9 | 5 | 2 | 1 | 0 | 0 | 70 |
| 11 | 0 | 0 | 0 | 0 | 1 | 2 | 5 | 6 | 6 | 4 | 2 | 1 | 1 | 0 | 0 | 28 |
| 12 | 0 | 0 | 0 | 0 | 0 | 1 | 2 | 2 | 2 | 2 | 1 | 1 | 0 | 0 | 0 | 11 |
| 13 | 0 | 0 | 0 | 0 | 0 | 0 | 1 | 1 | 1 | 1 | 0 | 0 | 0 | 0 | 0 | 4 |
| 14 | 0 | 0 | 0 | 0 | 0 | 0 | 0 | 0 | 1 | 0 | 0 | 0 | 0 | 0 | 0 | 1 |
| Sum | 331 | 3559 | 11937 | 20795 | 23321 | 18763 | 11611 | 5827 | 2480 | 926 | 313 | 99 | 29 | 9 | 0 | 100000 |

### 5.3.2 Load spectrum

Only wave loading is considered for most semi-submersible fatigue assessments [2] and is also solely considered in this fatigue assessment. Wind loading is usually ignored in all limit states for offshore and marine structures, since wind loading is a fraction of wave loading [56]. Moreover, the structure loads resulting from wind loading are lower. However, structure loads are of importance for example the drilling tower not considered in this fatigue assessment. These structures types consists of a large frontal area, heigh centre of area and small support footprint, resulting in large structure loads due to wind loading.

A sea state consists of waves with different heights, frequencies and headings. Normally, waves are distinguished in sea and swell waves [7]. Sea waves are characterised as short, irregular and local wind generated waves, while swell waves are long, smooth, regular waves, generated by a distant storm. The sea state of mixed waves, arranged by wave frequency, heading and energy, is normally described by a two-dimensional wave spectrum as illustrated by Figure 87.

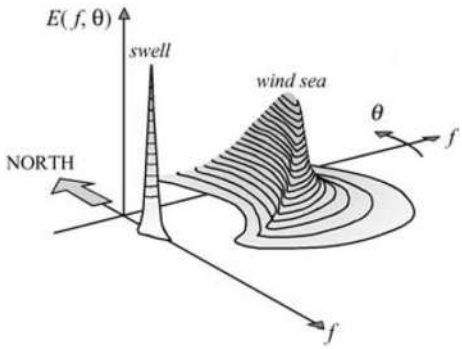


*Figure 87: Two-dimensional wave spectrum [7]*

Fatigue loading can be defined by three different modes shown in Figure 88. Most structural details in offshore and marine structures are predominantly subjected to mode-I loading, therefore uniaxial stress [35]. However, due to global or local loading and structure geometry, structural details may be subjected to normal and shear stresses; a multi-axial stress state. Since sea and swell waves have different wave heights, frequencies, headings and phases, the proportionality between mode-I and mode-III loading, i.e. normal and shear stress, may also change over time.

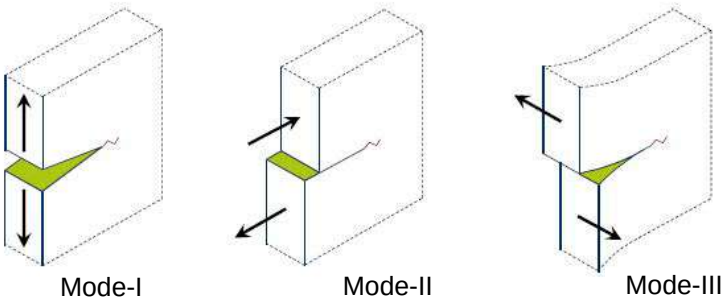


*Figure 88: Fatigue crack growth by different loading [57]*

Regardless of wave height, frequency or heading, bracings are predominantly globally axial loaded due to the larger axial stiffness compared to the lateral stiffness and large span. Due to floater deformations, the bracings are loaded by some global IPB and OPB. FEA concludes the ratio between bracing global bending and axial stress, i.e. $\sigma_{ben,global}/\sigma_{ax,global}$ and shear and normal stress, i.e. $\tau_{global}/\sigma_{n,global}$, is around 0.2 and below 0.1, respectively, for all headings. Moreover, Figure 98 illustrates the stress distribution around the circumference, $C$, for different wave frequencies. Although these stress distributions apply to local mode-I stress of the tubular joint, the saddle, located at $C = 1575\ mm$ and $C = 4600\ mm$ indicates an axial dominant loaded brace. Therefore, global loading and global structure geometry does not result in significant shear stress in the bracing structure. Sea and swell wave loading may result in different proportionality between global normal and shear stress, yet due to the larger axial stiffness compared to the lateral stiffness and large span, shear stress is insignificant. If a combination of sea and swell waves are considered, multiple heading combinations should be analysed, increasing the effort and computational costs of the fatigue assessment. Since global loading remains axial dominated, only sea waves are considered for this fatigue assessment.

Linear splitting forces with respect to wave amplitude of the reference semi-submersible are used to derive water loading per wave frequency and heading. The same approach is used as reported in Chapter 3.2.1.2 to convert splitting forces to water loading. Inertia loads are subtracted, which ANSYS counteracts by global accelerations to enforce static equilibrium. Maximum axial diagonal brace loading

per frequency and heading is determined by calculating the corresponding phases from Eq.5-1 by Eq.5-2. In Eq.5-1, $F_i$ and $M_i$ are the splitting forces, $z_w$ is the vertical distance from mid-deck to centre of water loading, as sketched in Figure 17, and $x_{column}$ and $y_{column}$ are the horizontal distances from mid-deck to column.

$$LC = \sqrt{\left(F_x + \frac{M_y}{z_w} + \frac{M_z}{y_{column}}\right)^2 + \left(F_y + \frac{M_x}{z_w} + \frac{M_z}{x_{column}}\right)^2} \qquad \text{Eq.5-1}$$

$$\varphi_{LC,\zeta} = \text{atan}\left(\frac{imag(LC)}{real(LC)}\right) \qquad \text{Eq.5-2}$$

Concluded for hinged bracings in Chapter 3.3.4.3, bracing loading results in small stress magnitudes at the brace-column connection. Therefore, bracing loading is neglected in the fatigue assessment. In Figure 89, splitting force RAO's are shown for the considered wave frequencies and headings. Wave frequencies, $\omega_\zeta$, range from 0.157 rad/s, i.e. 40 s, to 1.471 rad/s, i.e. 4.3 s, with steps of 0.057 rad/s.

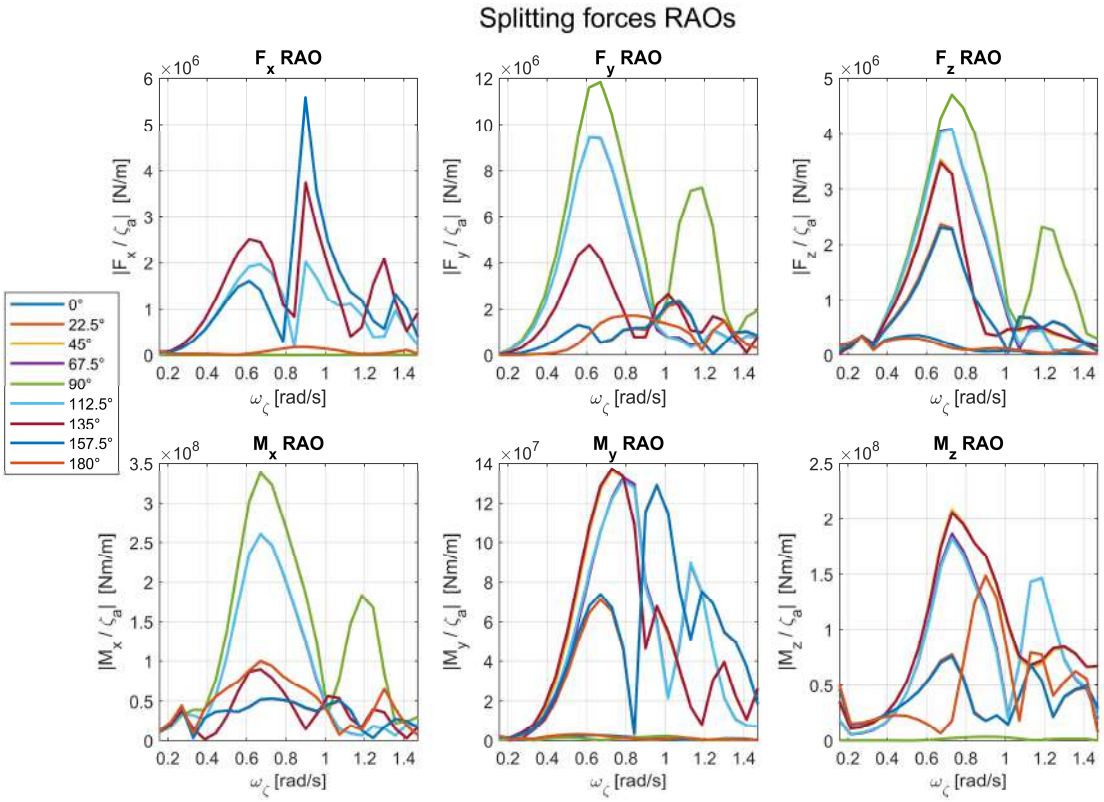


*Figure 89: Splitting forces RAO's fatigue assessment*

### 5.3.3 Stress range RAO's

The global structural surface model of configuration 2, including the modified tubular CHS X-joint shown in Figure 86, is used to derive nodal forces and moments at the X-joint. The FEA input is similar as discussed in Chapter 3 and APPENDIX E. Water loading is applied uniformly over de wetter surfaces. No local FEA of the tubular CHS X-joint is made, since small structural details in the semi-submersible hull not accounted for in the global structural surface model do not affect tubular CHS X-joint loading. The mesh at the tubular CHS X-joint is refined to accurately derive the nodal forces and moments around the circumference. Nodal moments at the tubular CHS X-joint derived from the FEA are shown in Figure 90 as example.

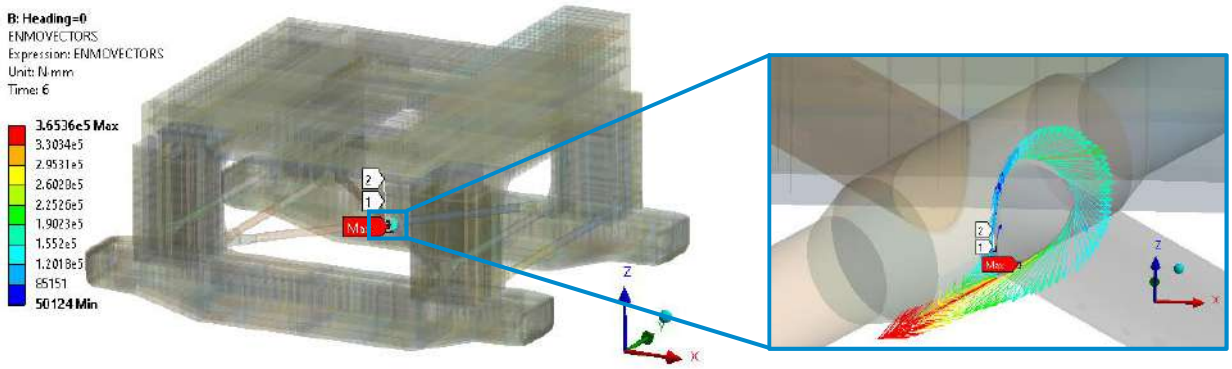


*Figure 90: FEA configuration 2 semi-submersible, highlighting nodal moments at the tubular CHS X-joint*

Reported previously, bracings are predominantly axial loaded at global level. At local level, multi-axial loading and some multi-axial stress is present at the tubular CHS X-joint. This is illustrated by chord weld toe line forces in Figure 94, principal stress in Figure 95 and principal vectors in Figure 96. The line forces are calculated through the same procedure as reported in Chapter 4.4.1, with respect to the local weld CSYS [x'y'z'] as sketched in Figure 71. Figure 94 shows nonzero line forces, $f_{y'}$ and $f_{z'}$, and moments, $m_{x'}$ and $m_{z'}$, resulting in shear stress in chord thickness direction and parallel to the weld seam. Therefore mode-II and mode-III loading at the tubular CHS X-joint is present.

The chord weld toe saddle is the critical location around the circumference of the tubular CHS X-joint, due to large $f_{x'}$ and $m_{y'}$ line forces, resulting large normal stress. This holds for most wave frequencies and headings, see Figure 98, and is similar to fatigue tests for axial loaded tubular joints, reported in Chapter 4. At the saddle location no mode-III loading is present, i.e. $f_{y'} \approx 0$ and $m_{z'} \approx 0$. Since the through-thickness shear loading, $f_{z'}$ and $m_{x'}$, at the saddle location are considerable lower than $f_{x'}$ and $m_{y'}$, mode-II loading is insignificant.

The principal vectors also demonstrate shear stress parallel to the weld seam is present between the crown and saddle locations, and is zero at the saddle location. Some through-thickness shear stress occurs at the saddle location, however principal vector angles show normal stress dominates.

Multi-axial fatigue is therefore neglected in this fatigue assessment. Mode-I membrane, bending and structural stress around the circumference is calculated by Eq.4-5. Hot spot stress ranges are derived by linear surface stress extrapolation, see Chapter 5.3.4.3.

Since load ranges are defined as $F_{in-phase} = -F_{out-of-phase}$, only in-phase load cases are analysed in FEA. Stress range RAO's are calculated as $\Delta\sigma = 2abs(\sigma_{in-phase})$. The structural stress range RAO's for the simple tubular CHS X-joint is shown in Figure 98 per wave frequency and heading.

### 5.3.4 Fatigue assessment concepts

Three different fatigue assessment concepts are applied in this study; the structural stress concept, developed by P. Dong et al. [3], the average effective notch stress concept, developed by H. den Besten [4], and the hot spot stress concept, based on DNV-GL guidelines [39]. Compared to common engineering fatigue assessment concepts, such as the nominal and hot spot concepts, the structural stress and average effective notch stress concepts are more detailed regarding the geometry and loading & response information involved. To elaborate, the stress extrapolation procedure of the hot spot stress concept captures $\sigma_f$ information, however is a fictitious stress. The structural stress concept calculates the actual $\sigma_f$ at the welded joint and accounts for thickness effects and loading modes through fitting. The average effective notch stress concept calculates both $\sigma_f$ and $\sigma_{se}$ at the welded joint, see Chapter 4.5.2, thus describes the total mode-I stress distribution.

In addition, the structural stress and average effective notch stress concepts are less sensitive to mesh specification, since nodal forces and moments from FEA are used to derive stresses analytically. Consequently, proven by fatigue resistance data plots of the structural stress concept and average effective notch stress concept, fatigue resistance scatter is lower compared to the nominal and hot spot concepts [3], [47].

Thus, ranking of fatigue assessment accuracy, $O$, is $O_e > O_s > O_h$, where subscript $e$, $s$ and $h$ represent the average effective notch stress, structural stress and hot spot stress fatigue assessment concepts, respectively. Consequently, $O_e$ comes with added effort, since detailed weld geometry needs to be defined, from which $\sigma_{se}$ is calculated analytically. However, the importance of including weld geometry of tubular joints in FEA is demonstrated in Chapter 4.4.2, therefore weld geometry needs to be defined regardless. Compared to the common effective notch stress concept, effort to derive notch stresses is reduced, since no detailed solid FEA is needed. The fatigue assessment concepts are explained below.

### *5.3.4.1 Structural stress concept*

The structural stress, derived from nodal forces and moments, is proven to be mesh-insensitive, with respect to element type and sizes compared to stresses directly derived from FEA, also demonstrated by P. Dong [49] and reported in Chapter 4.4.1. A single master S-N curve is developed by P. Dong et al. [3], based on a large amount of fatigue resistance data regardless of joint geometry and loading.

To account for thickness effects and loading modes, structural stress range RAO's, $\Delta\sigma_s$, are converted to effective structural stress range RAO's, $S_{\sigma_s,eff}$, shown by Eq.5-3. Here, $t^*$ is the relative thickness with respect to a unit thickness. The life integral, $I(r)$, shown in Eq.5-4, is a dimensionless function of the bending ratio between membrane and bending stress defined as $r = \frac{|\sigma_b|}{|\sigma_m|+|\sigma_b|}$.

$$S_{s,eff} = \frac{\Delta\sigma_s}{t^{*\frac{2-m}{2m}} \cdot I(r)^{\frac{1}{m}}} \qquad \text{Eq.5-3}$$

$$I(r)^{\frac{1}{m}} = 0.0011r^6 + 0.0767r^5 - 0.0988r^4 + 0.0946r^3 + 0.0221r^2 + 0.014r + 1.223 \qquad \text{Eq.5-4}$$

In Chapter 5.3.5 the design master S-N curve is presented.

### *5.3.4.2 Average effective notch stress concept*

An average effective notch stress is calculated by weld notch stress integration from weld toe to the material characteristic length, $\rho^*$. The semi-analytical weld toe notch stress distribution describes the mode-I stress as a summation of the self-equilibrating stress and structural field stress, using the structural stress range as input. In Chapter 4.5.2 and 4.6, the semi-analytical weld toe notch stress distribution and average effective notch stress is reported in more detail. In Chapter 4.5.2 it is demonstrated that the semi-analytical weld toe notch stress distributions are similar to detailed volume FEA for a variation of tubular joints.

In Figure 91 the tubular CHS X-joint weld geometry is illustrated for crown toe, saddle and crown heel. The saddle weld geometry is used to derive the average effective notch stress ranges. Similar as in Chapter 4.6, $\rho^*$ = 1.14 is adopted based on most likely estimates calculated by Y. Qin et al. for SSS planar joints.

Structure longevity is negatively affected by mean tensile stresses, which can originate from residual welding stress or mechanical loading. It is found however that when applying a pulsating tensile stress, i.e. $0 < r_{lr} < 0.9$, residual welding stresses should have a neglectable effect on fatigue lifetime, since residual welding stresses redistribute over time. J. Klassen et al. [54] has conducted LSS fatigue tests for as-welded and stress relieved heat-treated specimens and concluded that no clear residual welding stress influence on the fatigue life could be observed. Moreover, according to C.H. Jo et al. [36], after 20 cycles no residual stress is present in a LSS tubular joint. Residual welding stress is therefore neglected in this fatigue assessment. The bracing members of configuration 2 are buoyant, which results in mean axial tensile loading, IPB and OPB, due to outward floater deformations and lateral forcing of

buoyancy. Therefore, a mean stress is present at the tubular CHS X-joint. For the simple tubular CHS X-joint at the saddle location, a mean buoyancy tensile stress of 88 MPa is derived from FEA only accounting for static loading. The mean buoyancy tensile stress is accounted for by Walker's mean stress model. Per sea state, wave frequency and heading, the mean wave amplitude, $\bar{a}$, is calculated by Eq.5-10, assuming wave height of a sea state is Rayleigh distributed [7]. Here, $m_0$ is the zeroth order spectral moment of a wave spectrum, explained in Chapter 5.3.5. In-phase and out-of-phase stresses, which are linear with respect to wave amplitude, are then multiplied with $\bar{a}$ to obtain the in-phase and out-of-phase stresses per sea state, plus adding the mean buoyancy tensile stress, $\sigma_{mean}$, in Eq.5-6 and Eq.5-7. The stress ratio is determined by Eq.5-8. Similar to Chapter 4.6, the average effective notch stress is scaled with Walker's mean stress model to an effective one in Eq.5-9 by adopting $\gamma$ = 0.92 based on most likely estimates calculated by Y. Qin et al. [47] for SSS planar joints.

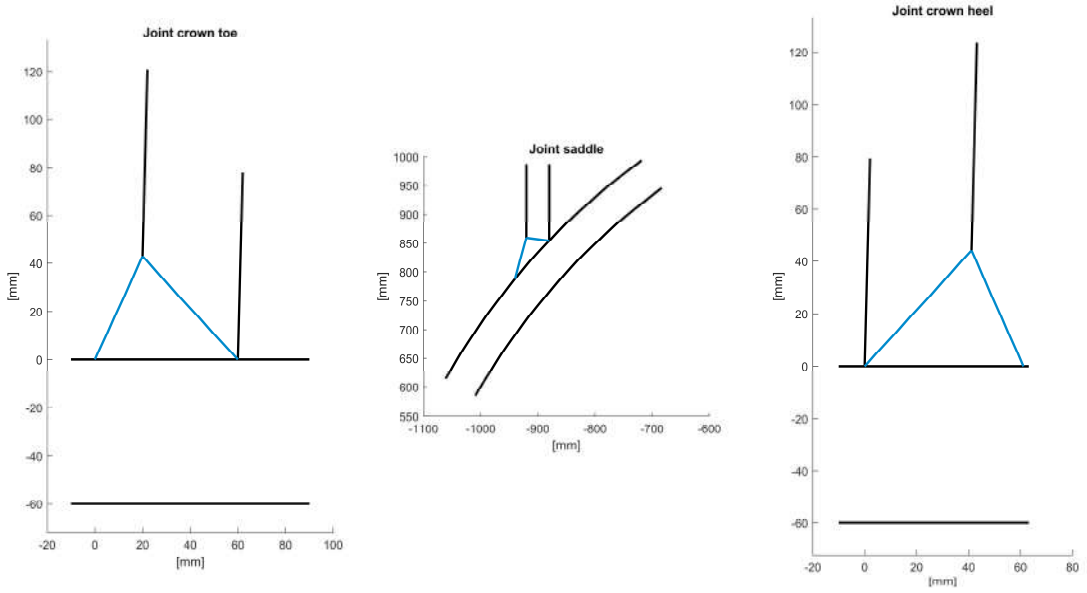


*Figure 91: Weld geometry tubular CHS X-joint*

$$\bar{a} = \sqrt{\frac{1}{2}\pi \cdot m_0} \qquad \text{Eq.5-5}$$

$$\sigma_{in-phase} = \bar{a} \cdot \sigma_{in-phase,RAO} + \sigma_{mean} \qquad \text{Eq.5-6}$$

$$\sigma_{out-of-phase} = \bar{a} \cdot \sigma_{out-of-phase,RAO} + \sigma_{mean} \qquad \text{Eq.5-7}$$

$$r_{lr} = \frac{\min(\sigma_{in-phase}, \sigma_{out-of-phase})}{\max(\sigma_{in-phase}, \sigma_{out-of-phase})} \qquad \text{Eq.5-8}$$

$$S_{e,eff} = \frac{\Delta\sigma_e}{(1 - r_{lr})^{1-\gamma}} \qquad \text{Eq.5-9}$$

Since similarity is proven between SSS planar joints and most LSS tubular joints, a SSS planar joint based design S-N curve is used and is presented in Chapter 5.3.5.

### *5.3.4.3 Hot spot stress concept*

In general, hot spot stress, $\sigma_h$, can be derived in FEA by three different methods [42]; through-thickness stress linearisation, linear or nonlinear surface stress extrapolation and by a single point criterion, also discussed in Chapter 4.3. This concept accounts for stress concentrations due to local structure geometry, however does not account for the nonlinear self-equilibrating stress. If stress extrapolation is used, $\sigma_h$ is a fictitious stress and captures structural field stress information.

In engineering practice, it is common to derive nominal stress ranges by hand calculations or FEA first. By multiplying the nominal stress range by hot spot SCF's, calculated through parametric formulas provided by guidelines, hot spot stress ranges are obtained.

Due to the increased chord diameter at the X-joint, chord nominal stresses are difficult to derive from FEA. The DNV-GL [39] linear surface stress extrapolation procedure for tubular joints is therefore used. Shown by Figure 97, the saddle location is critical with respect to stress magnitudes. Therefore, outer surface normal stresses perpendicular to the weld toe, i.e. in x'-direction sketched in Figure 71, are extracted from FEA at points $a = 0.2\sqrt{rt}$ and $b = \frac{\pi R}{36}$ at the saddle location, see Figure 92. The hot spot stress is then calculated through linear stress extrapolation, shown by Eq.5-10. The thickness effect is accounted for as demonstrated in Eq.5-11, where $t_{ref} = 32\ mm$ and $k = 0.25$.

$$\sigma_h = \sigma_{x',a} - \frac{\sigma_{x',a} - \sigma_{x',b}}{x'_a - x'_b} x'_a \qquad \text{Eq.5-10}$$

$$S_{h,eff} = \frac{\Delta\sigma_h}{\left(\frac{t_{ref}}{T}\right)^k} \qquad \text{Eq.5-11}$$

The advised shell element size between $T * T \leq e \leq 2T * 2T$, is followed. Fatigue resistance is defined by the 'T-curve' of DNV-GL, further discussed in Chapter 5.3.5.

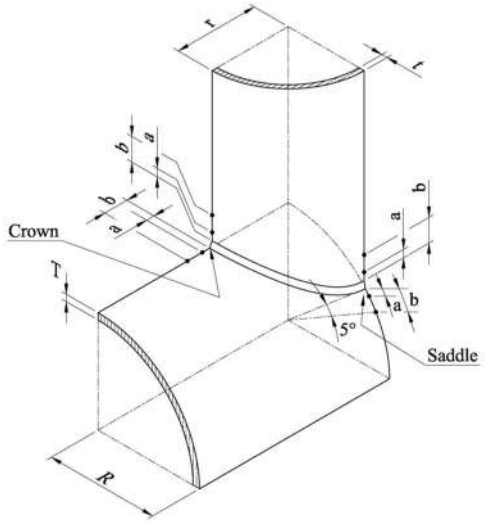


*Figure 92: Hot spot surface extrapolation points tubular joint [39]*

### 5.3.5 Fatigue damage accumulation

Fatigue damage accumulation is usually determined using a spectral or temporal approach. For this fatigue assessment a spectral approach is used, since regular waves and mode-I stress is considered only. Therefore, stress ranges do not change over time for a certain sea state and proportionality between normal and shear stress does not change over time. A temporal approach is normally considered more accurate, since the actual stress range per sea state and heading is computed, whereas the spectral approach uses an assumed distribution. Based on reports where different spectral methods are compared to a temporal approach [17], [58], [59], the spectral approach using a Rayleigh distribution is proven to be quite accurate. In these studies about 10% difference in fatigue damage was observed. The spectral approach for this fatigue assessment is explained below.

First, the stress response for both structural stress and average effective notch stress, defined as subscript $k$, is determined per sea state ($H_s$ and $T_z$) and heading, see Eq.5-12. The stress response is commonly referred to as a short-term stress range response per sea state. A Pierson-Moskowitz (PM) wave spectrum, shown in Eq.5-13, is selected as wave spectrum, $S_\zeta$, therefore a fully developed sea state is assumed.

$$S_{k,res} = \left|S_{k,eff}\right|^2 S_\zeta \qquad \text{Eq.5-12}$$

$$S_\zeta = \frac{H_s^2}{4\pi} \cdot \left(\frac{2\pi}{T_z}\right)^4 \cdot \omega_\zeta^{-5} \cdot \exp\left(-\frac{1}{\pi} \cdot \left(\frac{2\pi}{T_z}\right)^4 \cdot \omega_\zeta^{-4}\right) \qquad \text{Eq.5-13}$$

Assuming a Raleigh stress range distribution per sea state and heading, a constant amplitude stress range is calculated by Eq.5-14, also known as equivalent fatigue load (EFL). In this equation, $\sigma$ is the standard deviation of $S_{k,res}$, $\Gamma$ is the gamma function and $m$ is the design S-N curve slope.

$$EFL = 2\sqrt{2}\sigma\left(\Gamma\left(1+\frac{m}{2}\right)\right)^{1/m} \qquad \text{Eq.5-14}$$

The long-term fatigue damage is then calculated as Eq.5-15, where the sum is taken of the fatigue damage for each sea state $i$ and heading $j$. In Eq.5-15, $T_{0,i} = 2\pi\sqrt{\frac{m_0}{m_2}}$ is the zero-up crossing period, which estimates the number of cycles of a sea state, where $m_n = \int \omega^n S_{k,res} d\omega$. $p_{ij}$ is the probability of each sea state, which is computed by the worldwide scatter diagrams presented in Table 43, and heading probability shown in Table 42. The design life, $T_{life}$ is taken as 30 years and $C$ is the fatigue strength parameter of the design S-N curves shown in Table 44. $p_{op}$ = 0.85, since the semi-submersible is operating 85% of its lifetime, discussed in Chapter 5.3.1. The specified operational profile, design life and PM wave spectrum is equivalent to 9.79E7 load cycles, or mean wave period of 8.2 seconds.

$$D = p_{op}\sum_i\sum_j p_{ij}\frac{T_{life}}{C\cdot T_{0,i}}\cdot EFL^m \qquad \text{Eq.5-15}$$

Fatigue resistance is determined by design S-N curves shown in Figure 93. The effective structural stress fatigue resistance is derived by P. Dong et al. [3], resulting in the single-slope design master S-N curve. The design master S-N curve results from offsetting the mean fatigue resistance by 2 times the standard deviation, $2\sigma$. Therefore, the design master S-N curve is equivalent to a one-sided 97.7% probability of survival. In Chapter 4.6, average effective notch stress fatigue resistance similarity between SSS planar joints and LSS tubular joints is proven for most LSS tubular joints. A SSS planar joint based average effective notch stress design S-N curve can therefore be applied for LSS tubular joints. Similar to the design master S-N curve, $2\sigma$ is applied to construct a single-slope design S-N curve with a one-sided 97.7% probability of survival. DNV-GL [39] prescribes the 'T-curve' to assess tubular joints, based on tested tubular joints at large-scale. The design S-N curve is also constructed by a 2 times standard deviation offset of the mean fatigue resistance, thus also represents a one-sided 97.7% probability of survival. All design S-N curves are (mostly) based on specimens tested in-air. See Table 44 for the design S-N curve parameters of all fatigue assessment concepts.

Shown in Figure 93, the hot spot fatigue resistance is described by a dual-slope S-N curve, with a knee point at $N = 10^7$ cycles, whereas the other fatigue assessment concepts describe fatigue resistance by a single-slope S-N curve. A slope change is related to a change in initiation and growth contributions and loading modes. Offshore and marine structures are usually exposed to $N > 10^7$ cycles [39], which is also the case in this fatigue assessment. Incorporating a slope change therefore affects fatigue damage estimation significantly. Cycles between $10^4 \leq N < 10^7$ is usually defined as the medium cycle fatigue (MCF) range and $N \geq 10^7$ is defined as the high cycle fatigue (HCF) range. DNV-GL and IIW [52] both advise a knee point at $N = 10^7$ cycles based on internal test results.

The master S-N curve derived by P. Dong et al. [3] is predominantly based on fatigue tests where $10^2 \leq N_f < 10^7$. Shown by Figure 84, the design S-N curve of the average effective notch stress is predominantly based on fatigue tests where $10^4 \leq N_f < 10^7$. To study the presence of a slope change and to possibly establish a more accurate estimation of fatigue damage for $N > 10^7$, a recommendation for further research is to include more fatigue tests in the HCF region. However, design S-N curve parameters are difficult to derive in the HCF, due to the large fatigue resistance scatter and the low amount of failed fatigue tests available in literature.

*Table 44: Design S-N curve parameters*

| | **Effective structural stress concept, design master S-N curve** [3] | **Average effective notch stress concept, SSS planar joints see Figure 84** | **Hot spot stress concept** [39] | |
|---|---|---|---|---|
| Cycle range | $N < \infty$ | $N < \infty$ | $N < 10^7$ | $N \geq 10^7$ |
| $\log_{10}(C)$ | 12.94 | 14.43 | 12.16 | 15.61 |
| $m$ | 3.13 | 3.76 | 3 | 5 |

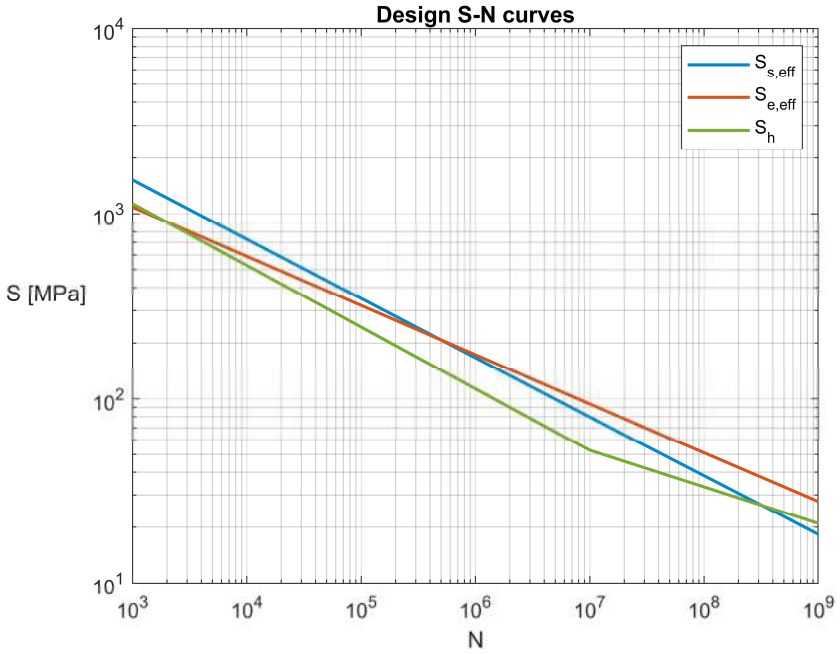


*Figure 93: Design S-N curves*

## 5.4 Results

The results of the fatigue assessment is presented in this chapter. Two different brace-brace geometries are studied; a simple tubular X-joint and complex tubular X-joint. The fatigue assessment of the simple tubular CHS X-joint in Chapter 5.4.1 concludes insufficient fatigue longevity. Therefore, a complex tubular CHS X-joint, including internal ring-stiffeners, is analysed in Chapter 5.4.2, resulting in sufficient fatigue lifetime.

### 5.4.1 Simple tubular CHS X-joint

The simple tubular joint geometry is summarised in Table 41 and shown in Figure 90. The stress distribution is discussed first, after which stress RAO's are presented. Finally, the fatigue damage of all fatigue assessment concepts is reported.

#### *5.4.1.1 Stress distribution*

The diagonal bracings are pre-dominantly globally axial loaded, as discussed in Chapter 5.3.2. At the tubular CHS X-joint multi-axial loading is present shown by Figure 94, where line forces are plotted for a certain wave frequency and heading with respect to the weld CSYS as sketched in Figure 71. The saddle location is critical with respect to stress magnitudes, where mode-I loading is dominant. At the saddle location no mode-III loading is present, i.e. $f_{y'} \approx 0$ and $m_{z'} \approx 0$. Since the through thickness shear loading, $f_{z'}$ and $m_{x'}$, at the saddle location are considerable lower than $f_{x'}$ and $m_{y'}$, mode-II loading is insignificant. The principal vector plot in Figure 96 also shows normal stress perpendicular to the weld seam is governing. Therefore, only mode-I stress is considered and multi-axial fatigue is neglected.

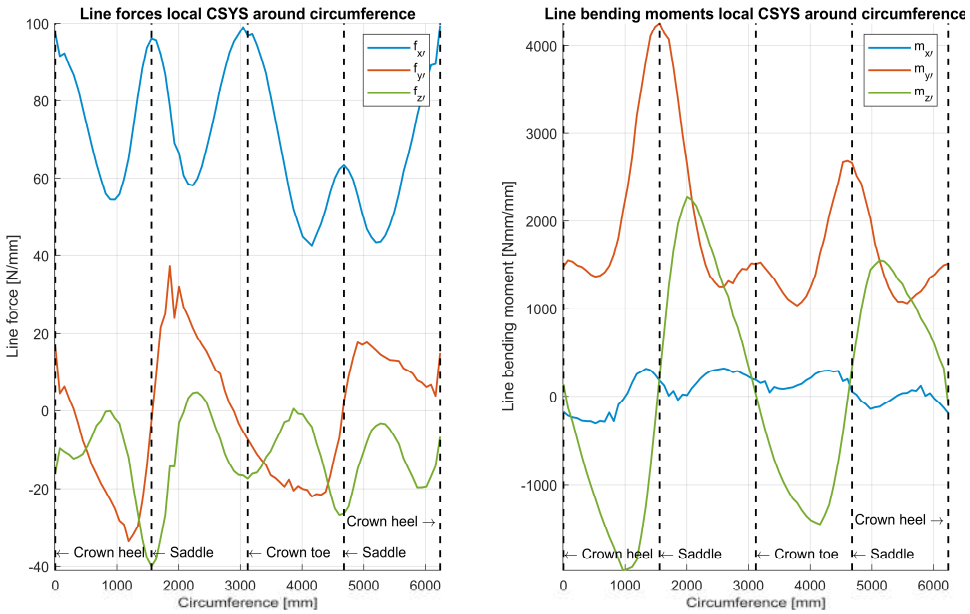


*Figure 94: Line forces and moments distribution of simple tubular CHS X-joint*

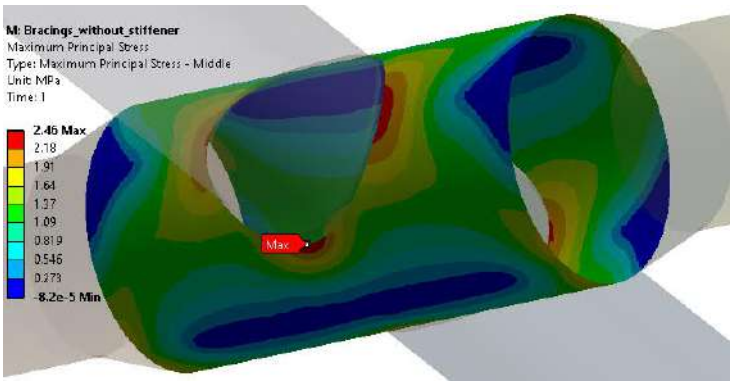


*Figure 95: Chord principal stress plot*

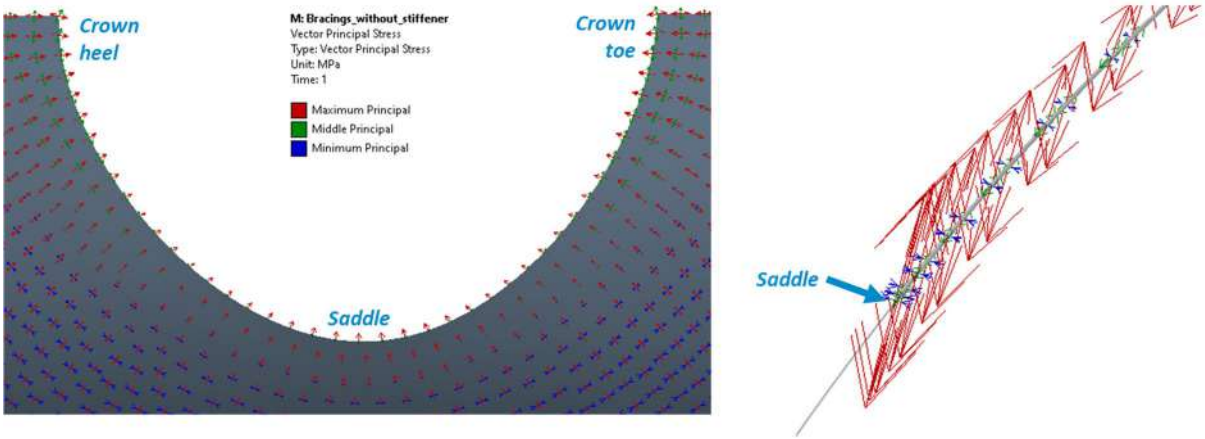


*Figure 96: Chord principal vector plot*

In Figure 97, the mode-I stress distribution around the circumference is shown for a certain wave frequency and heading. The stress distribution is plotted as a SCF between stress and nominal bracing stress. Compared to the axial loaded tubular CHS X-joint tested by O.D. Dijkstra et al. [37], structural stress concentration factors around the circumference are lower. Due to the stiffeners present in the chord diameter transitions, shown in Figure 86, smaller chord ovalisation occurs. Therefore, lower local bending moments are present at the chord weld toe. Since the modelled diameter transitions are fatigue sensitive locations that result in SCF's, stress magnitudes are checked in FEA. Assuming a mode-I

stress state, structural stress concentrations are 2.08 and 1.62 for the diameter transitions from large to small and small to large, respectively. Therefore these locations are not governing. Mode-I brace weld toe stress magnitudes are also below the considered chord weld toe stress magnitudes.

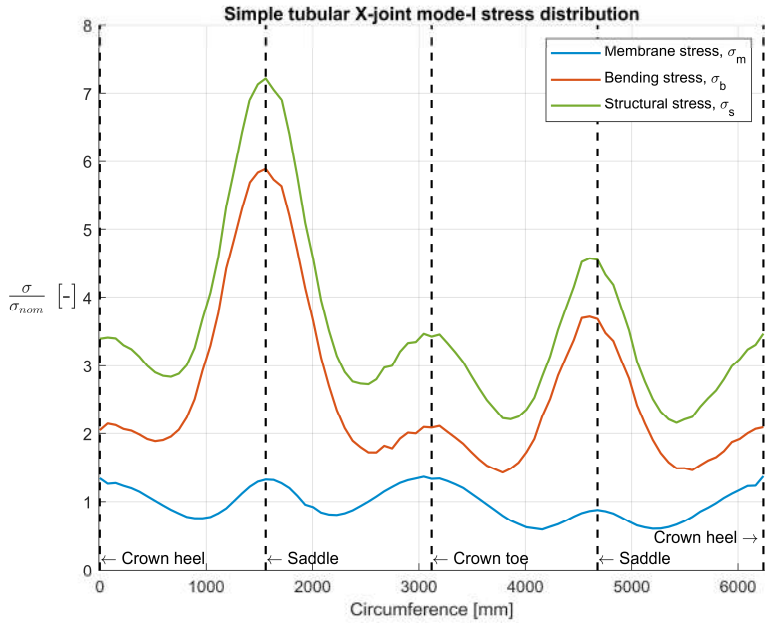


*Figure 97: Mode-I stress distribution of simple tubular CHS X-joint*

### 5.4.1.2 Structural stress RAO's

Mode-I structural stress RAO's of the chord weld toe around the circumference, $C$, per wave frequency and heading are plotted in Figure 98. The saddle locations, located at $C$ = 1575 $mm$ and $C$ = 4600 $mm$, have the largest stress magnitudes for most wave frequencies and headings, indicating an axial dominant loaded brace. Similar to the global strength assessment, headings 67.5 and 112.5 degrees result in the largest stress RAO's, however occur at frequencies where wave energy is lower with lower probability of occurrences. Therefore, wave loading at these headings result in moderate fatigue damage compared to other headings. Contrary, beam waves, equivalent to headings of 90 and 270 degrees, result in the largest fatigue damage, since stress RAO's are large at frequencies with large wave energy with high probability of occurrences. Above is also visible in the fatigue damage plot presented by Figure 99.

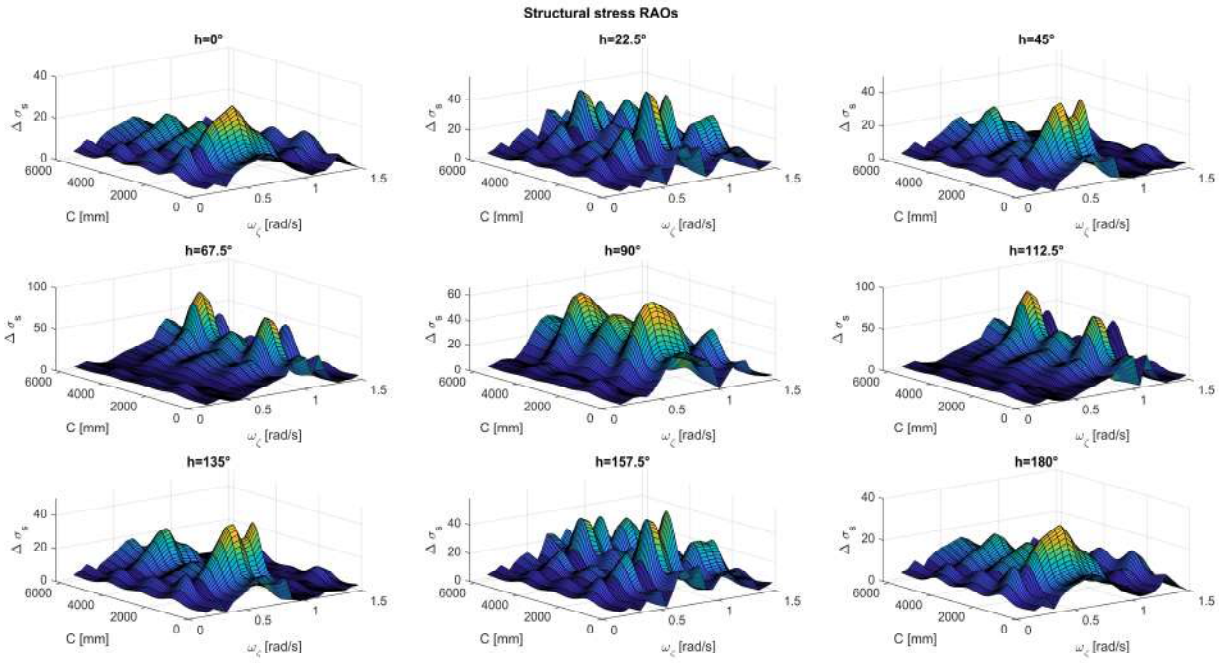


*Figure 98: Simple tubular CHS X-joint mode-I structural stress RAO's*

### 5.4.1.3 Fatigue damage

The structural stress concept fatigue damages at the saddle chord weld toe are shown in Figure 99 per sea state and wave heading. Here, the fatigue damage is not accounted yet for wave heading probability and operation lifetime distribution. Ultimately, the total damages for the structural stress concept, average effective notch stress concept and hot spot stress concept are $D_s$ = 51, $D_e$ = 62 and $D_h$ = 306, respectively. Since the damages should be below 1, the simple tubular CHS X-joint design is insufficient with respect to structural longevity.

To compare fatigue damages of the different fatigue assessment concepts, the hot spot stress T-curve of DNV-GL is modified to a single-slope design S-N curve, using MCF range parameters ($\log_{10}(C)$ = 12.16, $m$ = 3). The resulting fatigue damage is $D_h$ = 974, which is related to the lower fatigue resistance intercept and larger slope, possibly due to larger hot spot stress fatigue resistance scatter.

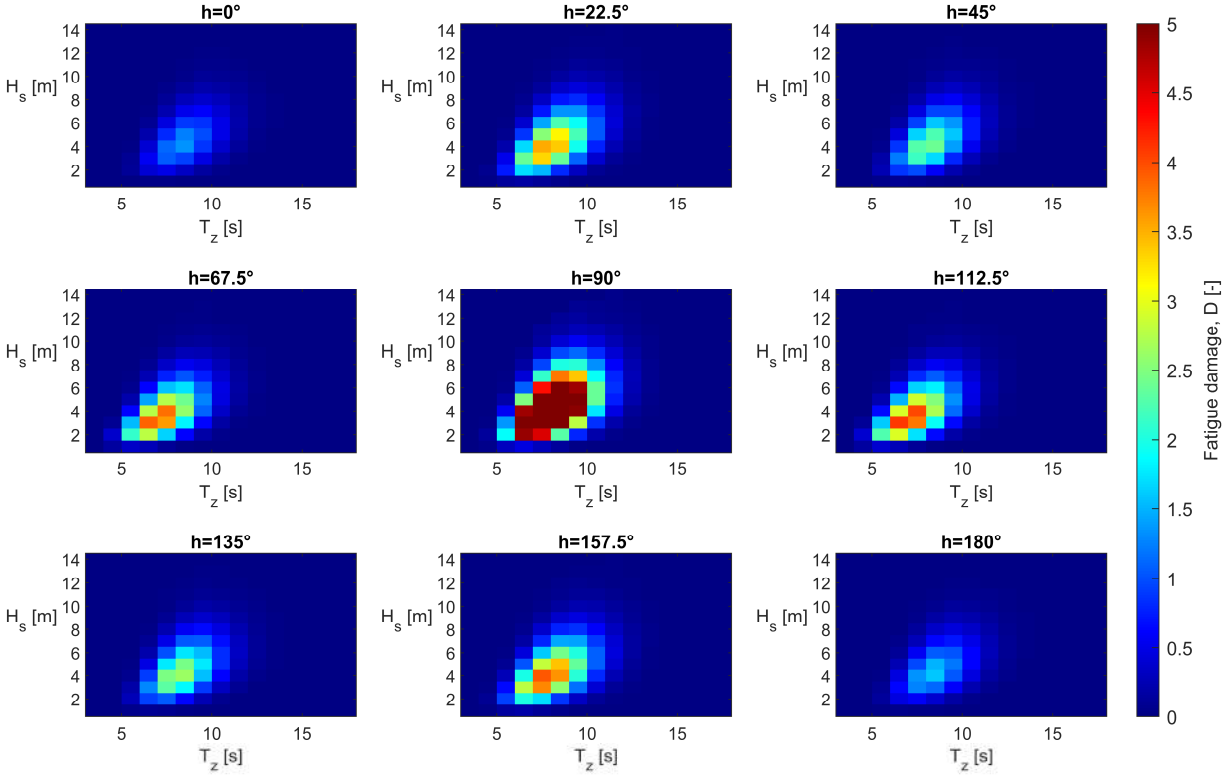


*Figure 99: Simple tubular CHS X-joint, structural stress concept fatigue damage*

## 5.4.2 Complex tubular CHS X-joint

Concluded for the simple tubular CHS X-joint, fatigue damages do not meet the required fatigue damage below 1. Therefore, the tubular joint design is modified to reduce stress ranges and therefore increase fatigue lifetime. Ring-stiffeners are added inside the chord member, therefore classifying the tubular joint as complex. Tubular diameters, wall thicknesses and weld geometry are kept constant. The design and stress distribution of the complex joint is reported in this chapter. Also, the effect on fatigue damage is discussed.

### 5.4.2.1 Design and stress distribution

Internal ring-stiffeners are frequently applied in tubular joints to increase ultimate strength and fatigue lifetime [60], [61], [62]. A ring-stiffener increases the tubular cross-section moment of inertia, resulting in a smaller chord ovalisation and therefore lower brace and chord bending moments. If the stiffeners are located around the saddle, chord deformation differences between crown and saddle cross-sections reduces as well, therefore a more uniform stress distribution along the circumference is present. Ring-stiffeners have disadvantages as well. For example, the stress intensity region increases, which is disadvantageous for crack growth rate. During fatigue tests of unstiffened and stiffened tubular CHS

joints, both loaded by the same hot spot stress range, the stiffened tubular CHS joint had a larger crack growth rate and therefore smaller fatigue lifetime. Due to the larger hot spot region, the initial surface crack aspect ratio increased, therefore the crack stress intensity increased as well. Moreover, the designer should design the complex tubular CHS joint such that stiffener stress magnitudes are lower compared to chord weld toe stress magnitudes, since internal fatigue damages are undesirable. Finally, brace stress intensifies at the location of the stiffener.

The ring-stiffener effectiveness depends on geometric and loading parameters. Based on literature [60], the effectiveness is the largest for large $\gamma = D/2T$ and $\tau = t/T$ ratio's and when loaded by axial forcing and/or out-of-plane bending. Since the effect of adding ring stiffeners is dependent on geometric and loading parameters, no guidelines or recommendations found in literature are applicable. Therefore, the tubular joint design is optimised through a parametric study by varying number of stiffeners, stiffener location, thickness and hole diameter. For the parametric study, the effect of ring-stiffeners is studied by shell FEA, using the same simple tubular CHS X-joint geometry. For brace loading, the ratio between bracing global bending and axial stress, i.e. $\sigma_{ben,global}/\sigma_{ax,global}$, is set to 0.2, which is similar as observed for the stress RAO's.

The parametric study results are shown in Figure 100, where the effect of parameter variation is plotted by mode-I chord saddle and stiffener structural stress concentration factors, with respect to bracing nominal loading. Results are elaborated below per parameter variation. # refers to the number of ring-stiffener present inside the chord, $\frac{X}{r}$ is the ratio between stiffener x-location, with respect to the coordinate system shown in Figure 101, and brace radius. The stiffener thickness is defined as $t_{stiff}$, whereas $D_{hole}$ and $D_{avg}$ are the ring-stiffener hole diameter and average chord diameter ($D_{avg} = D - T$).

First, increasing the number of stiffeners reduces stiffener stress. In case 1 stiffener is applied, the location is set to $X = 0r$, which is the saddle. Here, chord stress reduces significantly at the saddle, however at $X \approx 5t_{stiff}$ chord stress has increased. Moreover, 1 stiffener results in uneven tubular joint stress distribution and is therefore not preferred. 2 stiffeners are located at $X = 0.5r$ and in case of 4 stiffeners, the locations are set to $X = 0.5r$ and $X = 0.75r$. Since 4 stiffeners result in the lowest chord and stiffener SCF's and results in the most uniform stress distribution, this configuration is preferred.

A position at $X = 0r$ results in the highest achievable chord stress reduction, however is not preferred since stiffener stress is high. Intuitively, moving stiffeners away from the saddle reduces stiffener stress and increases chord stress.

By increasing stiffener thickness, stress reduces. However, not linear since stiffener stiffness increases as well.

The effect of stiffener hole diameter is studied by 2 stiffeners located at $X = 0.5r$. Increasing hole diameter reduces the in-plane stiffener stiffness, therefore reduces stiffener stress. Contrary, chord ovalisation increases, which affects the stress negatively at the saddle. Due to tubular chord stiffness, varying hole diameter for $\frac{D_{hole}}{D_{avg}} < 0.5$ does not affect chord and stiffener stress.

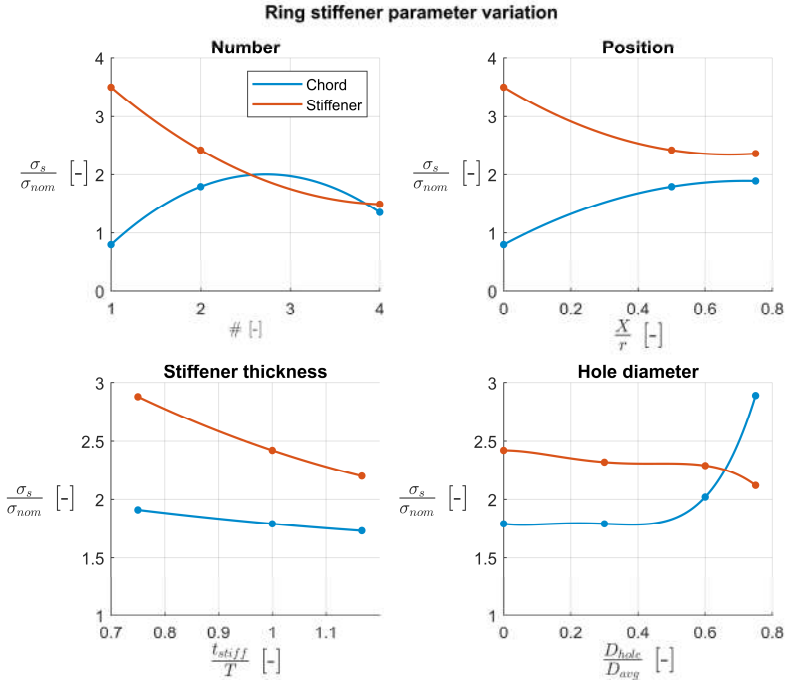


*Figure 100: SCF effect of ring stiffener parameter variation*

A tubular joint design is made based on the parametric study. The objective is to reduce chord stress at the saddle location to achieve a fatigue damage smaller than 1, while the stiffener stress magnitude is lower compared to the saddle chord stress, since a critical location with low accessibility is not preferred. The stiffener parameters of the tubular joint design are summarised in Table 45 and is shown by Figure 101. Concluded by Figure 100, increasing the number of stiffeners to 4 and increasing stiffener thickness, both reduces chord and stiffener stresses, therefore 4 ring stiffeners with thicknesses equivalent to the chord thickness are applied. The stiffeners are positioned at $X = 0.5r$ and $X = 0.75r$, since locating the stiffeners closer to the saddle results in higher stiffener stress. To distribute loading uniformly along the 4 ring stiffeners, hole diameters of located at $X = 0.5r$ are larger compared to the ring stiffeners located at $X = 0.75r$. Figure 102 presents the stress distribution around the circumference of the complex tubular joint, clearly illustrating the ring stiffener positions and a more uniform stress distribution. Compared to the simple tubular joint, a saddle structural stress reduction of 4.1 is achieved. The hot spot stress is reduced by a factor of 3.9. The tubular joint is loaded by a bending/axial loading ratio of 0.2, equivalent to the loading for the stress distribution shown in Figure 97. Structural SCF's of the ring stiffeners located at $X = 0.5r$ and $X = 0.75r$ are 1.45 and 1.29, respectively.

*Table 45: Stiffener parameters complex tubular joint design*

| Stiffener parameters | | |
|---|---|---|
| # [-] | 4 | |
| $X/r$ [-] | 0.50 | 0.75 |
| $t_{stiff}/T$ [-] | 1 | 1 |
| $D_{hole}/D_{avg}$ [-] | 0.75 | 0.60 |

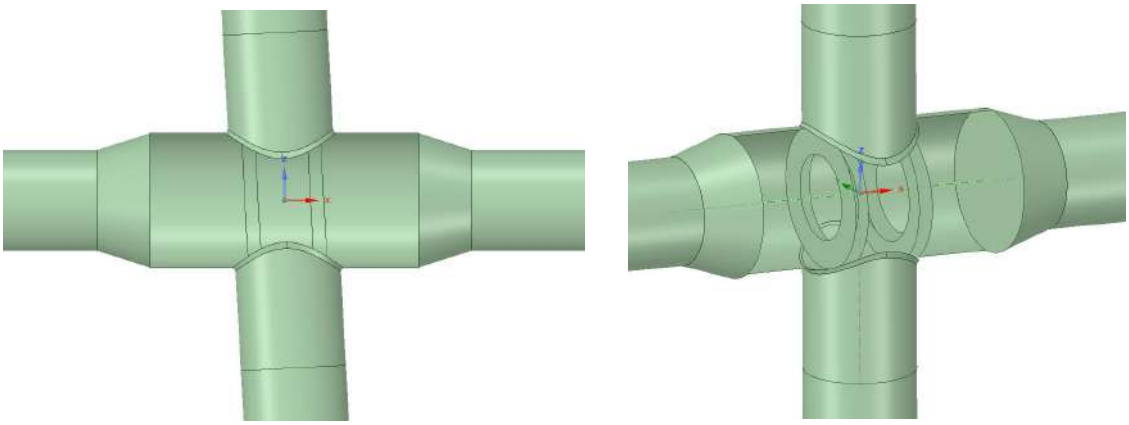

*Figure 101: Complex tubular joint surface model*

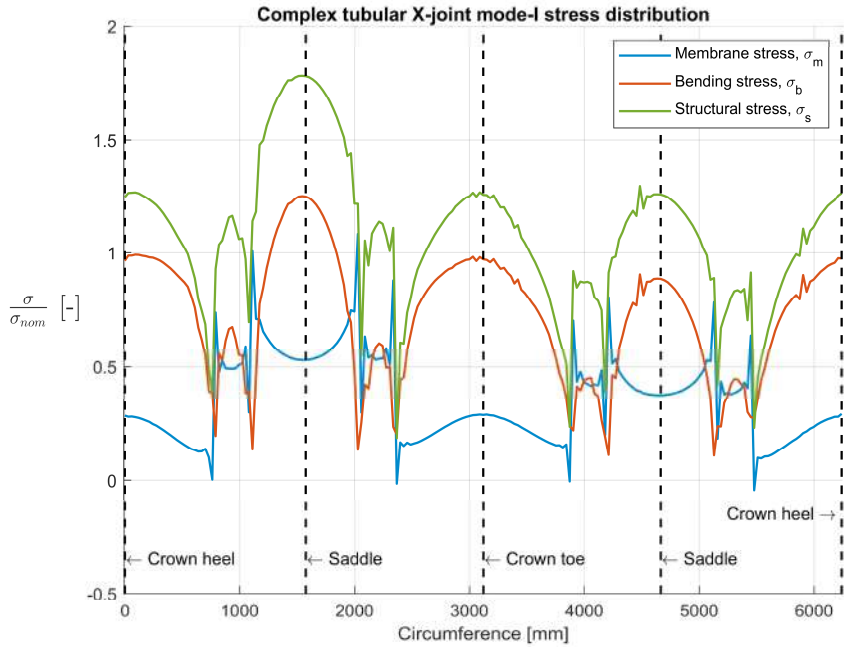


*Figure 102: Mode-I stress distribution of complex tubular joint*

### *5.4.2.2 Fatigue damage*

Since the saddle chord weld toe remains the critical location, structural stress RAO's and the mean buoyancy stress are divided by the stress reduction factor of 4.1. Similarly, hot spot stress RAO's are reduced by a factor of 3.9. The structural stress concept fatigue damage at the saddle crown weld toe is shown in Figure 103 per sea state and wave heading. Similar to the simple tubular joint, wave heading probability and operation lifetime distribution are not accounted for the damages in Figure 103. Total fatigue damages for the complex tubular joint are acceptable, since damages of 0.63 and 0.28 are achieved for the structural stress concept and average effective notch stress concept, respectively. The reduction in damage is most significant for the hot spot stress concept, where $D_h$ = 0.45. A single-slope T-curve with MCF range parameters results in $D_h$ = 16.

Since the hot spot stress ranges are now mostly below the knee point, the allowable number of cycles increase significantly due to the slope change present at $N = 10^7$. As discussed in Chapter 5.3.5, the design S-N curves of the structural stress and average effective notch stress concepts do not account for a slope change in the HCF region, while DNV-GL and IIW state a slope change is present based on internal test results. If a slope change is correct, the single-slope design curves of the structural stress and average stress concept are conservative in the HCF region. It is therefore recommended to include more fatigue tests of failed specimens in the HCF region and study the slope change.

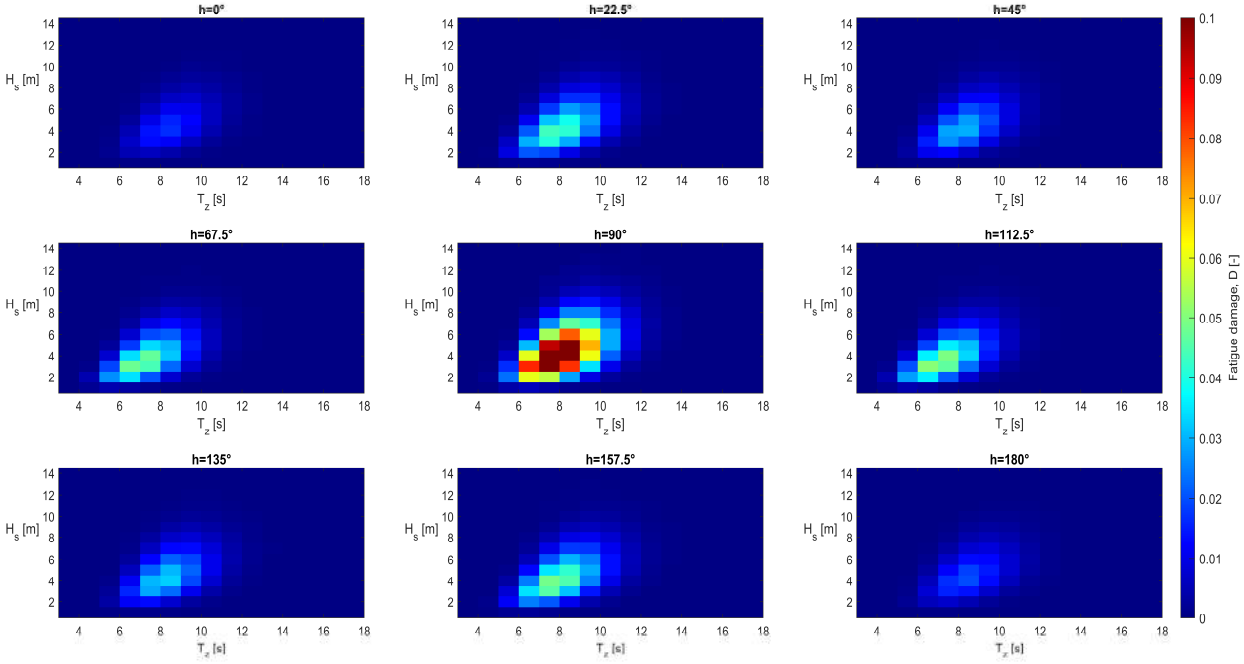


*Figure 103: Complex tubular joint, structural stress concept fatigue damage*

# 6 Conclusion

The assignment objectives were defined as follows. The first objective was to study the structural design impact on a twin-pontoon semi-submersible when applying different bracing configurations. Second, the aim was to perform a detailed fatigue assessment to accurately estimate the fatigue lifetime of a fatigue sensitive location. Finally, fatigue resistance similarity between SSS planar joints and LSS tubular joints is studied. The assignment main research question is defined as "*What is the impact of different bracing configurations on the structural design of a twin-pontoon semi-submersible in terms of weight, VCG, payload, structural redundancy and fatigue, and what is the fatigue lifetime of a critical connection when one bracing configuration is selected?*" The paragraphs below summarise the conclusions per topic.

**Semi-submersible loading and responses**
Semi-submersible hydromechanical loading and responses were studied in Chapter 2. Hydromechanical loads are the collective term of forces and moments caused by water loading and are the superposition of the wave, diffraction, radiation, and hydrostatic loading types. Responses governing for the ULS, ALS and FLS of a semi-submersible are referred to as characteristic responses. Through a hydrodynamic diffraction analysis, the influence of bracings on characteristic responses has been studied. Generally, an increase in bracing diameter results in an increase in characteristic response. However, bracings do not affect characteristic responses much, as differences below 11% are observed when varying bracing diameter. Compared to characteristic loading, characteristic deck mass accelerations are less affected when bracing diameter is varied. When the Morison equation is used to approximate the change in characteristic loading for varying bracing diameters, similar results are obtained compared to characteristic loading solely computed by AQWA.

**Global strength assessment**
Global strength assessments were performed in Chapter 3 using FEA for different bracing configurations shown in Figure 104. Each bracing configuration differentiates itself being beneficial for certain load cases, or is beneficial regarding fatigue sensitive locations. ULS and ALS were evaluated through global loading by known splitting forces of the reference semi-submersible and local bracing loading by the Morison equation. The structural design of semi-submersibles with different bracing configurations were modified to have similar structural performance compared to the reference semi-submersible. The bracing configurations were evaluated based on payload, structural VCG, structural redundancy and fatigue. Generally, the presence of transverse horizontal bracings affects structural performance most significantly, since a payload reduction of 22% is observed when not present, due to the dominant splitting force load case and ineffective load path. Adding diagonal bracings in the horizontal or vertical plane, reduces column and deckbox loading for the longitudinal shear, torsion moment and inertia load cases, resulting in a payload increase up to 5%. Omitting braces results in the lowest amount of fatigue sensitive locations. However, since the columns and deckbox structure needs strengthening, welding volume at other fatigue sensitive locations increases, which affects fatigue negatively. An overview of the bracing configuration ranking is provided in Table 46. $\Delta_{payload}$ and $\Delta_{VCG}$ are defined as payload and structural VCG differences with respect to the reference semi-submersible. Structural redundancy is mainly evaluated by the difference in number of bracing members, $\Delta_{\#bracings}$, where an increase in number of bracings is favourable. Fatigue is mainly evaluated by welding volume at identified fatigue sensitive locations, where a negative welding volume difference, $\Delta_{Vweld}$, with respect to the reference semi-submersible is advantageous. Bracing configuration 2 is preferred when payload, structural VCG, structural redundancy and fatigue are all of equal importance.

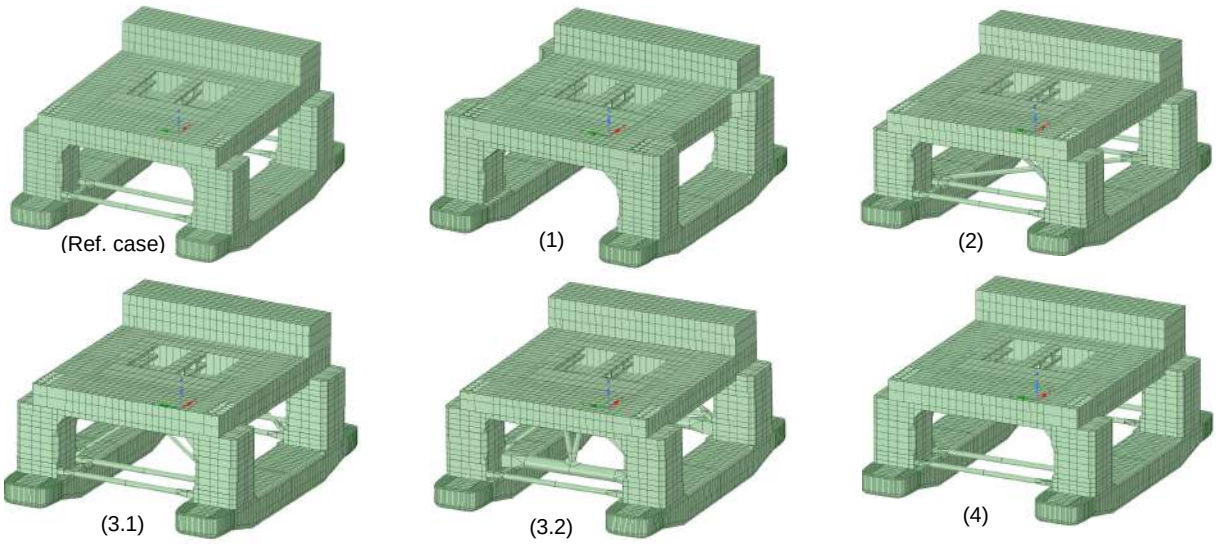


*Figure 104: Bracing configurations*

*Table 46: Ranking bracing configurations*

| Ranking | Payload | | Structural VCG | | Structural redundancy | | Fatigue | |
|---|---|---|---|---|---|---|---|---|
| | Config. | $\Delta_{payload}$ | Config. | $\Delta_{VCG}$ | Config. | $\Delta_{\#bracings}$ [-] | Config. | $\Delta_{Vweld}$ [dm$^3$] |
| 1 | 3.2 | +5% | 3.2 | -4% | 3.2 | 8 | 3.1 | -45 |
| 2 | 2 | +4% | 2 | -2% | 3.1 | 4 | Ref. case | 0 |
| 3 | 3.1 | +1% | 4 | 0% | 2 | 2 | 4 | +28 |
| 4 | Ref. case | 0% | 3.1 | 0% | 4 | 0 | 2 | +35 |
| 5 | 4 | -2% | Ref. case | 0% | Ref. case | 0 | 1 | +73 |
| 6 | 1 | -22% | 1 | +7% | 1 | -4 | 3.2 | +867 |

**SSS planar joint and LSS tubular joint fatigue resistance similarity**

The fatigue resistance similarity between SSS planar joints and LSS tubular joints has been examined in Chapter 4 by the hot spot stress and averaged effective notch stress concepts. Fatigue resistance data of SSS planar joint specimens were provided by TU Delft. Five LSS tubular joints with differences in geometry and boundary conditions were studied by shell FEA and volume FEA. LSS tubular joint fatigue test information was derived from literature, where the tubular and weld geometry, boundary conditions and fatigue lifetime was reported.

Including weld geometry in shell FEA results in better agreement of the structural stress compared to volume FEA, since chord local bending moments are more accurate. The significance of including weld geometry increases by larger weld size. Increasing weld length, $l_w$, reduces the weld notch angle, which lowers the chord nodal moments, since the weld nodal force direction is more aligned with the chord surface. Moreover, including weld geometry can result in different global stress flow. The studied LSS tubular joints demonstrate not including weld geometry in shell FEA can overestimate bending stress up to 208%.

The average effective notch stress of LSS tubular joints was computed through weld toe notch stress integration. The weld toe notch stress distributions, based on shell FEA structural stress, were verified by detailed volume FEA. For most LSS tubular joints, similarity with respect to SSS planar joints has increased for the average effective notch stress concept, compared to the hot spot stress concept. Most LSS tubular joints fit inside the average effective notch stress SSS planar joint fatigue resistance data. For divergent LSS tubular joints, dissimilarity is most likely linked to differences in actual and interpreted specimen boundary conditions and weld geometries. Fatigue resistance similarity, expressed as the strength scatter index, $T_{\sigma S}$, and intercept, $\log_{10}(C)$, of LSS tubular joints is increased compared to hot spot fatigue resistance, see Table 47. Differences in slope $m$ are similar, therefore similarity between SSS planar joints and LSS tubular joints is comparable to that respect. More LSS tubular joints should be studied to demonstrate similarity with higher confidence, shown by CLB and CUB.

*Table 47: Fatigue resistance similarity comparison*

| Similarity indicator | Specimen | Hot spot stress concept | | | Average effective notch stress concept | | |
|---|---|---|---|---|---|---|---|
| | | C95LB | $\mu$ | C95UB | C95LB | $\mu$ | C95UB |
| $T_{\sigma s}$ | SSS planar joints<br>LSS tubular joints | - | 1 : 2.18<br>1 : 2.15 | - | - | 1 : 1.64<br>1 : 1.91 | - |
| $\log_{10}(C)$ | SSS planar joints<br>LSS tubular joints | 13.13<br>12.27 | 13.86<br>12.89 | 14.58<br>13.52 | 14.44<br>13.61 | 14.94<br>14.19 | 15.43<br>14.76 |
| $m$ | SSS planar joints<br>LSS tubular joints | 3.21<br>2.81 | 3.51<br>3.08 | 3.83<br>3.36 | 3.57<br>3.13 | 3.76<br>3.37 | 3.98<br>3.61 |

**Fatigue assessment**

The brace-brace connection, classified as a tubular CHS X-joint, of bracing configuration 2 was analysed in the fatigue assessment. An operational profile with 85% operating time and worldwide operation was applied. At global level, bracings are mainly loaded by axial forcing for most wave frequencies and headings. At local level, i.e. at the tubular joint, multi-axial loading is present around the circumference. However, at the critical saddle location, mode-I stress dominates. Therefore, multi-axial fatigue is not considered. Mode-I tubular joint structural stress RAO's were derived by nodal forces and moments through FEA as input for the structural stress concept and average effective notch stress concept as fatigue assessment concepts. The X-joint fatigue damage was also assessed by the hot spot stress concept, based on DNV-GL guidelines. Hot spot stress ranges were calculated through linear surface stress extrapolation. The spectral approach by a Rayleigh distribution was used to estimate fatigue damage. Fatigue damages of $D_s$ = 51, $D_e$ = 62 and $D_h$ = 306 at the critical saddle location for the structural stress concept, average effective notch stress concept and hot spot stress concept, respectively, demonstrate the tubular joint design is insufficient with respect to the FLS. Therefore, a complex tubular CHS X-joint was designed with internal ring-stiffeners. The design was based on a parametric study, where ring-stiffener parameters were varied. Stress reduction factors of 3.9 and 4.1 were achieved for the different fatigue assessment concepts at the critical saddle location, resulting in fatigue damages of $D_s$ = 0.63, $D_e$ = 0.28 and $D_h$ = 0.45, thus acceptable. The reduction in fatigue damage for the hot spot stress concept is most significant due to the slope change accounted for in the HCF region. A single-slope hot spot stress T-curve with MCF range parameters results in $D_h$ = 974 and $D_h$ = 16 for the simple and complex tubular CHS X-joint, respectively. These higher fatigue damages are related to the lower fatigue resistance intercept and larger slope, possibly due to larger hot spot stress fatigue resistance scatter.

# 7 Discussion and recommendations

The interpretation and relevance of results are summarised in this chapter per topic. In addition, the limitations of this study are reported. Finally, recommendations are stated for further research.

## 7.1 Interpretations

**Semi-submersible loading and response**
The impact on loading and responses was studied through hydrodynamic diffraction analyses. Generally, an increase in bracing diameter results in an increase in characteristic response. However, bracings do not affect characteristic responses much, as differences below 11% are observed. Compared to characteristic loading, characteristic deck mass accelerations are less affected when bracing diameter is varied. Moreover, concluded for bracing configuration 4, bracing stresses are predominantly affected by global loading derived from splitting forces. Above concludes the global strength assessment can be simplified by only considering constant global loading, derived from splitting forces, to evaluate different bracing configurations more effectively. However, since the bracing designs were unknown at the beginning of this study, local bracing loading was accounted for by the Morison equation.

**Global strength assessment**
Payload, structural VCG, structural redundancy and fatigue rating of different bracing configurations were based on FEA global strength assessments of the ULS and ALS. Since the ULS and ALS define global structural dimensions of the semi-submersible design.

The structural design of semi-submersibles with different bracing configurations were modified through iterating to similar usage factors at the selected locations and areas, with respect to the reference semi-submersible. In addition, stress differences between outer plating and bulkheads were studied. Mass properties and parameters regarding structural redundancy and fatigue were derived from the final structural design.

The bracing configuration selection should be merely based on the semi-submersible's requirements. Therefore, the designer should first rank the requirements after which a bracing configuration can be designed. Shown by Table 46, if for instance payload and VCG are most important, configuration 3.2 would be the preferred choice. Configuration 3.1 is most favourite if the aim is to reduce the possibility of fatigue failure and to reduce maintenance and inspection costs.

**SSS planar joint and LSS tubular joint fatigue resistance similarity**
The average effective notch stress S-N plot of SSS planar joints and LSS tubular joints, see Figure 84, demonstrates fatigue resistance similarity between SSS planar joints and most LSS tubular joints. Similarity has increased with respect to $T_{\sigma S}$ and $\log_{10}(C)$, whereas slope $m$ similarity is comparable. Since not all LSS tubular joints fit inside the average effective notch stress S-N plot of SSS planar joints, similarity is partly confirmed.

**Fatigue assessment**
The operational profile is mostly based on the literature review, since owner's input is not available. The operational profile considered the semi-submersible is operating 85% of its lifetime, while it lays 15% of its life idle in a harbour. This distribution is considered conservative, since the transit basic condition is not taken into account. During the transit basic condition, characteristic loading is smaller compared to other basic conditions. Since characteristic loading is governing for bracing stresses, only considering the operational basic condition results in a overestimation of fatigue damage. It is expected the calculated fatigue damage is 2 times higher, compared to a operational profile where all basic conditions are considered.

Compared to common engineering fatigue assessment concepts, such as the nominal and hot spot stress concepts, the structural stress and average effective notch stress concepts are more detailed regarding the geometry and loading & response information involved. To elaborate, the structural stress concept calculates the actual $\sigma_f$ at the welded joint and accounts for thickness effects and loading modes through fitting. The average effective notch stress concept calculates both $\sigma_f$ and $\sigma_{se}$ at the welded joint, thus describes the total mode-I stress distribution. In addition, the structural stress and average effective notch stress concepts are less sensitive to mesh specification. Consequently, the fatigue resistance data plots of the structural stress concept and average effective notch stress concept demonstrate lower fatigue resistance scatter. Thus, ranking of fatigue assessment accuracy, $O$, is $O_e > O_s > O_h$, where subscript $e$, $s$ and $h$ represent the average effective notch stress, structural stress and hot spot stress fatigue assessment concepts, respectively. However, DNV-GL and IIW state a smaller slope is present in the HCF range, which is not accounted for in the structural stress and average effective notch stress concepts. Since fatigue resistance data is lacking in the HCF region for both the structural stress and average effective notch stress concepts, a slope change cannot be concluded and therefore possibly results in conservative fatigue damages.

A total fatigue damage below 1 was considered acceptable for the fatigue assessment. However, safety factors regarding environmental loading, manufacturing misalignments and defects, variable amplitude loading, structural redundancy and accessibility for inspection and maintenance are not accounted for.

## 7.2 Relevance

**Semi-submersible loading and responses**
The study on loading and responses, combined with the strength assessments, demonstrates the minor influence of local bracing loading. Therefore is neglectable for the global structural design. By deriving global water loading solely from splitting forces, load cases can be defined governing for the global structural design. This conclusion provides an approach for future conceptual global structural designs of semi-submersibles. It should be noted that above applies to the studied reference semi-submersible design. Ratios of frontal areas in surge, sway and heave directions of the floaters and bracings can give insight if local bracing loading is neglectable.

**Global strength assessment**
The literature review [2] identified a research gap regarding semi-submersible design. Semi-submersible designers do not state why their design is advantageous with respect to payload, redundancy, strength or fatigue in relation to the governing load cases. Using a different semi-submersible design, which alters in characteristic responses and structural stiffness properties, may result in different conclusions regarding payload, structural VCG, structural redundancy and fatigue. For example, adding horizontal diagonal bracings for a semi-submersible with lower floater stiffness in surge and sway directions, the column-deckbox connection and deckbox structure may benefit more. In addition, the effect of omitting brace reaction loading when applying hinged bracings is larger. However, ranking of the studied bracing configurations is not expected to differ for other semi-submersible designs. The relative differences in payload, structural VCG, structural redundancy and fatigue are also expected to be similar. According to a more recent study for the Wind Installation Vessel, currently being developed by Huisman, omitting transverse bracings result in a similar payload difference as concluded in this study. Above demonstrates the relevance regarding the global strength assessments performed for different bracing configurations. Therefore this study fills the first research gap identified in the literature review.

**SSS planar joint and LSS tubular joint fatigue resistance similarity**
In previous studies [47], [50], fatigue resistance similarity between SSS planar joints was studied. Due to the large scatter of SSS planar joints and LSS tubular joints observed during the literature review, similarity seemed lacking for the hot spot stress concept and was identified as the third research gap. This study concludes a reduced fatigue resistance scatter and intercept offset for LSS tubular joints by the average affective notch stress concept. Moreover, most LSS tubular joints fit inside the SSS planar joint fatigue resistance data. A SSS planar joint based design S-N curve is therefore applicable for tubular fatigue sensitive locations of semi-submersibles and other structures and increases the applicability of the average effective notch stress as fatigue assessment concept.

As concluded, more LSS tubular joints should be studied, therefore this study does not fulfil the research gap completely. Chapter 4 provides an approach to analyse other LSS tubular joints.

**Fatigue assessment**
Fatigue sensitive locations were studied in the literature review. Literature stress distributions and SCF's are not applicable due to geometric and loading differences. A detailed simple and complex tubular CHS X-joint design was therefore made at the brace-brace connection of configuration 2.

Chapter 5 can provide reference for future fatigue assessments using the structural stress and average effective notch stress as fatigue assessment concepts. Since marine and offshore structures, such as semi-submersibles [2], increasingly operate in remote areas, the demand to accurately estimate the fatigue damage increases as well. By assessing fatigue damage estimation in a more detailed manner, the possibility of service cracks reduces and maintenance and inspection work can be planned more precise.

## 7.3 Limitations

**Semi-submersible loading and responses**
The study on loading and responses is limited to varying horizontal transverse bracing diameters. Therefore, is not applicable to derive loading and response differences for other bracing configurations. Since this was not the main objective of this study, this limitation is of less importance compared to the limitations of other topics listed below.

**Global strength assessment**
Global water loading, derived from splitting forces, and local bracing loading, calculated by the Morison equation, were applied uniformly on wetted surfaces in FEA, see APPENDIX C. A non-uniform pressure distribution, derived from a hydrodynamic diffraction analysis, would be a more accurate load application. Since this results in more realistic non-uniform deformations and stresses. However, since small structural members, such as longitudinal stiffeners, are not present in the global strength models, load application by a non-uniform pressure distribution is ineffective.

The differences between the reference semi-submersible and semi-submersibles with different bracing configurations were mainly focused on differences in floater deformations and stresses for the selected locations and areas evaluated by the WSD check. In addition, stress differences between outer plating and bulkheads were studied. The structural design of semi-submersibles with different bracing configurations could therefore be more refined. However, also analysing the tween decks, frames and girders would be impractical. Because deformation and stress differences are more apparent at the selected locations and areas and outer plating and bulkheads, these parts were the main focus of the strength assessment. Moreover, since mass properties of the structural parts not considered have lower significance, differences in mass properties are not expected to change much.

**SSS planar joint and LSS tubular joint fatigue resistance similarity**
Emphasises was put on modelling the weld geometry accurately at the location of failure and weld height was kept constant along the circumference. Since this results in geometry less likely to be problematic for meshing in ANSYS. Because the weld geometry at the failure location is modelled as reported by the authors, errors regarding stress distributions and magnitudes are expected to be small. This is supported by similarity of calculated hot spot SCF's through FEA and measured hot spot SCF's reported by the authors.

Most hot spot SCF's of LSS tubular joints matched with measured hot spot SCF's by the authors. Moreover, analytical weld toe notch stress distributions were similar compared to detailed volume FEA. Dissimilarity for some LSS tubular joints can be related to divergent modelling assumptions compared to actual conditions. In the FEA, residual welding stresses are not accounted for. However, for a pulsating tensile stress, i.e. $0 < r_{lr} < 0.9$ similar to the tested LSS tubular joints, residual welding stresses should have a neglectable effect on fatigue lifetime, since residual welding stresses redistribute over time [54]. Moreover, according to C.H. Jo et al. [36], after 20 cycles no residual stress is present in a LSS tubular joint. Therefore, dissimilarity for some LSS tubular joints is most likely linked to differences in actual and interpreted specimen boundary conditions and weld geometries. In all studied fatigue test reports, the authors did not explicitly mention the restrained degree of freedoms at the supports. Moreover, all authors reported pictures of weld geometry of only one specimen, or provided a sketch of the weld geometry. Above uncertainties reduces modelling reliability and therefore accuracy of results. However, actual specimen boundary conditions and weld geometry is difficult to derive with absolute certainty based on the fatigue test reports alone.

Most importantly, due to the limited amount of LSS tubular joints studied, an increase in similarity for the average effective notch stress cannot be concluded in full.

**Fatigue assessment**
The fatigue assessment only focused on the brace-brace connection of bracing configuration 2. Since the semi-submersible consists of multiple fatigue sensitive locations, as discussed in Chapter 3.3.5.4, the fatigue assessment does not cover structural longevity of the entire semi-submersible.

## 7.4 Recommendations

Based on findings and limitations of this study, recommendations for future work is discussed below.

**Global strength assessment**
The structural design of semi-submersibles with different bracing configurations was modified through iterations to similar usage factors at the selected locations and areas, with respect to the reference semi-submersible. A more efficient method would be to write a script in FEA that modifies plate thickness based on usage factors. However, this process is difficult to implement, because all semi-submersibles with different bracing configurations required different locations of structural members, or/and added structural members. A possible approach is to modify the design globally first, after which plate thicknesses are modified by the script.

The semi-submersible design without bracings, configuration 1, was partly strengthened by increasing the column-deckbox connection knee joint size. The knee joint shape was not modified, see Figure 35. A more effective solution to reduce stress intensities is to apply a curved knee. Since stress intensity is related to a strain intensity, floater sway deformations are also lower, which is beneficial regarding dynamic floater motions studied in the vibration assessment. According to O.W. Blodgett [29], a curved knee joint reduces elastic angular deformations by a factor of two, compared to a knee joint with a bracket, similar to configuration 1. If a semi-submersible without bracings is to be designed, a curved knee joint is recommended to reduce the increase in structural mass and VCG.

**SSS planar joint and LSS tubular joint fatigue resistance similarity**
More LSS tubular joints should be studied to demonstrate similarity with higher confidence. It is expected by including more LSS tubular joints, average effective notch stress similarity indicators, $T_{\sigma S}$, $\log_{10}(C)$ and $m$, converge to magnitudes similar to SSS planar joints.

**Fatigue assessment**
The fatigue assessment only focused on the brace-brace connection of bracing configuration 2. Since the semi-submersible consists of multiple fatigue sensitive locations, as discussed in Chapter 3.3.5.4, fatigue assessments of all identified fatigue sensitive locations should be performed to ensure structural longevity of the entire semi-submersible.

DNV-GL [39] and IIW [52] both advise a knee point at $N = 10^7$ based on internal test results. The master S-N curve derived by P. Dong et al. [3] is predominantly based on fatigue tests where $10^2 \leq N_f < 10^7$. The design S-N curve of the average effective notch stress is predominantly based on fatigue tests where $10^4 \leq N_f < 10^7$. To study the presence of a slope change and to possibly establish a more accurate estimation of fatigue damage for $N > 10^7$, a recommendation for further research is to include more fatigue tests in the HCF region. However, design S-N curve parameters are difficult to derive in the HCF, due to the large fatigue resistance scatter and the low amount of failed fatigue tests available in literature.

To define an acceptable fatigue damage, safety factors for environmental loading and manufacturing misalignments and defects can be studied through a reliability analyses using FORM or Monte Carlo Simulations [21], [63]. Acceptable annual probabilities of failure and target reliabilities specified by [64] can be used as reference. Safety factors accounting for redundancy of structural members and accessibility for inspection and maintenance can be derived from guidelines, such as DNV-GL [28] or Eurocode [65].

# 8 References


[1] K. Torn, Artist, *THIALF en BYLGIA in Europoort 11-12-2016.* [Art]. 2016.

[2] D. Vis, “Literature review; Structural design semi-submersible,” Schiedam, 2021.

[3] P. Dong, M. Prager and D. Osage, “The design master S-N curve in ASME DIV 2 rewrite and its validations,” IIW, 2007.

[4] H. d. Besten, “Fatigue resistance of welded joints in aluminium high-speed craft: a total stress concept,” 2015.

[5] P. Wellens, “Motions & Loading of Structures in Waves,” TU Delft, Delft, 2019.

[6] W. M. J.M.J. Journée, Offshore Hydromechanics, Delft: Delft University of Technology, 2001.

[7] L. H. Holthuijsen, Waves in oceanic and coastal waters, New York: Cambridge University Press, 2007.

[8] DNV-GL, “DNVGL-RP-C103, Column-stabilised units,” DNV GL AS, 2015.

[9] Z. Wang, “Local Strength Analysis, Drilling Semi-Submersible,” Huisman Equipment, Schiedam, 2012.

[10] J. Morison, M. O'Brien, J. Johnson and S. Schaaf, “The force exerted by surface waves on piles,” PETROLEUM TRANSACTIONS, AIME, 1950.

[11] G. Clauss, E. Lehman and C. Östergaard, Offshore structures, Volume I: Conceptual Design and Hydromechanics, London: Springer, 1922.

[12] S. K. Chakrabarti, Handbook of Offshore Engineering, Elsevier Ltd., 2005.

[13] L. C. X. W. Jifu Zhou, “Hydrodynamic scaling and wave force estimation of offshore,” The Chinese Society of Theoretical and Applied Mechanics and Springer-Verlag GmbH Germany, Beijing, 2020.

[14] Z. Wang, “Motion Analysis, Drilling Semi-Submersible,” Huisman Equipment, Schiedam, 2012.

[15] ANSYS, “AQWA User Manual,” SAS IP, Inc, Canonsburg, 2012.

[16] Z. Wang, “Fatigue Analysis, Drilling Semi-Submersible,” Huisman Equipment, Schiedam, 2012.

[17] D. Schmidt, L. Manuel, H. H. Nguyen, L. V. S. Sagrilo and E. C. P. d. Lima, “Fatigue Reliability Analysis for Brace–Column Connection Details in a Semisubmersible Hull,” ASME, 2015.

[18] Y. G. Kok, “Fatigue analysis of semi-submersible,” 2017.

[19] J. M. Tromp, “The effect of braces in an asymmetric semi-submersible hull,” 2016.

[20] Z. Wang, “Global Strength Analysis, Drilling Semi-Submersible,” Huisman Equipment, Schiedam, 2012.

[21] O. F. Hughes and J. K. Paik, Ship structural analysis and design, New Jersey: The Society of Naval Architects and Marine Engineers, 2010.

[22] DNV-GL, “DNVGL-CG-0128; Buckling,” DNV GL AS, 2015.

[23] DNV-GL, “DNVGL-RP-C103, Column-stabilised units,” DNV GL AS, 2015.

[24] Huisman Equipment B.V., “General construction plan pontoon and column,” Huisman Equipment B.V., Schiedam, 2012.

[25] Huisman Equipment B.V., “General construction plan deckbox,” Huisman Equipment B.V., Schiedam, 2012.

[26] W. C. Young and R. G. Budynas, Roark's Formulas for Stress and Strain, McGraw-Hill, 2002.

[27] Huisman Equipment B.V., “General arrangement drilling semi-submersible,” Schiedam, 2012.

[28] DNV-GL, DNVGL-OS-C101, Design of offshore steel structures, DNVGL, 2015.

[29] O. W. Blodgett, Design of Welded Structures, Ohio: The James F. Lincoln Arc Welding Foundation, 1976.

[30] J. S. Hoving, “Structural Dynamics of Bottom Founded Offshore Structures,” TU Delft, Delft, 2019.

[31] W. Fei and L. Zheng, “Load Assessment on the Horizontal Braces of Semi-submersible Drilling Platform Under Ocean Wave,” King Fahd University of Petroleum & Minerals, Dharaan, 2016.

[32] R. Glasfeld, D. Jordan, M. Kerr and D. Zoller, “Review of structural details,” 1977.

[33] Offshore magazine, “Reviewing rig construction cost factors,” July 2012. [Online]. Available: https://www.offshore-mag.com/business-briefs/equipment-engineering/article/16760123/reviewing-rig-construction-cost-factors. [Accessed June 2021].

[34] H. d. Besten, “Fatigue damage criteria classification, modelling developments and trends for welded joints in marine structures,” Ships and Offshore Structures, 2018.

[35] P. v. Lieshout, H. d. Besten and M. Kaminski, “Comparative study of multiaxial fatigue methods applied to welded joints in marine structures,” Frattura ed Integrità Strutturale, 2016.

[36] C. H. Jo, S. W. Im, W. C. Cho and K. K. Park, “Fatigue crack in large-scale tubular joints for offshore structures,” Science China Technological Sciences, 2011.

[37] O. D. Dijkstra and J. Back, “Fatigue strength of tubular T- and X-joints,” Offshore Technology Conference, 1980.

[38] M. Zhao, S. Chiew and C. Lee, “Fatigue behaviour of rectangular built-up hollow section joint made of high strength steel S690,” Hokkaido University Collection of Scholarly and Academic Papers : HUSCAP, Hokkaido, 2013.

[39] DNV-GL, “DNVGL-RP-C203 Fatigue design of offshore steel structures,” DNV GL AS, 2020.

[40] J. Kuoppa, J. Samuelsson, J. Sperle and L. Rydahl, Design handbook; Structural design and manufacturing in high-strength steel, SSAB, 2012.

[41] AWS, “AWS D1.1; Structural Welding Code - Steel,” American Welding Society, Miami, 2010.

[42] E. Niemi, W. Fricke and S. Maddox, Structural Hot-Spot Stress Approach to Fatigue Analysis of Welded Components, Spinger, 2018.

[43] Z.-G. Xiao and K. Yamada, “A method of determining geometric stress for fatigue strength evaluation of steel welded joints,” International Journal of Fatigue, 2004.

[44] M. Efthymiou, “Development of SCF Formulae and Generalised Influence Functions for Use in Fatigue Analysis,” Shell Internationale Petroleum Maatschappij B.V., 1988.

[45] P. Smedley and P. Fisher, “Stress Concentration Factors for Simple Tubular Joints,” ISOPE, 1991.

[46] J. Wægter, “Stress concentrations in simple tubular joints,” 2009.

[47] Y. Qin, H. d. Besten, S. Palkar and M. L. Kaminski, “Mid- and High-Cycle Fatigue of Welded Joints in Steel Marine Structures: Effective Notch Stress and Total Stress Concept Evaluations,” Internation Journal of Fatigue, 2021.

[48] A. Romeijn, “The fatigue behaviour of multplanar tubular joints,” Heron, 1994.

[49] P. Dong, “A structural stress definition and numerical implementation for fatigue analysis of welded joints,” International Journal of Fatigue, 2001.

[50] Y. Qin, H. d. Besten, S. Palkar and M. L. Kaminski, “Fatigue design of welded double-sided T-joints and double-sided cruciform joints in steel marine structures: A total stress concept,” John Wiley & Sons Ltd., 2019.

[51] Gangsteel, “BS 4360 Weldable Steel Plate,” [Online]. Available: https://gangsteel.net/product/Carbon/Q/BS-4360/2012/0914/50C.html. [Accessed 7 2021].

[52] A. F. Hobbacher, “The new IIW recommendations for fatigue assessment of welded joints and components—A comprehensive code recently updated,” International Journal of Fatigue , 2009.

[53] K. Rother and W. Fricke, “Effective notch stress approach for welds having low stress concentration,” International Journal of Pressure Vessels and Piping, 2016.

[54] J. Klassen, N. Friedrich, W. Fricke, T. Nitschke-Pagel and K. Dilger, “Influence of residual stresses on fatigue strength of large-scale welded assembly joints,” International Institute of Welding, 2016.

[55] DNV-GL, “DNVGL-CG-0130; Wave loads,” DNV GL AS, 2018.

[56] S. E. Hirdaris, W. Bai, D. Dessi, A. Ergin, X. Gue, O. A. Hermundstad, R. Huijsmans, K. Iijima, U. D. Nielsen, J. Parunov, N. Fonseca, A. Papanikolaou, K. Argyriadis and A. Incecik, “Loads for use in the design of ships and offshore structures,” Ocean Engineering, 2014.

[57] H. d. Besten, “Fatigue strength in marine structures (lectures),” TU Delft, Delft, 2020.

[58] J. P. Quigley, Y. L. Lee and L. Wang, “Review and Assessment of Frequency-Based Fatigue Damage Models,” SAE; Society of Automotive Engineers, 2016.

[59] P. Ragan and L. Manuel, “Comparing Estimates of Wind Turbine Fatigue Loads using Time-Domain and Spectral Methods,” Wind Engineering, 2007.

[60] A. Varias, “Fatigue of tubular joints: Effect of ring stiffeners on stress concentration,” Arnhem, 1994.

[61] M. M. K. Lee and A. Llewelyn-Parry, “Strength of ring-stiffened tubular T-joints in offshore structures - a numerical parametric study,” Journal of Constructional Steel Research, 1998.

[62] D. S. R. Murthy, A. M. Rao and P. Gandhi, “Stress concentration in internally ring stiffened steel tubular joints used in offshore structures,” The International Society of Offshore and Polar Engineers, Seoul, 1990.

[63] S. K. Choi, R. V. Grandhi and R. A. Canfield, “Reliability-based Structural Design,” Springer-Verlag London Ltd., London, 2007.

[64] DNV, “Structural reliability analysis of marine structures,” Det Norske Veritas, 1992.

[65] Eurocode, “EN-13001-3-1; Cranes - General Design - Part 3-1: Limit States and proof competence of steel structures,” Koninklijk Nederlands Normalisatie-instituut, Delft, 2018.

[66] L. C. Bian and J. K. Lim, “Fatigue strength and stress concentration factors of CHS-to-RHS T-joints,” Journal of Constructional Steel Research, 2003.

[67] J. G. Wilde and A. McDonald, “The influence of joint dimensions on the fatigue strength of welded tubular joints,” International Journal of Fatigue, 1980.

[68] A. Schumacher and A. Nussbaumer, “Experimental study on the fatigue behaviour of welded tubular K-joints for bridges,” Engineering Structures, 2005.

# APPENDIX

| | |
|---|---|
| APPENDIX A | Input ANSYS AQWA hydrodynamic diffraction analysis |
| APPENDIX B | Input ANSYS AQWA hydrodynamic response analysis |
| APPENDIX C | Input ANSYS Workbench FEA |
| APPENDIX D | Global strength assessment stress results and WSD check bracing configurations |
| APPENDIX E | LSS tubular joint fatigue resistance tests |

# APPENDIX A Input ANSYS AQWA hydrodynamic diffraction analysis

In this section, the input for the AQWA hydrodynamic diffraction analysis of the simple geometry is reported. The hydrodynamic diffraction analysis in ANSYS Workbench is able to account for diffraction and radiation forces using a panel method based on the 3D-geometry the user specifies. When solved, typical RAO's, such as for the motion or splitting forces can be retrieved.

**Geometry**

An example of the 3D geometry is depicted in Figure 105. The simple geometry has the same overall dimensions as the reference semi-submersible as shown in Figure 106. The operational condition is used as basic condition, corresponding to a draught of 20 meters. The hull is modelled using surfaces which are connected by forming one part to ensure a connected mesh for the complete structure. The geometry used for the Morison equation validation was modelled using different parts for the hull and the bracings to be able to calculate the different force components. The bracings were connected to the hull by "structure to structure joints."

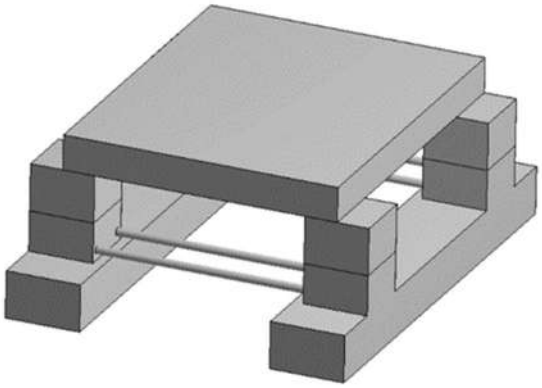

*Figure 105: Simple geometry 3D model*

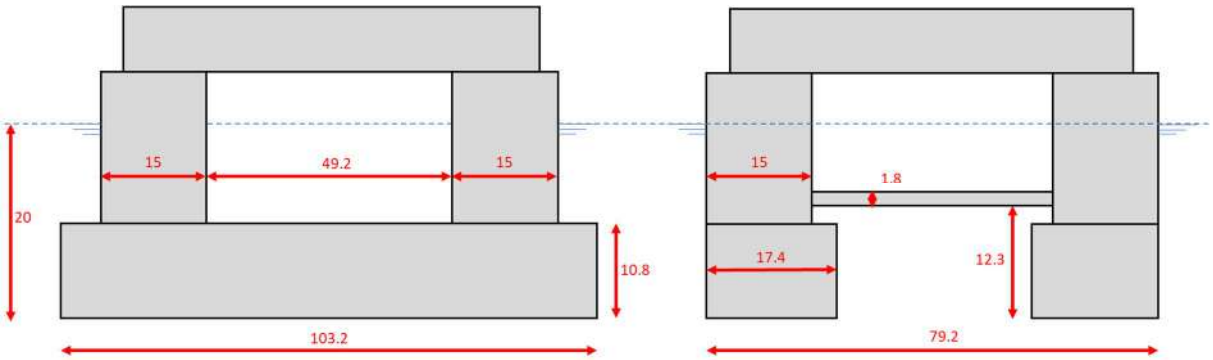


*Figure 106: Dimensions simple geometry*

The point mass with its location and inertia properties specified in Table 48 was assigned to the semi-submersible part. The location of the point mass and the inertia coefficients were retrieved from the Motion Analysis report [14]. No additional damping coefficients were included in the diffraction analyses.

*Table 48: Point mass properties*

| | | | |
|---|---|---|---|
| **Mass** | Program controlled (48570 mT for the geometry as depicted in Figure 105) | | |
| **Mass location (w.r.t. global coordinate system)** | X = 39.6 m | Y = 0 m | Z = 26.2 m |
| **Inertia properties** | Ixx = 3.77E+10 kgm$^2$ | Iyy = 4.19E+10 kgm$^2$ | Izz = 4.65E+10 kgm$^2$ |

**Mesh specification**
The surfaces were meshed using quad elements illustrated in Figure 107. The relevance centre was set to fine and the maximum element size was specified as 2 meters. No mesh convergence study was performed.

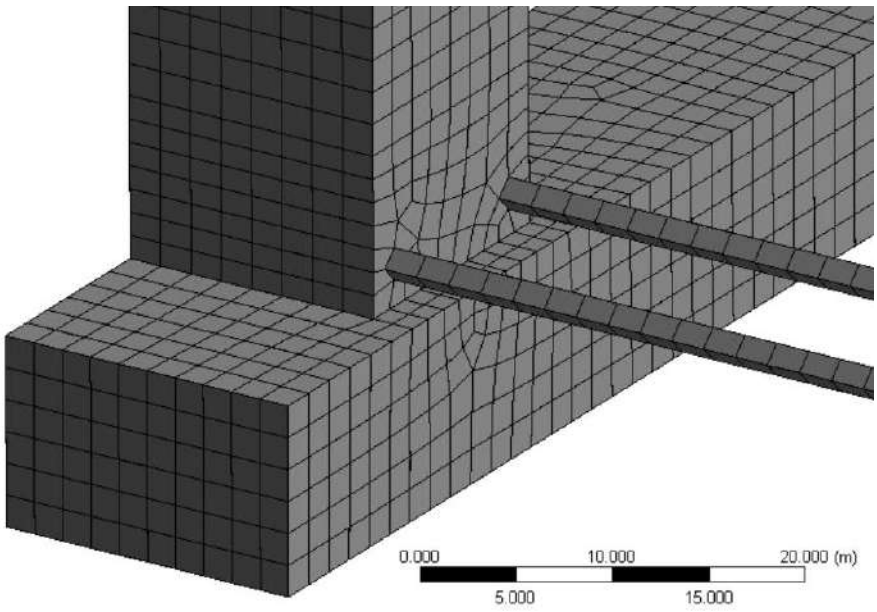


*Figure 107: Mesh elements simple geometry*

**Environment**
A standard water depth of 1000 meters was used to simulate deep water conditions. The density of water was specified as 1025 kg/m$^3$ and the gravitational acceleration was 9.81 m/s$^2$. The wave heading range was program controlled set from -180 to 180 degrees with intervals of 15 degrees. The wave periods were manually defined with 4 seconds as the shortest and 30 seconds as the longest wave period. The number of intermediate wave periods was set to 60 to be able to calculate RAO's with narrow peaks accurately.

# APPENDIX B Input ANSYS AQWA hydrodynamic response analysis

As input for the hydrodynamic response analysis, the diffraction analysis was coupled to this system. Therefore, the same system input, such as geometry, mesh and environment applies to this system. The response analysis uses the results of the diffraction analysis in the frequency domain to compute the motions and forces in the time domain.

**Analysis settings**
A regular wave response analysis was specified to validate the results of the Morison equation. The time interval was set to 0.5 seconds, which was considered accurate enough to simulate occurring motions and forces.

**Regular wave**
The semi-submersible was loaded by a unidirectional regular wave based on Airy wave theory, where the user can specify the amplitude, period and heading the waves have. A program controlled wave ramp was specified to reduce the transient motions at the beginning of the analysis.

**Deactivated freedoms**
For the response analysis the surge, sway and yaw motions were restrained. The yaw motion is restrained to keep the wave heading constant, while the surge and sway constrains keep the vessel on its x- and y-coordinates. However, the constraining surge and sway omits first order surge and sway motions, although these are included in the Morison load calculation. The surge and sway motions are restrained because otherwise the semi-submersible would drift away from its location. Resulting in unrealistic low surge and sway water flow velocities and therefore forces at the bracings. A solution could be to add a mooring system to the analyses to restrain the semi-submersible that still enables surge and sway motions. However, this would increase the complexity of the analysis as mooring stiffness and fairlead and anchor points have to be specified.

# APPENDIX C Input ANSYS Workbench FEA global strength assessment

**Workflow**

The workflow used in Workbench is shown in Figure 108. Illustrating the semi-submersible and bracing structure is imported and meshed separately to reduce the effort of pre-processing parts if only one is modified.

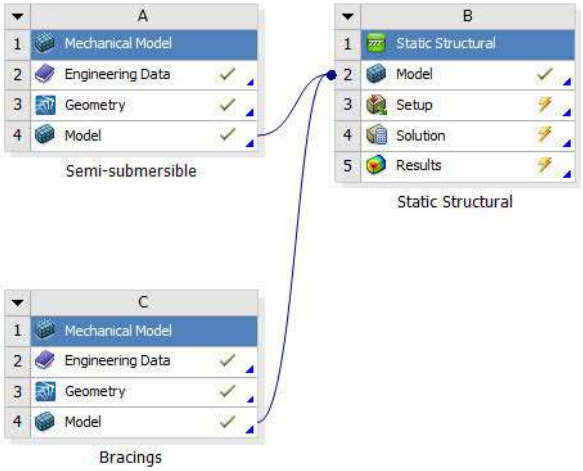


*Figure 108: ANSYS Workbench workflow*

**Material specification**

Standard linear elastic structural steel was used for all surfaces. The relevant properties are shown in Table 49.

*Table 49: Properties of structural steel*

| Property structural steel | Value |
|---|---|
| Density | 7850 kg/m$^3$ |
| Young's modulus | 200000 MPa |
| Shear modulus | 166667 MPa |
| Poisson's ratio | 0.3 |

**Geometry**

A 3D surface geometry of the semi-submersible similar to the reference semi-submersible was made. The model for the global strength analysis included the main structural components of the semi-submersible, such as transverse and longitudinal bulkheads and main stiffeners. The deck horizontals were also taken into account. The stiffeners between the frames (typical HP260x10) are not modelled, as this results in a model too large to be computationally efficient to evaluate the different bracing designs. The semi-submersible is modelled such that the stiffness distribution is roughly similar to the actual semi-submersible. Therefore, stress distributions are also similar. In Figure 109, screenshots of the semi-submersible geometry used for the global strength assessment are shown. The thicknesses allocated to the surfaces were based on the reference semi-submersible and are summarised in Table 50 and Figure 111.

*Table 50: Thicknesses semi-submersible components*

| Part | Component | | Thickness [mm] |
|---|---|---|---|
| Pontoons | Outer plating | | 18 |
| | Transverses | | 12 |
| | Longitudinals | | 14 |
| | Horizontals | | 15 |
| Columns | Outer plating | All other | 18 |
| | | Brace-column connection | 60/25 |
| | Transverses | All other | 15 |
| | | Brace-column connection | 40 |
| | Longitudinals | | 15 |
| | Horizontals | All other | 15 |
| | | Brace-column connection | 40 |
| Deckbox | Transverses | Frames | 12 |
| | | Bulkheads | 20 |
| | Longitudinals | Frames | 12 |
| | | Bulkheads | 20 |
| | Horizontals | Bottom and main deck | 20 |
| | | Lower and tween deck | 12 |

In the geometry section, point masses were added based on the operational basic condition. The point masses were allocated to the portside and starboard side pontoons and deckbox as shown by Figure 110. Regarding the settings of the point masses, the behaviour was set to deformable to allow deformations of the deckbox and pontoon structure. For the pontoons, the point masses are distributed over all the surfaces present. For the deckbox, the point masses are distributed over all the in-plane surfaces with respect to the gravitational acceleration, i.e. the transverse and longitudinal geometry are loaded by the point masses. In Table 51 point mass properties of the different parts in operation condition are reported, where the centre of gravity of the different parts are with respect to the centre of mass of the semi-submersible. It should be noted that the mentioned point masses are valid for the reference case, resulting in equilibrium between mass and hydrostatic pressure at 20 m draught. For the other bracing designs the point mass in the pontoons are modified to achieve equilibrium.

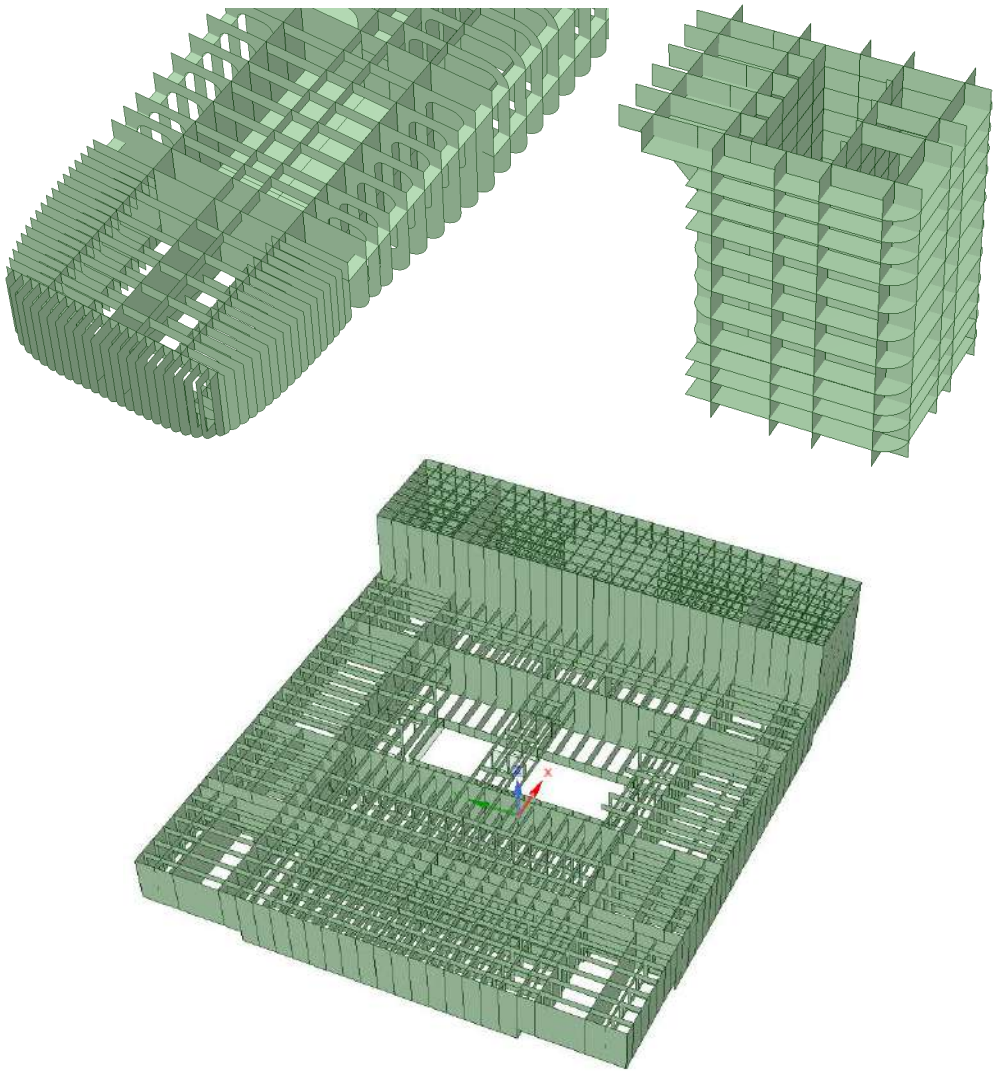

*Figure 109: Inner structural components of pontoon (top left), column (top right) and deckbox (bottom)*

*Table 51: Point mass properties operational basic condition, reference case*

| Point mass | Mass [t] | CoG (x,y,z) [mm] | | Ixx [tm$^2$] | Iyy [tm$^2$] | Izz [tm$^2$] |
|---|---|---|---|---|---|---|
| | | Port | Starboard | | | |
| Deckbox | 10024 | (-842, -16800, 12664) | (-842, 16800, 12664) | 1.21E+6 | 8.25E+6 | 6.63E+6 |
| Pontoon | 5123 | (-911, -30900, -23516) | (-911, 30900, -23516) | 0 | 2.20E+6 | 0 |

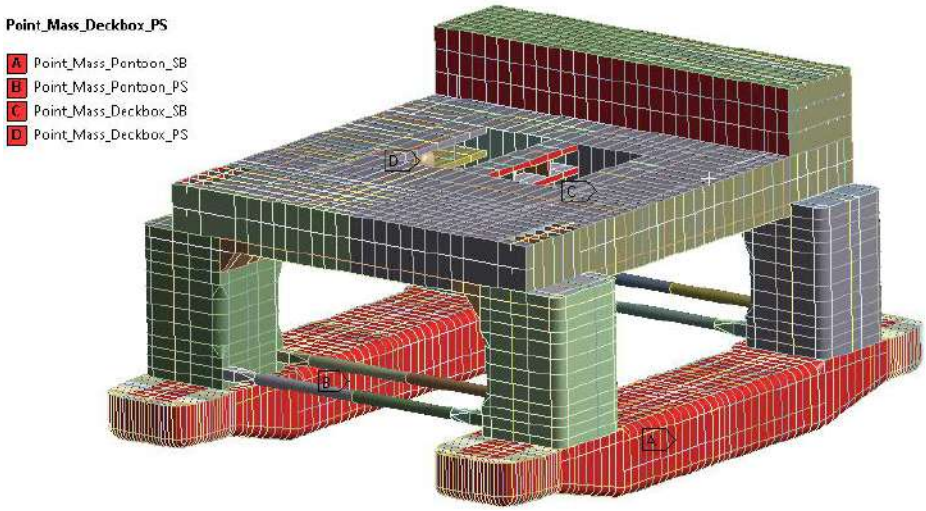


*Figure 110: Point masses FEA analysis*

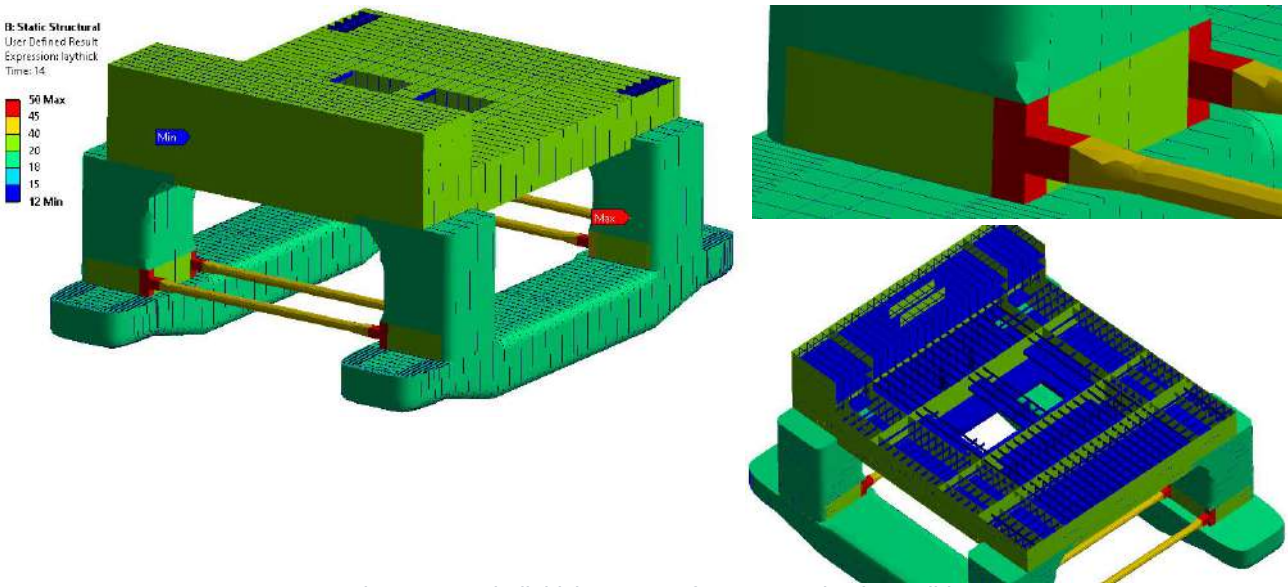


*Figure 111: Shell thicknesses reference semi-submersible*

**Mesh specification**

All surfaces were meshed with standard SHELL181 elements using quad shapes. For the semi-submersible the default size was set to 1200 mm and is refined to 600 mm at the brace-column connection. Bracing mesh size was set to 600 mm. Other than standard settings, the “Capture Curvature” setting was set to “No” to avoid disproportional mesh refined areas such as at the transition from tubular to square bracings. No mesh convergence study was performed, since the semi-submersibles with different bracing configurations were meshed according to the same mesh specification.

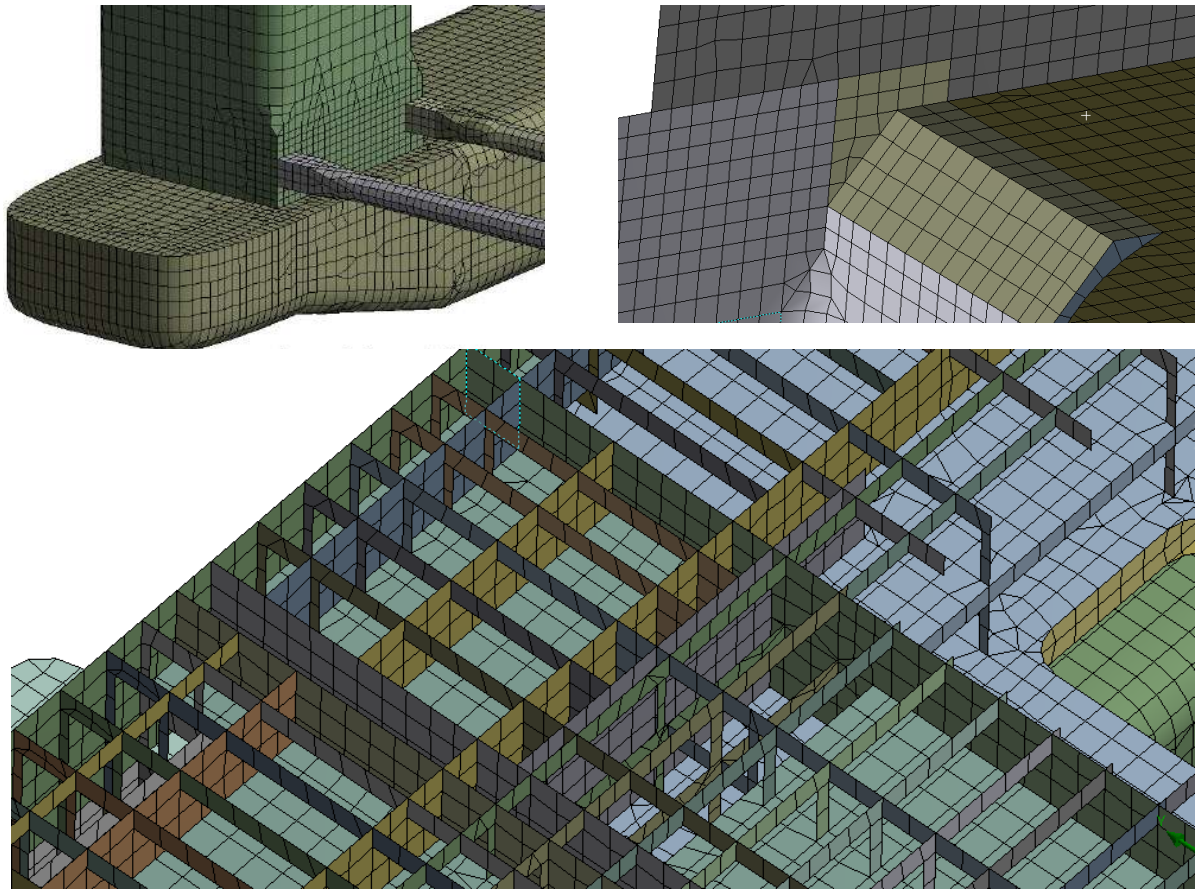

*Figure 112: Mesh specification pontoon+bracings+column (top left), column+deckbox (top right) and inner members deckbox (bottom)*

**Load specification**

*1. Standard earth gravitational acceleration*
To enable the structural and applied point masses, standard earth gravitational acceleration was inserted.

*2. Hydrostatic pressure*
Hydrostatic pressure was applied to the outer hull of the semi-submersible and bracings for an operational draught of 20 m. Water density was set to 1025 kg/m$^3$.

*3. Water loading semi-submersible hull*
Water loading based on the splitting forces as reported in Chapter 3.2.1.2 was applied to the wetted areas as shown in Figure 113 as remote forces and moments. The point of application of the remote loads was assumed to be the centre of the wetted surfaces, therefore [x=39.6m, y=31.135m, z=7.868m] for the portside hull and [x=39.6m, y=-31.135m, z=7.868m] for the starboard hull with respect to the main coordinate system.

*4. Water loading bracing*
Also covered in Chapter 3.2.1.2, the bracing loading was applied to the outer surfaces of the bracings using remote forces and moments. Just as the water loading for the semi-submersible hull, the point of application was set to the centre of selected area per bracing.

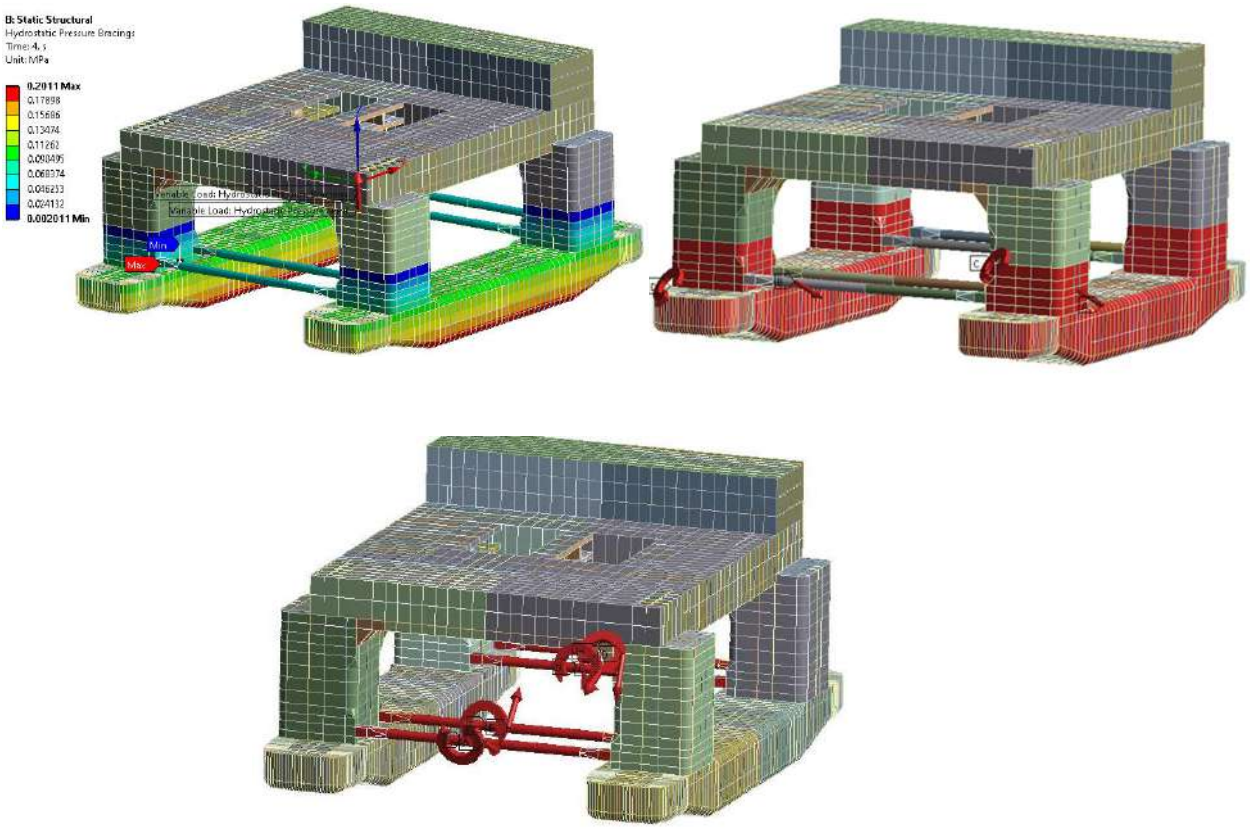


*Figure 113: Load specification of hydrostatic pressure (top left), global water loading semi-submersible (top right) and local water loading bracings (bottom)*

**Boundary conditions**

The model was constrained by a remote displacement applied to one edge of the deckbox geometry. The remote displacement restrains all the DOF of the edge, leading to a solvable model. The behaviour of the remote displacement was set to “Deformable”, therefore the edge can deform freely and no additional stress occurs at the edge. See the left screenshot of Figure 114 where the selected edge is highlighted.

To simulate the floating nature of the vessel, therefore restraining point loads cannot be present, the “Inertia Relief” setting is turned on. When imbalance occurs between loads, ANSYS calculates the inertia loads needed to keep the model in equilibrium. ANSYS therefore applies translational and rotational accelerations to all bodies. In the right screenshot of Figure 114 the Inertia Relief setting is shown.

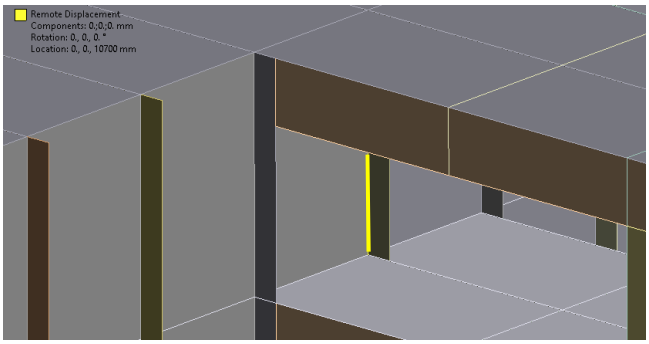


Details of "Analysis Settings"

| | |
|---|---|
| **Step Controls** | |
| Number Of Steps | 14. |
| Current Step Number | 4. |
| Step End Time | 4. s |
| Auto Time Stepping | Program Controlled |
| **Solver Controls** | |
| Solver Type | Program Controlled |
| Weak Springs | Off |
| Solver Pivot Checking | Program Controlled |
| Large Deflection | Off |
| Inertia Relief | On |
| Quasi-Static Solution | Off |

*Figure 114: Boundary conditions showing remote displacement (left) and inertia relief setting (right)*

# APPENDIX D Global strength assessment stress results and WSD check bracing configurations

From Table 52 to Table 56, the stresses and WSD check of the selected areas and locations are presented for the final structural designs of semi-submersibles with different bracing configurations.

*Table 52: Maximum equivalent stress at selected locations, Configuration 1 final design*

| Limit state | Area / location | | Yield check | | | Buckling check | | | | |
|---|---|---|---|---|---|---|---|---|---|---|
| | | | FEA $\sigma_{eq}$ | Gov. load case | $\frac{\eta}{\eta_p}$ | FEA $\sigma_x$ | FEA $\sigma_y$ | FEA $\tau_{xy}$ | Gov. load case | $\frac{\eta}{\eta_p}$ |
| ULS | 2 | Column outer plating | 261 | $F_S$ | 0.92 | 218 | 45 | 2 | $F_S$ | 0.82 |
| | 3.1 | Column-deckbox connection, bracket | 280 | $F_S$ | 0.99 | 210 | 0 | 104 | $F_S$ | 0.99 |
| | 3.2 | Column-deckbox connection, outer plating | 188 | $F_S$ | 0.66 | 192 | 22 | 45 | $F_S$ | 0.71 |
| | 4.1 | Bottom deck, transverse | 265 | $F_S$ | 0.93 | 185 | 37 | 8 | $F_S$ | 0.63 |
| | 4.2 | Bottom deck, longitudinal | | | | -* | | | | |
| | 5.1 | Main deck, transverse | 236 | $F_S$ | 0.83 | 235 | 8 | 12 | $F_S$ | 0.86 |
| | 5.2 | Main deck, longitudinal | | | | 99 | 15 | 40 | $F_S$ | 0.47 |

** tensile stress only*

*Table 53: Maximum equivalent stress at selected locations, Configuration 2 final design*

| Limit state | Area / location | | Yield check | | | Buckling check | | | | |
|---|---|---|---|---|---|---|---|---|---|---|
| | | | FEA $\sigma_{eq}$ | Gov. load case | $\frac{\eta}{\eta_p}$ | FEA $\sigma_x$ | FEA $\sigma_y$ | FEA $\tau_{xy}$ | Gov. load case | $\frac{\eta}{\eta_p}$ |
| ULS | 1.1 | Mid- transverse bracing | 250 | $F_S$ | 0.88 | 180 | 0 | 0 | $F_S$ | 0.95 |
| | 1.2 | Mid- diagonal bracing | 181 | $F_{comb}$ | 0.63 | 93 | 0 | 0 | $F_{comb}$ | 0.99 |
| | 2 | Column outer plating | 268 | $F_S$ | 0.94 | 221 | 57 | 1 | $F_S$ | 0.86 |
| | 3.1 | Column-deckbox connection, bracket | 280 | $a_T$ | 0.98 | 220 | 0 | 98 | $a_T$ | 1.00 |
| | 3.2 | Column-deckbox connection, outer plating | 225 | $a_T$ | 0.79 | 207 | 8 | 35 | $a_T$ | 0.85 |
| | 4 | Bottom deck | 179 | $F_{comb}$ | 0.63 | - | | | | |
| | 5.1 | Main deck, transverse | 193 | $M_T$ | 0.68 | 116 | 76 | 59 | $M_T$ | 0.61 |
| | 5.2 | Main deck, longitudinal | | | | 91 | 12 | 18 | $F_{comb}$ | 0.38 |
| ALS* | 1.1 | Mid-bracing | 338 | $F_S$ | 0.95 | 205 | 0 | 0 | $F_S$ | 0.82 |
| | 1.2 | Mid- diagonal bracing | 185 | $F_{comb}$ | 0.52 | 91 | 0 | 0 | $F_{comb}$ | 0.84 |
| | 2 | Column outer plating | 251 | $F_S$ | 0.71 | 205 | 53 | 1 | $F_S$ | 0.64 |
| | 3.1 | Column-deckbox connection, bracket | 263 | $a_T$ | 0.74 | 212 | 0 | 97 | $a_T$ | 0.77 |
| | 3.2 | Column-deckbox connection, outer plating | 264 | $a_T$ | 0.74 | 206 | 10 | 42 | $a_T$ | 0.69 |
| | 4 | Bottom deck | 164 | $F_{comb}$ | 0.46 | - | | | | |
| | 5.1 | Main deck, transverse | 185 | $M_T$ | 0.52 | 112 | 65 | 52 | $M_T$ | 0.44 |
| | 5.2 | Main deck, longitudinal | | | | 93 | 8 | 12 | $a_V$ | 0.30 |

* *ALS: damaged scenario 1, aft transverse bracing suppressed, see Chapter 3.3.2.2*

*Table 54: Maximum equivalent stress at selected locations, Configuration 3.1 final design*

| Limit state | Area / location | | Yield check | | | Buckling check | | | | |
|---|---|---|---|---|---|---|---|---|---|---|
| | | | FEA $\sigma_{eq}$ | Gov. load case | $\frac{\eta}{\eta_p}$ | FEA $\sigma_x$ | FEA $\sigma_y$ | FEA $\tau_{xy}$ | Gov. load case | $\frac{\eta}{\eta_p}$ |
| ULS | 1.1 | Mid-transverse bracing | 245 | $F_S$ | 0.86 | 146 | 0 | 0 | $F_S$ | 0.73 |
| | 1.2 | Mid-diagonal bracing | 222 | $F_{comb}$ | 0.78 | 218 | 0 | 0 | $F_{comb}$ | 0.97 |
| | 2 | Column outer plating | 260 | $F_S$ | 0.91 | 221 | 54 | 1 | $F_S$ | 0.87 |
| | 3.1 | Column-deckbox connection, bracket | 256 | $F_S$ | 0.90 | 204 | 0 | 98 | $F_S$ | 0.95 |
| | 3.2 | Column-deckbox connection, outer plating | 226 | $F_S$ | 0.80 | 202 | 18 | 45 | $F_S$ | 0.83 |
| | 4 | Bottom deck | 205 | $F_{comb}$ | 0.72 | - | | | | |
| | 5.1 | Main deck, transverse | 185 | $M_T$ | 0.65 | 112 | 100 | 59 | $M_T$ | 0.63 |
| | 5.2 | Main deck, longitudinal | | | | 91 | 6 | 12 | $a_V$ | 0.37 |
| ALS * | 1.1 | Mid-transverse bracing | 345 | $F_S$ | 0.97 | 169 | 0 | 0 | $F_S$ | 0.68 |
| | 1.2 | Mid-diagonal bracing | 211 | $F_S$ | 0.59 | 207 | 0 | 0 | $F_S$ | 0.73 |
| | 2 | Column outer plating | 243 | $F_S$ | 0.68 | 205 | 50 | 1 | $F_S$ | 0.64 |
| | 3.1 | Column-deckbox connection, bracket | 245 | $F_S$ | 0.69 | 189 | 0 | 85 | $F_S$ | 0.69 |
| | 3.2 | Column-deckbox connection, outer plating | 215 | $F_S$ | 0.61 | 197 | 15 | 50 | $F_S$ | 0.67 |
| | 4 | Bottom deck | 182 | $F_{comb}$ | 0.51 | - | | | | |
| | 5.1 | Main deck, transverse | 175 | $F_{comb}$ | 0.49 | 121 | 82 | 51 | $M_T$ | 0.47 |
| | 5.2 | Main deck, longitudinal | | | | 87 | 8 | 13 | $F_S$ | 0.28 |

** ALS: damaged scenario 1, aft transverse bracing suppressed, see Chapter 3.3.3.2*

*Table 55: Maximum equivalent stress at selected locations, Configuration 3.2 final design*

| Limit state | Area / location | | Yield check | | | Buckling check | | | | |
|---|---|---|---|---|---|---|---|---|---|---|
| | | | FEA $\sigma_{eq}$ | Gov. load case | $\frac{\eta}{\eta_p}$ | FEA $\sigma_x$ | FEA $\sigma_y$ | FEA $\tau_{xy}$ | Gov. load case | $\frac{\eta}{\eta_p}$ |
| ULS | 1.1 | Mid-transverse bracing (D=1.8m) | 126 | $F_S$ | 0.44 | 82 | 0 | 0 | $F_S$ | 0.46 |
| | 1.2 | Mid-transverse bracing (D=4.2m) | 106 | $F_S$ | 0.37 | 78 | 0 | 0 | $F_S$ | 0.28 |
| | 1.3 | Mid-diagonal bracing (D=1.4m) | 213 | $a_T$ | 0.75 | 215 | 0 | 0 | $a_T$ | 0.78 |
| | 1.4 | Mid- diagonal bracing (D=1.8m) | 121 | $a_T$ | 0.43 | 113 | 0 | 0 | $a_T$ | 0.40 |
| | 2 | Column outer plating | 253 | $F_S$ | 0.89 | 214 | 51 | 1 | $F_S$ | 0.84 |
| | 3.1 | Column-deckbox connection, bracket | 251 | $a_T$ | 0.88 | 198 | 0 | 104 | $a_T$ | 0.99 |
| | 3.2 | Column-deckbox connection, outer plating | 160 | $a_T$ | 0.56 | 145 | 9 | 35 | $a_T$ | 0.87 |
| | 4 | Bottom deck | 196 | $F_{comb}$ | 0.69 | - | | | | |
| | 5.1 | Main deck, transverse | 176 | $M_T$ | 0.62 | 104 | 101 | 56 | $M_T$ | 0.61 |
| | 5.2 | Main deck, longitudinal | | | | 92 | 8 | 19 | $F_{comb}$ | 0.39 |
| ALS 1* | 1.1 | Mid-transverse bracing (D=1.8m) | 324 | $F_S$ | 0.91 | 156 | 0 | 0 | $F_S$ | 0.46 |
| | 1.2 | Mid-transverse bracing (D=4.2m) | 90 | $F_S$ | 0.32 | 67 | 0 | 0 | $F_S$ | 0.28 |
| | 1.3 | Mid-diagonal bracing (D=1.4m) | 263 | $F_S$ | 0.93 | 259 | 0 | 0 | $F_S$ | 0.78 |
| | 1.4 | Mid- diagonal bracing (D=1.8m) | 87 | $a_T$ | 0.25 | 81 | 0 | 0 | $a_T$ | 0.40 |
| | 2 | Column outer plating | 246 | $F_S$ | 0.69 | 211 | 54 | 1 | $F_S$ | 0.84 |
| | 3.1 | Column-deckbox connection, bracket | 267 | $F_S$ | 0.75 | 220 | 0 | 104 | $F_S$ | 0.99 |
| | 3.2 | Column-deckbox connection, outer plating | 179 | $a_T$ | 0.50 | 159 | 13 | 50 | $a_T$ | 0.87 |
| | 4 | Bottom deck | 192 | $F_{comb}$ | 0.54 | - | | | | |
| | 5.1 | Main deck, transverse | 187 | $M_T$ | 0.53 | 123 | 94 | 56 | $M_T$ | 0.61 |
| | 5.2 | Main deck, longitudinal | | | | 88 | 7 | 17 | $F_{comb}$ | 0.39 |
| ALS 2* | 1.1 | Mid-transverse bracing (D=1.8m) | 106 | $F_S$ | 0.30 | 67 | 0 | 0 | $F_S$ | 0.30 |
| | 1.2 | Mid-transverse bracing (D=4.2m) | 86 | $F_S$ | 0.30 | 60 | 0 | 0 | $F_S$ | 0.17 |
| | 1.3 | Mid-diagonal bracing (D=1.4m) | 239 | $a_T$ | 0.84 | 240 | 0 | 0 | $a_T$ | 0.70 |
| | 1.4 | Mid- diagonal bracing (D=1.8m) | 87 | $a_T$ | 0.25 | 81 | 0 | 0 | $a_T$ | 0.23 |
| | 2 | Column outer plating | 221 | $F_S$ | 0.62 | 188 | 48 | 1 | $F_S$ | 0.59 |
| | 3.1 | Column-deckbox connection, bracket | 262 | $a_T$ | 0.74 | 222 | 0 | 107 | $a_T$ | 0.83 |
| | 3.2 | Column-deckbox connection, outer plating | 171 | $a_T$ | 0.48 | 161 | 8 | 45 | $a_T$ | 0.56 |
| | 4 | Bottom deck | 189 | $F_{comb}$ | 0.53 | - | | | | |
| | 5.1 | Main deck, transverse | 165 | $M_T$ | 0.46 | 101 | 91 | 51 | $M_T$ | 0.45 |
| | 5.2 | Main deck, longitudinal | | | | 88 | 8 | 17 | $F_{comb}$ | 0.29 |

** ALS 1: damaged scenario 1, aft 4.2m transverse bracing suppressed, see Chapter 3.3.3.3*
*** ALS 2: damaged scenario 2, aft middle 1.8m diagonal bracings suppressed, see Chapter 3.3.3.3*

*Table 56: Maximum equivalent stress at selected locations, Configuration 4 final design*

| Limit state | Area / location | | Yield check | | | Buckling check | | | | |
|---|---|---|---|---|---|---|---|---|---|---|
| | | | FEA $\sigma_{eq}$ | Gov. load case | $\frac{\eta}{\eta_p}$ | FEA | | | Gov. load case | $\frac{\eta}{\eta_p}$ |
| | | | | | | $\sigma_x$ | $\sigma_y$ | $\tau_{xy}$ | | |
| ULS | 1 | Mid-transverse bracing | 235 | $F_S$ | 0.83 | 156 | 0 | 0 | $F_S$ | 0.77 |
| | 2 | Column outer plating | 274 | $F_S$ | 0.96 | 225 | 55 | 1 | $F_S$ | 0.88 |
| | 3.1 | Column-deckbox connection, bracket | 282 | $a_T$ | 0.99 | 222 | 0 | 92 | $a_T$ | 0.98 |
| | 3.2 | Column-deckbox connection, outer plating | 268 | $a_T$ | 0.94 | 212 | 8 | 45 | $a_T$ | 0.89 |
| | 4 | Bottom deck | 203 | $F_{comb}$ | 0.71 | - | | | | |
| | 5.1 | Main deck, transverse | 188 | $M_T$ | 0.66 | 113 | 102 | 60 | $M_T$ | 0.64 |
| | 5.2 | Main deck, longitudinal | | | | 91 | 10 | 16 | $F_{comb}$ | 0.37 |
| ALS * | 1 | Mid-transverse bracing | 335 | $F_S$ | 0.94 | 171 | 0 | 0 | $F_S$ | 0.67 |
| | 2 | Column outer plating | 255 | $F_S$ | 0.72 | 203 | 50 | 1 | $F_S$ | 0.64 |
| | 3.1 | Column-deckbox connection, bracket | 293 | $F_S$ | 0.83 | 228 | 0 | 108 | $F_S$ | 0.85 |
| | 3.2 | Column-deckbox connection, outer plating | 254 | $F_S$ | 0.72 | 222 | 11 | 55 | $F_S$ | 0.76 |
| | 4 | Bottom deck | 192 | $F_{comb}$ | 0.54 | - | | | | |
| | 5.1 | Main deck, transverse | 174 | $M_T$ | 0.49 | 123 | 97 | 45 | $M_T$ | 0.47 |
| | 5.2 | Main deck, longitudinal | | | | 93 | 8 | 8 | $a_V$ | 0.30 |

** ALS: damaged scenario 1, aft transverse bracing suppressed, see Chapter 3.3.4.2*

# APPENDIX E LSS tubular joint fatigue resistance tests

The LSS tubular joint specimen boundary conditions, geometry details and FEA modelling interpretations are reported below. An important note for all specimens is that emphasises is put on modelling the weld geometry accurately at the location of failure. Weld height is kept constant around the circumference of the joint, since it results in geometry less likely to be problematic for meshing in ANSYS.

## E1: Specimen 1; Jo et al., CHS K-joint loaded by IPB

**Specimen**

Tubular CHS K-joint, as shown in Figure 115. Braces are welded by a groove weld around the full circumference of the joint. The upward tensile forcing results in IPB dominant loading at the tubular joint and therefore tensile stress at the crown heel weld toe, which is the failure location shown in Figure 116. Weld geometry modelled for the shell and volume FEA is based on Figure 116, where $\delta = 18.5°$ and $l_e = t/4 \approx 5\,mm$ for the crown heel location.

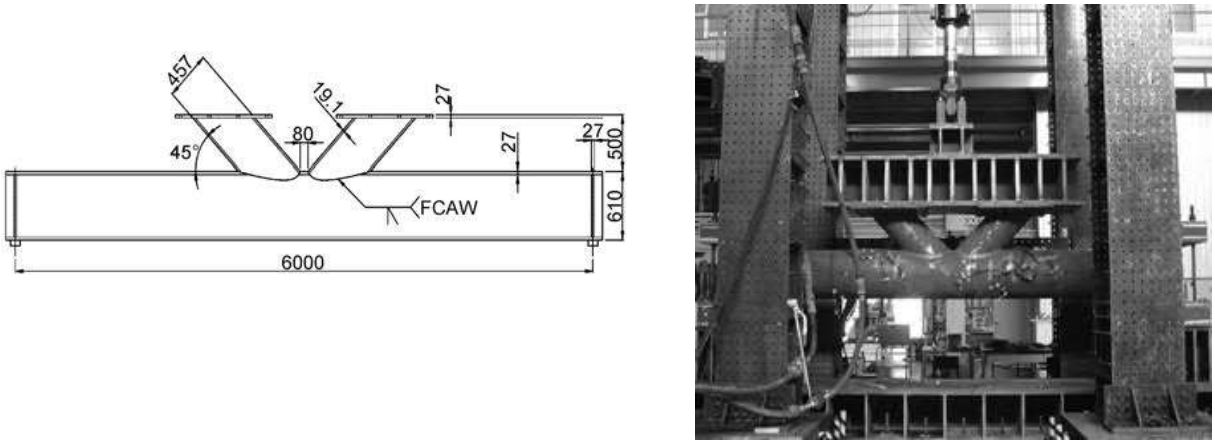


*Figure 115: Jo et al. fatigue test specimen (left) and test set-up (right)*

**Boundary conditions**

The chord tubular is free to deform in axial direction, while rotation fixed. Other support details are not mentioned. However, the bottom of the chord is simply supported in the FEA performed by the authors, therefore specimens are assumed simply supported. The report does not specify if the specimens or FEA are simply supported at a point or edge around the circumference. Simply supported at a point is not likely to be feasible for the fatigue test, therefore simply supported edges at the bottom of the chord, with a width of 200 mm (≈1/3D), are assumed.

The braces are tensile loaded in vertical direction, where loading is applied by a stiff girder, therefore loading can be assumed rigid for FEA. All specimens are loaded by a load ratio of 0.1, the crown heel connection is therefore tensile loaded as well. Load ranges are given, however mean loading or minimum and maximum stresses are not specified.

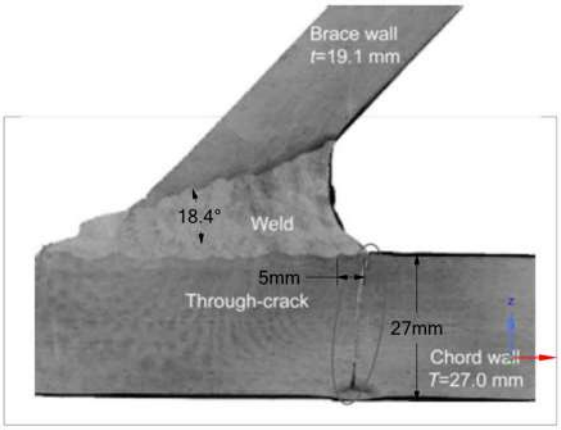


*Figure 116: Jo et al. crown heel through-thickness crack, with joint dimensions sketched*

### E2: Specimen 2-4; Dijkstra et al., CHS T- and X-joints loaded by AF or IPB

**Specimen**
Tubular CHS T- and X-joints. Chord diameters varied from 168 to 914 mm. Specimens were loaded by AF or IPB. A X-joint specimen in the test structure is shown on the left of Figure 117. On the right of Figure 117, the weld geometry at the saddle location for a 914.4-31.7 mm chord and 457.2-15.9 mm brace is shown. Based on the sketched weld geometry, $\delta$ = 77° and $l_e = t/1.5 \approx 11\ mm$ is adopted for the saddle weld geometry of the shell and volume FEA. According to the author, the through thickness crack is shown, however is not clearly visible due to the pdf quality. The assumed crack path is between the blue dashed lines sketched in Figure 117.

A description of crack growth is available, namely for specimens with $0.25 \leq \beta \leq 0.5$, the crack always initiated at the chord weld toe. The crack then propagates along the weld seam. When the crack exceeds about 1/4 of the brace diameter, the crack advances through the thickness of the chord. For specimens with $\beta$ = 1 and $\tau$ = 1, two possible crack initiation points exists, namely at the weld root and chord weld toe. Since only weld toe fatigue cracks are studied in this study, specimens with $\beta$ = 1 and $\tau$ = 1 are not considered. Also, specimens tested in seawater are not included in this study.

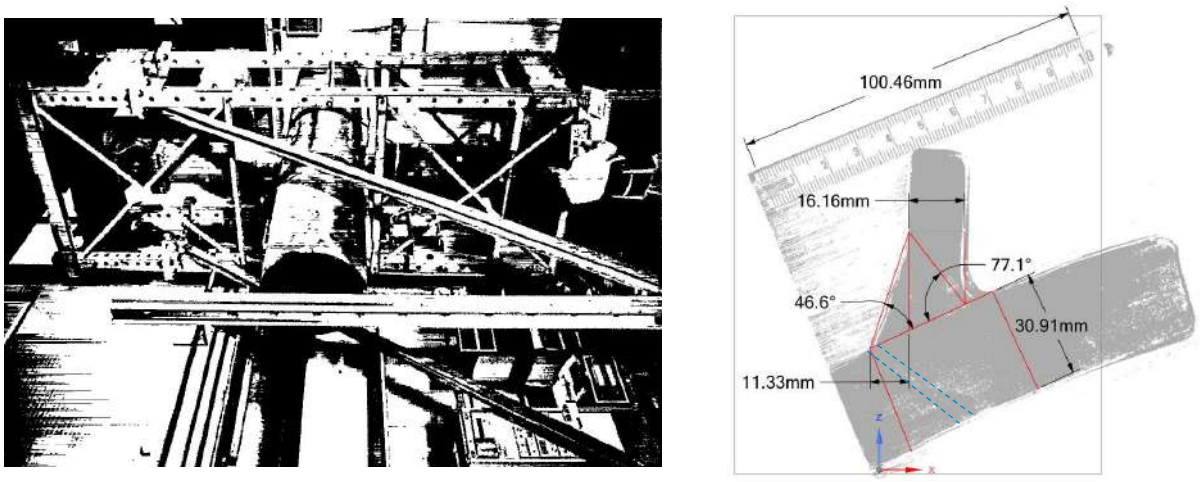


*Figure 117: Fatigue test X-joint Dijkstra et al. (left) and failed saddle with weld dimensions $\delta$ and $l_e$ sketched (right)*

Bracing length of the specimens is not reported, therefore lengths are estimated based on pictures shown in the report. Shell FEA where bracing length was varied with 200 mm and 100 mm for the axial loaded T-joint and IPB T-joint, respectively, equivalent to a reduction of 34% in bracing length, resulted in nodal force and moment differences of about 1.5%. Since loading is defined as rigid in the FEA, loading is applied uniformly around the circumference at the selected nodes which cannot deform relatively to each other. Therefore, forcing is not affected by the tubular joint stiffness differences and therefore bracing length does not affect results much. However, if bracing length would be shortened further to out of proportion lengths, therefore relatively small brace lengths compared to diameters, results are likely to be affected since stress cannot distribute adequately.

**Boundary conditions**
The report states that all supports in test rigs are hinges to avoid secondary effects, therefore simply supported boundary conditions at the bottom side of the chord are assumed. Support reaction forces are distributed through the modelled stiffener located the supports, similar to the K-joint specimen. No details with respect to load application are specified, loading is therefore assumed to be rigid, i.e. the test structure stiffness is assumed to be larger than the test specimens.

### E3: Specimen 5; Zhao et al., SHS T- joint loaded by AF, IPB and OPB

**Specimen**

SHS tubular T-joints, with combined AF, IPB and OPB loading, see Figure 118. Two geometric equivalent specimen are tested, the fatigue tests of these specimen differ in loading amplitudes. In Figure 119 the reported weld geometry is shown. Based on the reported weld geometry, $\delta$ = 45° and $l_e = t = 12\,mm$ is adopted for the weld geometry of the shell and volume FEA. The crack initiation points are reported as shown in Figure 120, illustrating chord weld toe cracks. The failure locations, defined as the location where a through thickness crack is observed, are not specified.

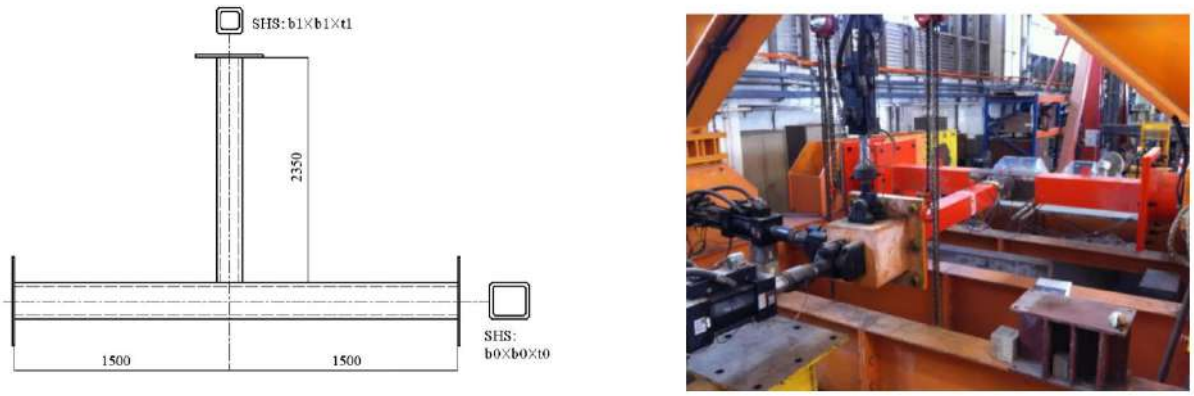


*Figure 118: Zhao et al. fatigue test specimen (left) and test set-up (right)*

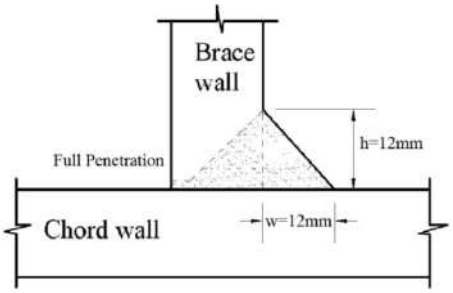


*Figure 119: Zhao et al. weld geometry*

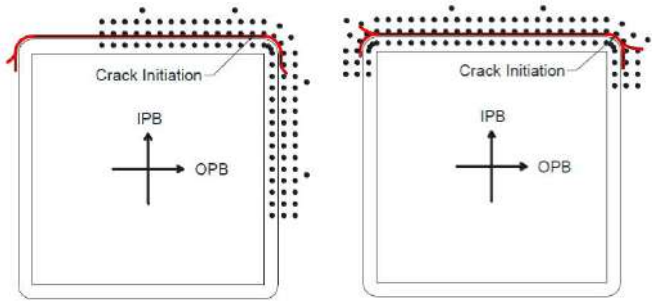


*Figure 120: Zhao et al. crack initiation points specimen load case 1 (left) and load case 2 (right)*

**Boundary conditions**

The report does not specify the supports for the specimens, however based on Figure 118, clamped chord ends are assumed.

All different loading types are applied simultaneously, i.e. no phase difference is present between loading types. It is not reported if loading is applied rigidly. Based on Figure 118, the test structure has a higher stiffness compared to the specimen, therefore rigid loading is assumed.